# Understanding and Controlling the Morphologies of Polyurethane-Based Particles in Aqueous Dispersions

Ellen Jean Wilson



The University of Sheffield

Department of Chemistry

Supervisors: Dr Oleksandr O. Mykhaylyk and Professor Anthony J. Ryan

Thesis submitted for the degree of Doctor of Philosophy

October 2023

# **Declaration**

The work described in this thesis was carried out at the University of Sheffield under the supervision of Dr Oleksandr O. Mykhaylyk and Prof. Anthony J. Ryan, between October 2019 and October 2023 and has not been submitted, either wholly or in part, for this or any other degree. All work is the original work of the author except where acknowledged.

Ellen Wilson

October 2023

Department of Chemistry

University of Sheffield

# **Abstract**

Aqueous polyurethane modified acrylics (PUMAs) offer a low solvent route to environmentally friendly, high-performance coatings for paint producers like AkzoNobel. For effective product development, it is necessary to understand the control of the morphologies in dispersions.

The structural morphology of the polyurethane (PU) component is studied by small angle X-ray scattering (SAXS) on aqueous dispersions with varying compositions. This reveals a major population of spherical particles, and a minor population of supramolecular structures, formed by hydrogen-bonding of acidic fragments, and controlled by the acid content of the composition. Particle radius follows a surface charge model, developed for similarly amphiphilic acrylic statistical copolymers. *In situ* grazing incidence SAXS reveals that particles do not coalesce during drying, remaining discrete, embedded in a matrix comprising the minor population. Particle interfaces, and microphase separation of hard blocks and soft segments within particles, form short-range periodic structures in the films.

Various synthetic routes to aqueous PUMA dispersions are considered. It is found that adding acrylic monomer as the solvent for PU prepolymer synthesis yields the most uniform PUMA particles with the least scattering contribution from interparticle interactions. SAXS analysis is carried out on 16 PUMAs (or PU/polystyrenes) and their precursors, made with 3 methacrylic and styrene monomers, at 4 PU/monomer ratios. Structural models, featuring homogeneous spheres, core-shell particles and dissolved supramolecular structures, are applied to analyse SAXS profiles, and reveal that precursor particle morphology depends on monomer/PU compatibility. For PUMAs and PU/polystyrenes, hydrophobic butyl methacrylate and styrene generate core-shell

particles, while methyl methacrylate's higher water solubility results in more intricate morphologies. Morphology evolution during polymerisation of precursors to PUMAs is studied by time-resolved *in situ* SAXS. Application of structural models to the time-resolved data, on a representative composition, is interpreted in terms of monomer migration from reservoir droplets, and the polymerisation and phase separation kinetics.

# **Conferences and Awards**

September 2020 S4SAS - virtual meeting

February 2021 Global Women's Breakfast – Virtual

May 2021 Online Short Talk - IUPAC\_MACRO 2020+ - Virtual

conference

May 2021 **Poster Presentation** – SGS Showcase – Virtual

February 2022 Global Women's Breakfast – Sheffield, UK

June 2022 Poster Presentation- International Colloids Conference –

Lisbon, Portugal

June 2022 Oral Presentation – Bombannes Summer School on

Scattering Methods Applied to Soft Condensed Matter -

Bombannes, France

June 2022 Oral Presentation – Coatings Science International –

Noordwijk, Netherlands

July 2022 Oral Presentation – Macro Young Researchers' Meeting –

Nottingham, UK

September 2022 Oral Presentation – Polymer Group Third Year

Presentations - Sheffield, UK

November 2022 GI-SAXS Conference – Hamburg, Germany

April 2023 Poster Presentation – Faraday Joint Interest Group

Meeting – Sheffield, UK

June 2023 **Oral Presentation** – Coatings Science International,

Noordwijk, Netherlands

Outstanding Online Short Talk Award at IUPAC Macro 2020+ Virtual Meeting

**Science Award** for 30-minute oral presentation at Coatings Science International 2022

# Acknowledgements

Firstly, I would like to thank Sasha and Tony for their help and support throughout this project. The challenges that the chemistries have presented could not have been overcome without the expertise of a physicist and a chemist, and I count myself fortunate to have had access to the best. It has been a pleasure being a part of the Ryan-Mykhaylyk group, and a joy to work in D42 with a fantastic bunch of people.

I am extremely grateful for AkzoNobel's generous funding of this project, and everybody who has contributed: Niels Elders, Mo Amirilargani, Keimpe van den Berg, Lambert Baij, Nico van Beelen, Annemie Brinkman, Connie Hermans, Neal Williams, Rob Bradley and Krisztina Erdelyi-Brooks. Thanks in particular to the synthesis skills of Niels and Mo in Sassenheim, and Rob and Krisztina in Slough, for producing all of the samples used across all four years of the project. Additionally, Niels' contributions to the data interpretation and continued project development have been invaluable, and I'm extremely appreciative for all the time he's given me.

Thank you to the staff at I22 Diamond Light Source (SM30206), Tom, Courtney, Adam and Matt for their contributions to the collection of *in situ* reaction data.

There are too many people who have supported me along the way to list them here, but I hope you know who you are, and how grateful I am. However, I cannot not overlook the fact that this thesis would not exist without Luke. Thank you for showing me unwavering love (I know I've been a nightmare at times), for being my biggest cheerleader, for encouraging me to take opportunities when imposter syndrome said otherwise, for being a much better cook than I am, and for being there for me through absolutely everything. I can't wait to adventure in Lund.

# **Author Contributions**

Syntheses of the polyurethane dispersions were carried out by Niels Elders,<sup>a</sup> with the exception of the sample HB50\_SS1000a, which was synthesised by Krisztina Erdelyi-Brooks.<sup>b</sup>

All PUMAs discussed in Chapter 5 were synthesised by Niels Elders,<sup>a</sup> and all PUMAs discussed in Chapter 6 were synthesised by Mohammad Amirilargani.<sup>a</sup>

Gel permeation chromatography was carried out by Connie Hermans.<sup>c</sup> The preparation of samples and initial analysis of data was done by Niels Elders.<sup>a</sup>

Matrix assisted laser desorption ionisation data collection was done by Sophia van Mourik,<sup>d</sup> and atomic force microscopy by Anna Newman.<sup>d</sup>

All other work was done by me, under the supervision of my industry supervisor, Dr Niels Elders,<sup>a</sup> and academic supervisors, Dr Oleksandr Mykhaylyk<sup>d</sup> and Prof. Anthony Ryan.<sup>d</sup>

# **Affiliations**

- a. Akzo Nobel Car Refinishes BV, Department of Resin Technology, 2717 AJ
   Sassenheim, The Netherlands
- b. Formerly of Akzo Nobel, Wexham Road, Slough, SL2 5DS, UK
- c. Akzo Nobel Car Refinishes BV, Department of Analytical Services, 2717 AJ
   Sassenheim, The Netherlands
- d. Department of Chemistry, University of Sheffield, Western Bank, Sheffield S37HF, UK

# <u>Nomenclature</u>

Abbreviation/Symbol	Definition	Units
θ	Scattering Angle	0
ξ	Scattering Length Density	cm <sup>-2</sup>
$ ho_m$	Mass density	gcm <sup>-3</sup>
$\sigma^*$	Multiplicative standard deviation	
$\gamma(r)$	Correlation function	
$oldsymbol{\phi}$	Volume fraction	
$oldsymbol{\phi}_{ ext{PU,AF}}/oldsymbol{\phi}_{ ext{PU,tot}}$	Fraction of PU found as acidic fragments	Vol frac
X	Mole fraction	
$\Psi(\mathbf{r})$	Distribution function of parameter r	
A	Scattering amplitude	cm <sup>-1/2</sup>
AFM	Atomic Force Microscopy	
a.u.	Arbitrary units	
b	Kuhn length	Å
ВА	Butyl Acrylate	
BD	Butane diol	
<b>b</b> e	Scattering length of an electron	cm
Bis-GMA	Bisphenol-A-glycidyl dimethacrylate	
BMA	Butyl methacrylate	
$B_{v}$	Porod constant	cm <sup>-1</sup>
CS <sub>B</sub>	Cross-sectional area of molecule B	cm <sup>2</sup>
C <sub>tot</sub>	Total concentration	mass %
d	Correlation Length	nm
DBTDL	Dibutyl tin dilaurate	
DLS	Dynamic light scattering	
DMPA	Dimethylolpropionic acid	
DSC	Differential scanning calorimetry	
EDA	Ethylene diamine	
ESRF	European Synchrotron Radiation Facility	
FTIR	Fourier transform infrared	
GISAXS	Grazing incidence small angle X-ray scattering	
GPC	Gel permeation chromatography	
HB	Hard block	
HDI	Hexamethylene diisocyanate	
HEMA	Hydroxyethyl methacrylate	
HMDI	Hydrogenated methylene diphenyl diisocyanate	
HSPs	Hansen solubility parameters	

**iBMA** iso-Butyl methacrylate

IPDI Isophorone diisocyanate

*I(q)* Scattered intensity cm<sup>-1</sup>

**k** Fraction of anionic groups at particle interface

**L** Length of polymer chain Å

**m** Number of scattering populations

MALDI Matrix-assisted laser desorption ionisation

 $M_{B,p}$  Mass of B per particle

MDI Methylene diphenyl diisocyanate

MEK Methyl ethyl ketone
MMA Methyl methacrylate

**M**<sub>n</sub> Number average molecular weight

 $M_p$  Mass of one particle

 $M_{\rm w}$  Molecular weight gmol<sup>-1</sup>

N Number of particles

**n** Number of Kuhn lengths per chain

 $N_A$  Avogadro's number Mol<sup>-1</sup>

 $N_{B,p}$  Number of molecules of B per particle

**n**<sub>i</sub> Number of atoms of i per polymer repeat unit

**NMP** *N*-methyl-2-pyrrolidone

PA Polyacrylate

PBMA Pol(butyl methacrylate)
PDI Polydispersity index
PEG Polyethylene glycol

**PiBMA** Poly(*iso-b*utyl methacrylate)

PIW Polymer-into-water emulsification

**PMMA** Poly(methyl methacrylate)

P(q) Form factorPS Polystyrene

PTMO Poly(tetramethylene oxide)

**PU** Polyurethane

**PUD** Polyurethane dispersion

**PUMA** Polyurethane modified acrylic

Q'Relative scattering invarianta.u.qScattering vectorÅ-1rRadiusnmRMean radiusnm

**rbf** Round-bottomed flask

 $egin{array}{lll} m{r_{co}} & & {\sf Radius~of~particle~core} & & {\sf nm} \\ m{R_{co}} & & {\sf Mean~radius~of~particle~cores} & & {\sf nm} \\ m{R_g} & & {\sf Radius~of~gyration} & & {\sf nm} \\ \end{array}$ 

RT Room temperature

**SA**<sub>frac</sub> Surface area fractional coverage of hydrophiles

SAXS
Small angle X-ray scattering
SED
Solvent emissions directive
SLD
Scattering length density
SLS
Static light scattering

S(q)Structure factorSSSoft segment

tBHPtert-Butyl hydroperoxidetcTransmission coefficient

**TEA** Triethylamine

**TEM** Transmission electron microscopy

 $T_g$ Glass transition temperature°C $t_s$ SAXS sample thicknesscm $t_{sh}$ Particle shell thicknessnm $T_{sh}$ Mean particle shell thicknessnm

**USAXS** Ultra-small angle X-ray scattering

**v** Parameter relating to solvent interactions

V<sub>B</sub> Volume of molecule B cm<sup>3</sup>

VOCs Volatile organic compounds

 $V_p$  Volume of one particle cm<sup>3</sup>

WAXS Wide angle X-ray scattering

WIP Water-into-polymer emulsification

**x** Fraction of acrylic inside particles Vol frac

 $\mathbf{z}_i$  Electrons per atom of i

# **Contents**

D	eclarati	on		ii
Α	bstract			. iii
C	onferer	nces a	and Awards	v
Α	cknowl	edgei	ments	. vi
Α	uthor C	ontri	butions	vii
N	omencl	lature	<u> </u>	viii
1	Cha	pter	1 - Introduction	1
	1.1	Coa	tings	1
	1.2	Poly	mers	2
	1.3	Poly	rurethane	3
	1.4	Aqu	eous Polyurethane Dispersions	7
	1.4.	1	Polyurethane Dispersion Methodologies	10
	1.5	Poly	rurethane Modified Acrylics	14
	1.6	Sma	ıll-angle X-ray Scattering	18
	1.6.	1	Applications of SAXS	19
	1.6.	2	In situ SAXS methods for dispersions and colloidal systems	26
	1.7	Aim	S	28
	1.8	Refe	erences	30
2	Cha	pter	2 - Materials and Methods	36
	2.1	Mat	erials	36
	2.1.	1	Supplied Materials	36
	2.1.	2	PUD Syntheses	36
	2.1.	3	Reaction of 2:1 HMDI:DMPA	39
	2.1.	4	PUMA Syntheses	39
	2.2	Cha	racterisation of Materials by Small-Angle X-ray Scattering	41
	2.2.	1	General Principles	41
	2.2.	2	Grazing Incidence SAXS	45
	2.2.	3	Scattering by Particle Dispersions	45
	2.2.	4	SAXS Data Treatment	50
	2.2.	5	SAXS Data Collection	52
	2.2.	6	In-situ SAXS	54
	2.2.	7	Intermediate Sample Aging Check by SAXS	63
	2.3	Oth	er Characterisation Methods	64
	2.3.	1	Solution Density Measurements	64

	2.3	.2	Atomic Force Microscopy	65
	2.3	.3	Matrix Assisted Laser Desorption Ionisation	65
	2.3	.4	Fourier Transform Infrared Spectroscopy	66
	2.3	.5	Gel Permeation Chromatography	66
	2.4	Refe	erences	68
3	Cha	apter	3 – Investigation Into the Morphologies of Aqueous Polyurethane Dispersions	70
	3.1	Intro	oduction	70
	3.2	Sam	ples	71
	3.3	Resu	ults and discussion	72
	3.3	.1	Investigation into Scattering from Microphase Separation	75
	3.3	.2	Investigation into Scattering from Internal Water Pockets	76
	3.3	.3	Investigation into A Second Population of Acidic Fragments	77
	3.3	.4	Analysis of PUDs as Two-Population Systems	83
	3.3	.5	Particle Size Control	90
	3.4	Con	clusions	94
	3.5	Refe	erences	96
4	Cha	apter 4	4 - Morphology Evolution During Drying of Polyurethane Dispersions	98
	4.1	Intro	oduction	98
	4.2	Sam	ples and data collection	99
	4.3	Resu	ults and Discussion	. 100
	4.3	.1	Morphology Evolution in situ During the Drying of PU Dispersion	. 100
	4.3	.2	Reversibility of Film Formation	. 105
	4.3	.3	Investigation into the Effect of PU Composition on the Film Morphology	. 106
	4.4	Con	clusions	.111
	4.5	Refe	erences	. 113
5	Cha	apter !	5 - Investigations Into PUMA Synthesis Methods	. 115
	5.1	Intro	oduction	. 115
	5.1	.1	The PU Seed Particle Method	115
	5.1	.2	The Monomer Solvent Method	115
	5.1	.3	Other variations of PUMA particle synthesis	118
	5.1	.4	The Emulsification Step	118
	5.2	Sam	ples	120
	5.3	Resu	ults and Discussion	120
	5.3	.1	PU Seed Particle vs Monomer Solvent Methods	120
	5.3	.2	Chain Extension Post Acrylic Polymerisation	125
	5.3	.3	Emulsification	

	5.4	Conclusions		
	5.5	References	131	
6	Cha	apter 6 – Effect of PUMA Composition on Structures in Dispersion	133	
	6.1	Introduction	133	
	6.2	PUMA Samples	134	
	6.3	SAXS Models	136	
	6.3	.1 Model A – Mixed Phase Spherical Particles and Supramolecular Structures	136	
	6.3	.2 Model B – Core-shell Particles and Supramolecular Structures	139	
	6.4	Static SAXS analysis	142	
	6.4	.1 Precursor Dispersions	142	
	6.4	.2 PUMA Dispersions	155	
	6.5	In Situ Polymerisation of Precursors to PUMAs	159	
	6.5	.1 Selection of Reaction Conditions	159	
	6.5	.2 Polymerisations of iBMA PUMAs	163	
	6.5	.3 Polymerisations of BMA and Styrene PUMAs	168	
	6.5	.4 Polymerisation of MMA PUMAs	170	
	6.6	Conclusions	174	
	6.7	References	177	
7	Cha	apter 7 - Conclusions and Future Work	180	
	7.1	Conclusions	180	
	7.2	Future Work	185	
	7.3			
8		References		
•	Cha	Referencesapter 8 - Appendices	188	
	<b>Cha</b> 8.1		188	
		apter 8 - Appendices	188 189	
	8.1	Time Resolved GPC for PU Prepolymer	188 189 191	
	8.1 8.2	Time Resolved GPC for PU Prepolymer  PUD SAXS data plotted on absolute scale of intensity	188 189 191	
	8.1 8.2 8.3	Time Resolved GPC for PU Prepolymer  PUD SAXS data plotted on absolute scale of intensity  MALDI Sample Preparation and Data Collection	188189191192	
	8.1 8.2 8.3 8.4	Time Resolved GPC for PU Prepolymer  PUD SAXS data plotted on absolute scale of intensity  MALDI Sample Preparation and Data Collection  PUD Solution Density Measurements	188189191192194	
	8.1 8.2 8.3 8.4 8.5	Time Resolved GPC for PU Prepolymer  PUD SAXS data plotted on absolute scale of intensity  MALDI Sample Preparation and Data Collection  PUD Solution Density Measurements  Subtraction of thermal background from film scattering	188189191192194	
	8.1 8.2 8.3 8.4 8.5 8.6	Time Resolved GPC for PU Prepolymer  PUD SAXS data plotted on absolute scale of intensity  MALDI Sample Preparation and Data Collection  PUD Solution Density Measurements  Subtraction of thermal background from film scattering  The Gaussian Distribution	188189191192194195	
	8.1 8.2 8.3 8.4 8.5 8.6 8.7	Time Resolved GPC for PU Prepolymer  PUD SAXS data plotted on absolute scale of intensity  MALDI Sample Preparation and Data Collection  PUD Solution Density Measurements  Subtraction of thermal background from film scattering  The Gaussian Distribution  Lognormal Distribution of Particle Sizes	188189191192194195	
	8.1 8.2 8.3 8.4 8.5 8.6 8.7	Time Resolved GPC for PU Prepolymer  PUD SAXS data plotted on absolute scale of intensity  MALDI Sample Preparation and Data Collection  PUD Solution Density Measurements  Subtraction of thermal background from film scattering  The Gaussian Distribution  Lognormal Distribution of Particle Sizes  The "blob" model	188189191192194195195	
	8.1 8.2 8.3 8.4 8.5 8.6 8.7 8.8	Time Resolved GPC for PU Prepolymer  PUD SAXS data plotted on absolute scale of intensity  MALDI Sample Preparation and Data Collection  PUD Solution Density Measurements  Subtraction of thermal background from film scattering  The Gaussian Distribution  Lognormal Distribution of Particle Sizes  The "blob" model  Densities of Polymethacrylics, Polystyrene, and Monomers  Code for two-population fitting of PUD and PUMA samples	188189191192194195197	
	8.1 8.2 8.3 8.4 8.5 8.6 8.7 8.8 8.9	Time Resolved GPC for PU Prepolymer  PUD SAXS data plotted on absolute scale of intensity  MALDI Sample Preparation and Data Collection  PUD Solution Density Measurements  Subtraction of thermal background from film scattering.  The Gaussian Distribution  Lognormal Distribution of Particle Sizes  The "blob" model.  Densities of Polymethacrylics, Polystyrene, and Monomers.  Code for two-population fitting of PUD and PUMA samples  0.1 Code used for fitting of supramolecular structures (pop2)	188189191192194195195197	

8.10.4	Code for fitting of homogeneously phase-mixed PU/acrylic particles	199
8.10.5	Code for fitting of core-shell PUMA or PU/monomer particles	200
8.10.6	Code for partially reacted core-shell particles	202
8.11 Re	ferences	206

# **Chapter 1 - Introduction**

## 1.1 Coatings

Decorative paints generally comprise four key ingredients: pigments, binders, additives and solvent. The pigment provides colour and hiding properties whereas the polymer binder delivers mechanical properties and adhesion. The binding component of a coating forms a film by either coalescence of particles or cross linking. In the case of decorative paint products, film formation occurs during loss of the majority of the solvent. Wall and ceiling paints are predominantly aqueous systems whereas wood and metal paints are traditionally solvent based. Additives are required for specific functionality and the solvent carries through dissolution or dispersion of all the other ingredients.

Most solvents are organic - including alcohols, hydrocarbons, esters, glycol ethers and ketones — or water.¹ Some, such as White Spirit or lacquer thinners, are mixtures of these chemical substances. Most of these organic solvents are classed as volatile organic compounds (VOCs), especially those with low boiling points. In 1999, the Solvent Emissions Directive (SED) was created "to prevent or reduce the direct and indirect effects of emissions of volatile organic compounds into the environment, mainly into air, and the potential risks to human health, by providing measures and procedures to be implemented for certain activities".² This applied to both coatings manufacturing and applications of coatings, due to the high volumes of VOCs present in products at that time. In addition to their global warming potential, a 2002 study found increased cases of lung cancer for those employed as painters and lacquerers, and various cancers for paint and varnish plant workers.³ Although the SED ended in

2014, there is still drive for a reduction in the use of VOCs. Continual legislative pressure on manufacturers has resulted in an increase in the availability and variety of aqueous coatings as low-VOC alternatives.<sup>4–7</sup>

### 1.2 Polymers

The binding component of paints is usually composed of polymers, such as polyacrylics, polyvinyls, alkyds, or polyurethane (PU). Polymers are high molecular weight molecules composed of long chains of monomer units linked together. Homopolymers consist of a single type of monomer unit (Figure 1.1a), whereas copolymers are made up of two or more different types of monomers. Copolymers can have different arrangements of monomers, ranging from block copolymers (Figure 1.1b) to statistical copolymers (Figure 1.1c). Statistical copolymers exhibit a random distribution of monomer units. Block copolymers exhibit the structure of two homopolymers linked together, with the two types of monomers arranged in distinct regions.

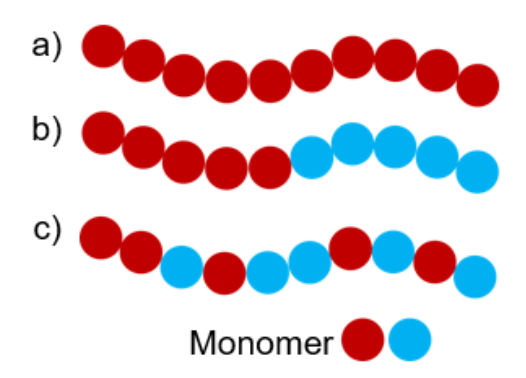


Figure 1.1: Schematic of a) a simple homopolymer, b) a block copolymer, and c) a statistical copolymer where each circle represents a single monomer unit

Polymerisations are generally classified into two broad categories: addition polymerisation and step-growth polymerisation. An addition polymer possesses the same molecular formula as the monomer(s) from which it is derived, such as polystyrene shown in Figure 1.2.

Figure 1.2: Polymerisation of styrene to form polystyrene as a representative example of addition polymerisation.

For most step-growth polymers, the structure of the polymer differs from that of the monomers, and it can usually be degraded back to the monomers by chemical means. In most cases, for example the formation of polyester (Figure 1.3) from a hydroxy acid, the polymer lacks atoms that are present in the monomer due to formation of a byproduct small molecule condensate.

$$n \text{ HO-R} \xrightarrow{O} \text{HO} \stackrel{O}{\underset{\text{n-1}}{|}} \text{O} \xrightarrow{} \text{HO} \text{H}_2\text{O}$$

Figure 1.3: Condensation polymerisation of a hydroxy acid to form a polyester with loss of water.

## 1.3 Polyurethane

Not all step-growth polymerisations form a condensate. PU is a step-growth polymer with a structure that differs from the monomers due to the proton transfer, from the alcohol to the isocyanate, that occurs during the urethane reaction (Figure 1.4).

$$R-N=C=O \longrightarrow R \xrightarrow{H} C \xrightarrow{O} R$$

Figure 1.4: Schematic showing the proton transfer occurring during the urethane formation reaction from an isocyanate and an alcohol.

PU is known for its ability to form abrasion-resistant films that are flexible, tough and solvent resistant.<sup>7,10</sup> PU is synthesised by the reaction of aliphatic or aromatic diisocyanates with a blend of reactive, di-functional monomers. Traditionally, this blend comprises a long-chain polyol and a chain extender such as a short-chain diol or diamine. As such, there is some statistical character to the structure of PUs. Common polyols, such as hydroxyl-terminated polyester,<sup>6,11,12</sup> polyether<sup>12–19</sup> or polycarbonate,<sup>15,20</sup> incorporate soft, flexible regions into the polymer chains. In contrast, rigid polar segments are formed from diisocyanate and chain extender.<sup>18,21,22</sup> Selection of a diamine chain extender results in urea linkages into the polymer chain structure (Figure 1.5).<sup>5,21,22</sup>

Figure 1.5: Formation of polyurethane-ureas from diamines, diisocycanates and polyols

Alternatively, examples can be found of PU chain extension with water.<sup>11–13</sup> Its reaction with isocyanates also produces urea linkages via formation of a carbamic acid and release of CO<sub>2</sub> to generate an amine, that subsequently reacts with an isocyanate (Figure 1.6).

Figure 1.6: Chain extension of PU using water with the formation of a carbamic acid and subsequent release of CO<sub>2</sub>

The superior mechanical and film formation properties of PUs are attributed to phase separation within the polymer. This occurs because the soft polyol phase can partition on the microscale from the polar, hydrogen-bonding urethane and urea hard blocks. This gives PUs block copolymer character. Furthermore, a high proportion of long, flexible polyol in the polymer chains can produce a crystalline soft segment (Figure 1.7).<sup>5,23,24</sup>

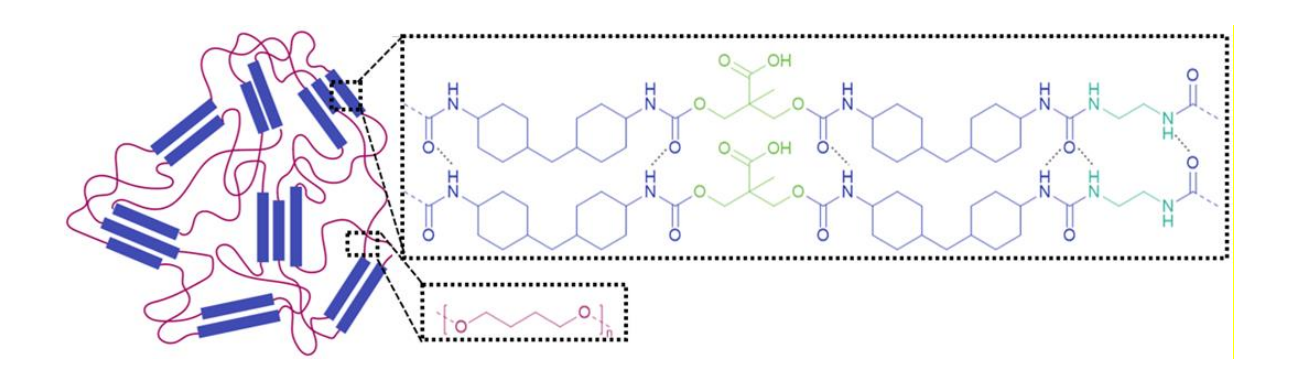


Figure 1.7: Schematic illustrating the phase separation of polyurethane into hard blocks that can hydrogen bond, and polyether soft blocks, for the compositions study in this thesis.

It has long been known that the properties of PUs can be tailored by systematic variation of the chemical structures and relative proportions of these polar and non-polar segments. As such, a wide range of properties can be targeted with PU coatings. In 1998, Sánchez-Adsuar et al. reported an increase in hard and soft phase mixing as the hard block content increased. The polyether chain mobility was restricted by the rigid regions, preventing phase separation of the two components. In addition, the observed wider molecular weight distribution obtained at high polyol content was

attributed to a reduced reaction rate; when there is a larger proportion of polyol, the proportion of reactive isocyanate groups is diluted.<sup>25</sup>

According to Kim at al., the degree of phase separation of PU can be reduced by a decrease in the length of polyol.<sup>26</sup> In their work, the glass transition temperatures (T<sub>g</sub>s) of the hard and soft segments shifted closer as the polyester (soft segment) chain length decreased, eventually converging. This is indicative of phase mixing, as measured by differential scanning calorimetry (DSC). Chen and co-workers observed the same trend with polyethylene glycol (PEG) (Table 1.1).<sup>13</sup> The T<sub>g</sub>s migrated as PEG chain length decreased, becoming indistinguishable at M<sub>n</sub>=400 gmol<sup>-1</sup>. These results were found to be true for isocyanates based on both toluene diisocyanate and isophorone diisocyanate (IPDI).

Table 1.1: DSC results showing change in hard and soft segment  $T_g$ s with PEG chain length, reported by Yang et al.<sup>13</sup>

	M <sub>n</sub> of PEG /g mol <sup>-1</sup>	T <sub>g</sub> soft segment /°C	T <sub>g</sub> hard segment /°C
	400	41	
Toluene	600	10	48
Diisocyanate- based	1000	8	50
	2000	-15	55
	400	-4	
Isophorone	600	-8	45
Diisocyanate- based	1000	-8	46
	2000	-17	50

Runt and co-workers have demonstrated that the chemistry of the polyol is influential on the degree of phase separation.<sup>15</sup> For example, using small-angle x-ray scattering (SAXS) they quantified the degree of phase separation with different polyols. As expected, the results indicated that separation was up to three times greater using a polyether polyol than when using a polycarbonate, as the latter can form hydrogen-

bonding pseudo cross links with the hard segment, whereas the hydrogen bonding capabilities of the polyether are significantly less.

Xiu et al. demonstrated that polyester soft phases have a higher degree of crystallinity than polyethers,<sup>23</sup> with increased interactions between the chains. Consequently, the films formed from polyester-based PUDs exhibited improved mechanical properties. However, Sonnenschein and co-workers have demonstrated that high crystallinity is still achievable with a polyether soft segment.<sup>24</sup> Their "almost co-continuous lamellar structures" demonstrated exceptional tensile and elastic properties in comparison with alternative, non-crystalline PUs of similar compositions.

## 1.4 Aqueous Polyurethane Dispersions

Originally, all polyurethanes were made in organic solvents. The discovery that water can also be used as the solvent to disperse PU particles, when hydrophilic monomers are incorporated, led to the appearance of aqueous PU dispersions (PUDs) on the market in the 1960's. In response to environmental legislative pressure for low VOC, "green" chemistries, the range of available high performance, aqueous PUDs has expanded. 4-7,10,16,19,27,28 Hydrophilic groups incorporated into the chain act as "internal emulsifiers" that ensure colloidal stability. These can be non-ionic – for example terminal or lateral poly(ethylene oxide) segments 5,16 – or ionic, including cationic and anionic variants 16. Non-ionic emulsifying groups offer advantages in terms of low viscosities. However, ionic monomers are generally the preferred option for dispersions with good stability and films with low water sensitivity. 5,14

Anionic monomers are the most popular choice of hydrophilic stabilising group.<sup>5</sup> Carboxylate, sulfonate and phosphate-containing monomers are widely used and studied. A base, often triethylamine, ensures deprotonation of the acid groups and

therefore colloidal stability.<sup>4,5,7,29</sup> A recent review from Jaudouin et al. identifies dimethylolpropionic acid (DMPA) (Figure 1.8) as the most frequently incorporated hydrophilic monomer, which is known to be attractive in terms of cost and effective performance.<sup>29</sup> Although the primary hydroxyl groups are already more reactive,<sup>22</sup> the steric hindrance of DMPA further ensures side reactions of isocyanate with the carboxylic acid group are avoided.<sup>5,16</sup>

Figure 1.8: Structure of dimethylolpropionic acid

Hydrophilic acidic moieties favourably migrate to the particle-water interface of PUD particles (Figure 1.9). There are many literature examples demonstrating that increasing acid content increases interfacial tension and repulsion between polymer particles, <sup>5,12,13,30</sup> as well as controlling particle size. <sup>16,19,25,30–33</sup>

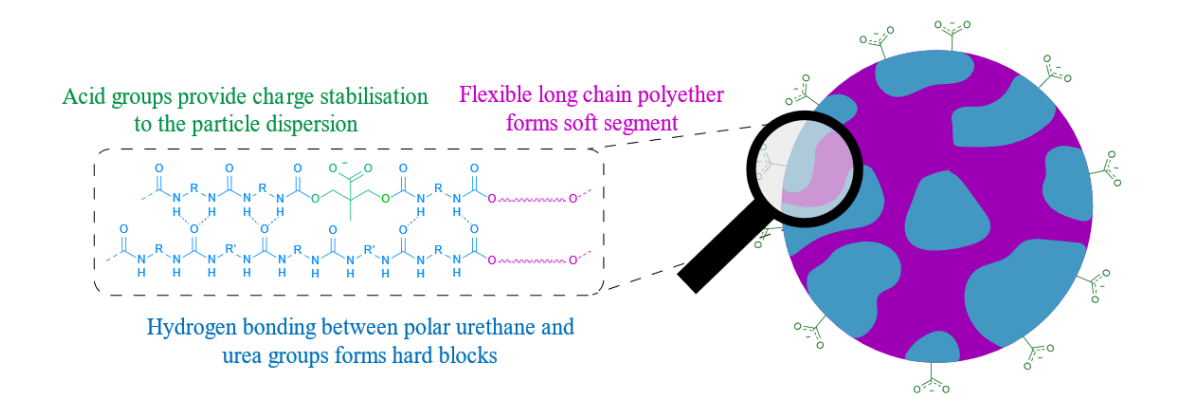


Figure 1.9: Structure of a polyurethane particle in aqueous dispersion with phase separation and the migration of hydrophilic acid groups to the polymer/water interface

It is well documented that the size of PUD particles can be controlled by DMPA content. Satguru et al. identified a critical DMPA concentration of 0.25 mmolg<sup>-1</sup> to form stable particles with PUs comprising IPDI and polycaprolactone diol. Alang et al. studied the stability of PUDs containing DMPA, with a backbone of

IPDI and a polyether or polyester.<sup>30</sup> They found that, at a carboxylic acid group content of 1.2 wt%, particles reached a minimum size. When this was increased to 1.5 wt%, the polymer was fully soluble preventing a dispersion forming. They also reported that, at low acid content, one polyester - poly(hexane neopentyl adipate) glycol - gave smaller particles than when substituted by another - poly(ethylene—butylene adipate) glycol. They propose that, when the acid content is low, the structure of the polyol becomes a contributing factor in the stability of the polymer particles in dispersion.

According to Satguru et al, DMPA-stabilised PUDs are swollen with water. <sup>16</sup> Based on the results from small- angle neutron scattering (SANS), they proposed a morphology of water rich areas distributed throughout the polymer particles. More recent publications are in agreement with these findings.  $^{6,10,27,31,34,35}$  Li et al. studied the morphology of isocyanate-terminated PU chains in dispersion using self-consistent field theory. <sup>27</sup> The theoretical results are shown in Figure 1.10 as a plot of water volume fraction ( $\phi$ ) vs distance from the particle centre (r). This shows that, for PUs made with IPDI, polyether and DMPA, a PU particle could contain as much as 40 vol% water (Figure 1.10, closed circles) at the centre (r = 0 nm) when the particle contains 5 wt% DMPA. The calculations also suggest that, although a peak in data set 1 (Figure 1.10, open circles) shows that most of the hydrophilic DMPA is on the outside of the particles, a significant volume of water is trapped inside the particle, most likely attached to the minority of interior DMPA moieties. This theoretical finding rationalises the presence of water within an otherwise hydrophobic structure.

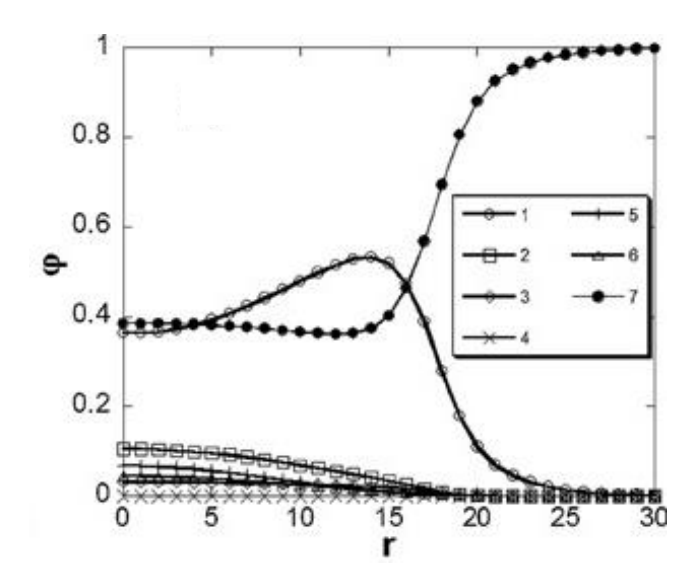


Figure 1.10:Morphology investigations of PU particles using self-consistent field theory.<sup>27</sup> Equilibrium radial volume fraction  $\varphi(r)$  distribution of each prepolymer and water as a function of distance from the (swollen) micelle centre r (nm). The labels refer to different PU molecule compositions: (1) IPDI<sub>4</sub>-DMPA<sub>2</sub>-Polyol<sub>1</sub>, (2) IPDI<sub>2</sub>-Polyol<sub>1</sub>, (3) IPDI<sub>3</sub>-DMPA<sub>1</sub>-Polyol<sub>2</sub>, (6) IPDI<sub>4</sub>-DMPA<sub>1</sub>-Polyol<sub>2</sub>, and (7) water.

#### 1.4.1 Polyurethane Dispersion Methodologies

The earliest method of PUD synthesis is widely recognised as "the acetone method".<sup>5,28</sup> Many modifications and alternatives have since been developed, yet all begin with the formation of a prepolymer. These are relatively short PU chains capped with terminal isocyanate groups, usually formed in a polar organic solvent such as acetone, *N*-methyl-2-pyrrolidone (NMP) or methyl ethyl ketone (MEK). A chain extender is reacted into the polymer later in the process to form linkages with the terminal isocyanates, giving the final, high molecular weight PUs.

Xu et al. have investigated various prepolymer synthesis methods comparing all reactants added simultaneously in the one-shot method to sequential addition of polyols in two-shot methods.<sup>30</sup> They report that both variations, after chain extension, gave dispersions of similar shelf-life, average particle size and appearance. These findings are in opposition to the common belief that a two-shot method is necessary for an even distribution of acidic monomers in PU chains.<sup>30</sup> In principle, this seems

reasonable due to the difference in reactivity of DMPA and polyols.<sup>36</sup> Che et al. provide evidence for this, reporting that the stability of PUDs is related to the feeding rate of the reactants.<sup>37</sup>

lonomer syntheses require a neutralisation step, such that the prepolymer can be dispersed in water, which can be done before or after dispersal. Nanda and Wicks studied the effect of neutralisation, in relation to dispersion, for both the acetone<sup>6</sup> and prepolymer mixing<sup>31</sup> methods. Dispersions that were neutralised 70% before and 30% after dispersion gave larger particles and were more viscous than those that were neutralised to a greater proportion pre-dispersion. They propose that any protonated acid groups are trapped inside the particle upon dispersion. Then, when deprotonated upon dispersion, more water is dragged into the particle interior.

#### 1.4.1.1 The Acetone Process

For the acetone process, chain extension is carried out in an organic solvent, such as acetone or MEK (Figure 1.11). The chains are neutralised in the case of ionomers, then dispersed in water and the organic solvent distilled from the dispersion. This method is known to give highly repeatable results and good control of products as the reactions are carried out in homogeneous media,<sup>4–6</sup> and the passage from organic to aqueous solvation is gradual.<sup>11</sup>

Figure 1.11: Schematic of the acetone process for PUD synthesis

#### 1.4.1.2 The Prepolymer Mixing Method

Large volumes of organic solvent can be avoided by use of the alternative prepolymer mixing method (Figure 1.12). In this case, the prepolymer is dispersed in water prior to chain extension. Only small volumes of organic solvent may be required to reduce the viscosity of the prepolymer for dispersion.<sup>4–6,11,26</sup> Xu and co-workers have studied the stability of PUDs thinned with various solvents.<sup>30</sup> They report that NMP resulted in more stable dispersions than acetone, MEK or *N,N*–dimethyl formamide. They suggest that this is because the NMP remains at the particle interface once dispersed in water.

Figure 1.12: Schematic of the prepolymer mixing method for PUD synthesis

Upon dispersion, prepolymers will begin to react slowly with the water. A diamine is generally employed as chain extender as its reaction with isocyanate is far faster than that of water, especially when the temperature is kept sufficiently low<sup>5,19,22,26,28</sup>. Although the pre-polymer mixing process offers the economic and environmental advantage of lower solvent usage, there is a penalty in the quality of the resulting products. Chain extension in heterogeneous media gives lower quality dispersions, with a greater variation in polymer structures.<sup>4,5,16</sup> Nanda and Wicks report that the prepolymer method requires a greater proportion of acid groups than the acetone process to form stable particles.<sup>6</sup>

#### 1.4.1.3 Other Methods of PUD synthesis

Modifications to the two main methods - acetone process (Figure 1.11) and prepolymer mixing (Figure 1.12) - have been developed to produce high quality

dispersions with low solvent usage. For example, the melt dispersion process uses amines or ureas to cap the prepolymer with urea or biuret groups, prior to dispersion. These hydrophilic groups allow the prepolymer to be dispersed without the use of a co-solvent, following which they are chain extended with formaldehyde.<sup>4,5,11</sup>

Alternatively, the so-called ketamine process has proven to give dispersions of quality most similar to those obtained via the acetone process (Figure 1.13).<sup>26</sup> Diamine chain extenders are blocked with ketones to give ketimines. These can be mixed with prepolymers prior to dispersion without a reaction with terminal isocyanate groups. Addition of water simultaneously disperses the prepolymer and liberates the diamine, initiating chain extension. The same process can be carried out with hydrazine, blocked by ketones to give ketazines. This provides a route to extremely UV-resistant, carbazide-containing PUs that cannot be melted or dissolved, so are inaccessible by other means.<sup>4,5</sup>

Figure 1.13: Reversible blocking of diamine and hydrazine with ketones

# 1.5 Polyurethane Modified Acrylics

Further expanding the accessible properties of PUDs, developments exploit the complementary properties of acrylic polymers by combining them to produce hybrid aqueous dispersions. Acrylics contribute strong adhesion, improved pigment compatibility and UV stability as well as reducing cost.<sup>38–40</sup> Polyurethane modified

acrylic (PUMA) dispersions are synthesised via emulsion polymerisation from a PUD seed particle, <sup>10,39,41–44</sup> or by using acrylic monomer as a solvent in the synthesis of PU prior to dispersion. <sup>45,46</sup> The final PUMA particles are achieved with free radical polymerisation in the aqueous dispersion. Due to the hydrophobicity of the polyacrylate (PA) phase, it is logical to assume that PA is found on the inside of the particle, and only PU is found at the particle-water interface. This core-shell morphology has been reported frequently for particles of this nature. <sup>10,41,42,44,47–56</sup>

There are many literature examples of particle size increasing with addition of acrylic monomers to the PUD, indicative of monomers swelling the PU seeds. <sup>25,38,40,42–44,48,49,56,57</sup> When dried, the resulting films are made up of PA domains within a PU continuous phase. Hirose et al. report on this increase in particle size with acrylic addition. <sup>41</sup> They observed gradual growth initially followed by a sudden size increase at acrylic content >20 vol%. Since then, others have reported similar particle growth behaviour <sup>48,58</sup> the conclusion being that PU is unable to stabilise swollen particles of high acrylic content, thus several fuse to make new particles and, in doing so, lower the total surface area.

Li, Chiu and Don considered the Gibbs free energy of five possible morphologies of PUMA particles, comprising an polypropylene glycol based PU and methyl methacrylate (MMA) PA.<sup>51</sup> Using interfacial tension measurements, they determined that a PA core, surrounded by a region of phase-mixed polymers and encapsulated by a PU shell (Figure 1.14a), was the most thermodynamically favourable structure. This was slightly more stable than a pure core/shell morphology (Figure 1.14b). When the hydrophobicity of the PU was increased by inclusion of bisphenol A, the lowest free energy state became a homogenous, phase-mixed structure (Figure 1.14c).

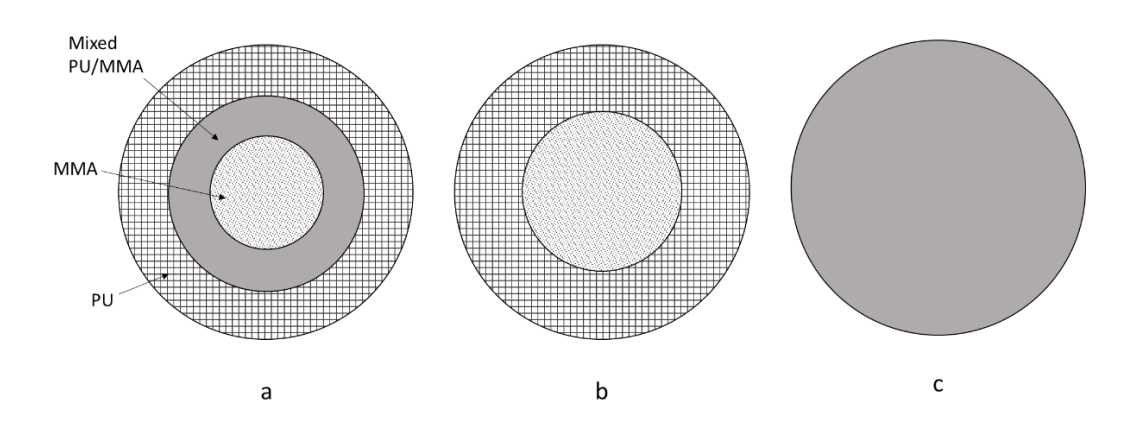


Figure 1.14: Possible PU/PMMA particle morphologies considered by Li, et al.<sup>51</sup> with a) found to be most thermodynamically stable in most cases, b) slightly less favourable pure core-shell structure and c) phase mixed morphology seen on increasing PU hydrophobicity

Jiang et al. reported that thermal annealing resulted in increased phase separation for their PUMA hybrid particles,<sup>10</sup> as quantified by DSC, suggesting that the equilibrium morphology is not initially achieved, rather an element of kinetic control is preventing thorough phase separation, and thermal annealing allows for rearrangement of chains.

Multiple comparative studies of PUMA particles with non-hybrid PUD and PA emulsion blends have been conducted. 10,39,40,43,53,55,58,59 The findings are all in good agreement and demonstrate that hybrid particles give films with far superior mechanical properties than blends. This is attributed to a better distribution of acrylic regions in the continuous PU film and more intimate phase mixing. One such study from Brown et al. considers phase mixing of a commercial PU and a mixed-monomer PA at a 50/50 ratio of PU/PA. 39 Their findings indicate that 19-28% of the PU and 37-45% of the PA is found in the interphase region of films made from hybrid PUMA dispersions. In contrast, interphase regions of simple PU and PA blends contain only 2-21% and 0-19% of the PU and PA respectively. This was reflected in the superior mechanical properties of the PUMA hybrid films, and a better distribution of acrylic domains according to atomic force microscopy (AFM).

The degree of phase mixing can be affected by grafting, which is used to form physical cross-links between PU and PA. This is most often achieved by capping isocyanate-terminated PU prepolymers with a hydroxyacrylate monomer, commonly hydroxyethyl methacrylate (HEMA).<sup>32,46,47,54,55,60–64</sup> Degrandi-Contraires et al. used this technique to form covalent links between PU and PA upon free radical polymerisation of acrylic monomers.<sup>54</sup> They reported a homogenous, phase-mixed morphology when the PU content was 5 wt% or 25 wt% of the total polymer mass. When PU content was raised to ≥50 wt%, core-shell morphologies were observed by transmission electron microscopy.

Alvarez and co-workers synthesised a PU seed, using cross-linking bis-phenol-A-glycidyl dimethacrylate (bis-GMA) and 1,4-butanediol (BD) chain extenders.<sup>65</sup> Following the addition and polymerisation of acrylic monomers, significantly larger particles were obtained with bis-GMA compared to those chain extended with BD, at 60 nm and 45 nm, respectively (Table 1.2). It is suggested that this is related to the low efficiency of chain extension of Bis-GMA, where the shorter chains reduce chain entanglement despite cross-linking, and, therefore, the particle size can increase.

Table 1.2: Results of Alvarez et al.<sup>65</sup> demonstrating particle size increase with increasing Bis-GMA cross-linker content in chain extender blend used for PUMA particle production

Bis-GMA / 1,4-butandiol	Mean particle	
chain extender	size /nm	
0 / 100	45	
30 / 70	55	
50 / 50	55	
70 / 30	53	
100 / 0	60	

In contrast, Zhu et al. saw a decrease in particle size with increasing cross-linker content, using trihydroxymethyl propane triacrylate (Table 1.3).<sup>25</sup> They attribute this to closer packing caused by cross-linking.

Table 1.3: Results of Zhu et al.<sup>25</sup> showing particle size decreasing with increasing cross-linker content such as trihydroxymethyl propane triacrylate for PUMA particle production.

Cross-linker content /wt% of acrylic monomers	Mean particle size /nm
0.0	74.7
2.0	66.9
5.0	61.0

Similarly, Chai, Jin and Tan used glycidyl methacrylate to cross-link PU and PA.<sup>44</sup> Without crosslinks, they observed core-shell structures with three distinct T<sub>g</sub>s originating from the PA and the two (soft and hard) PU phases. In contrast, the cross-linked particles formed an interpenetrating network of PU through the PA core. Only two T<sub>g</sub> peaks were observed as the peaks from PU hard segment and PA became indistinguishable due to the phase mixing. This structural difference was also observed by transmission electron microscopy in the work of Mehrava et al.<sup>47</sup> Micrographs displayed a core-shell structure for ungrafted PUMAs, and increasing homogeneity with cross-linking.

# 1.6 Small-angle X-ray Scattering

SAXS is a key structural characterisation technique for enabling molecular-scale study of a material. The size, shape, structure, and orientation of molecules or particles, as well as their organisation in solution or bulk systems, are all revealed by the scattering of a sample in the small-angle region of X-ray scattering patterns. This approach offers advantages over popular real-space imaging methods because it collects and averages structural information from millions of particles in a system. Often, SAXS is combined with transmission electron microscopy (TEM)<sup>42,55,66</sup>, AFM<sup>50,55,67</sup> or other microscopy techniques<sup>67–71</sup> to give information on both global and local structural morphologies.

SAXS is an appealing method for soft condensed matter research for a number of reasons. Very little sample is needed for measurements since the X-ray beam interacting with the sample is typically on a fraction of a millimetre scale. For synthetic polymeric samples, the beam, especially of SAXS laboratory instruments, is usually non-destructive. Structural morphology can be assessed in a single measurement on a broad range of sizes - from 1 nm up to around 500 nm (Figure 1.15).<sup>72</sup>

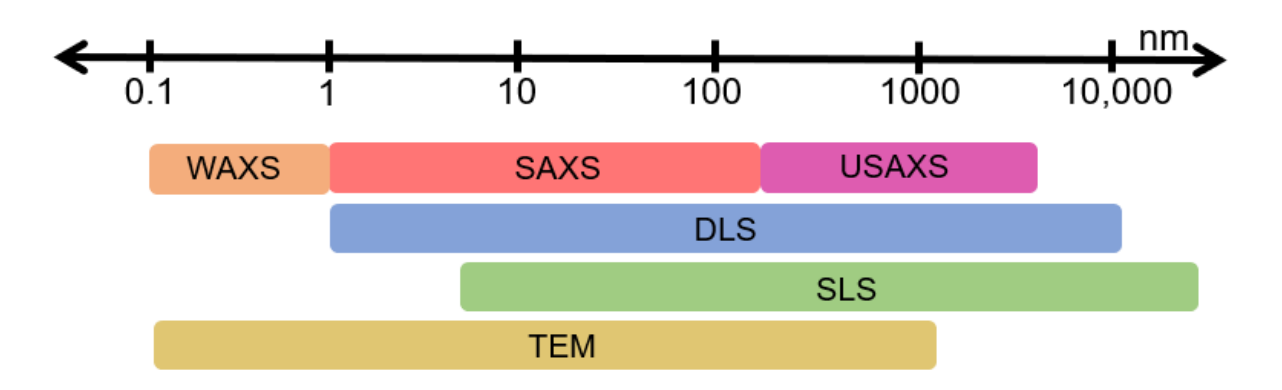


Figure 1.15: Comparison of size ranges accessible by wide angle x-ray scattering (WAXS), SAXS, ultra-SAXS (USAXS), dynamic light scattering (DLS), static light scattering (SLS) and TEM

Both dynamic and static light scattering methods can quantify particle size in the same size range, but do not give the same detail on shape and internal structure. SAXS poses advantages over light scattering methods due to at least two important factors: a higher energy X-ray beam penetrating through material, and the Raleigh-Gans-Debye approximation applicable to X-ray scattering measurements within a wide subnanoscopic and nanoscopic range.<sup>72</sup>

## 1.6.1 Applications of SAXS

#### 1.6.1.1 SAXS for soft matter

SAXS has found useful application right across the broad field of soft matter.<sup>73</sup> In particular, SAXS has been used extensively to investigate the periodicity of stacked lamellar in semi-crystalline polymers.<sup>74–82</sup> For example, Rule et al. used the

characteristic 2D SAXS behaviour of oriented polymer structures (Figure 1.16) to follow the annealing of poly(ethylene terephthalate). Comparison to computational model structures allowed quantitative insight into the growth of crystallites.

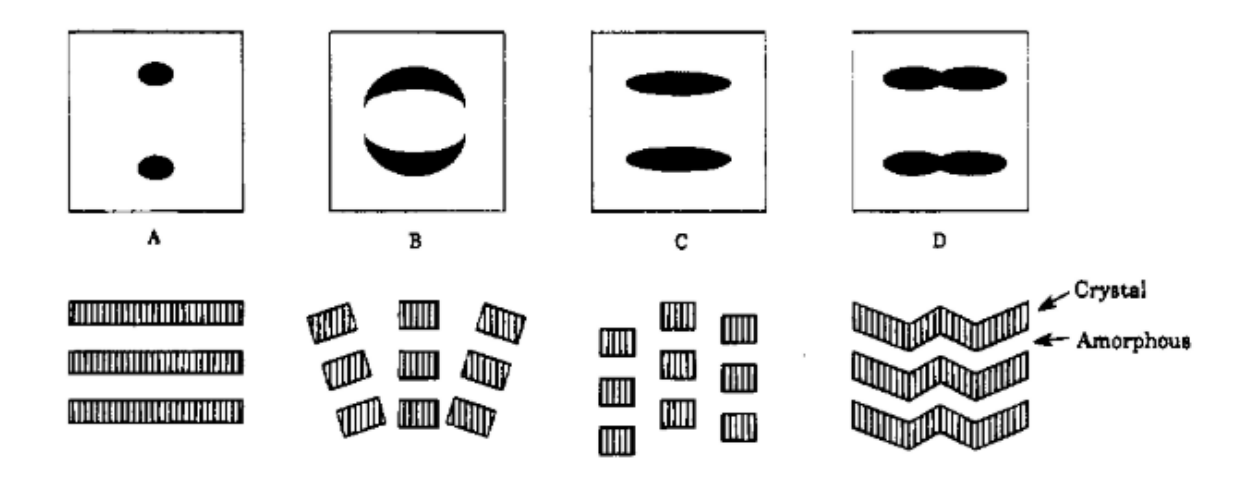


Figure 1.16: Characteristic 2D SAXS patterns from common orientated polymer structures, taken from Rule et al.<sup>79</sup>

In the field of solutions in soft matter, small-angle scattering is used to describe polymeric micelles, 83–85 polymers in solution, 86–88 emulsions, 89,90 and to quantify particle size, structure and polydispersities. 50,91–95 Due to the poor electron density contrast between many polymers and their solvents, the electron density of the solvent is often adjusted in a technique known as contrast matching. For aqueous systems, sucrose is a popular choice of contrast matching agent due to its solubility and low propensity for interaction with the particles of interest. 50,93,95

#### 1.6.1.2 SAXS for phase separated PU

It has been shown that SAXS is a useful tool for studying microdomain structures, particularly for phase separation in PUs.<sup>74,96,97</sup> Leung and Koberstein demonstrated this by using SAXS to measure hard-domain thickness, diffuse boundary thickness, domain surface-to-volume ratio and purity of microphases in their PU elastomers.<sup>98</sup> Similar thorough SAXS analysis methods were used in an earlier work by Koberstein

and Stein to compare overall degree of phase separation and boundary thickness for cross-linked PUs with a symmetric and an asymmetric isocyanate.<sup>74</sup>

SAXS patterns in the work of Terban et al.  $^{97}$  show peaks indicative of the hard domain d-spacing in their thermoplastic PUs based upon  $M_n = 1000$  poly(tertramethylene oxide) (PTMO), BD and methylene diphenyl diisocyanate (MDI), or hexamethylene diisocyanate (HDI) (Figure 1.17a). For HDI at 46% hard block (HB) content and MDI at 43% HB content, d-spacing was calculated to be 9.3 nm and 11.2 nm, respectively. Broad peaks in the wide angle x-ray scattering (WAXS) region (Figure 1.17b) are indicative of predominantly amorphous content.

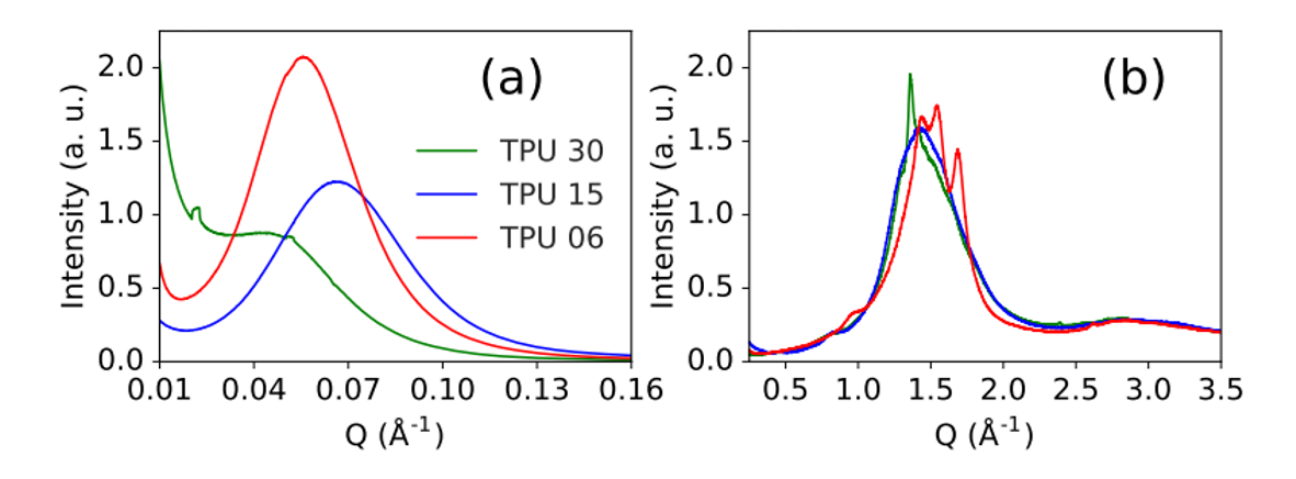


Figure 1.17: a) SAXS and b) WAXS of TPUs comprising: MDI, BDO, PTMO at 43%HB (TPU-15); HDI, BDO, PTMO at 46% HB (TPU-06); MDI, BDO, polyesterol (TPU-30) at 44% HB. Taken from the work of Terban et al.<sup>97</sup>

Bras et al. used SAXS to observe the occurrence of phase separation during the reaction to form PU,<sup>99</sup> according to the increase in the relative scattering invariant, Q' (Figure 1.18, squares). Simultaneously, Fourier transform infrared spectroscopy (FTIR) was used to follow the formation of hydrogen bonds through the carbonyl absorption peaks (Figure 1.18, circles). The onset of hydrogen bond formation was taken as the time at which the intensity increase in the peak at 1700 cm<sup>-1</sup>, corresponding to hydrogen-bonded carbonyl, accelerated. Their data shows a 4-minute time difference

between the onset of phase separation, and the appearance of hydrogen bonding in the carbonyls. As such, they conclude that the driving force for the formation of internal structure in PUs is the thermodynamic advantage of a reduced enthalpy of mixing from the separation of the incompatible had and soft phases, rather than the formation of hydrogen bonds.

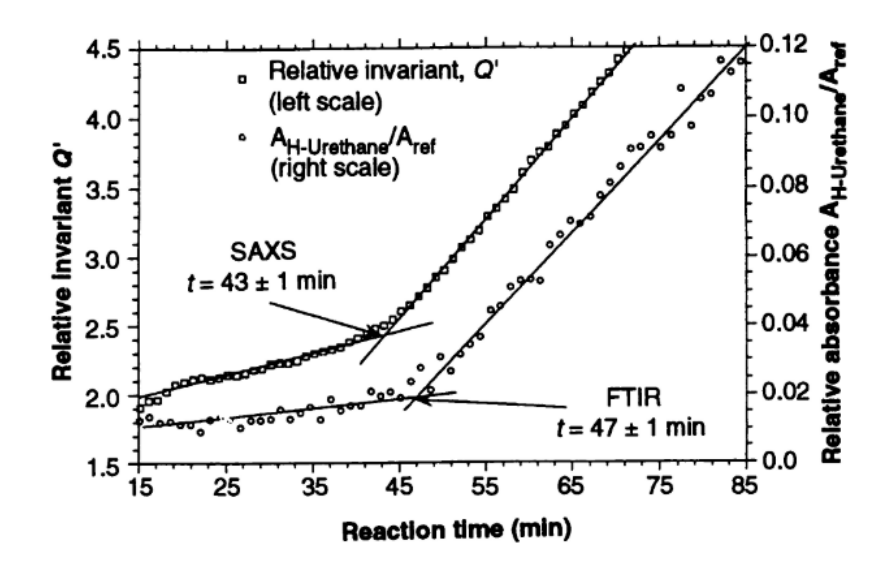


Figure 1.18: The SAXS relative invariant (Q') and the normalised FTIR absorbance associated with the hydrogen-bonded urethane plotted against time for the reaction to form segmented block PU. Tangents are fitted to both data sets to estimate the onset of microphase separation (t = 43 min from Q') and hydrogen bonding (t = 47 min from FTIR). Taken from the work of Bras et al.<sup>99</sup>

The structure of hard block comprising MDI and BD and has been thoroughly investigated by Blackwell et al. $^{100-102}$  using x-ray diffraction. They identify a unit cell with P1 symmetry, consisting of stacked chains stabilised by successive hydrogen bonding perpendicular to the chain axis.

#### 1.6.1.3 SAXS for PUDs and PUMA

SAXS has also been applied to the study of aqueous PUD particles. Bolze et al. applied SAXS to their polyether-based PUDs, decomposing the scattering intensity into: scattering from particle shape and size ( $I_{sh}(q)$ ); scattering from internal inhomogeneities in electron density ( $I_{in}(q)$ ); a cross term of the two former contribution ( $I_{in,sh}(q)$ ) (Figure 1.19).<sup>95</sup>

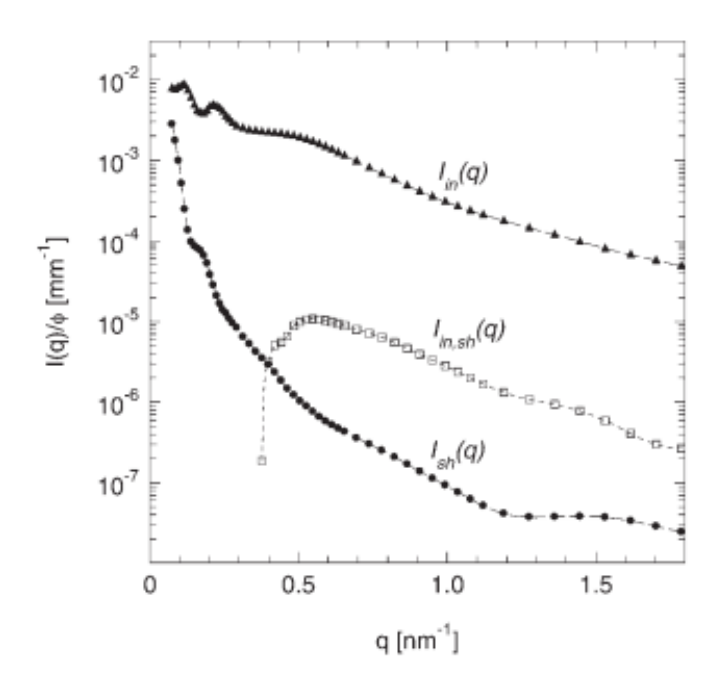


Figure 1.19: Decomposition of the scattering from PUD into three contributions, from the particle shape and structure ( $I(q)_{sh}$ ), internal inhomogeneities in electron density ( $I(q)_{in}$ ) and a cross term of these two contributions ( $I(q)_{in,sh}$ ). Taken from the work of Bolze et al.<sup>95</sup>

Using contrast matching with sucrose, the scattering from internal inhomogeneities was further decomposed into scattering from a core-shell structure ( $I_{cs}(q)$ ) and scattering arising due to the semi-crystalline nature of the polymer ( $I_{cryst}(q)$ ) (Figure 1.20).

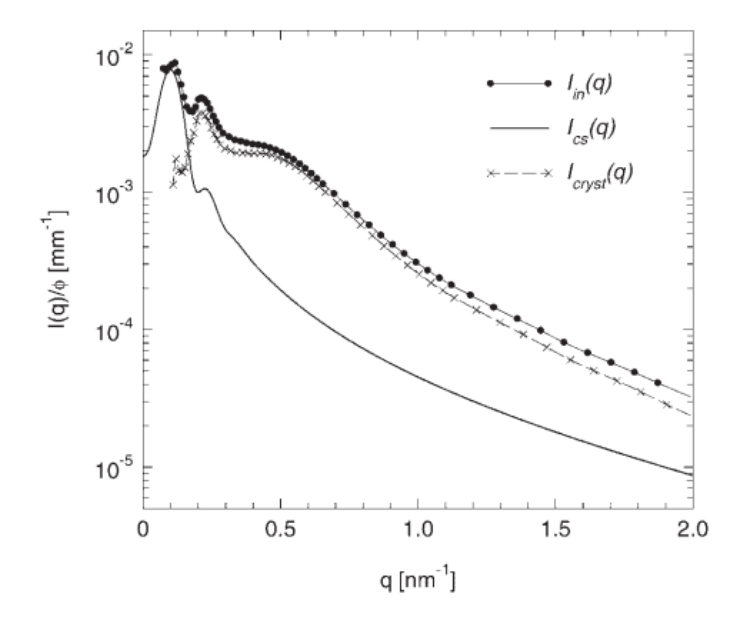


Figure 1.20: Decomposition of the PUD scattering arising from internal inhomogeneities ( $l_{in}(q)$ ), into scattering from the core-shell structure ( $l_{cs}(q)$ ) and scattering arising from the semi-crystalline nature of the polymer ( $l_{cryst}(q)$ ). Taken from the work of Bolze et al.<sup>95</sup>

They conclude that the particles comprise a 1 nm thick electron-rich shell of acidic stabilising groups and a hydrophobic PU core of 28 nm radius. Additionally,  $I_{cryst}(q)$  indicates a phase-separated lamellar structure within the PU particles of alternating amorphous and crystalline regions. It is speculated that the crystalline part comprises ordered hard block, however it is acknowledged that polyether is known to form crystalline structures in some cases.

SAXS has shown to be applicable to studying PUMA systems.<sup>42,45,50,55,103</sup> Peruzzo et al. studied PU and PUMA films by SAXS.<sup>55</sup> A scattering maximum was observed at 0.1 Å<sup>-1</sup> for pure PU, and 0.138 Å<sup>-1</sup> for PA (Figure 1.21).

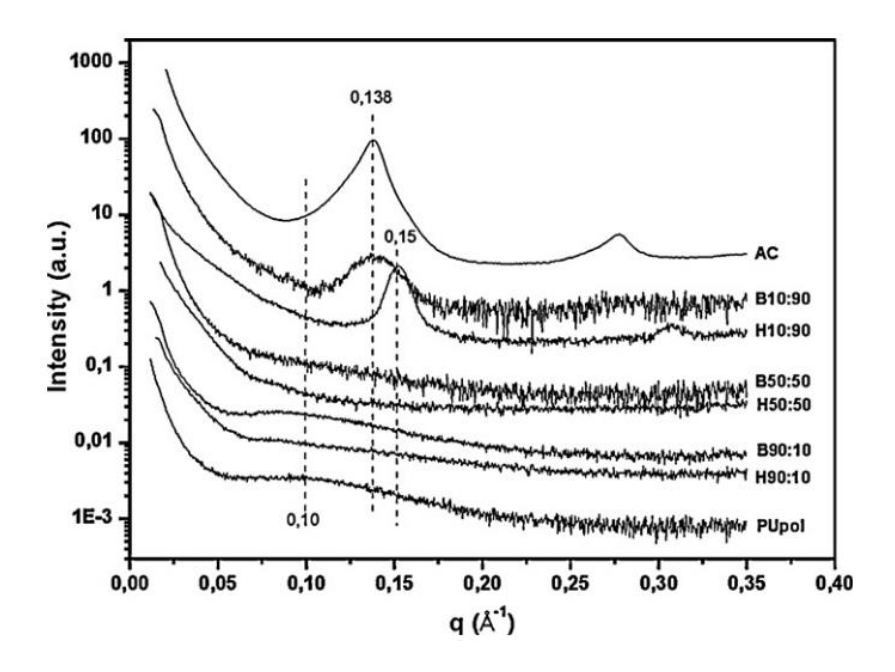
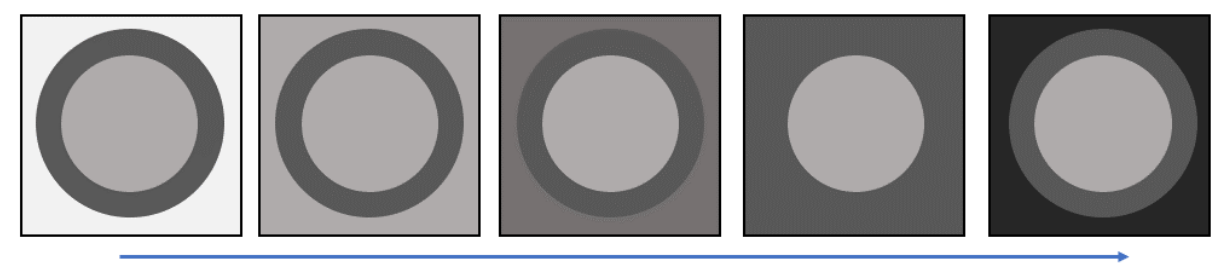


Figure 1.21: SAXS profiles of pure PU (PUpol), pure PA (AC), hybrid (H) and blend (B) samples. Ratios give PU:AC by wt%. From Peruzzo et al.<sup>55</sup>

Observation of the effect of acrylic addition to PU to make hybrid particles revealed a reduction in the 0.1 Å<sup>-1</sup> peak height. A featureless pattern was obtained at equal masses of PU and PA, indicative of a phase-mixed, homogenous morphology. Interestingly, this was not true of the physical blends of PU and PA due to low interpenetration of the polymers. Instead, a second peak at 0.15 Å<sup>-1</sup> appeared on the

spectrum at 90 wt% PA component, arising from two separate phases with good scattering length density contrast.

Previous research in our group has used SAXS to study PUMA core-shell particles provided by AkzoNobel. In 2007, Mykhaylyk et al. published on their SAXS modelling of PUMA dispersions,<sup>50</sup> using the indirect Fourier transform to obtain pair density distribution functions representing particles in real space. Scattering length density ( $\xi$ ) contrast matching using aqueous sucrose solutions was employed to obtain independent scattering patterns for the core and shell (Figure 1.22).



Increasing  $\xi_{solvent}$ 

Figure 1.22: Schematic of the effect of contrast marching by changing the scattering length density of a solvent ( $\xi_{\text{solvent}}$ ) to isolate different components of the core-shell particle structure. The second image and the fourth image from the left correspond to two cases when the solvent matches scattering length density of the particle core and the particle shell, respectively.

The scattering length density, and therefore composition, of each phase could be well estimated from the corresponding contrast-matched sucrose solution. The experimental density values for core and shell were in good agreement with the known values for PA and PU respectively. The pair distance distribution functions were analysed simultaneously for all sucrose concentrations. It was found that a model for core-shell particles with stochastic deviation in electron density of the shell was most suitable. This confirmed the expected morphology of PA core and a phase separated PU shell (Figure 1.23). Deviations in the core density back-calculated from SAXS analysis suggested that some PU is found within the acrylic core, such that it comprises an interpenetrating network of PU chains through PA.



Figure 1.23: Morphology of a PUMA particle with acrylic core (red) and PU shell consisting of hard segment domains (blue) and continuous soft segment (yellow) as determined by Mykhaylyk et al.<sup>50</sup> using SLD contrast matching technique and pair distance distribution function analysis.

### 1.6.2 *In situ* SAXS methods for dispersions and colloidal systems

Due to the abundance of information accessible from SAXS data, it has proven a useful method for following the development of morphology during synthesis and processing of a material. Often, specialist set-ups are required for the collection of this time-resolved SAXS data. For example, in order to carry out *in situ* SAXS studies on the growth of silica nanoparticles, Tobler et al. constructed flow through apparatus (Figure 1.24).<sup>104</sup> A quartz capillary formed the SAXS cell, connected at each end to Teflon tubing. A peristaltic pump ensured circulation of the silica-containing solution from a beaker, which was continuously stirred. SAXS patterns were collected every 5 minutes, successfully providing information on the growth of the silica particles during the reaction.

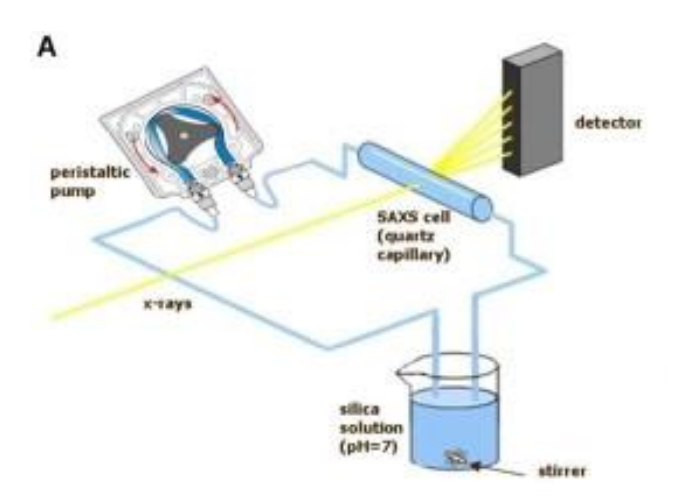


Figure 1.24:Set up used by Tobler et al to carry out in situ SAXS studies during the growth of silica nanoparticles<sup>104</sup>

The Armes group in Sheffield have published extensively on polymerisation-induced self-assembly of diblock copolymers, often using SAXS to investigate morphological changes. Derry et al. provide an *in-situ* SAXS example, monitoring the formation of, and transformation of, spherical micelles, worms and vesicles in dispersion. The polymerisation was carried out in a glass capillary placed in the beam of a synchrotron X-ray source. As the reaction was performed in a solvent, the reaction mixture was homogenous and no agitation or stirring was required. Generation of additional free radical species by high intensity X-rays caused the reaction to proceed to completion in 120 minutes, far quicker than the 500 minutes required under standard laboratory conditions.

Building on this, Brotherton et al. carried out a similar investigation using emulsion polymerisation in aqueous media.<sup>106</sup> To obtain sufficiently small monomer droplets, constant and efficient stirring was required throughout the *in situ* collection of SAXS patterns. A cell was designed to cater for these requirements (Figure 1.25), with a reaction volume (2 ml) that allowed for a variety of post-mortem analyses.

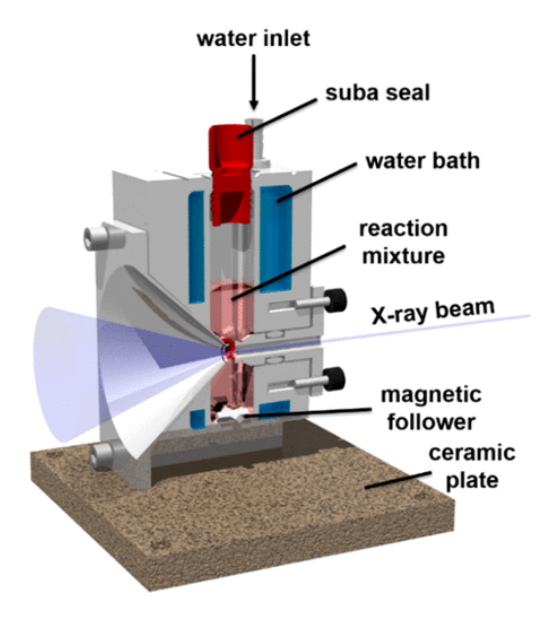


Figure 1.25: Specialist cell designed to provide continuous stirring for collection of time-resolved SAXS data during emulsion polymerisation.

Similarly, *in situ* grazing incidence SAXS (GISAXS) has been used to understand the phase separation behaviour of block copolymers.<sup>107–112</sup> For example, Ogawa et al. observed the development of phase separation morphology during the spin coating of poly(styrene-*b*-2-vinylpyridine) by GISAXS.<sup>111</sup> In the bulk, this symmetric copolymer is known to form lamellar structures,<sup>113</sup> however under the shear forces of spin coating and fast solvent evaporation, vitrification of the polymers occurred when they had a lamellar structure perpendicular to the substrate.

### 1.7 Aims

It is one of AkzoNobel's primary goals to reduce carbon emissions in their operations by 50%, compared to 2018.<sup>114</sup> For the performance coatings sector, one of the ways to do this is to provide more aqueous-based products to replace the solvent-borne alternatives. In order to do this in an efficient and effective way, it is necessary to understand how synthesis and compositional changes affect the performance of the final product.

Due to the range of accessible PU and acrylic compositions, PUMAs offer an effective pathway to expanding the range of aqueous high-performance coatings. Indeed, they are already commercially available for some applications. The complexity of the combined PU and acrylic chemistries, however, means that understanding the control of the final product properties is not straightforward. Films properties are highly dependent on the structures in dispersion (Figure 1.26), therefore control of the polymer morphologies in the wet state is of utmost importance. Additionally, how these morphologies evolve during film formation must be understood.

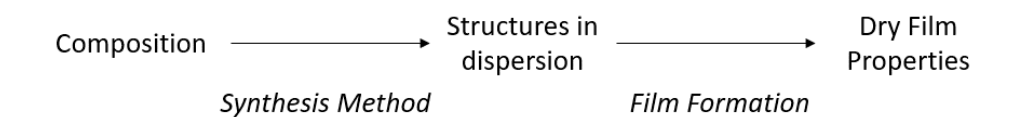


Figure 1.26: Basic schematic of factors influencing final film properties of a PUMA coating

The goal of this thesis is primarily to better understanding of the control of PUMA particle structures in dispersion. More specifically, it aims to address the following key questions:

- 1. How does composition control morphology in PUDs, of similar composition to the PU phase in PUMAs? If this can be understood, then the individual PU and acrylic effects on PUMA particles can be isolated. The key compositional changes to be investigated are hard block/soft segment ratio, acid content, and soft segment molecular weight.
- 2. How does the synthesis method effect the structures that form in PUMA dispersion? There are various PUMA synthesis methods used in the literature which could affect morphologies, therefore affording an element of property control.
- 3. For one synthesis method, what is the effect of changing the PUMA composition? More specifically, the effect of PA identity should be probed by studying PUMAs containing PA homopolymers, and the outcome of changing PU/PA ratio for each explored.
- 4. How are PUMA morphologies reached, and can this be answered using *in situ* SAXS data collection?
- 5. How do structures evolve during the film formation process from PU-based aqueous dispersions? Moreover, how does the composition control the structures in the final film?

### 1.8 References

- 1 Coating Industry (Paints, Lacquers and Varnishes), OECD, 2014.
- 2 Department for Environment Food and Rural Affairs, *Environmental Permitting Guidance The Solvent Emissions Directive*, 2010.
- 3 L. Morris Brown, T. Moradi, G. Gridley, N. Plato, M. Dosemeci and J. Fraumeni, *J. Occup. Environ. Med.*, 2002, **44**, 258–264.
- 4 D. Dieterich, *Prog. Org. Coatings*, 1981, **9**, 281–340.
- 5 B. K. Kim, *Colloid Polym. Sci.*, 1996, **611**, 599–611.
- 6 A. K. Nanda and D. A. Wicks, *Polymer (Guildf).*, 2006, **47**, 1805–1811.
- 7 H. Honarkar, *J. Dispers. Sci. Technol.*, 2018, **39**, 507–516.
- 8 P. J. Flory, *Principles of Polymer Chemistry*, Cornell University Press, New York, 1953.
- 9 W. H. Carothers, *J. Am. Chem. Soc.*, 1929, **51**, 2548–2559.
- 10 B. Jiang, J. G. Tsavalas and D. C. Sundberg, *Polymer (Guildf).*, 2018, **139**, 107–122.
- 11 A. Barni and M. Levi, *J. Appl. Polym. Sci.*, 2003, **88**, 716–723.
- 12 M. L. Hsaing, C. H. Chang, M. H. Chan and D. Y. Chao, *J. Appl. Polym. Sci.*, 2005, **96**, 103–112.
- 13 J. Yang, Z. Wang, Z. Zeng and Y. Chen, *J. Appl. Polym. Sci.*, 2002, **84**, 1818–1831.
- 14 F. Chen, J. Hehl, Y. Su, C. Mattheis, A. Greiner and S. Agarwal, *Polym. Int.*, 2013, **62**, 1750–1757.
- 15 R. Hernandez, J. Weksler, A. Padsalgikar, C. Taeyi, E. Angelo, J. S. Lin, L. C. Xu, C. A. Siedlecki and J. Runt, *Macromolecules*, 2008, **41**, 9767–9776.
- 16 R. Satguru, J. McMahon, J. C. Padget and R. G. Coogan, *J. Coatings Technol.*, 1994, **66**, 47–55.
- T. C. Wen, Y. J. Wang, T. T. Cheng and C. H. Yang, *Polymer (Guildf).*, 1999, **40**, 3979–3988.
- M. S. Sánchez-Adsuar, M. Mercedes Pastor-Blas and J. M. Martín-Martínez, *J. Adhes.*, 1998, **67**, 327–345.
- 19 M. A. Pérez-Limiñana, F. Arán-Aís, A. M. Torró-Palau, A. C. Orgilés-Barceló and J. M. Martín-Martínez, *Int. J. Adhes. Adhes.*, 2005, **25**, 507–517.
- 20 B. K. Kim, T. K. Kim and H. M. Jeong, *J. Appl. Polym. Sci.*, 1994, **53**, 371–378.
- 21 T. Li, C. Zhang, Z. Xie, J. Xu and B. H. Guo, *Polymer (Guildf).*, 2018, **145**, 261–271.
- 22 I. Yilgör, E. Yilgör and G. L. Wilkes, *Polymer (Guildf).*, 2015, **58**, A1–A36.

- 23 Y. Xiu, D. Wang, C. Hu, S. Ying and J. Li, *J. Appl. Polym. Sci.*, 1993, **48**, 867–869.
- 24 M. F. Sonnenschein, Z. Lysenko, D. A. Brune, B. L. Wendt and A. K. Schrock, *Polymer (Guildf).*, 2005, **46**, 10158–10166.
- 25 X. Zhu, X. Jiang, Z. Zhang and X. Z. Kong, *Prog. Org. Coatings*, 2008, **62**, 251–257.
- 26 B. K. Kim and J. C. Lee, *J. Polym. Sci. Part A Polym. Chem.*, 1996, **34**, 1095–1104.
- F. Li, R. Tuinier, I. Van Casteren, R. Tennebroek, A. Overbeek and F. A. M. Leermakers, *Macromol. Theory Simulations*, 2016, **25**, 16–27.
- 28 H. T. Lee, S. Y. Wu and R. J. Jeng, *Colloids Surfaces A Physicochem. Eng. Asp.*, 2006, **276**, 176–185.
- 29 O. Jaudouin, J. J. Robin, J. M. Lopez-Cuesta, D. Perrin and C. Imbert, *Polym. Int.*, 2012, **61**, 495–510.
- 30 S. Zhang, H. Lv, H. Zhang, B. Wang and Y. Xu, *J. Appl. Polym. Sci.*, 2006, **101**, 597–602.
- 31 A. K. Nanda, D. A. Wicks, S. A. Madbouly and J. U. Otaigbe, *J. Appl. Polym. Sci.*, 2005, **98**, 2514–2520.
- 32 M. Li, E. S. Daniels, V. Dimonie, E. D. Sudol and M. S. El-Aasser, *Macromolecules*, 2005, **38**, 4183–4192.
- 33 X. Wang, G. Ma and M. Zheng, *J. Coatings Technol. Res.*, 2018, **15**, 1217–1227.
- 34 I. Soutar, L. Swanson, T. Annable, J. C. Padget and R. Satgurunathan, *Langmuir*, 2006, **22**, 5904–5910.
- 35 H. S. Choi, S. T. Noh and K. B. Choi, *J. Ind. Eng. Chem.*, 1999, **5**, 52–58.
- 36 S. Zhang, W. Miao and Y. Zhou, *J. Appl. Polym. Sci.*, 2004, **92**, 161–164.
- 37 H. Che, N. G. Wang, F. H. Chen and H. T. Zhang, *J. Hubei Univ. (Nat Sci Ed.)*, 1998, **20**, 165.
- 38 H. T. Lee and C. C. Wang, *J. Polym. Res.*, 2005, **12**, 271–277.
- 39 R. A. Brown, R. G. Coogan, D. G. Fortier, M. S. Reeve and J. D. Rega, *Prog. Org. Coatings*, 2005, **52**, 73–84.
- D. Kukanja, J. Golob, A. Zupancic-Valant and M. Krajnc, *J. Appl. Polym. Sci.*, 2000, **78**, 67–80.
- 41 M. Hirose, F. Kadowaki and J. Zhou, *Prog. Org. Coatings*, 1997, **31**, 157–169.
- 42 I. Drake, G. Cardoen, A. Hughes, A. I. Nakatani, B. Landes, J. Reffner and R. Even, *Polymer (Guildf).*, 2019, **181**, Online.
- 43 V. D. Athawale and M. A. Kulkarni, *Prog. Org. Coatings*, 2009, **65**, 392–400.
- 44 S. L. Chai, M. M. Jin and H. M. Tan, *Eur. Polym. J.*, 2008, **44**, 3306–3313.

- 45 G. Martínez-Rugerio, Á. Alegría, A. Arbe, V. Daniloska and J. Colmenero, *Mater. Today Commun.*, 2016, **8**, 100–107.
- 46 E. Degrandi-Contraires, R. Udagama, E. Bourgeat-Lami, T. Mckenna, K. Ouzineb and C. Creton, *Macromolecules*, 2011, **44**, 2643–2652.
- 47 S. Mehravar, N. Ballard, A. Agirre, R. Tomovska and J. M. Asua, *Macromol. Mater. Eng.*, 2019, **304**, 1800532.
- 48 Y. H. Guo, S. C. Li, G. S. Wang, W. Ma and Z. Huang, *Prog. Org. Coatings*, 2012, **74**, 248–256.
- 49 H.-J. Adler, K. Jahny and B. Vogt-Birnbrich, *Prog. Org. Coatings*, 2001, **43**, 251–257.
- O. O. Mykhaylyk, A. J. Ryan, N. Tzokova and N. Williams, *J. Appl. Crystallogr.*, 2007, **40**, 506–511.
- 51 C. Li, W. Chiu and T. Don, *J. Polym. Sci. Part A Polym. Chem.*, 2007, **45**, 3359–3369.
- 52 M. Hirose, J. Zhou and K. Nagai, *Prog. Org. Coatings*, 2000, **38**, 27–34.
- 53 S. L. Chai and H. M. Tan, *J. Appl. Polym. Sci.*, 2008, **107**, 3499–3504.
- E. Degrandi-Contraires, R. Udagama, T. McKenna, E. Bourgeat-Lami, C. J. G. Plummer and C. Creton, *Int. J. Adhes. Adhes.*, 2014, **50**, 176–182.
- P. J. Peruzzo, P. S. Anbinder, O. R. Pardini, J. Vega, C. A. Costa, F. Galembeck and J. I. Amalvy, *Prog. Org. Coatings*, 2011, **72**, 429–437.
- 56 Y. Lu, Y. Xia and R. C. Larock, *Prog. Org. Coatings*, 2011, **71**, 336–342.
- 57 L. Sheng, X. Zhang, Z. Ge, Z. Liang, X. Liu, C. Chai and Y. Luo, *J. Coatings Technol. Res.*, 2018, **15**, 1283–1292.
- 58 L. Chen and S. Chen, *Prog. Org. Coatings*, 2004, **49**, 252–258.
- 59 H. Tanaka, Y. Suzuki and F. Yoshino, *Colloids Surfaces A Physiochemical Eng. Asp.*, 1999, **153**, 597–601.
- 60 P. H. Barbeau, J. F. Gerard, B. Magny and J. P. Pascault, *J Polym Sci B Polym Phys*, 2000, **38**, 2750–2768.
- R. Udagama, E. Degrandi-Contraires, C. Creton, C. Graillat, T. F. L. McKenna and E. Bourgeat-Lami, *Macromolecules*, 2011, **44**, 2632–2642.
- A. Lopez, E. Degrandi, E. Canetta, J. L. Keddie, C. Creton and J. M. Asua, *Polymer (Guildf).*, 2011, **52**, 3021–3030.
- A. Lopez, E. Degrandi-Contraires, E. Canetta, C. Creton, J. L. Keddie and J. M. Asua, *Langmuir*, 2011, **27**, 3878–3888.
- 64 Y. Wei, Y. Luo, B. Li and B. Li, *Colloid Polym Sci*, 2006, **284**, 1171–1178.
- 65 G. A. Alvarez, M. Fuensanta, V. H. Orozco, L. F. Giraldo and J. M. Martín-Martínez, *Prog. Org. Coatings*, 2018, **118**, 30–39.
- T. J. Neal, D. L. Beattie, S. J. Byard, G. N. Smith, M. W. Murray, N. S. J. Williams,

- S. N. Emmett, S. P. Armes, S. G. Spain and O. O. Mykhaylyk, *Macromolecules*, 2018, **51**, 1474–1487.
- 67 E. Chmielewská, L. Sabová, H. Peterlik and A. Wu, *Brazilian J. Chem. Eng.*, 2011, **28**, 63–71.
- 68 H. Schnablegger and Y. Singh, *The SAXS Guide*, Anton Paar GmbH, Austria, 3rd edn., 2013.
- 69 Enyi Chi, M. An, G. Yao, Y. Li and Z. Wang, *Polym. Sci. Ser. A*, 2019, **61**, 906–912.
- 70 H. P. Martin, N. J. Brooks, J. M. Seddon, P. F. Luckham, N. J. Terrill, A. J. Kowalski and J. T. Cabral, *Soft Matter*, 2016, **12**, 1750–1758.
- 71 R. M. Fernandez, K. A. Riske, L. Q. Amaral, R. Itri and M. T. Lamy, *Biochim. Biophys. Acta Biomembr.*, 2008, **1778**, 907–916.
- R. J. Roe, *Methods of X-ray and neutron scattering in polymer science*, Oxford University Press, New York, 2000.
- P. Lindner and T. Zemb, Neutron, X-ray and Light Scattering: Introduction to an Investigative Tool for Colloidal and Polymeric Systems, Elsevier Science Ltd, Amsterdam, 1991.
- 74 J. T. Koberstein and R. S. Stein, *J. Polym. Sci. Part A-2, Polym. Phys.*, 1983, **21**, 1439–1472.
- 75 B. Crist, *J. Appl. Crystallogr.*, 1979, **12**, 27–33.
- 76 Z. Kifle, I. R. Harrison and R. M. Herman, *J. Polym. Sci. Part B Polym. Phys.*, 1986, **24**, 633–655.
- 77 W. Wilke and M. Bratrich, *urn:issn:0021-8898*, 1991, **24**, 645–650.
- 78 N. Stribeck, Colloid Polym. Sci., 1993, **271**, 1007–1023.
- 79 R. J. Rule, D. H. Mackerron, A. Mahendrasingam, C. Martin and T. M. W. Nye7, *Macromolecules*, 1995, **28**, 8517–8522.
- 80 G. Hauser, J. Schmidtke and G. Strobl, *Macromolecules*, 1998, **31**, 6250–6258.
- 81 N. S. Murthy, Z. G. Wang and B. S. Hsiao, *Macromolecules*, 1999, **32**, 5594–5599.
- 82 B. Goderis, H. Reynaers, M. H. J. Koch and V. B. F. Mathot, *J Polym Sci B Polym Phys*, 1999, **37**, 1715–1738.
- J. S. Pedersen and M. C. Gerstenberg, *Macromolecules*, 1996, **29**, 1363–1365.
- 84 B. Chu, G. Wu and D. K. Schneider, *J. Polym. Sci. Part B Polym. Phys.*, 1994, **32**, 2605–2614.
- J. S. Pedersen, I. W. Hamley, C. Y. Ryu and T. P. Lodge, *Macromolecules*, 2000, **33**, 542–550.
- 86 K. Terao, N. Morihana and H. Ichikawa, *Polym. J.* 2014 463, 2013, 46, 155–159.
- 87 M. Rawiso, R. Duplessix and C. Picot, *Macromolecules*, 1987, **20**, 630–648.

- 38 J. S. Pedersen and P. Schurtenberger, *Europhys. Lett.*, 1999, **45**, 666.
- 89 R. Akkal, N. Cohaut, M. Khodja, T. Ahmed-Zaid and F. Bergaya, *Colloids Surfaces A Physicochem. Eng. Asp.*, 2013, **436**, 751–762.
- 90 Y. T. Lee, D. S. Li, J. Ilavsky, I. Kuzmenko, G. S. Jeng, M. O'Donnell and L. D. Pozzo, *J. Colloid Interface Sci.*, 2019, **536**, 281–290.
- 91 P. Salgi and R. Rajagopalan, Adv. Colloid Interface Sci., 1993, 43, 169–288.
- 92 J. Brunner-Popela and O. Glatter, *J. Appl. Crystallogr.*, 1997, **30**, 431–442.
- 93 N. Dingenouts, J. Bolze, D. Pötschke and M. Ballauff, *Adv. Polym. Sci.*, 1999, **144**, 1–47.
- 94 T. J. Neal, A. J. Parnell, S. M. King, D. L. Beattie, M. W. Murray, N. S. J. Williams, S. N. Emmett, S. P. Armes, S. G. Spain and O. O. Mykhaylyk, *Macromolecules*, 2021, **54**, 1425–1440.
- J. Bolze, M. Ballauff, T. Rische, D. Rudhardt and J. Meixner, *Macromol. Chem. Phys.*, 2004, **205**, 165–172.
- 96 L. Yingjie, T. Gao, J. Liu, K. Linliu, C. R. Deeper and B. Chu, *Macromolecules*, 1992, **25**, 7365–7372.
- 97 M. W. Terban, K. Seidel, E. Poselt, M. Malfois, R. P. Baumann, R. Sander, D. Paulus, B. Hinrichsen and R. E. Dinnebier, *Macromolecules*, 2020, **53**, 9065–9073.
- 98 L. M. Leung and J. T. Koberstein, *J. Polym. Sci. Part A-2, Polym. Phys.*, 1985, **23**, 1883–1913.
- W. Bras, G. E. Derbyshire, D. Bogg, J. Cooke, M. J. Elwell, B. U. Komanschek,
   S. Naylor and A. J. Ryan, *Science (80-.)*, 1995, 267, 996–999.
- 100 J. Blackwell and K. H. Gardner, *Polymer (Guildf).*, 1979, **20**, 13–17.
- 101 J. R. Quay, Z. Sun, J. Blackwell, R. M. Briber and E. L. Thomas, *Polymer (Guildf).*, 1990, **31**, 1003–1008.
- 102 J. Blackwell and C. D. Lee, J. Polym. Sci. Part A-2, Polym. Phys., 1983, 21, 2169–2180.
- A. Kyritsis, P. Pissis, O. P. Grigorieva, L. M. Sergeeva, A. A. Brouko, O. N. Zimich, E. G. Privalko, V. I. Shtompel and V. P. Privalko, *J. Appl. Polym. Sci.*, 1999, 73, 385–397.
- 104 D. J. Tobler, S. Shaw and L. G. Benning, *Geochim. Cosmochim. Acta*, 2009, **73**, 5377–5393.
- M. J. Derry, L. A. Fielding, N. J. Warren, C. J. Mable, A. J. Smith, O. O. Mykhaylyk and S. P. Armes, *Chem. Sci.*, 2016, **7**, 5078–5090.
- 106 E. E. Brotherton, F. L. Hatton, A. A. Cockram, M. J. Derry, A. Czajka, E. J. Cornel, P. D. Topham, O. O. Mykhaylyk and S. P. Armes, *J. Am. Chem. Soc.*, 2019, 141, 13664–13675.
- 107 D.-M. Smilgies, *J. Polym. Sci.*, 2021, pol.20210244.

- J. Zhang, D. Posselt, D.-M. Smilgies, J. Perlich, K. Kyriakos, S. Jaksch and C. M. Papadakis, *Macromolecules*, 2014, 47, 5711–5718.
- 109 G. Fleury, D. Hermida-Merino, D. Jingjin, K. Aissou, A. Bytchkov and G. Portale, *Adv. Funct. Mater.*, 2019, **29**, 1806741.
- 110 K. W. Chou, B. Yan, R. Li, E. Q. Li, K. Zhao, D. H. Anjum, S. Alvarez, R. Gassaway, A. Biocca, S. T. Thoroddsen, A. Hexemer and A. Amassian, *Adv. Mater.*, 2013, **25**, 1923–1929.
- 111 H. Ogawa, M. Takenaka, T. Miyazaki, A. Fujiwara, B. Lee, K. Shimokita, E. Nishibori and M. Takata, *Macromolecules*, 2016, **49**, 3471–3477.
- 112 G. E. Stein, E. J. Kramer, X. Li and J. Wang, *Macromolecules*, 2007, **40**, 2453–2460.
- 113 M. F. Schulz, A. K. Khandpur, F. S. Bates, K. Almdal, K. Mortensen, D. A. Hajduk and S. M. Gruner, *Macromolecules*, 1996, **29**, 2857–2867.
- 114 Sustainability | AkzoNobel, https://www.akzonobel.com/en/about-us/sustainability-#tabld=making-buildings-greener, (accessed 4 September 2023).

# **Chapter 2 - Materials and Methods**

# 2.1 Materials

#### 2.1.1 Supplied Materials

Polyurethane dispersions (PUDs) and polyurethane-modified acrylics or styrene (PUMAs) were kindly provided by AkzoNobel (Sassenheim, NL) and were used as received. Tert-butyl hydroperoxide (tBHP) (70 wt% in water), sodium ascorbate and iron sulfate heptahydrate were purchased from Sigma-Aldrich (Gillingham, UK) and used as received.

### 2.1.2 PUD Syntheses

PUD samples were prepared from hydrogenated methylene diphenyl diisocyanate (HMDI), dimethylolpropionic acid (DMPA), ethylene diamine (EDA) and a range of poly(tetramethylene oxide) (PTMO) diols, with nominal  $M_n$  of 650,1000 and 2000 gmol<sup>-1</sup> (Table 2.1). Hard block refers to the PU proportion made up of HMDI, DMPA and ethylene diamine (Figure 2.1).

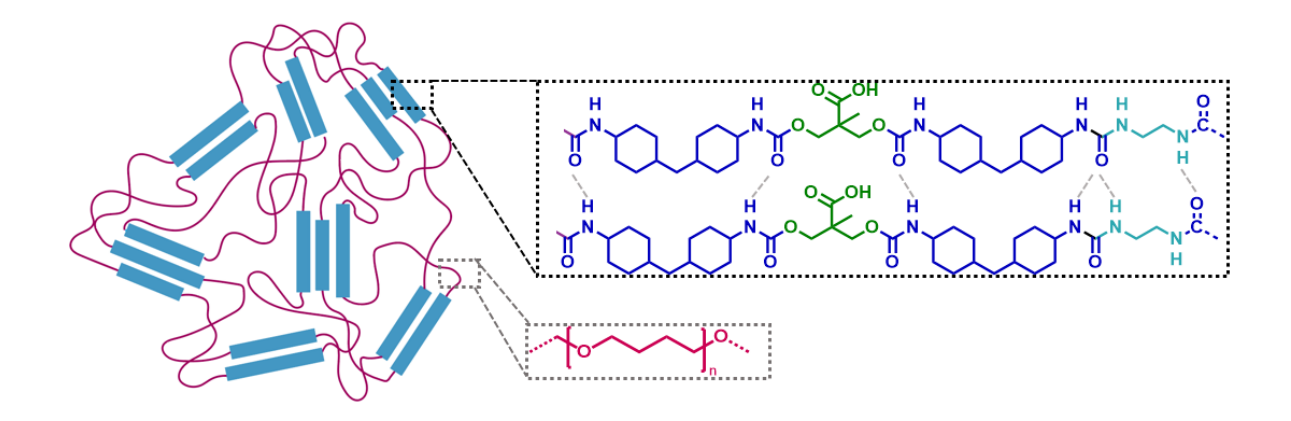


Figure 2.1: Micro-phase separation of hard blocks (blue rectangles, black box) exhibiting hydrogen bonding (grey lines), and soft segments (purple lines, grey box) in polyurethane.

Table 2.1: Summary of PUD compositions and nomenclature. COOH content is calculated according
to the formulation and masses used in synthesis.

Sample	Polymer Hard Block Content (wt%)	Soft Segment M <sub>n</sub> (gmol <sup>-1</sup> )	Polymer COOH Content /wt%
HB50_SS1000a	50	1000	2.40
HB50_SS650	50	650	1.52
HB60_SS650	60	650	2.83
HB70_SS650	70	650	4.15
HB50_SS1000b	50	1000	2.40
HB60_SS1000	60	1000	3.57
HB70_SS1000	70	1000	4.72
HB50_SS2000	50	2000	3.29
HB60_SS2000	60	2000	4.23
HB70_SS2000	70	2000	5.22

Samples are named such that the hard block content and PTMO molecular weight are given, e.g.,  $HB50\_SS1000$  refers to a PUD with 50% hard block and PTMO soft segment of  $M_{\rm n} = 1000$  gmol<sup>-1</sup>. The PUDs were obtained by applying the pre-polymer mixing method (Figure 2.2) using the materials ratios and PTMO molecular weights indicated in Table 2.2.

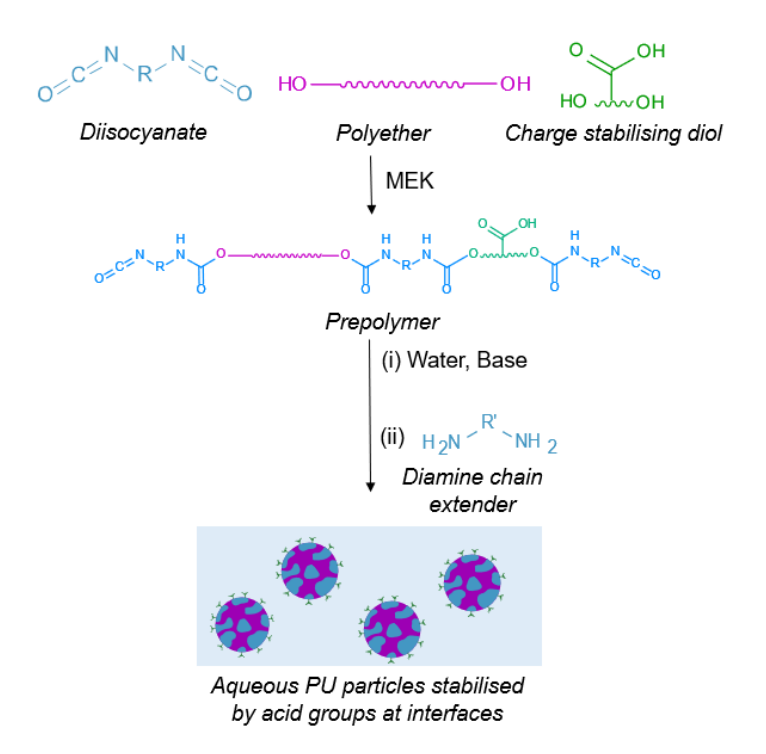


Figure 2.2: Schematic of the pre-polymer mixing method for PUD synthesis

Table 2.2: Details of materials and formulations used in the synthesis of PUDs

Synthetic step	Component	HB50_ SS1000a	HB50_ SS650	HB50_ SS1000b	HB50_ SS2000	HB60_ SS650	HB60_ SS1000	HB60_ SS2000	HB70_ SS650	HB70_ SS1000	
PU pre-polymer synthesis	PTMO Mn=650 gmol <sup>-1</sup> (g)	-	95.90	-	-	75.56	-	-	56.68	-	-
	PTMO Mn=1000 gmol <sup>-1</sup> (g)	139.51	-	95.74	-	-	75.18	-	-	56.19	-
	PTMO Mn=2000 gmol <sup>-1</sup> (g)	-	-	-	95.01	-	-	74.86	-	-	56.22
	Dimethylol propionic acid (g)	19.96	8.70	13.70	18.47	15.97	19.99	23.66	23.26	26.36	29.06
	Hydrogenated methylene diisocyanate (g)	113.47	83.60	77.87	72.9	92.62	88.26	84.18	102.59	99.45	96.37
	Methyl ethylketone (g)	54.59	47.06	46.82	46.60	46.92	46.73	46.55	46.51	46.37	46.28
	Dibutyl tin dilaurate (g)	0.15	0.10	0.10	0.10	0.10	0.10	0.10	0.10	0.10	0.10
	Triethylamine (g)	0.30	0.13	0.21	0.28	0.24	0.30	0.36	0.35	0.40	0.44
Dilution	Methyl ethylketone (g)	109.97	78.41	78.05	77.65	75.85	75.56	75.25	75.18	78.50	74.82
Neutralisation	Triethylamine (g)	14.01	6.10	9.60	12.94	11.20	14.01	16.59	16.31	18.48	20.37
Emulsification	Water (g)	607.84	464	470	475	468	472	477	478	494	484
Chain	Ethylenediamine (g)	6.07	4.47	4.17	3.90	4.95	4.73	4.86	5.50	5.31	5.17
extension	Water (g)	33.59	17.88	16.68	15.60	19.8	18.92	19.44	22.00	21.24	20.68
MEK evaporation	Methyl ethylketone (g)	-164.56	-125.47	-124.87	-124.25	-122.77	-122.29	-121.80	-121.69	-124.87	-121.1
Final PL	JD solid content (%)	30.3	30.7	32.9	26.9	24.7	25.0	23.3	18.2	19.7	16.9

All PU prepolymers were made at an NCO/OH molar ratio of 1.5. A 1 L 4-necked flask, equipped with a mechanical stirrer, a reflux condenser, and a thermocouple was charged with PTMO, DMPA and HMDI under N<sub>2</sub> atmosphere. Methyl ethylketone (MEK) was added to dilute the PU monomer constituents to 80 wt%. Dibutyl tin dilaurate (DBTDL) (0.05 wt% with respect to the mass of PU monomers) was added as catalyst, and triethylamine (TEA) (2 mol% relative to DMPA content) was added to increase the solubility of DMPA by deprotonation of the acid groups. The reaction mixture was heated to 95 °C while applying mild agitation. After 4 hours reaction time, the PU pre-polymer solution was cooled to 50 °C while simultaneously diluting further to 60 wt% PU by slowly adding more MEK. Further TEA (93 mol% with respect to DMPA content) was added to the flask allowing 5 minutes for neutralisation of the carboxylic acid groups to occur. Next, the 95 mol% neutralised PU pre-polymer solution in MEK, at 50 °C, was added to a 1 L cylinder glass reactor containing water at 30 °C (PU solution / water ratio of 40/60) over 3 minutes while stirring well. The emulsified PU pre-polymer was chain extended by addition of aqueous EDA solution (20 wt% in water) over 10 minutes, to achieve a theoretical chain extension of 70%  $(NH_2/NCO = 0.7)$ . Finally, MEK was removed from the PUD by vacuum distillation (< 80 mbar at 50 °C) and the dispersion filtered through a 125 µm gauze.

#### 2.1.3 Reaction of 2:1 HMDI:DMPA

A 50 mL round bottom flask (under N<sub>2</sub> atmosphere), equipped with a reflux condenser, was charged with DMPA (1.28 g, 9.55 mmol), HMDI (5.00 g, 19.1 mmol), MEK (25.11 g), DBDTL (0.01 g) and TEA (0.96 g, 9.55 mmol). The resulting solution was heated for 4 hours at 65 °C while stirring. Full conversion was measured using isocyanate back titration. Next, the temperature of the 20 wt% PU-prepolymer solution in MEK was lowered to 50 °C and the solution transferred to a flask containing 250 mL of water at 30 °C, with stirring. The resulting dispersion was stirred for 24 hours at 40 °C to enable the NCO/water reaction. Finally, MEK was removed from the PUD by vacuum distillation (<60 mbar at 50 °C) using a rotary evaporator.

# 2.1.4 PUMA Syntheses

PUMA was synthesised via the prepolymer method of PU production, using methyl methacrylate (MMA), butyl methacrylate (BMA), *iso*-butyl methacrylate (iBMA), or styrene monomers as the thinning solvent during prepolymer production (Figure 2.3).

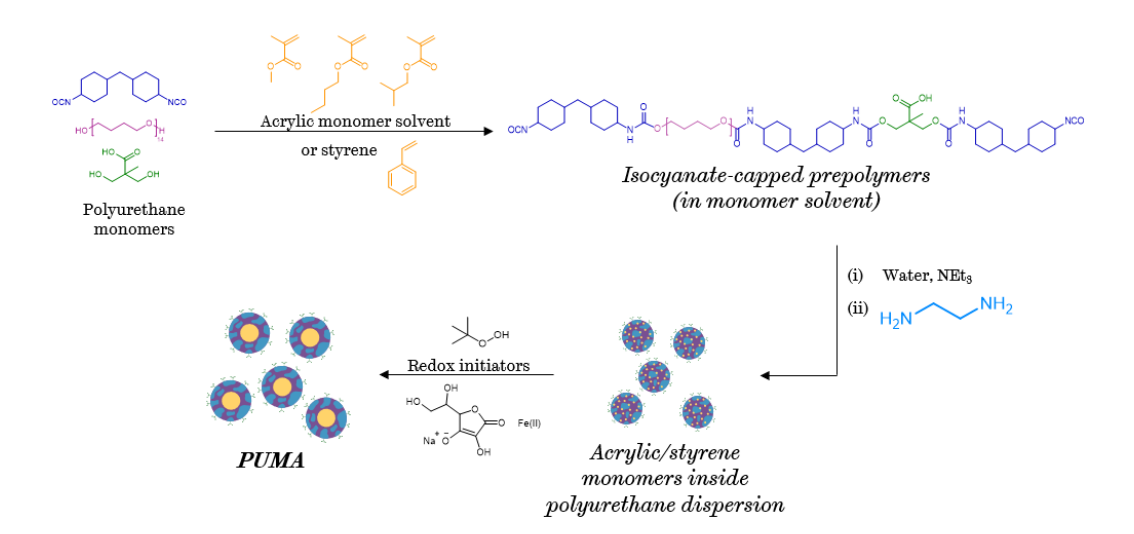


Figure 2.3: Schematic showing the steps in the PUMA production method

A 1 L 4-necked flask (under N<sub>2</sub> atmosphere), equipped with a mechanical stirrer, a reflux condenser, and a thermocouple was charged with PTMO of *Mn* = 1000 gmol<sup>-1</sup>, DMPA and HMDI to reach the hard block content shown in Table 2.3. A portion of the required monomer solvent (Table 2.3) was added to thin the reaction mixture. DBTDL (0.05 wt% with respect to the mass of PU monomers) was added as catalyst, and triethylamine (TEA) (10 mol% relative to DMPA content) was added to increase the solubility of DMPA by deprotonation of the acid groups.

Table 2.3: Summary of PUMA samples studied in the project, including the identity of the methacrylic or styrene monomer, the polyurethane/polyacrylic (or polystyrene) ratio, PU/PA, and the hard block (HB) content of the PU.

Name	Monomer	PU/PA	PU HB content /wt%
MMA20_HB45		80/20	45%
MMA30_HB50		70/30	50%
MMA40_HB55	MMA	60/40	55%
MMA50_HB60		50/50	60%
BMA20_HB45	ВМА	80/20	45%
BMA30_HB50		70/30	50%
BMA40_HB55		60/40	55%
BMA50_HB60		50/50	60%
iBMA20_HB45		80/20	45%
iBMA30_HB50	;DMA	70/30	50%
iBMA40_HB55	iBMA	60/40	55%
iBMA50_HB60		50/50	60%
STY20_HB45	Styrene	80/20	45%
STY30_HB50		70/30	50%
STY40_HB55		60/40	55%
STY50_HB60		50/50	60%

The reaction mixture was heated to 95 °C while applying mild agitation. After 4 hours reaction time, the PU pre-polymer solution was cooled to 60°C while simultaneously diluting further with monomer to reach the required PU/monomer ratio (Table 2.3).

Further TEA (85 mol% with respect to DMPA content) was added allowing 5 minutes for neutralisation of the carboxylic acid groups to occur. Next, the neutralised PU prepolymer solution in monomer solvent, at 65 °C, was added to a 1L glass cylinder reactor containing water at 30 °C (PU/monomer solution / water ratio 40/60) followed by stirring well for 5 minutes. The emulsified PU pre-polymer in monomer was chain extended by addition of aqueous EDA solution (20 wt% in water) over 10 minutes at 35 °C, to achieve a theoretical chain extension of 70% (NH<sub>2</sub>/NCO = 0.7).

Half of each batch was sealed and transported to Sheffield with acrylic monomers unreacted. The other half of each was heated to 40 °C under N<sub>2</sub>, and the acrylic/styrene polymerisation initiated using *t*BHP (70% in water) followed one minute later by a solution of sodium ascorbate (0.05 g) and iron sulfate heptahydrate (0.006 g) in deionised water (1ml). The temperature was monitored, and a second dose of tBHP, followed by sodium ascorbate (0.025 g) in deionised water (0.5 ml) was delivered 30 minutes after the first.

# 2.2 Characterisation of Materials by Small-Angle X-ray Scattering

# 2.2.1 General Principles

During SAXS data collection, a sample is exposed to an X-ray beam in transmission mode (Figure 2.4) (with the exception of grazing incidence SAXS (GISAXS), which operates on the principle of grazing incidence of X-rays). The X-ray beam interacts with the electrons in the sample. There are two ways that this interaction can happen: absorption or scattering. Compton – or inelastic – scattering involves the loss of photon energy on collision with an electron. The resulting scattered radiation has a different wavelength, and is incoherent, with the incident radiation. Thomson – or elastic - scattering occurs when photons collide with electrons without energy transfer. The

electrons begin to oscillate at the same frequency as the X-rays. As a result, the electrons emit radiation with the same wavelength as the incoming radiation. The outgoing radiation scatters in all directions, and the scattered intensity is related by a scattering angle of  $2\theta$  to the incoming beam (Figure 2.4).  $2\theta$  is inherently related to the wavelength of the X-ray radiation<sup>3,4</sup> ( $\lambda$ ) (Equation 2.1), therefore the scattering signal is often represented as a function of the scattering vector modulus, q:

$$q = \frac{4\pi sin\theta}{\lambda} \quad [Eq. 2.1]$$

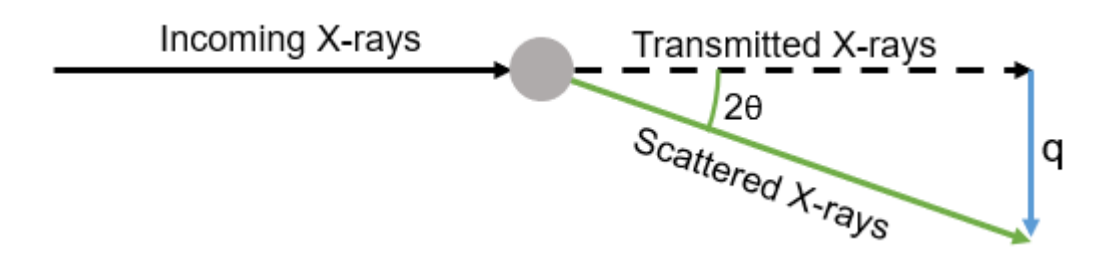


Figure 2.4: Schematic diagram of the interaction of a scattering object with an incoming X-ray beam. Some of the X-rays are not scattered (black, dashed line). The X-rays that are scattered by the object are deflected in all directions.

The scattering occurs over the entire irradiated volume of the sample, resulting in coherent waves that then produce interference patterns at the detector.  $^{2,5}$  Any structures in the sample are represented by these patterns. There is a relationship between real space - represented by the distance (d) - and reciprocal space - represented by q:

$$d = \frac{2\pi}{q} \quad [Eq. 2.2]$$

Bragg's law for the period of a repeating structure invokes that large objects scatter at smaller angles, and smaller objects at large angles. As irradiated electrons in the sample will likely interact with, and scatter, the incoming X-rays, this implies that, for

a solution of polymer particles, both the solvent molecules and the particles will undergo X-ray scattering. The resulting pattern will be superimposed scattering signals produced by all the irradiated objects.

The scattering ability of a material is dependent on its electron density (or scattering length density, SLD). For polymers, when mass density ( $\rho_m$ ) and material composition are known, SLD ( $\xi$ ) is given by:

$$\xi = \frac{b_{\rm e}\rho_{\rm m}N_{\rm A}}{M}\Sigma n_i z_i \quad [Eq. 2.3]$$

where  $b_e$  is the scattering length of a single electron in cm,  $N_A$  is Avagadro's constant in mol<sup>-1</sup>, M is the molar mass of one polymer repeat unit in gmol<sup>-1</sup>,  $n_i$  is the number of atoms of element i in the repeat unit, and  $z_i$  is the number of electrons per atom of i.

The contrast in SLDs of a system's constituent parts, such as particles and solvent, determines the intensity of a sample's scattering:

$$contrast = (\xi_{particle} - \xi_{solvent})^2$$
 [Eq. 2.4]

The scattering pattern of the particles will be very weak or impossible to discern from the background scattering if the two SLDs are similar.

During SAXS data collection, a detector senses scattered X-rays and logs their twodimensional position in relation to the incident beam. The q range over which the data is collected depends on the detector's shape, size, and distance from the sample (Figure 2.5).

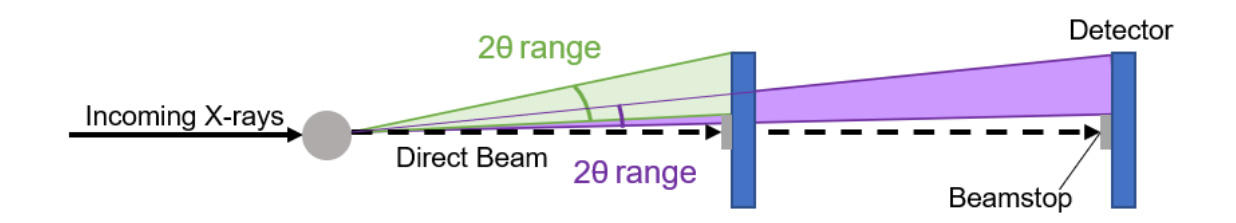


Figure 2.5: Effect of camera length on the resolution of an X-ray scattering instrument. At shorter camera lengths the instrument allows resolution of greater 20 (green) whereas a longer camera length resolves smaller 20 (purple). Some X-rays are not scattered (black dotted line) and are blocked by a beamstop.

Scattering intensity, I(q), usually expressed in reciprocal units of length, corresponds to the number of X-ray photons that are detected as a function of scattering vector. In theory, the scattering object shape, molecule configuration and positions of the atoms in relation to one another, averaged over the entire irradiated sample volume, can be determined from the scattered X-rays, which can be seen as a 2D interference pattern.

The pattern of scattered X-rays will be isotropic, or symmetrical with respect to the centre of the incoming beam, if the structural morphology in the sample has no preferable orientation. The simplest way to analyse an isotropic scattering pattern is to azimuthally integrate the 2D pattern, which results in a 1D curve of I(q) against q (Figure 2.6).

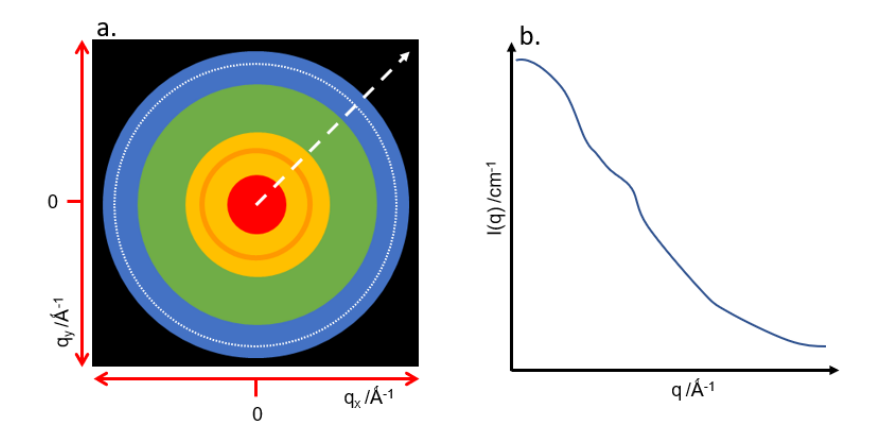


Figure 2.6: (a) A representative schematic of an isotropic 2D scattering pattern, which is identical in all radial directions from the X-ray beam centre. An azimuthal integration of this pattern occurs along each circle (azimuth line shown by dotted line), representing a particular radial position on the detector, resulting in a 1D curve where each point corresponds to the radial positions (shown by the dashed white vector) associated with a q value. (b) Azimuthal integration results in a representative I(q) against q graph.

### 2.2.2 Grazing Incidence SAXS

GISAXS is a technique often used to study the surface of a sample. The principles of scattering remain applicable if the angle of grazing incidence ( $\theta_i$ ) (Figure 2.7) is kept large in comparison to the critical angle ( $\theta_c$ ).  $\theta_c$  is an inherent property of a material, and at  $\theta_i < \theta_c$ , the sample becomes totally reflecting.<sup>2</sup>

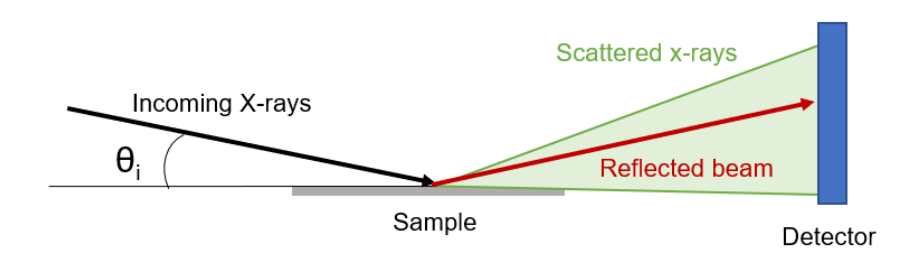


Figure 2.7: Set up for GISAXS, where  $\theta_i$  is the incident angle of the incoming X-ray beam.

Depth dependent information can be obtained by varying  $\theta_i$ , and therefore penetration depth of the X-rays.

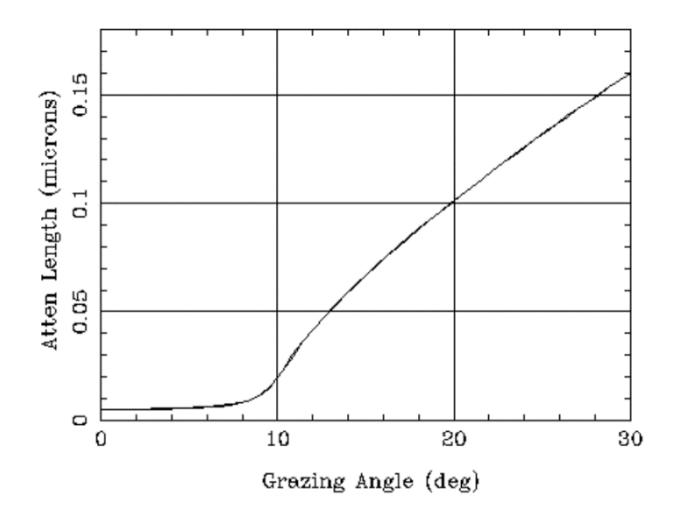


Figure 2.8: X-ray attenuation length as a function of grazing incidence angle in X-ray scattering for a polymer film (poly(methyl methacrylate)), calculated using an online tool.<sup>6</sup>

#### 2.2.3 Scattering by Particle Dispersions

Many details about the particles in a sample can be learned from the one-dimensional profile of the particle scattering. The scattered intensity from uniform particles,  $I_p(q)$ , depends on the form factor, P(q), and the structure factor, S(q), and increases with the

SLD contrast  $(\Delta \xi)^2$  (described in Equation 2.4), particle volume  $(V_p)$ , and volume fraction of the particles  $(\phi)$ :

$$I_p(q) = (\Delta \xi)^2 \cdot \phi \cdot V_p \cdot P(q) \cdot S(q)$$
 [Eq. 2.5]

The size and shape of the particles is represented by the form factor and, in general, it is expressed via the following equation:

$$P(q) = \frac{1}{(\Delta \xi)^2 V_{\rm p}} \int \gamma(r) e^{-iqr} dr \quad [Eq. 2.6]$$

where  $\gamma(r)$  is the correlation function of the particle (Figure 2.9a).<sup>7</sup> For a homogenous spherical particle of radius r, P(q) and  $V_p$  are expressed as:

$$P(q) = \frac{9(\sin(qr) - qr\cos(qr))^{2}}{(qr)^{6}} \quad [Eq. 2.7]$$

$$V_{part} = \frac{4}{3}\pi r^3 \quad [Eq. 2.8]$$

As such, the intensity minima in the scattered intensity profile of a spherical particle occurs at q-values corresponding to solutions of the equation  $\tan(qr) = qr$  (Figure 2.9b). In particular, the first intensity minimum corresponds to the solution of  $qr \approx 4.49$ .

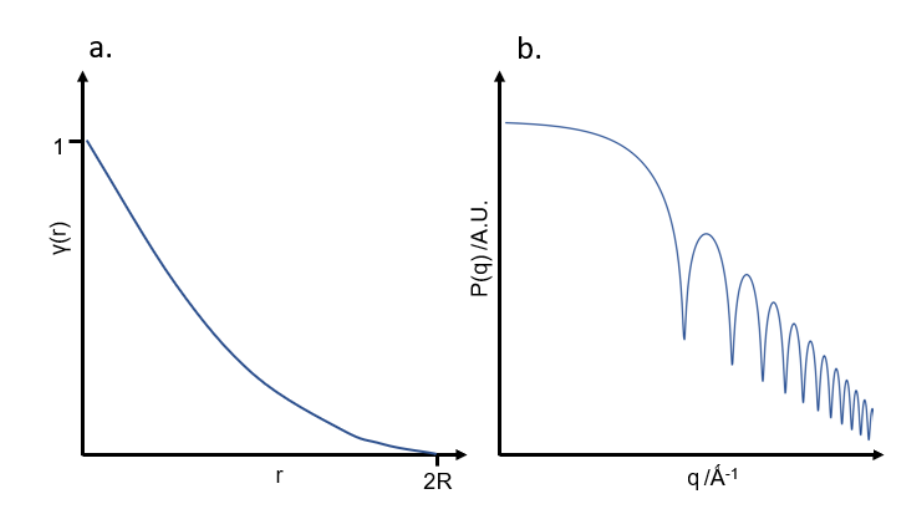


Figure 2.9: A representative (a) correlation function for a spherical scattering object, and (b) the corresponding form factor

The structure factor (S(q)) in Equation 2.5 describes how particles interact in a system. It is expressed as a summation of cross-terms describing how particles are located with respect to each other (Equation 2.9).

$$S(q) = 1 + \frac{1}{N} \sum_{i=1}^{N} \sum_{j \neq i}^{N} e^{iq(r_j - r_i)} \quad [Eq. 2.9]$$

where N is the number of particles, and  $(r_j - r_i)$  is the distance between two particles. For a diluted sample, the interparticle distances averaged over the entire system are equal to zero and, according to Equation 2.9, S(q) = 1. However, for a concentrated dispersion, the interparticle distance is controlled by the particle size and interaction forces. Thus, the effect of structure factor is prominent and the 1D scattering profile becomes far more complex (Figure 2.10). In order to rule out the influence of interparticle interactions, care is frequently taken to ensure samples are sufficiently dilute before collection of SAXS data where P(q) contains the information of interest.

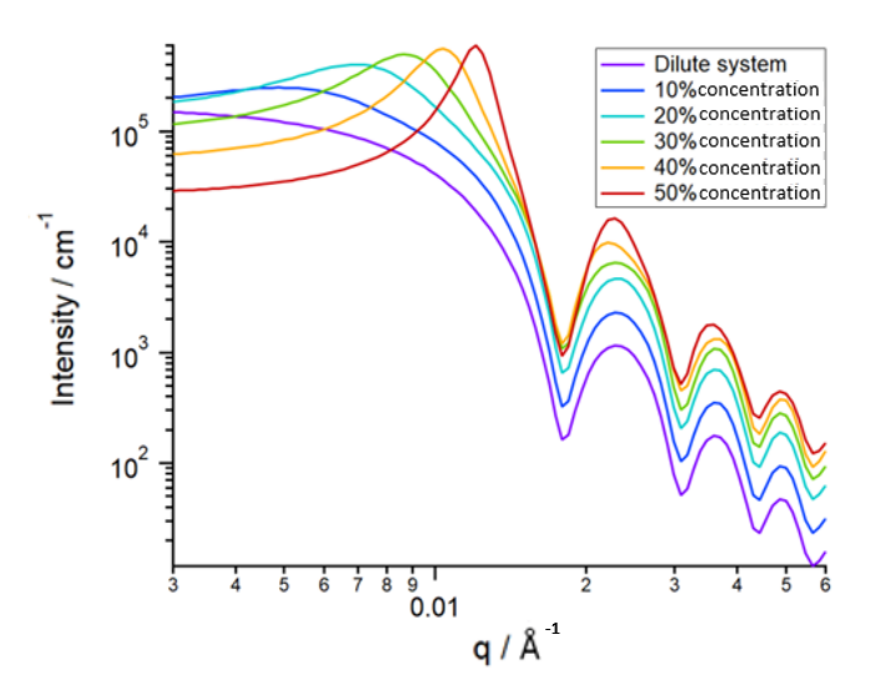


Figure 2.10: Simulated scattering profiles for hard spheres with an average radius of 25 nm (5% particle size dispersity) showing the effect of structure factor with increasing particle concentration.

Polydispersity presents challenges in the SAXS analysis of polymer particles and colloids. SAXS patterns represent scattering from all irradiated particles, and consequently the resulting pattern from a polydisperse sample is the sum of the individual particle contributions. With increasing polydispersity, the form factor minima (Figure 2.9b) become less defined (Figure 2.11), and meaningful analysis of the particles' structural detail is increasingly difficult.<sup>2,8</sup>

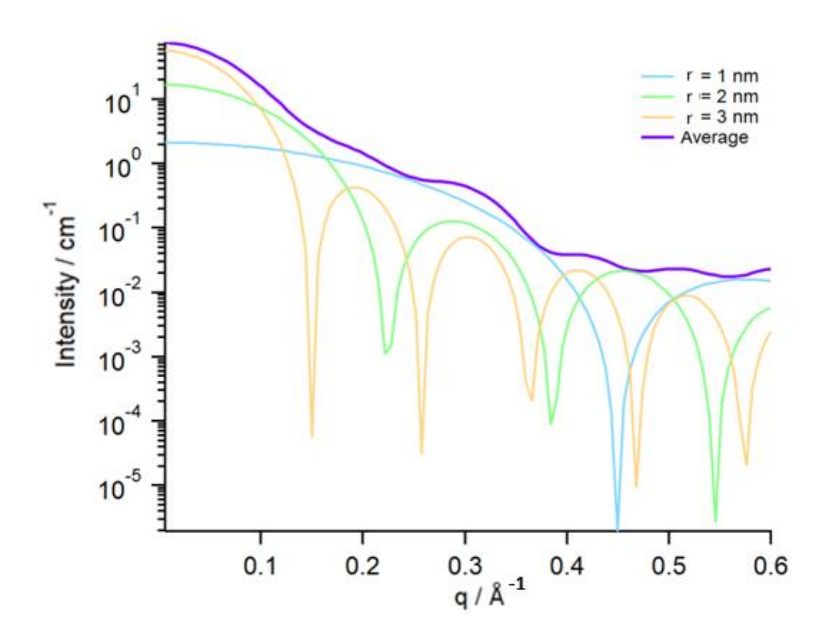


Figure 2.11: Simulated scattering profile showing the average scattering (purple) from a solution of three populations of spheres of different radius (r) (green, blue and yellow) to illustrate the effect of polydispersity.

The scattered intensity of a population of particles with variable sizes is described by Equation 2.10, where the size polydispersity is counted by integration over both the size distribution function ( $\Psi(r)$ ), and the form factor defined by the particle size (P(q,r)), at a concentration of N particles per unit sample volume.

$$I(q) = NS(q) \int_{0}^{\infty} \dots \int_{0}^{\infty} P(q, \mathbf{r}) \Psi(\mathbf{r}) dr_{1} \quad [Eq. 2.10]$$

This can be expanded to give a more general equation for application to other structural parameters that may also have a polydispersity.

$$I(q) = NS(q) \int_{0}^{\infty} ... \int_{0}^{\infty} P(q, r_1, ..., r_k) \Psi(r_1, ..., r_k) dr_1 ... dr_k \quad [Eq. 2.11]$$

where  $P(q,r_1,...,r_k)$  is the form factor defined by a k number of r parameters describing a certain particle morphology, and  $\Psi(r_1,...,r_k)$  is the multi-dimensional distribution function of these parameters.

Various mathematical equations exist, describing the P(q) for different particle shapes.<sup>4,9,10</sup> There are also general theorems such as the Guinier and Porod laws which are based on general scattering principals.<sup>7,11</sup>

At small angles, any particle form factor can be approximated to a Gaussian curve. According to Guinier,<sup>7</sup> the curvature of this Gaussian is dependent on the particle size, denoted by radius of gyration ( $R_g$ ):

$$I(q) \approx a_0 e^{\frac{R_g^2 q^2}{3}}$$
 [Eq. 2.12]

 $R_{\rm g}$  is defined as the root mean square distance of all points in the particle from the centre of mass, therefore is independent of shape. For a dilute system, with  $I(0) = a_0$ ,  $R_{\rm g}$  can be derived from Equation 2.12 at  $R_{\rm g}q << 1$ .

A Guinier plot of  $\ln[I(q)]$  vs  $q^2$  will give a slope of gradient equal to  $-(R_g^2)/3$ . Additionally, the intercept,  $\ln[\phi\Delta\xi^2V_p]$ , contains information on concentration, contrast and particle volume.

The Porod law relates to scattering of a two-phase system (e.g. particle dispersions) at high q, which contains details about interphase surfaces.<sup>11</sup> Scattering intensity in the Porod region is dependent on the Porod constant,  $B_v$ :

$$I(q) = B_{\rm v}q^4$$
 [Eq. 2.13]

 $B_v$  can be measured from the plot of  $I(q)^*q^4$  vs q as a constant at high q. Interphase surface area per volume ( $S_v$ ) can be obtained from  $B_v$ :

$$B_{\rm v} = 2\pi (\Delta \xi)^2 S_{\rm v} \quad [Eq. 2.14]$$

There are some parametrisation approaches such as unified fit<sup>12</sup> and Guinier-Porod model<sup>13</sup> where both laws are combined together for describing scattering patterns representing complex multi-hierarchical morphologies.

### 2.2.4 SAXS Data Treatment

To obtain scattering intensity data on an absolute scale (usually expressed in units of cm<sup>-1</sup>), it is necessary to ensure patterns are appropriately normalised, and any background subtracted.

Normalised scattering profiles ( $I_{\rm exp,norm}$ ) are obtained by dividing the experimental data ( $I_{\rm exp}$ ) by sample thickness ( $t_{\rm s}$ ), acquisition time (T), and transmission coefficient (tc) of the material.

$$I_{\text{exp,norm}} = \frac{I_{\text{exp}}}{t_{\text{s}} \times T \times tc}$$
 [Eq. 2.15]

While T and  $t_s$  are known from the experimental setup, tc must be measured. This requires comparing the intensity of a direct beam ( $I_{db}$ ) (Figure 2.12a), with that of a beam passing through the sample ( $I_s$ ) (Figure 2.12b). This can be done during acquisition using devices such as a photo-diode beam stop, or before/after acquisition using removable photo diodes or certain detectors with a wide dynamic range of photon counting, such as a pixel detector.

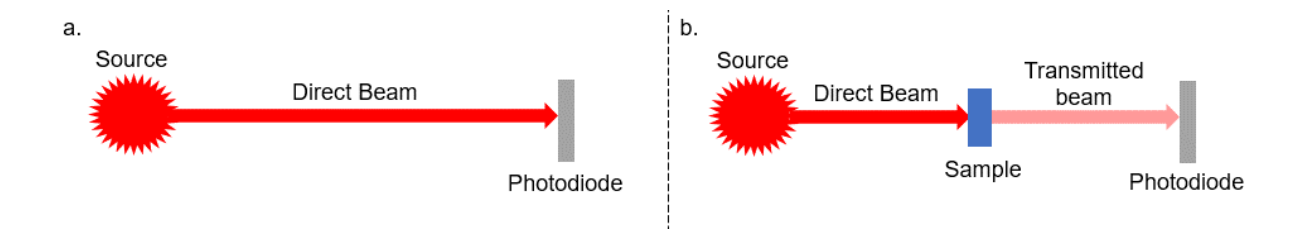


Figure 2.12: Measurement of the flux of a) a direct beam ( $l_{db}$ ) and b) transmitted flux through a sample ( $l_{s}$ ) for calculation of sample transmission coefficient.

If the device is susceptible to background noise, or dark counts ( $I_{dc}$ ), this is factored into the calculation of tc (Equation 2.16) by measuring counts with no X-ray beam.

$$tc = \frac{I_s - I_{dc}}{I_{db} - I_{dc}}$$
 [Eq. 2.16]

For most instruments, a correction factor is required to account for the intensity differences caused by factors such as beam size, flux of the x-rays source, or detector sensitivity. As such, the scattering of a calibrant is collected using the instrument setup to be applied to samples, and the intensity compared to a known standard. Glassy carbon<sup>14</sup> or water,<sup>15</sup> once normalised by Equation 2.15, is commonly used for this calibration.

For SAXS data of a sample of colloidal particles in dispersion, it is necessary to remove background scattering caused by the irradiated solvent, and the sample holder capillary, to obtain the scattering from just the particles. The user must therefore collect and normalise the scattering profiles of the empty sample holder ( $I_{cap,norm}$ ) and the solvent in the sample holder ( $I_{sol+cap,norm}$ ). The scattering from the solvent ( $I_{sol,norm}$ ) (Figure 2.13) is given by:

$$I_{\text{sol,norm}} = I_{\text{sol+cap,norm}} - I_{\text{cap,norm}}$$
 [Eq. 2.16]

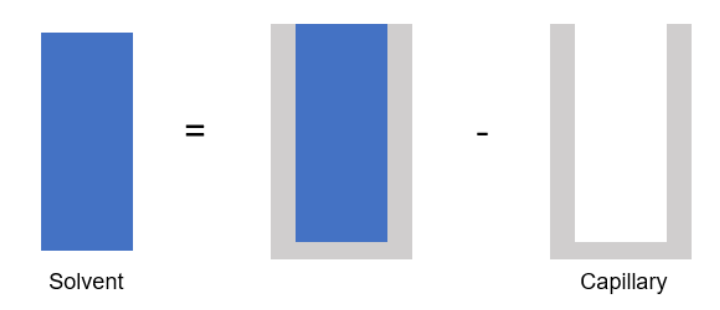


Figure 2.13: Schematic representing the processing of solvent and capillary SAXS profiles to obtain the scattering from the solvent

For a dispersion containing  $\phi$  vol% of particles, the final, normalised scattering profile of the particles ( $I_{part,norm}$ ) is obtained by subtracting the solvent and capillary scattering from the normalised experimental data (Figure 2.14).

$$I_{\text{part,norm}} = I_{\text{exp,norm}} - I_{\text{cap,norm}} - (1 - \phi) * I_{\text{sol,norm}}$$
 [Eq. 2.17]

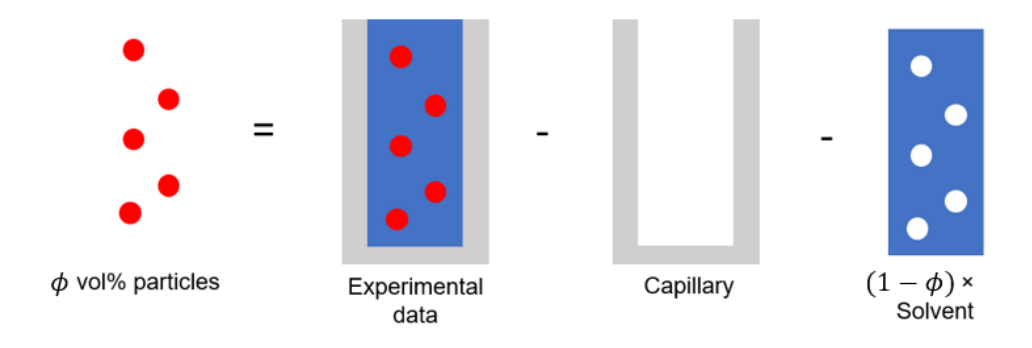


Figure 2.14: Schematic representing the processing of experimental data collected on particles in solvent to obtain the scattering from the particles.

#### 2.2.5 SAXS Data Collection

The data were collected either using a laboratory SAXS instrument or large-scale synchrotron facilities. SAXS data of dispersions were collected in transmission geometry. A flow-through cell, comprised of a borosilicate glass capillary (WJM-Glas, Berlin) (2 mm diameter), connected to an injection syringe and a waste container using plastic tubing, was used for the measurements. After data collection, further data reduction (background subtraction, data merging, data modelling) was carried out

using Irena SAS macros<sup>16</sup> for Igor Pro. For background subtraction, scattering of the empty flow cell, and the flow cell containing just water, were collected, integrated and normalised. For all X-ray scattering measurements, water was used as a calibrant for absolute intensity.<sup>15</sup>

### 2.2.5.1 Laboratory SAXS

SAXS patterns were recorded using a Xeuss 2.0 laboratory beamline (Xenocs, Grenoble, France), equipped with a liquid gallium Metal-jet X-ray source generating characteristic radiation at  $\lambda=1.34$  Å (Excellium, Kista, Switzerland). Scattering patterns were collected using a Pilatus 1M two-dimensional hybrid pixel detector (Dectris, Barden-Daetwil, Switzerland). Scattering data were collected over the range of 0.005 Å<sup>-1</sup>  $\leq q \leq 0.2$  Å<sup>-1</sup>. The sample-to-detector distance was measured using silver behenate standard. Two-dimensional scattering patterns were integrated to give one-dimensional profiles and normalised using the XSACT software package (Xenocs, Grenoble, France) supplied with the instrument.

The sample chamber was placed under vacuum to eliminate scattering from air for all SAXS collected in transmission geometry. For data collection on PUDs, dispersions were diluted in deionised water to concentrations of 1 wt% PU. Dried films were prepared from PUDs at their original concentration (of about 30 wt%, Table 2.1) by drop casting onto Kapton sheets and drying for 48 hours at ambient conditions. *In situ* GISAXS measurements were performed during the drying of sample *HB50\_SS1000a*, from a 33 wt% dispersion drop-cast on a glass slide, with the sample surface tilted to an angle of 0.3 ° relative to the incident beam. Data were collected continuously for one hour, with each frame spanning a period of 5 minutes.

### 2.2.5.2 SAXS at the European Synchrotron Radiation Facility

SAXS for optimisation of the capillary method (Section 2.2.6.1) was carried out at the European Synchrotron Radiation Facility (ESRF, station ID02, Grenoble, France) using monochromatic X-ray radiation ( $\lambda = 0.995 \text{ Å}$ ) over q range of 0.002 - 0.15 Å<sup>-1</sup>, and a Rayonix MX-170HS CCD detector.<sup>18</sup>

### 2.2.5.3 SAXS at Diamond Light Source

PUMA dispersion SAXS and *in situ* data collection using the syringe pump method (Section 2.2.6.2) was carried out at Diamond Light Source (Beamline I22, Didcott UK) using monochromatic X-ray radiation ( $\lambda = 1.24 \text{ Å}$ ) over a q range = 0.002 – 0.2 Å<sup>-1</sup> on a 2D Pilatus 2M pixel detector (Dectris, Switzerland).<sup>19</sup> Data was integrated and normalised using DAWN software package (Diamond Light Source, UK).<sup>20</sup>

### 2.2.6 *In-situ* SAXS

Due to the short timescale of the acrylic polymerisation reaction, the high flux and subsequent short acquisition times of synchrotron radiation was required to collect time-resolved SAXS patterns *in situ*. Due to the setup of beamlines, it was necessary to find a method whereby the reaction could be initiated remotely, and data acquired within a relatively short period of time (< 1 minute for some reactions) using an appropriate 2 mm thick sample holder at a temperature of 40 °C. Methods that worked at low concentrations were desirable, such that the effect of S(q) would be minimized to simplify the task of obtaining information from the SAXS data about particle morphology from P(q).

### 2.2.6.1 Optimisation of the capillary method

Optimisation of the conditions for following the acrylic reaction using SAXS *in situ* were carried out on sample *iBMA50\_HB60* (Table 2.3). A set of offline laboratory experiments were performed to optimise the synthesis conditions prior to carrying out SAXS at the beamline. Recording temperature to monitor an exotherm was chosen as the most appropriate way to screen whether a set of reaction conditions was suitable for the acrylic polymerisation.

Initially a relatively large round bottom flask (rbf) was used, and temperature measured using a digital probe. This method showed that an exotherm of +8.5 °C occurred when following the procedure supplied by AkzoNobel (Section 2.1.3), with a final PUMA concentration of 34 wt% on a 50 ml scale (Table 2.4, Reaction 1). The method was repeated at a dilution of 12 wt% final PUMA concentration, and a much smaller exotherm of only +3 °C observed (Table 4, Reaction 2).

Table 2.4: Conditions for test reactions to refine a method for the collection of SAXS data in situ during the polymerisation of acrylic in a PUD dispersion to make PUMA.

Reaction	Volume /ml (vessel)	Final polymer concentration /wt%	Set Temperature /°C	Exotherm /°C
1	50 (rbf*)	34	40	+ 8.5
2	60 (rbf*)	12	40	+ 3
3	60 (rbf*)	12	40 (prepared at 8 including initiator addition)	Not visible
4	2 (vial)	12	40	+ 2
5	~0.2 ml (capillary)	12	50 (prepared at 0 including initiator addition)	+ 2.3

<sup>\*</sup> rbf refers to a round bottomed flask

This was repeated with the reaction mixture cooled to 8 °C during the addition of initiators (Table 2.4, Reaction 3). Figure 2.15 shows that no exotherm was observed at this temperature, suggesting that the initiation had not taken place. The reaction

mixture was placed at a later stage in a pre-heated oil bath at 40 °C, however there was no visible exotherm or any sudden increases in heating rate of the reaction mixture.

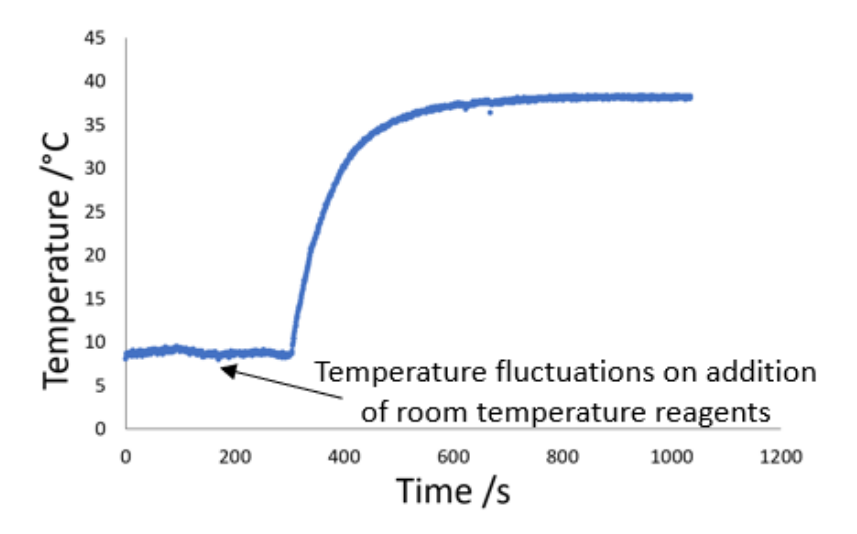


Figure 2.15: Temperature profile recorded during Reaction 3 (Table 4)

In order to replicate synthesis conditions for time-resolved SAXS measurements, a similar experiment was performed using a significantly smaller sample volume (Table 2.4, Reaction 4). It was expected that reactions at smaller volumes would produce lesser exotherms, therefore a more precise temperature probe attached to a Raspberry Pi device<sup>21</sup> was used to record temperature readings every 0.6 s. Figure 2.16 shows the temperature profile recorded for the reaction repeated at 12 wt% final PUMA concentration, at 40 °C on a 2 ml scale. A rapid temperature increase of +2 °C was observed with the maximum temperature reached 170 s after addition of the sodium ascorbate/iron sulphate initiator solution, suggesting that the polymerisation was successful under these dilute, small scale conditions.

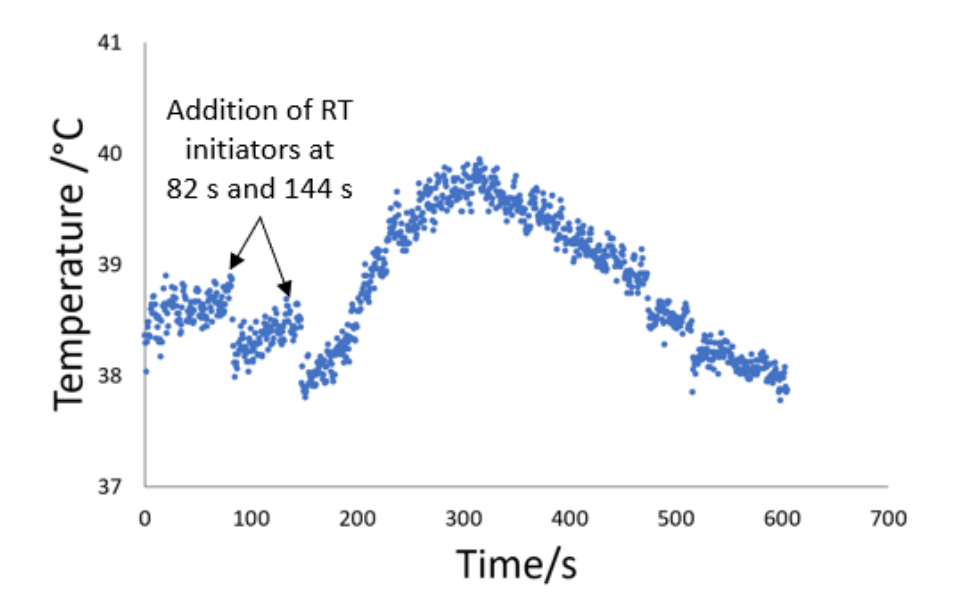


Figure 2.16: Temperature profile recorded during Reaction 4 using small sample volume (Table 2.4)

These preliminary tests in a synthetic laboratory suggested that the reaction was viable at low volumes and dilute concentrations (Reaction 4, Table 2.4 and Figure 2.16) and would not react during preparation if kept sufficiently cool (Reaction 3, Table 2.4 and Figure 2.15), therefore could be heat initiated. The SAXS patterns of the resulting products are shown in Figure 2.17.

Comparison of these SAXS curves with a sample synthesised in the industrial laboratory, by AkzoNobel, shows that all the tested reaction conditions produced particles of a similar average size and morphology, with differences in polydispersity. This is most likely due to the smaller scale and dilute conditions giving a lesser exotherm, so initiation of the reaction is not uniform across all particles in the sample. This effect is most significant for Reaction 3 (Table 2.4, Figure 2.17) where gradual heating of the sample has most likely caused staggered, non-uniform reaction initiation.

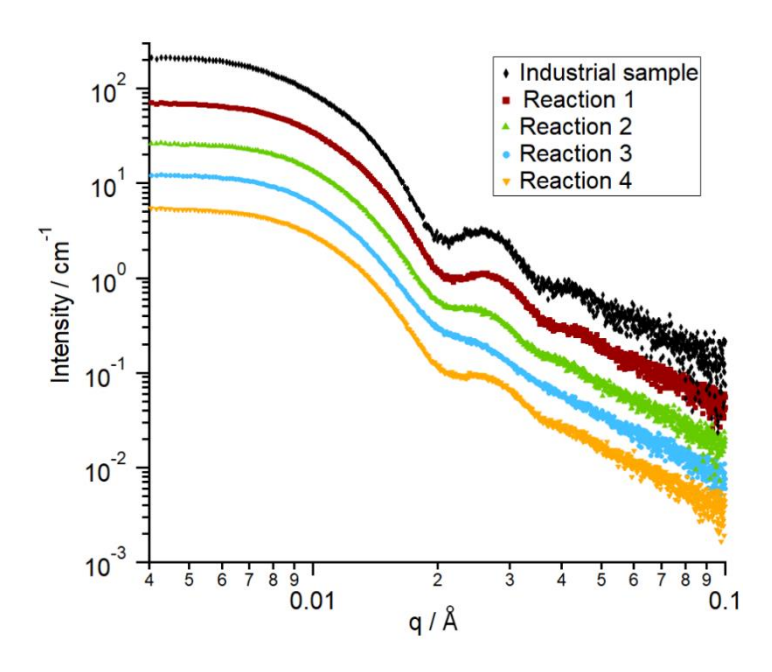


Figure 2.17: SAXS profiles of the products of test reactions carried out for the optimisation of an in situ SAXS data collection method (labelled as Reactions 1-4), compared to a bench-mark sample produced industrially (labelled as Industrial sample).

The final test (Reaction 5, Table 2.4) was carried out in a capillary to check the viability of using this sample holder as a reaction vessel for *in situ* SAXS measurements. The reaction mixture was prepared in an ice bath and a small volume (~ 0.2 ml) transferred to a cooled capillary that was then coupled with the Raspberry Pi temperature probe. The capillary was transferred to an oil bath preheated to 50 °C to initiate the reaction. It was expected that the exotherm would be minimal. Therefore, the oil bath temperature was raised compared to other experiments to accelerate the reaction to increase sensitivity of the exotherm measurements. As an exotherm exceeding the oil bath temperature was recorded (Figure 2.18), this reaction was deemed to be successful.

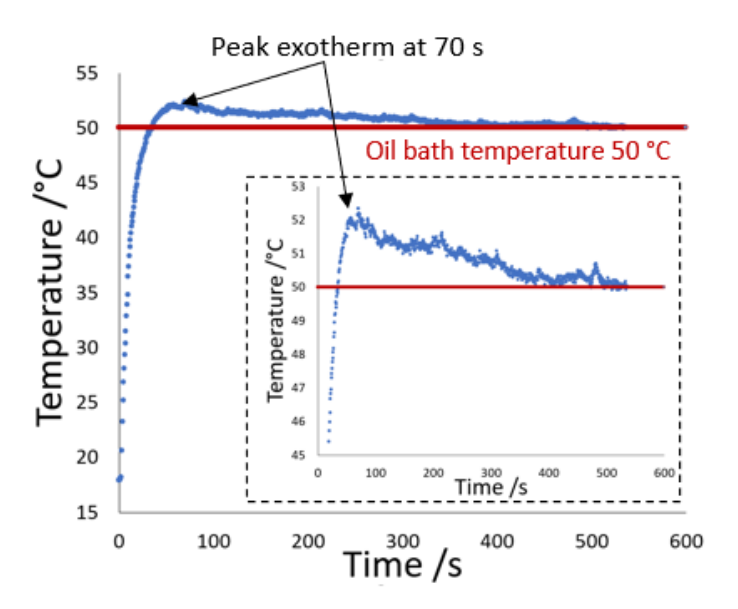


Figure 2.18: Temperature profile recorded during Reaction 5 (blue points) (see Table 4). The start of the measurements corresponds to the time the loaded capillary was placed in the preheated oil bath. The red line shows the oil bath temperature.

The tested reaction conditions were used as guidance for setting up *in situ* SAXS measurements at the ESRF beamline. 2 ml of the reaction mixture was prepared in a nitrogen-flushed vial kept in an ice bath and transferred to a pre-cooled borosilicate glass capillary (2mm diameter). The sample temperature was controlled by a heating/cooling capillary holding stage (Linkam Scientific Instruments Ltd., Tadworth, UK) (Figure 2.19) that was pre-cooled to 5 °C and held at this temperature. The reaction was initiated by heating the capillary using a temperature ramp of 30 °Cmin<sup>-1</sup> from 5 °C to 40 °C. SAXS data were simultaneously collected every 5 seconds until no more changes were observed in the integrated 1D SAXS profiles.

The data showed that the final product had a very different morphology to the samples prepared in a synthetic laboratory (Figure 2.20). The industrial sample shows the pattern of minima characteristic of spherical particles with relatively low polydispersity (Figure 2.9b), and a plateau at low q followed by a slope of  $\sim q^4$  on a log/log plot. The sample synthesised in the capillary on the beamline does not show these distinct features of spherical particles, so either possess a different morphology, or is

extremely polydisperse. Moreover, the transition from plateau to slope is located at higher q, suggesting smaller scattering objects.

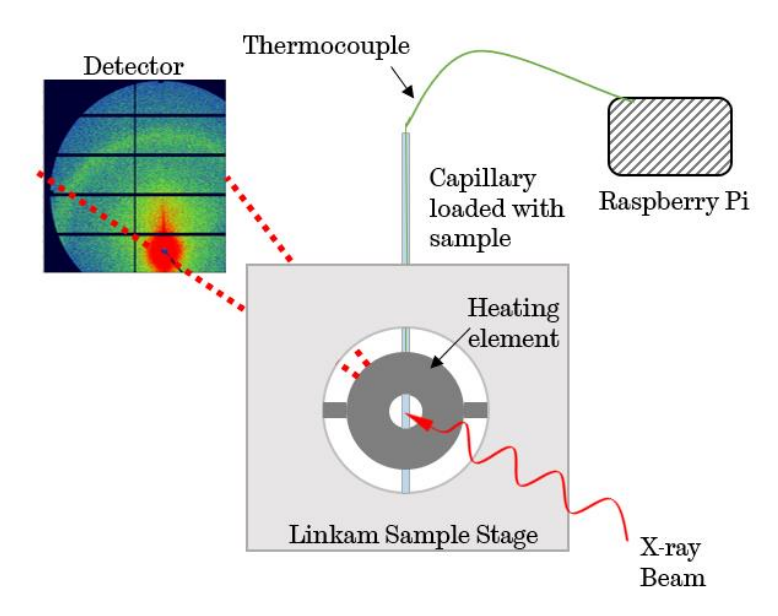


Figure 2.19: Schematic of the set up for collection of in situ SAXS data during PUMA particle synthesis using a borosilicate glass capillary as a sample holder and a linkam heating/cooling stage for the reaction initiation.

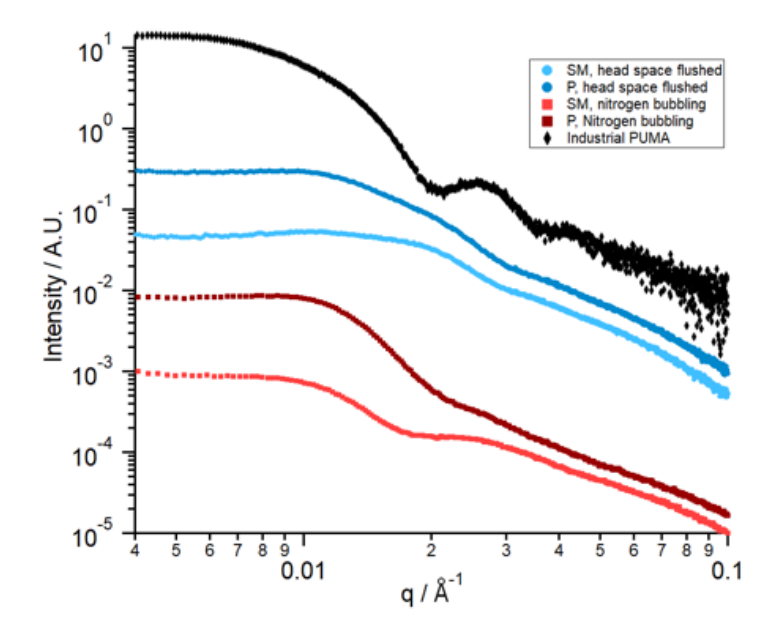


Figure 2.20: SAXS profiles of starting material containing unreacted acrylic (SM) and final PUMA products (P) for reactions carried out in capillaries at the optimised conditions with nitrogen flushing before the reaction (head space flushed) and bubbling through the mixture (Nitrogen bubbling). A SAXS profile of the same PUMA particle dispersions synthesised in AkzoNobel's industrial laboratory (Industrial PUMA) is given for a comparison. Data are displaced on the intensity axis to avoid overlap of the SAXS patterns.

Further repeats were carried out with extensive nitrogen bubbling through diluted, unreacted PUMA before addition of the initiator solutions and loading into the capillary. The SAXS profile for these showed further deviations in morphology compared to the industrially synthesised PUMA particles, used as a benchmark (Figure 2.20). Comparison of the starting mixtures shows large differences in the scattering profile when nitrogen bubbling through the sample was carried out, possible due to the formation of bubbles.

Comparing these findings with the results of the test reactions (Figure 2.17), it follows that the scale of the reaction in the capillary was unsuitable for a meaningful replication of the reactions performed using laboratory conditions.

## 2.2.6.2 The Syringe Pump Method

Based on the results of the optimisation experiments using a borosilicate capillary, an alternative method was developed such that the reaction was carried out using a relatively large reagent mixture volume of about 50 ml.

Each unreacted PUMA reagent mixture was diluted to 6 wt% of the final PUMA product using deionised water that had been flushed with nitrogen, to give a final volume of 50 ml in a sealed round bottom flask. This was equipped with a thermocouple, a nitrogen inlet, an air outlet and Teflon tubing connections to a borosilicate glass capillary flow cell, further connected to a 50 ml withdrawing syringe mounted in a syringe pump (Harvard Apparatus) (Figure 2.21). The flask containing the reagent mixture was heated to 40 °C using a water bath, under a constant stream of nitrogen, with stirring to ensure homogenisation. *t*BHP (70% in water, 0.06 ml) was injected into the polymer solution. Stock solutions of sodium ascorbate (0.55 g) in deionised water (5 ml) and iron sulfate heptahydrate (0.0186 g) in deionised water (5 ml) were prepared. The

reductant solution (0.5 ml), made by adding iron solution to sodium ascorbate solution in a ratio of 2:1, was loaded into the initiator injecting syringe, and mounted in a second syringe pump.

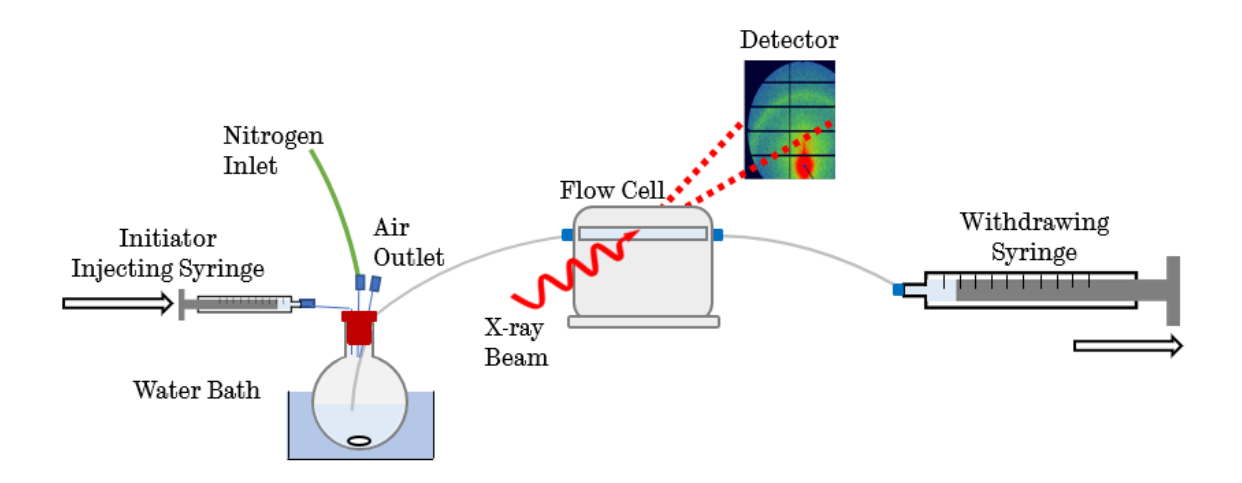


Figure 2.21: Schematic showing the set-up used for the collection of SAXS data in situ during the polymerisation of acrylic monomers in PUD to make PUMA particles, termed "the syringe pump method".

After hutch safety checks had been completed, the shutter was opened remotely and the withdrawing syringe pump, programmed to draw the mixture through the capillary at 2 ml min<sup>-1</sup>, was triggered. The reaction was initiated by the initiator-injecting syringe pump delivering reductant solution (0.6 ml) at 1 mlmin<sup>-1</sup> and, simultaneously, SAXS acquisition was triggered to record scattering patterns every 3 seconds (Figure 2.21). The beginning of the reaction (t = 0 s) was taken as the point at which the 1-dimensional integrated SAXS profiles started to change, and the end of the reaction was taken as the point at which no change was seen between SAXS profiles.

The scattering patterns of PUMA particle dispersions synthesised using either the syringe pump method or the industrial laboratory method appear very similar, showing the same characteristic P(q) features at the same q positions (Figure 2.22).

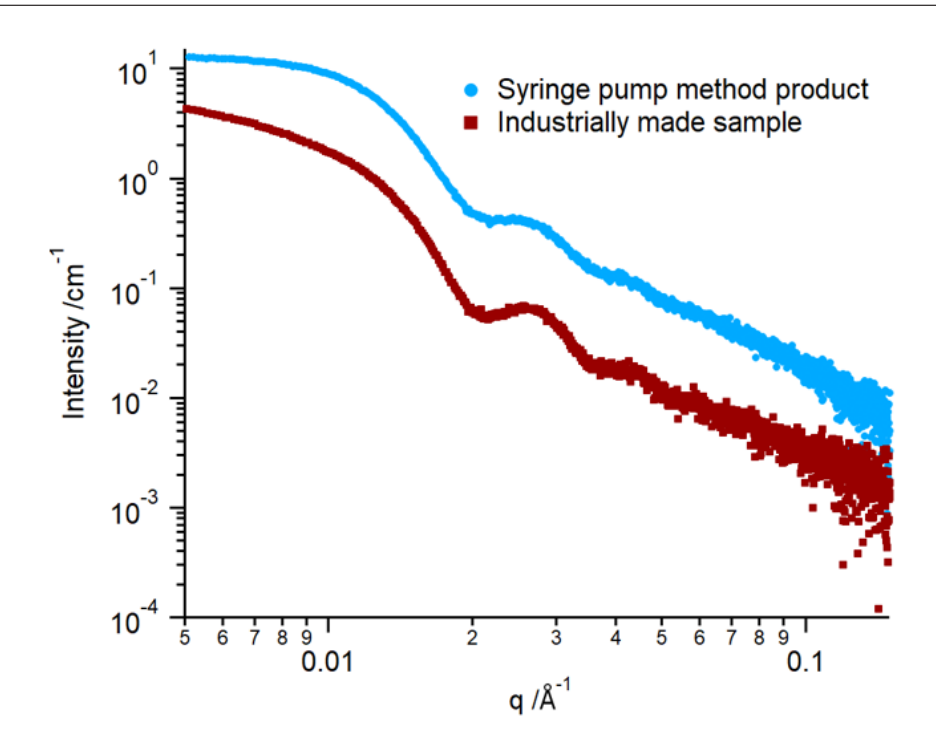


Figure 2.22: SAXS profiles of PUMA iBMA50\_HB60 as the product of the in situ SAXS reaction using the syringe pump method (blue), and the industrial laboratory method (red). The scattering profile for the industrial sample was collected at 1 wt% PUMA dispersion, whereas the in situ method was carried out at 6 wt%, causing the ~ 6x difference in intensity.

Some differences between the profiles at low q arise from S(q) due to the particle repulsion, which is more pronounced at the higher concentration used for the sample synthesised by the syringe pump method.

Thus, the syringe pump method was deemed successful for reasonable replication of the industrial process and used for collection of all *in situ* SAXS data.

# 2.2.7 Intermediate Sample Aging Check by SAXS

It was important to ensure that the time delay cause by the transportation of samples containing unreacted monomer was not influencing the final morphology. At the AkzoNobel labs in Sassenheim, NL, a 1 L batch of *iBMA50\_HB60* was halved prior to polymerisation of the iBMA. The first portion was polymerised immediately (*iBMA50\_D0*), and the remainder retained for 25 days before polymerisation

( $iBMA50\_D25$ ). In the displaced SAXS data (Figure 2.23a), there is negligible difference in P(q), with characteristic spherical particle features at the same q.

When presented on an absolute intensity scale (Figure 2.23b), the data overlaps very well, aside from an intensity deviation at low *q*. In this region, the data is very sensitive to small fluctuations in beam position and the precision of background subtraction, therefore differences in sample structure cannot be confidently used to justify this deviation. It was deemed that the time delay caused by transportation to Sheffield from Sassenheim would not be problematic for consistent replication of the industrial process.

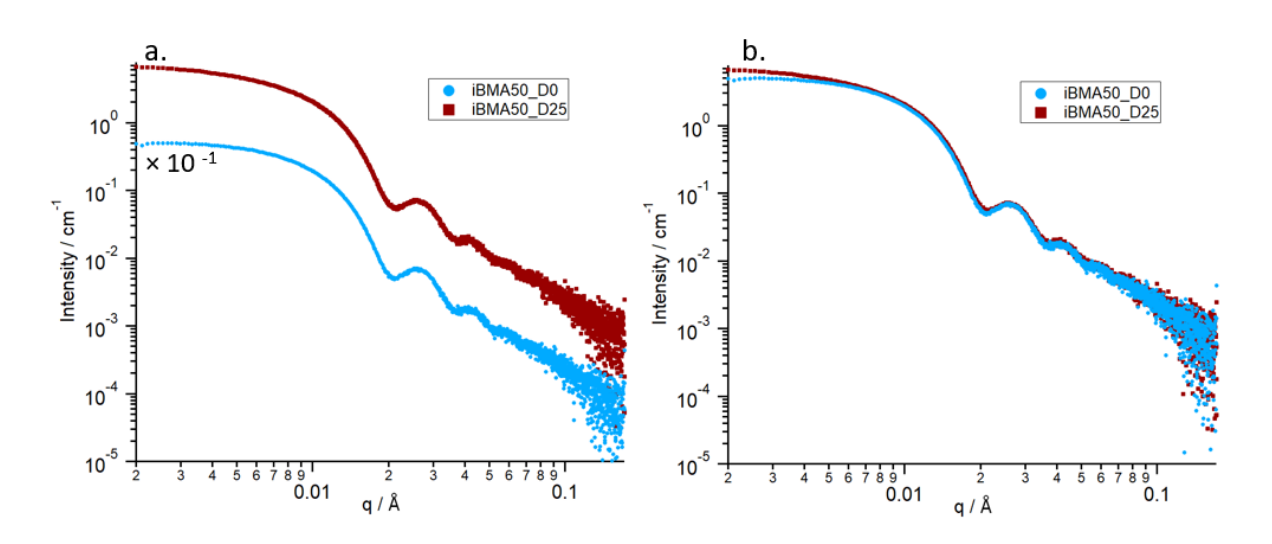


Figure 2.23: SAXS profiles of iBMA50\_HB60 with acrylic polymerisation carried out immediately after dispersion (iBMA50\_D0, blue circles) and after 25 days (iBMA50\_D25, red squares) a) displaced by the indicated factor, and b) on absolute scale

# 2.3 Other Characterisation Methods

### 2.3.1 Solution Density Measurements

Densities of PUD solutions were measured using an Anton Paar DMA 5000M U-tube style densitometer. All measurements were recorded at 20 °C. The equipment was calibrated using deionised water assuming a density of 0.9982 g cm<sup>-3</sup> at 20 °C.<sup>22</sup> The sample chamber was washed with deionised water, dried with compressed air,

washed with ethanol and further dried before each test. Samples were prepared at the desired PU concentration in deionised water, and injected into the instrument using a syringe.

### 2.3.2 Atomic Force Microscopy

Atomic force microscopy (AFM) imaging was performed using tapping mode on a 3100 Dimension scanning probe microscope (Veeco) equipped with a Nanoscope 3A feedback controller. NuNano SCOUT 350 RAI tips were used with a resonance frequency near 340 kHz. The images were processed using the open-source software Gwyddion (version 2.59).<sup>23</sup> Dispersion AFM samples were prepared by spin coating PUD onto single-crystal silicon wafer at 5000 rpm for 30 seconds. To preserve the morphology of PU particles in dispersion, these samples were prepared from low-concentration dispersion to ensure rapid drying. Thus, prior to the spin coating, the assynthesised PUDs were diluted to by a factor of ten using deionised water. The silicon wafer surfaces were preliminarily cleaned for 5 minutes using a Henniker oxygen plasma oven. For the study of dried films, PUDs were applied to a glass slide as a ~24 µm thick coating and allowed to air dry for at least 48 hours before AFM scanning.

#### 2.3.3 Matrix Assisted Laser Desorption Ionisation

PUD samples were diluted with methanol (1:10) and 10  $\mu$ l of each fraction was spotted onto a 96-well stainless-steel matrix assisted laser desorption ionisation (MALDI) target plate. Spots were left to dry at room temperature and then overlaid, using a Fisnar F200N automatic dispenser (flowrate 1.2 ml/hr), with a  $\alpha$ -Cyano-4-hydroxycinnamic acid matrix (5 mgml<sup>-1</sup> in methanol /0.1% (v/v) trifluoracetic acid).

The data were acquired using a Waters MALDI Synapt G2 instrument in negative mode, over a mass range of 50 – 3000 gmol<sup>-1</sup> for 120 seconds, powered by a solid-state laser with a repetition rate of 1000 Hz.

## 2.3.4 Fourier Transform Infrared Spectroscopy

Fourier Transform Infrared (FTIR) spectra were recorded on a Perkin-Elmer Spectrum RX System using attenuated total reflection. Samples were prepared by drying as thin films for 48 hours at room temperature, to eliminate the signal arising from the strong absorption from water.

### 2.3.5 Gel Permeation Chromatography

Gel permeation chromatography (GPC) was carried out selectively on the product of the reaction of 2:1 HMDI:DMPA, and the *HB60\_SS1000* prepolymer reaction, at the point of completion. The free isocyanate in the samples was quenched by diluting in dry ethanol (100 wt%), and one drop of DBTDL added to catalyse the OH-NCO reaction at room temperature. Data was collected at 1 mlmin<sup>-1</sup> using tetrahydrofuran/acetic acid as eluent, on an APC low 200 125 45 column equipped with a refractive index detector.

To check the PU-prepolymer molecular weight distribution as a function of reaction time, the prepolymer synthesis of *HB60\_SS1000* (Table 2.2) was followed by GPC. A 1 L 4-necked flask (under N<sub>2</sub> atmosphere), equipped with a mechanical stirrer, a reflux condenser, and a thermocouple was charged with PTMO (*Mn* = 1000 gmol<sup>-1</sup>), DMPA and MEK. The mixture was heated to 70 °C using an oil bath while applying mild agitation. Next, HMDI was added as fast as possible making sure the exotherm did not exceed 92 °C (~15 min addition time). The batch temperature was maintained at 92 °C and samples (~2 g) taken after 1, 2, and 3 hours from the moment of complete

HMDI addition. The free isocyanate in the samples was quenched by diluting in dry ethanol (100 wt%), and one drop of DBTDL added to catalyse the OH-NCO reaction at room temperature. The molecular weight distributions of the quenched samples were analysed by GPC.

# 2.4 References

- J. H. Hubbell, W. J. Veigele, E. A. Briggs, R. T. Brown, D. T. Cromer and R. J. Howerton, *J. Phys. Chem. Ref. Data*, 2009, **4**, 471.
- 2 H. Schnablegger and Y. Singh, *The SAXS Guide*, Anton Paar GmbH, Austria, 3rd edn., 2013.
- 3 L. Wang, P. D. Topham, O. O. Mykhaylyk, H. Yu, A. J. Ryan, J. P. A. Fairclough and W. Bras, *Macromol. Rapid Commun.*, 2015, **36**, 1452–1452.
- 4 R. J. Roe, *Methods of X-ray and neutron scattering in polymer science*, Oxford University Press, New York, 2000.
- 5 J. H. Hubbell, *J. Phys. Chem. Ref. Data*, 1979, **8**, 69–106.
- 6 Eric Gullikson (CXRO), 2023.
- A. Guinier and G. Fournet, *Small-Angle Scattering of X-Rays*, John Wiley & Sons, Incorporated, New York, 1955.
- 8 M. Engel, S. Tinka and B. Stuhn, in *Methods in Physical Chemistry*, eds. R. Schafer and P. C. Schmidt, John Wiley & Sons, Incorporated, 1st edn., 2012, pp. 297–324.
- 9 O. Kratky and G. Porod, *J. Colloid Sci.*, 1949, **4**, 35–70.
- 10 P. Debye, J. Phys. Colloid Chem., 1947, **51**, 18–32.
- 11 G. Porod, *Small-Angle X-ray Scattering*, Academic Press, New York, 1982.
- 12 G. Beaucage, *J. Appl. Crystallogr.*, 1995, **28**, 717–728.
- 13 B. Hammouda, *J. Appl. Crystallogr.*, 2010, **43**, 716–719.
- 14 F. Zhang, J. Ilavsky, G. G. Long, J. P. G. Quintana, A. J. Allen and P. R. Jemian, *Metall. Mater. Trans. A*, 2010, **41**, 1151–1158.
- 15 D. Orthaber, A. Bergmann and O. Glatter, *J. Appl. Crystallogr.*, 2000, **33**, 218–225.
- 16 J. Ilavsky and P. R. Jemian, *J. Appl. Crystallogr.*, 2009, **42**, 347–353.
- 17 B. Lee, C.-T. Lo, S. Seifert and R. E. Winans, *J. Appl. Crystallogr.*, 2006, **39**, 749–751.
- T. Narayanan, M. Sztucki, T. Zinn, J. Kieffer, A. Homs-Puron, J. Gorini, P. Van Vaerenbergh and P. Boesecke, *J. Appl. Crystallogr.*, 2022, **55**, 98–111.
- A. J. Smith, S. G. Alcock, L. S. Davidson, J. H. Emmins, J. C. Hiller Bardsley, P. Holloway, M. Malfois, A. R. Marshall, C. L. Pizzey, S. E. Rogers, O. Shebanova, T. Snow, J. P. Sutter, E. P. Williams and N. J. Terrill, *J. Synchrotron Radiat.*, 2021, 28, 939–947.
- M. Basham, J. Filik, M. T. Wharmby, P. C. Y. Chang, B. El Kassaby, M. Gerring, J. Aishima, K. Levik, B. C. A. Pulford, I. Sikharulidze, D. Sneddon, M. Webber, S. S. Dhesi, F. Maccherozzi, O. Svensson, S. Brockhauser, G. Náray and A. W.

Ashton, J. Synchrotron Radiat., 2015, 22, 853-858.

- 21 H. C. Wright, D. D. Cameron and A. J. Ryan, *HardwareX*, 2022, **12**, e00365.
- 22 S. Kell, *J. Chem. Eng. Data*, 1975, **2**, 97–105.
- 23 D. Nečas and P. Klapetek, Cent. Eur. J. Phys., 2012, **10**, 181–188.

# <u>Chapter 3 – Investigation Into the Morphologies</u>

# of Aqueous Polyurethane Dispersions

# 3.1 Introduction

It is well established that aqueous polyurethane dispersions (PUDs) contain spherical particles.<sup>1–7</sup> Moreover, the literature is in agreement that, when the polyurethane (PU) particles are stabilised by incorporation of hydrophilic groups, the particle size is controlled by the hydrophile content.<sup>1,3,8–11</sup> The most popular choice of hydrophilic monomer is dimethylolpropionic acid (DMPA),<sup>6</sup> which imparts charge stabilisation when the acid moiety is deprotonated by a base.

This relationship between particle size and hydrophile content mirrors the behaviour of aqueous dispersions of amphiphilic statistical acrylic copolymers, according to the findings of Neal et al. 12,13 They proposed a particle surface charge (PSC) model that identifies a critical surface area coverage of hydrophilic monomers (*SA*<sub>frac</sub>), for a given hydrophile/hydrophobe monomer pair, as the key factor controlling particle size. Consequently, the PSC model can be used as a predictive tool to select an appropriate composition to achieve a target particle size for their amphiphilic copolymer systems. Their analysis also indicates that a greater surface area coverage of hydrophiles is necessary for stable particles containing a comonomer with higher hydrophobicity. 13 Although considerable research has been devoted to the effect of composition on particle size 1,3,9-11,14 and coating properties, 14-17 limited literature exists on the morphology of PUDs in the wet state, 1,5 which is critical for designing film-forming materials with targeted properties. Bolze et al. used a contrast variation small angle

X-ray scattering (SAXS) technique to study the structure of one PUD composition.<sup>5</sup> They concluded that the particle structure comprised an acid-rich shell, and phase separation between hard and soft segments of PU. Moreover, small angle neutron scattering (SANS) was used by Satguru et al., who reported a different "open, water swollen" morphology for aqueous PUD particles.<sup>1</sup>

Both of these interpretations of PU particle morphology were made based on just one PUD formulation. Studying the effect of the PU chemistry on the morphologies revealed by scattering data would offer more insight into the controlling factors. This chapter comprehensively investigates the impact of composition - including polyether molecular weight, hard block content, and COOH concentration - on the morphology of PUs in aqueous dispersion. Specifically, SAXS is employed to probe particle size and shape, and evidence for phase separation and water presence is critically examined. The origins of a second population of particles are investigated with respect to composition, and results are further corroborated by atomic force microscopy (AFM), matrix-assisted laser desorption/ionization (MALDI), gel permeation chromatography (GPC) and Fourier-transform infrared spectroscopy (FTIR).

# 3.2 Samples

PUD samples were produced at three different hard block contents - where hard block refers to the PU proportion made up of hydrogenated methylene diphenol diisocyanate (HMDI), DMPA and ethylenediamine (Table 3.1) - and with three different molecular weights of poly(tetramethylene oxide) (PTMO) forming the soft segment (SS). As DMPA is contained in the hard block (Figure 1.9), samples with higher hard block content contain more acid. For PTMO with a higher *Mn*, the fraction of reactive OH groups per unit mass of PTMO is reduced.

Name	Hydrogenated methylene diphenyl diisocynate	Dimethylolpropionic acid	Ethylenediamine	Poly(tetramethylene oxide)
Structure	OCN NCO	НО ОН	H <sub>2</sub> N NH <sub>2</sub>	H O OH
Abbreviation	HMDI	DMPA	EDA	PTMO

Table 3.1: Chemical structures and abbreviations of monomers used in the synthesis of PUDs.

As such, to maintain the NCO/OH ratio of 1.5, the amount of DMPA, and therefore acid groups, is increased (Table 3.2). To highlight the chemical composition of the samples, the hard block content and the soft segment molecular weight are used for the sample names, e.g.,  $HB50\_SS1000$  refers to a PUD with 50% hard block and soft segment of  $Mn = 1000 \text{ gmol}^{-1}$  (Table 3.2).

Table 3.2: Summary of key compositional details for PUDs studied in this work.

Sample	Polymer Hard Block Content (wt%)	Soft Segment M <sub>n</sub> (gmol <sup>-1</sup> )	Polymer COOH Content /wt%
HB50_SS650	50 wt%	650	1.52
HB60_SS650	60 wt%	650	2.83
HB70_SS650	70 wt%	650	4.15
HB50_SS1000	50 wt%	1000	2.40
HB60_SS1000	60 wt%	1000	3.57
HB70_SS1000	70 wt%	1000	4.72
HB50_SS2000	50 wt%	2000	3.29
HB60_SS2000	60 wt%	2000	4.23
HB70_SS2000	70 wt%	2000	5.22
2:1 HMDI:DMPA	100%	-	6.84

# 3.3 Results and discussion

It is well established that PU forms particles in dispersion.<sup>1–3,5,6,14,15</sup> The total scattering intensity from a dispersion of multiple populations of scattering objects, including particles, can be expressed in a general form as:

$$I_{\text{tot}}(q) = \sum_{i=1}^{m} I_{i}(q) = \sum_{i=1}^{m} N_{i}S_{i}(q) \int_{0}^{\infty} ... \int_{0}^{\infty} P_{i}(q, r_{1}, ..., r_{k_{i}}) \Psi_{i}(r_{1}, ..., r_{k_{i}}) dr_{1} ... dr_{k_{i}} \quad [Eq. 3.1]$$

where m is the number of populations;  $I_i(q)$ ,  $P_i(q,r_1,...,r_{k_i})$  and  $\Psi_i(r_1,...,r_{k_i})$  are the scattering intensity, the form factor (including volume and excess scattering length density of the components) defined by a  $k_i$  number of r parameters, and the multivariate normalized distribution function  $\left[\int_0^\infty \Psi_i(r_1,...,r_{k_i})dr_1...dr_{k_i}=1\right]$  of  $i^{\text{th}}$  population, respectively.  $N_i$  is the number density of the  $i^{\text{th}}$  population expressed as  $N_i = \frac{\phi_i}{\int_0^\infty V_i(r_1,...,r_{k_i})\Psi_i(r_1,...,r_{k_i})dr_1...dr_{k_i}}$ , where  $\phi_i$  and  $V_i(r_1,...,r_{k_i})$  are the volume fraction and the object volume of the population. For the sake of simplicity, it is assumed in Equation 3.1 that only objects belonging to the same population interact with each other, which is expressed via an effective structure factor term  $S_i(q)$ . For a single population of spherical particles (m=1), Equation 3.1 can be rewritten as

$$I_{\text{tot}}(q) = I_1(q) = N_1 S_1(q) \int_{0}^{\infty} P_1(q, r) \Psi_1(r) dr \quad [Eq. 3.2]$$

In addition, dispersity of only a single parameter, such as particles radius (r) is considered in Equation 3.2. The form factor of a spherical particle is expressed as

$$P_1(q,r) = (\Delta \xi)^2 V_1^2(r) \frac{9(\sin(qr) - qr\cos(qr))^2}{(qr)^6}$$
 [Eq. 3.3]

where  $\Delta \xi$  is the difference in scattering length density between the particles and the solvent, and  $V_1(r) = \frac{4}{3}\pi r^3$  is the particle volume.

While the SAXS profiles (Figure 3.1 a-c) of the PUDs can be fit by Equations 3.2 and 3.3 at low q, this becomes insufficient for describing the data at  $q > 0.03 \text{ Å}^{-1}$  (Figure 3.1d,  $I_1(q)$ ). This indicates that there is an additional scattering signal contributing

significantly to the total intensity in this region. Moreover, despite the low PU concentration used for this data collection, some of the SAXS profiles exhibit a noticeable broad structure peak at low q (q < 0.02 Å<sup>-1</sup>) (Figure 3.1), indicating interactions between neighbouring particles causing structural arrangement across the sample.

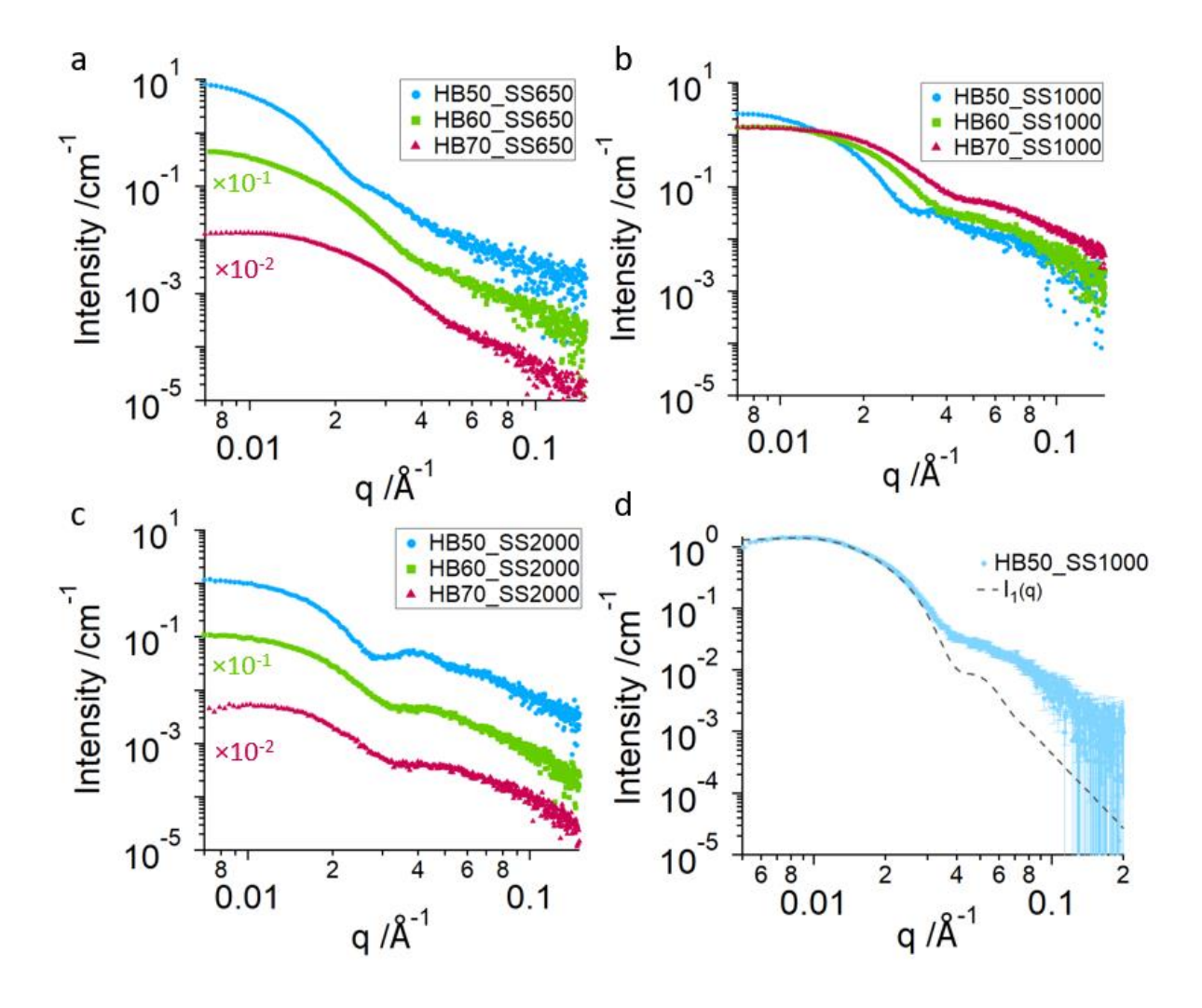


Figure 3.1: SAXS profiles for 1 wt% aqueous dispersions of PU, containing soft segment of Mn: a) 650 gmol<sup>-1</sup>, b) 1000 gmol<sup>-1</sup> and c) 2000 gmol<sup>-1</sup>, with 50% hard blocks (blue circles), 60% hard blocks (green squares), and 70% hard blocks (red triangles). Some of the profiles are offset by the indicated factor to avoid their overlap. d) Examples of the fitting of the analytical expression for scattering from a single population of spherical particles to the scattering at low q for one of the compositions.

Such interactions are caused by repulsion between acidic moieties present on the surface of particles and, in accordance with this, the most acidic sample (*HB70\_SS2000*) shows the most significant structure peak. This phenomenon is well-

established for charged nanoparticles in dispersion,  $^{12,13,18,19}$  where the interaction length depends on several factors, including polymer concentration, charge on the particle surface, and the dielectric constant of the solvent.  $^{20,21}$  Previous research  $^{13}$  has demonstrated that, while the Hayter-Penfold approximation for a charged sphere structure factor  $^{22}$  is a physically more appropriate expression for describing particles undergoing charge repulsion, the hard-sphere structure factor, solved with the Percus-Yevick closure relation,  $^{23,24}$  provides a sufficient analytical expression for the structure peak in the data modelling. This is commonly used in scattering analysis for counting the effect of particle interactions. The parameters of interest in this study - namely r,  $\Psi_1(r)$ , and particle morphology – are contained in the form factor and are essentially independent of the structure factor expression selected.

# 3.3.1 <u>Investigation into Scattering from Microphase Separation</u>

The diffuse scattering at  $q > 0.04 \, \text{Å}^{-1}$  has been observed previously for a similar system by Bolze et al.<sup>5</sup> The SAXS profile of a PUD was decomposed into scattering from the particle shape and size, and scattering from internal inhomogeneities in electron density (Figures 1.19 and 1.20). This data revealed a morphology of core-shell particles, comprising a 1 nm thick electron-rich shell of acidic stabilising groups, and a hydrophobic PU core with a radius of 28 nm. The diffuse excess scattering at greater angles was attributed to a phase-separated lamellar structure within the PU particles, characterised by alternating amorphous and crystalline regions. While it is speculated that the crystalline part may comprise ordered hard block, it is acknowledged that polyether is known to form crystalline structures in some cases. Unfortunately, the study was performed using only one molecular composition.

Based on this interpretation, a change in the hard block/soft segment ratio would directly control the nature and amount of phase separation in the PU particles, with the maximum phase separation achieved at 50/50. As such, a significant difference in the intensity of this excess scattering feature would be observed, decreasing in intensity from 50 wt% to 70 wt% hard block content. However, SAXS profiles of the PUDs show the opposite trend in the region of the excess scattering, exhibiting a maximum intensity contribution at 70 wt% hard block, and not 50 wt% (Figure 3.1b, and Appendix, Figure 8.2).

These findings suggest that phase separation within the particles is not the source of the excess scattering. It is worth noting, however, that the possibility of microphase separation occurring cannot be ruled out, with low scattering intensity in this region that does not significantly influence the overall SAXS profile.

## 3.3.2 Investigation into Scattering from Internal Water Pockets

Satguru et al. reported that PU particles in aqueous dispersion have an "open, water-swollen" structure.¹ They proposed a morphology that includes water-rich areas within the particles, although they acknowledge that the model applied to their SANS data was limited in its ability to provide unambiguous information on the particle morphology. The presence of water inside the molecules has since been corroborated by the self-consistent field theory calculations of Li et al.² Pedersen et al. proposed a "blob" model to describe the concentration fluctuation in micelles resulting from solvent swelling². This was adapted to investigate the presence of water pockets in the PU particles (Equation 8.7-8.10, Appendix). However, least squares regression fitting to the SAXS data (Figure 3.2) did not yield suitable parameters to describe the scattering

profile, indicating that water pockets associated with the PU molecules could not be the source of the observed scattering.

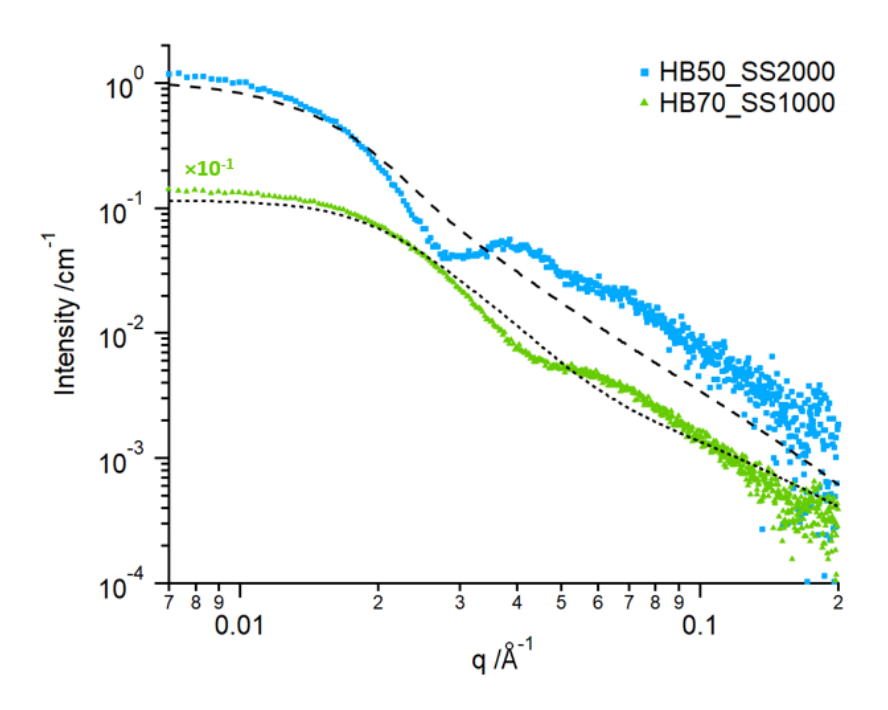


Figure 3.2: Best fits of the "blob" model (Equations 8.7-8.10, Appendix) to SAXS profiles of representative PUDs for a sample containing 50% hard block with soft segment of Mn = 2000 gmol<sup>-1</sup> (blue squares and dashed line), and a sample containing 70% hard block with soft segment of Mn = 1000 gmol<sup>-1</sup> (green triangles and dotted line). One profile is offset by the indicated factor.

## 3.3.3 <u>Investigation into A Second Population of Acidic Fragments</u>

The model structures suggested in the literature did not adequately describe the scattering in Figure 3.1, so it was concluded that it does not arise from internal inhomogeneities such as phase separation or water pockets within the particles. It was considered that, due to the high proportion of acid in the polymer composition, and the statistical nature of the polymer architecture, it was possible that some polymer chains and/or short fragments may be highly charged and dissolved in the water phase, or present in smaller structures, rather than being found in the particles. To test this hypothesis, MALDI analysis was employed to look for these fragments.

Representative MALDI spectra were obtained in negative mode for PUD samples containing soft segment of  $Mn = 2000 \text{ gmol}^{-1}$  (Figure 3.3), as the scattering profiles for these PUs exhibit a significant contribution from this excess scattering.

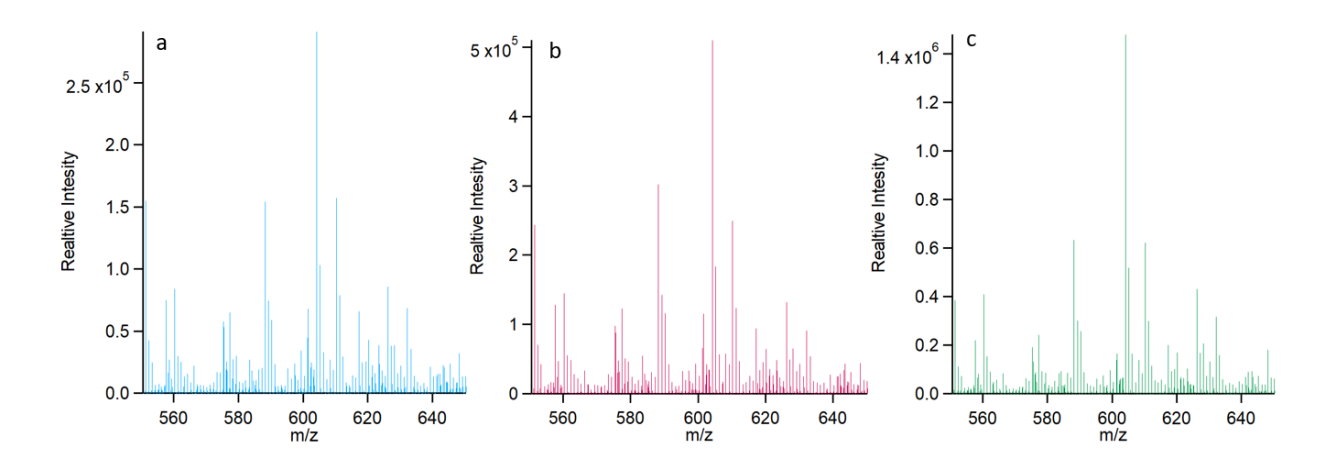


Figure 3.3: MALDI spectra, collected in negative mode, for samples containing soft segment of Mn = 2000 gmol<sup>-1</sup>, with a) 50% hard block, b) 60% hard block, and c)70% hard block. The most prominent peak in all spectra falls at 604 m/z, corresponding to the deprotonated form of the molecule HMDI – DMPA- HMDI, capped with amines from the isocyanate/water reaction

All three spectra exhibit their most prominent peak at 604 m/z. This can be attributed to the HMDI-DMPA-HMDI molecule, with amine caps and deprotonated acid group (Figure 3.4).

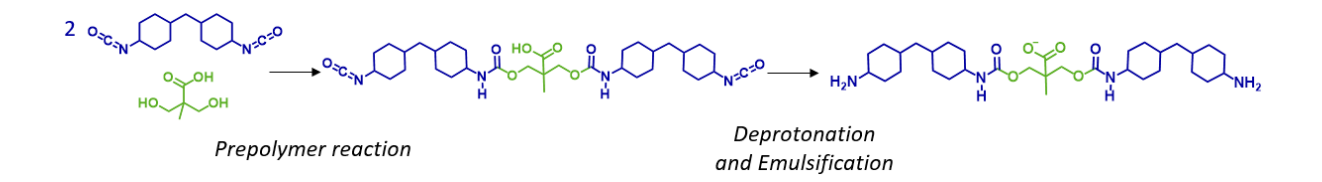


Figure 3.4: Schematic illustrating the steps in the formation of amine-capped HMDI-DMPA-HMDI molecules during the production of PUD.

Due to the excess of HMDI in the prepolymer reaction, it is statistically probable that such HMDI-DMPA-HMDI fragments would form as a significant number fraction of the distribution of PU chains. The isocyanate groups have been converted to amines, due to the reactivity of isocyanate with a large excess of water. Although the reaction of isocyanate with the chain extending amine is ~100 times faster than the reaction with water, the volume of water molecules compared to chain extender is such that,

statistically, the water reaction is dominant, forming the amine-capped fragments. Due to their enhanced hydrophilicity, it is entirely plausible that these acidic fragments would form a second, separate population in the dispersions.

To further investigate this interpretation of the data, these fragments were targeted in synthesis using a 2:1 ratio of HMDI:DMPA. GPC of the product, quenched with ethanol (Figure 3.5), shows a distribution of fragments comprising *n* HMDI and *n*-1 DMPA, however the dominant product is the targeted HMDI-DMPA-HMDI.

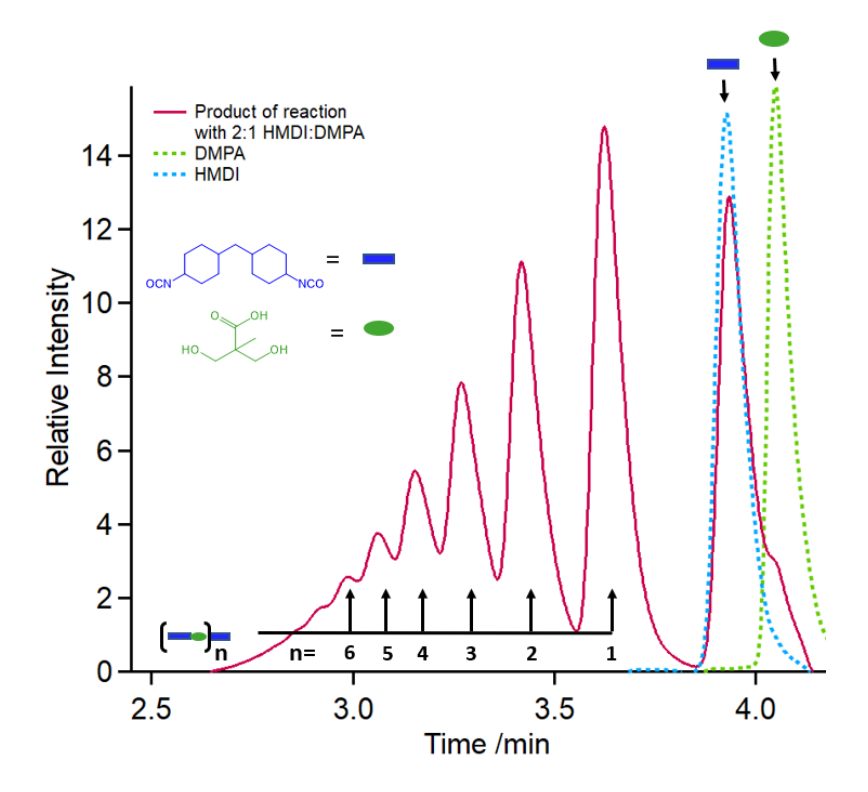


Figure 3.5: GPC spectra for the product of prepolymer synthesis with 2:1 HMDI: DMPA (red line), pure HMDI (blue dashed line) and pure DMPA (green dashed line). The origin of peaks is shown by blue rectangles and green ovals, representing HMDI and DMPA respectively. 'n' describes the composition of the fragments, which comprise n DMPA and (n+1) HMDI.

There is also a large population of unreacted HMDI, however there is very little unreacted DMPA, with only a slight shoulder in the GPC at the expected elution time. This same distribution can be seen in the GPC spectrum of the product of the prepolymer reaction, quenched with ethanol (Figure 3.6). Due to the instrument setups at the time of data collection, the retention times are not directly comparable to

Figure 3.5, however the similarity in the relative retention times of the populations is indicative of the presence of the same molecules. This is affirmed by the behaviour in peak intensity with respect to prepolymer reaction time (discussed in Figure 8.1).

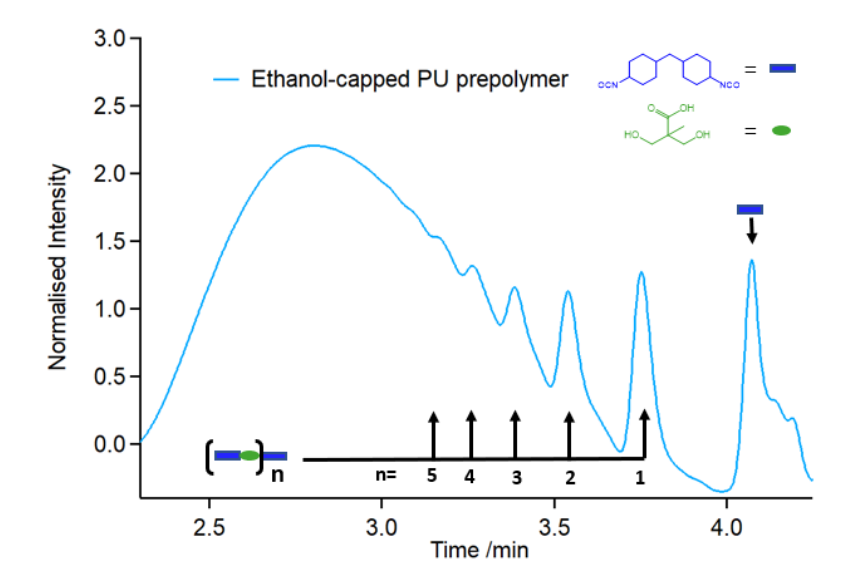


Figure 3.6: GPC spectra for the product of prepolymer synthesis of a sample containing 60% hard block, and soft segment of Mn = 1000 gmol<sup>-1</sup>. The origin of peaks is shown by blue rectangles and green ovals, representing HMDI and DMPA respectively. 'n' describes the composition of acidic fragments, which comprise n DMPA and (n+1) HMDI.

FTIR data collected on the products of the 2:1 HMDI:DMPA reaction shows the C=O absorbance for urethane at 1700 cm<sup>-1</sup> and the absorbance arising from the bend of the N-H neighbouring the urethane carbonyl at 1630 cm<sup>-1</sup> (Figure 3.7). The C=O signal is shifted from the expected frequency for free C=O (~1730 cm<sup>-1</sup>), evident of ordered hydrogen bonding in the sample.<sup>27,28</sup>

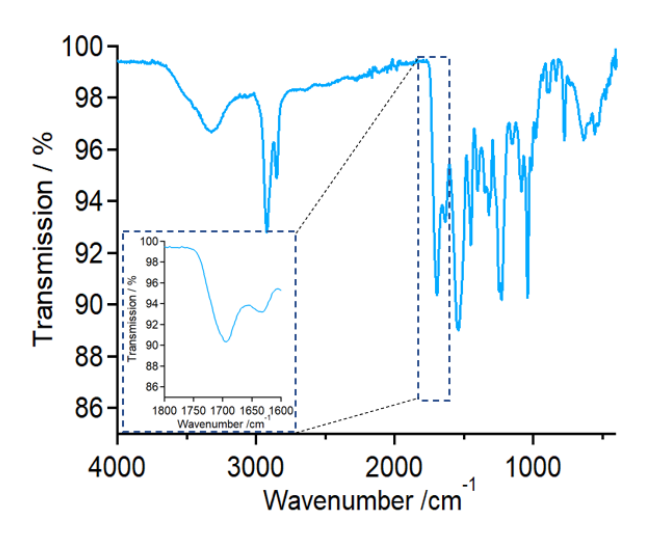


Figure 3.7: FTIR spectra of the product of 2:1 HMDI:DMPA. The inset shows the region of hydrogen-bonded C=O stretching (1700 cm<sup>-1</sup>), shifted to a lower wavenumber than free urethane C=O (~1730 cm<sup>-1</sup>), and N-H neighbouring C=O bending (1630 cm<sup>-1</sup>).

Similar molecules are known to form polymer-like supramolecular structures by strongly hydrogen bonding through donor and acceptor groups on neighbouring molecules.<sup>29–32</sup> Quantum mechanical calculations from Yılgör et al. show that urethanes form extremely strong hydrogen bonds, with energies in the region of 46 – 52 kJmol<sup>-1</sup>.<sup>28</sup> Therefore, the collection of acidic fragments seen in GPC, when taken into water, can associate to form a large supramolecular structure through this hydrogen bonding (Figure 3.8).

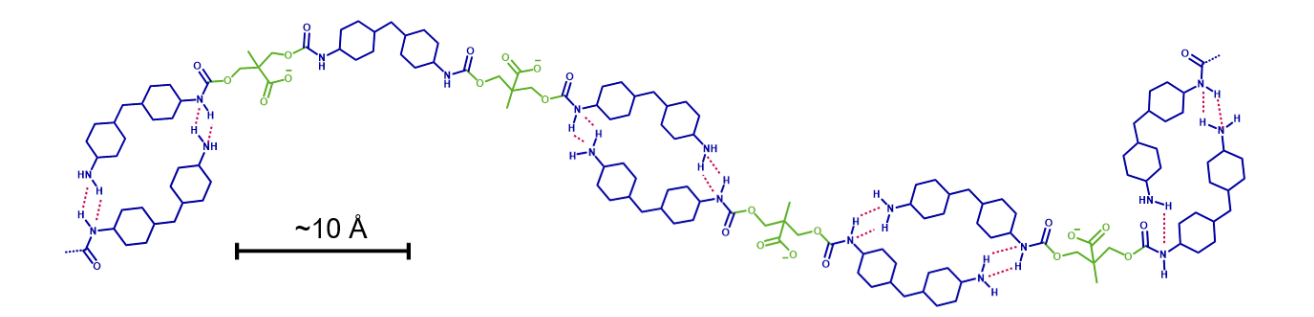


Figure 3.8: Fragments of  $HMDI_nDMPA_{n-1}$ , seen in the GPC spectrum of the products of the 2:1 HMDI:DMPA reaction, capped with amine due to the reaction of isocyanate with water, hydrogen bonding (shown by dashed red lines) to form a supramolecular structure. The hydrophobic HMDI is shown in blue, and the hydrophilic deprotonated DMPA in green. The 10 Å scale bar is given as a reference.

There is rotational freedom in the molecules, especially about the central carbon in both HMDI and DMPA, resulting in a structure mirroring that of randomly folded chain.

SAXS data were collected on the supramolecular structure (Figure 3.8), by dispersing the products of the 2:1 reaction of HMDI:DMPA in water. The profiles show very similar features for this structure and the excess scattering observed in the PUD SAXS profiles in the area of interest ( $q > 0.04 \text{ Å}^{-1}$ ) (Figure 3.9). This indicates that the local structure – namely the folding of the supramolecular structure - is likely to be the same.

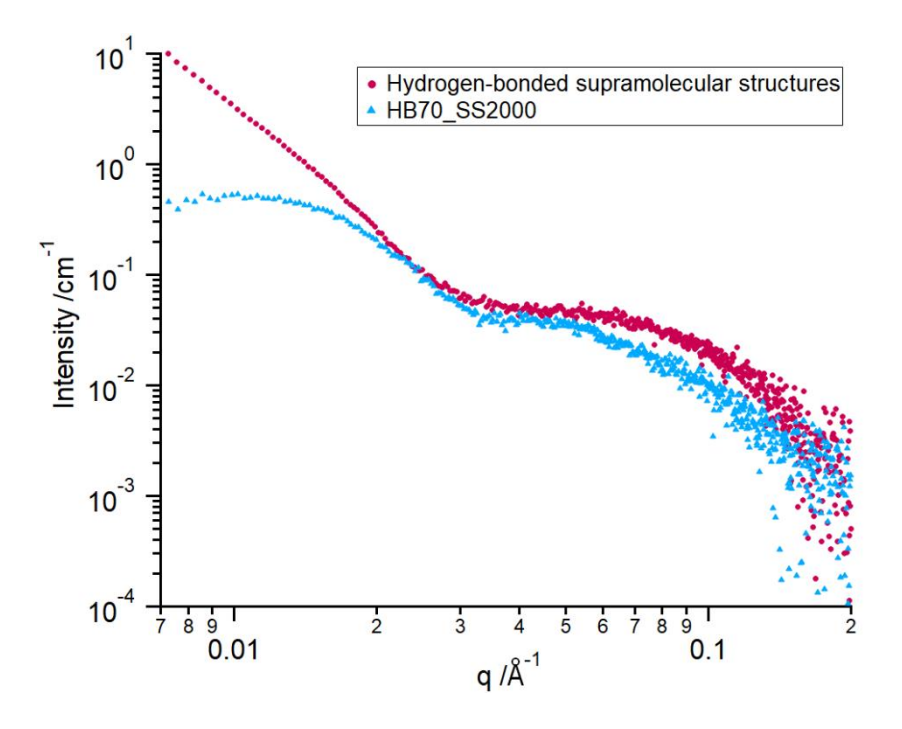


Figure 3.9: SAXS profile for the product of the 2:1 reaction of HMDI:DMPA hydrogen-bonded into supramolecular structures (red), at 1.5 wt% in water, compared to a representative PUD sample (blue) at 1 wt% PU in water. The overlap in profiles demonstrated that the origin of the scattering in the region  $q > 0.04 \, \text{Å}^{-1}$  is the hydrogen-bonded supramolecular structures.

The upturn at q < 0.02 Å<sup>-1</sup> indicates that larger structures, such as aggregates, have formed in the solution of supramolecular structures that are not present in the PUD samples. This could be a result of the difference in the total charge density across the solution, or the extra solvent required in the synthesis to reduce viscosity prior to emulsification, effecting how the structures initially form in water.

This confirms that the excess scattering is due to the formation of these acidic fragments of PU during the prepolymer reaction, capped with amines, and hydrogen bonded to form a supramolecular polymer-like structure.

## 3.3.4 Analysis of PUDs as Two-Population Systems

It follows that this population can be described by an analytical expression for the scattering from polymers in solution. The total scattering, in this case, is a result of scattering from a two-population system (m = 2), summing the contributions from the spherical particles (i = 1) and these acidic fragments (i = 2) (Figure 3.1d).

As the folding of supramolecular structures in solution mirrors that of polymers (Figure 3.8), the form factor of scattering can be described using the generalised analytical expression for a single population of dissolved polymer chains:<sup>33</sup>

$$P_2(q) = (\Delta \xi)^2 V^2 \left[ \frac{1}{v x^{1/2\nu}} \gamma \left( \frac{1}{v}, x \right) - \frac{1}{v x^{1/2\nu}} \gamma \left( \frac{1}{v}, x \right) \right] \quad [Eq. 3.4]$$

where V is the volume of one chain,  $\Delta \xi$  is the difference in scattering length densities between the polymer and the solvent, and  $\gamma$  is the incomplete Gamma function,

$$\gamma\left(\frac{1}{\nu},x\right) = \int_0^x e^{-t} t^{\left(\frac{1}{\nu}-1\right)} dt \quad [Eq. 3.5]$$

and it is assumed that there are no polydisperse parameters  $(\Psi_i(r_1,...,r_{k_i})=1)$ .

 $\nu$  is a parameter arising from solvent interactions with the polymer and is related to the gradient of the intensity of scattering at high q:

$$I(q) \sim q^{-\frac{1}{v}}$$
 [Eq. 3.6]

and

$$x = \frac{q^2 n^{2v} b^2}{6} \quad [Eq. 3.7]$$

where n is the number of Kuhn lengths b in the fully extended polymer chain of length b. This relates to the radius of gyration of the coiled polymer ( $R_g$ ) by:

$$R_g^2 = \frac{n^{2\nu}b^2}{6}$$
 [Eq. 3.8]

Thus, the contour length can be expressed as:

$$L = nb = \left(\frac{R_g\sqrt{6}}{b^{(1-\nu)}}\right)^{\frac{1}{\nu}}$$
 [Eq. 3.9]

 $R_g$  and v are obtained from SAXS data fitting, and the value of b was estimated to be 10 Å. This is approximately equal to half the length of the HMDI-DMPA-HMDI fragment (Figure 3.8), therefore is a reasonable estimate of the rigidity and is in agreement with values found in the literature for PU. $^{34-37}$  Using molecular masses and known lengths of constituent monomers, L can be converted to a molecular weight of a supramolecular structure ( $M_{\rm W,AF}$ ), assuming they consist of a single-chain of the polymer-like architecture. A best estimate for the mass density of the acidic fragments ( $\rho_{\rm m,AF}$ ) is taken from the calculated value for the hard block (Appendix 8.4) due to the similarity in compositions.  $M_{\rm W,AF}$  can be converted to a volume occupied by these acidic fragments,  $V_{\rm AF}(R_{\rm g})$ , using:

$$V_{\rm AF}(R_{\rm g}) = \frac{M_{\rm w,AF}}{\rho_{\rm m,AF}}$$
 [Eq. 3.10]

The scattering length density contrast between the acidic fragments ( $\xi_{AF}$ ) and the water ( $\xi_{water}$ ) is defined as:

$$\Delta \xi_{AF} = \xi_{AF} - \xi_{water}$$
 [Eq. 3.11]

with  $\xi_{AF}$  and  $\xi_{water}$  calculated by the equation for scattering length density (Equation 2.3).

At  $I_2(q \to 0)$ ,  $\frac{1}{\nu x^{1/2\nu}} \gamma\left(\frac{1}{\nu}, x\right) - \frac{1}{\nu x^{1/2\nu}} \gamma\left(\frac{1}{\nu}, x\right) = 1$ , and it is assumed that there is negligible interaction between the supramolecular structures, therefore S(q) = 1. As such, the scattering intensity arising solely from the supramolecular structures can be simplified to:

$$I_2(q \to 0) = (\Delta \xi_{AF})^2 \cdot \phi_{AF} \cdot V_{AF} \quad [Eq. 3.12]$$

Since  $V_{AF}(R_g)$  and  $I_2(q=0)$  can be calculated from model parameters produced by best fits to SAXS profiles, and  $\Delta \xi_{AF}$  is known, the volume fraction of supramolecular structure,  $\phi_{AF}$  is obtained from Equation 3.12.

The distribution of PU between the spherical particles and the acidic fragments is constrained by the total volume fraction of PU ( $\phi_{tot}$ ) known from the sample preparation. Consequently, the volume fraction of spherical PU particles ( $\phi_{part}$ ) is given by

$$\phi_{\text{part}} = \phi_{\text{tot}} - \phi_{\text{AF}}$$
 [Eq. 3.13]

In addition, the scattering length density of the spherical particles ( $\xi_{part}$ ) should be adjusted according to the change in the PU particle composition as a result of the formation of a second population comprising acidic PU fragments (Table 3.2):

$$\xi_{\text{part}} = \frac{\xi_{\text{PU}} - \frac{\phi_{\text{AF}}}{\phi_{\text{tot}}} \cdot \xi_{\text{AF}}}{1 - \frac{\phi_{\text{AF}}}{\phi_{\text{tot}}}} \quad [Eq. 3.14]$$

where the total scattering length density of each PU,  $\xi_{PU}$ , (Table 3.3) and acidic fragments ( $\xi_{AF}$ ) is calculated from the measured densities and the known compositions (Eq. 2.3).

Table 3.3: Calculated average scattering length densities for the total PU ( $\xi_{PU}$ ) (Equation 2.3), and for the primary particle population ( $\xi_{part}$ ) from Equation 3.14.

Sample	ξ <sub>PU</sub> / 10 <sup>10</sup> cm <sup>-2</sup>	ξ <sub>part</sub> / 10 <sup>10</sup> cm <sup>-2</sup>
HB50_SS650	10.16	10.11
HB60_SS650	10.24	10.16
HB70_SS650	10.28	10.19
HB50_SS1000b	10.15	9.93
HB60_SS1000	10.13	9.95
HB70_SS1000	10.28	10.06
HB50_SS2000	10.28	9.80
HB60_SS2000	10.28	9.82
HB70_SS2000	10.24	9.77

This gives the values for contrast term,  $\Delta \xi = \xi_{part} - \xi_{water}$ , in Equation 3.3.

Direct methods of size distribution analysis for the primary population of spherical particles are not possible due to the structure factor arising from particle charge repulsion, even at low concentrations, and the minor population of supramolecular structures contributing to the total scattering. Instead, various size distributions were considered, and analytical expressions fit to the data to find the most appropriate to describe these particle size distributions. Gaussian size distributions (Equation 8.3, Appendix) gave either satisfactory or poor fits to the experimental SAXS data, due to the presence of larger particles skewing the distribution, particularly in  $HB60\_SS650$ . However, Lognormal size distribution of particle radii (Equation 8.4, Appendix) gave good fits to all the experimental data. Such distribution is known to be common to particulate systems<sup>38,39</sup> so this expression was selected to describe  $\Psi_1(r)$ .

Simultaneous fitting of both populations, using Equation 3.1, gives the parameters in Table 3.4, and fittings shown in Figure 3.10. Fits were performed by fixing the known values  $[\xi_{PU}, \xi_{AF}, \xi_{water}, \phi_{tot}, \rho_{m,AF}]$  and allowing the desired parameters  $[R, \sigma, \phi_{AF}, R_g, \nu]$  by

least squares of regression method. Volume terms and  $\phi_{part}$  are calculated within the software according to the relevant equations. The total fitting model is given in Appendix 8.10. Using the appropriate data treatment methods for Lognormal distributions<sup>39,40</sup> (Appendix 8.7), the geometric mean of r (R) and multiplicative standard deviation ( $\sigma^*$ ) were calculated (Table 3.4).

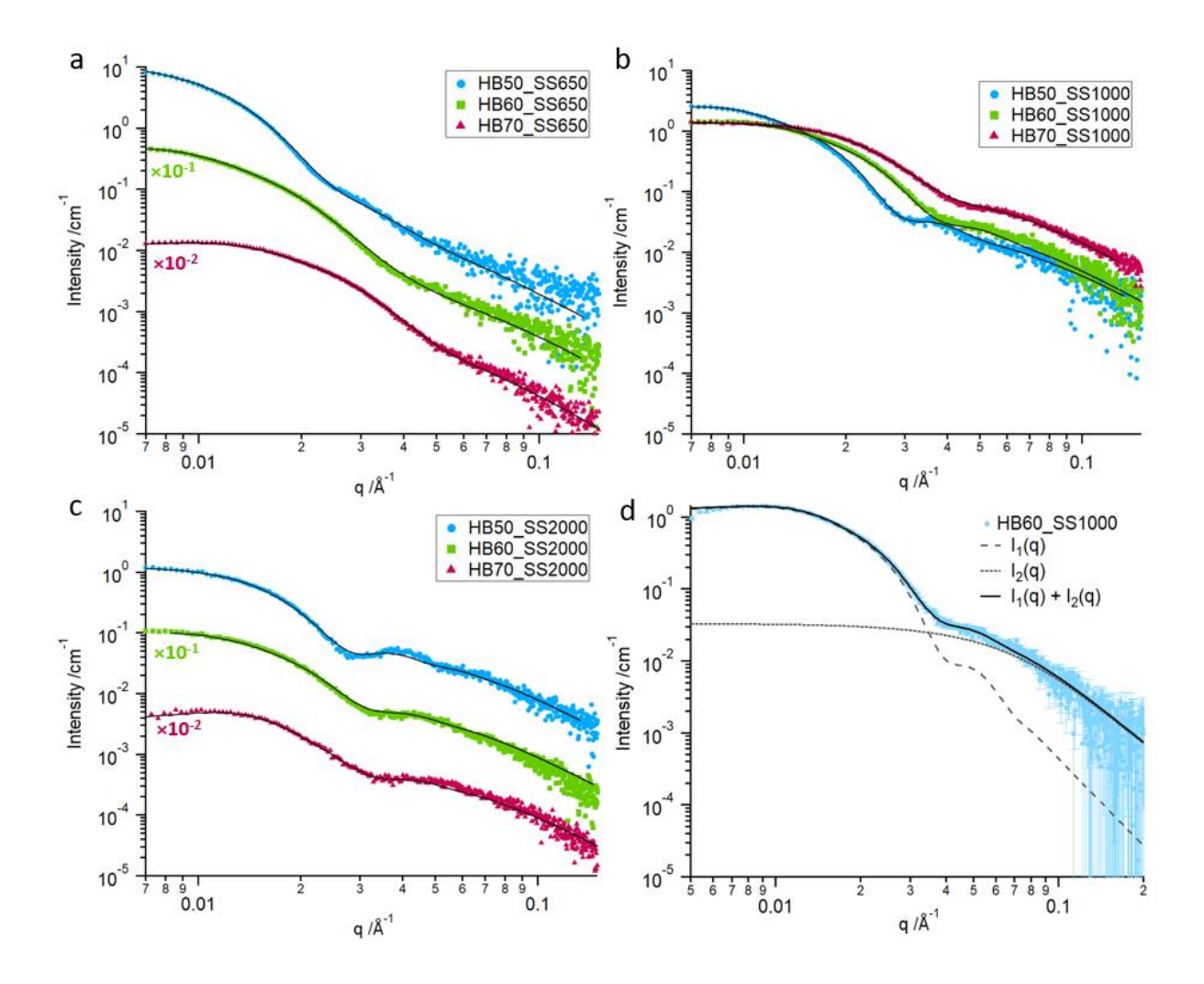


Figure 3.10: SAXS profiles for 1 wt% aqueous dispersions of PU, containing soft segment of Mn: a) 650 gmol<sup>-1</sup>, b) 1000 gmol<sup>-1</sup> and c) 2000 gmol<sup>-1</sup>, with 50% hard blocks (blue circles), 60% hard blocks (green squares), and 70% hard blocks (red triangles). Some of the profiles are offset by the indicated factor to avoid their overlap. Solid curves show fitting of the SAXS model for two PU populations i.e., spherical particles and supramolecular structures. Figure d) shows the decomposition of the SAXS model into scattering from two populations for a representative PUD.

Table 3.4: Parameters obtained from the simultaneous fitting of an analytical expression of scattering intensity combining contributions from spherical particles and collapsed hydrogen-bonded polymer chains. R is the geometric mean particle radius with multiplicative standard deviation  $\sigma^*$ . The proportion of PU distributed as supramolecular structures is quantified by  $\phi_{AF}/\phi_{tot}$ . Rg gives the radius of gyration of these structures, and v is a structural parameter that indicates solubilisation of these polymer-like structures.

5115	Spherical Particle Parameters		Hydrogen-bonded polymer chain parameters		
PUD sample	R/nm	$\sigma^*$	$\phi_{ ext{PU,AF}}/\phi_{ ext{PU,tot}}$	$R_g$ /nm	ν
Supramolecular Structures	-	_	-	2.2	0.33
HB50_SS650	17.9	1.21	0.029	2.8	0.31
HB60_SS650	11.2	1.39	0.066	2.4	0.31
HB70_SS650	8.30	1.33	0.085	2.7	0.32
HB50_SS1000	14.8	1.15	0.112	2.6	0.33
HB60_SS1000	11.2	1.17	0.114	2.9	0.33
HB70_SS1000	10.1	1.19	0.184	2.9	0.30
HB50_SS2000	15.1	1.09	0.215	2.9	0.33
HB60_SS2000	13.5	1.14	0.253	3.0	0.34
HB70_SS2000	12.8	1.09	0.290	2.8	0.34

The size of the supramolecular structures is reasonably consistent between the samples, with 2.4 nm  $\leq R_g \leq$  3.0 nm. The value of  $\nu$ , for all PUDs, is found to be in the range of 0.30 - 0.34, indicating the structure of collapsed polymer chains. This deviation from the value for a self-avoiding walk ( $\nu = 3/5$ )<sup>33</sup> arises from the incompatibility of the acidic fragment components that make up the supramolecular structures, and the water. It is likely that the fragments dissolved during the emulsification step of the synthesis, when methyl ethyl ketone (MEK) was still present in the solution. On removal of the MEK, the solvent becomes less ideal, leaving collapsed chains in the aqueous dispersions. This is indicated by excessive foaming on removal of the MEK, due to the acidic fragments exhibiting surfactant behaviour between MEK and water.

The fraction of the PU distributed as acidic fragments in supramolecular structures (quantified as  $\phi_{AF}/\phi_{tot}$ ) shows a strong dependence on acid content (Figure 3.11). It is

logical that higher proportion of DMPA in the formulation increases the likelihood of forming these molecules. It is noteworthy that up to 30% of the PU can form supramolecular structures. This is a significant proportion making this an important finding for understanding these materials.

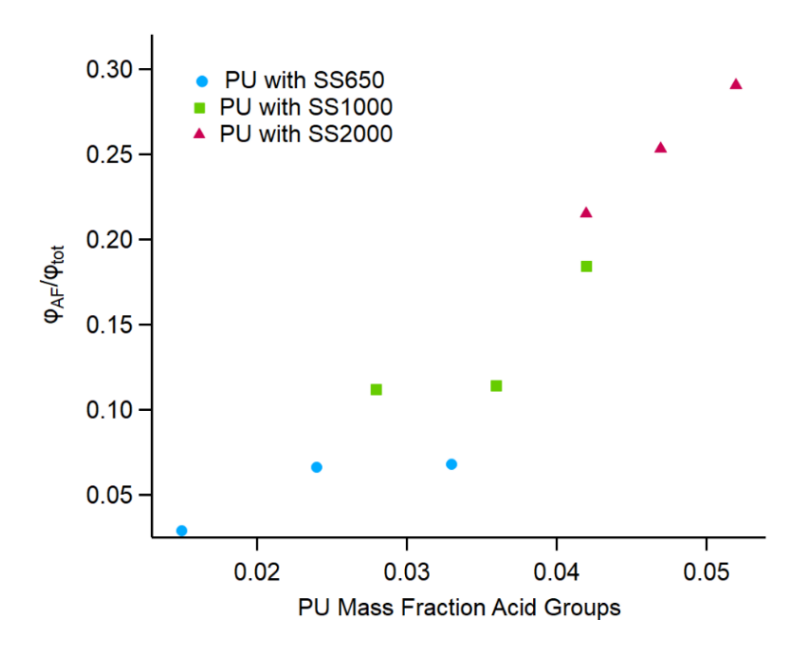


Figure 3.11: Relationship between the acid content used in the original PU formulation, and the volume fraction of PU found in hydrogen bonded supramolecular structures of HMDI<sub>n</sub>DMPA<sub>n-1</sub> molecules. Samples contain polyether of Mn 650 gmol<sup>-1</sup> (blue circles), Mn 1000 gmol<sup>-1</sup> (green squares), or Mn 2000 gmol<sup>-1</sup> (red triangles).

This distribution of the PU, between supramolecular structures of acidic fragments and spherical particles, can also be confirmed in AFM images (Figure 3.12).

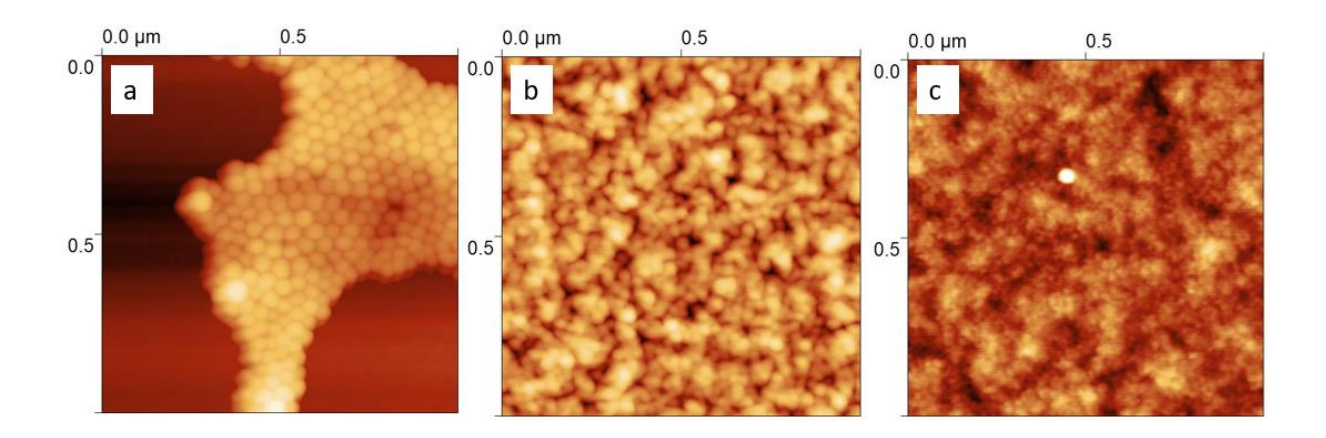


Figure 3.12: Representative AFM image of PUD samples spin coated on silica wafer at 50% hard block content, made with soft segment of Mn = a) 650 gmol<sup>-1</sup>, b) 1000 gmol<sup>-1</sup>, and c) 2000 gmol<sup>-1</sup>.

Spherical particles can be clearly seen in the AFM image collected on the spin-dried sample of  $HB50\_SS650$  (Figure 3.11a), which contains the least volume of supramolecular structures (2.9 vol% of the total PU). The resolution of the spherical particles worsens as the proportion of supramolecular structures increases to 11.2 vol% and 22.5 vol% for  $HB50\_SS1000$  (Figure 3.11b) and  $HB50\_SS2000$  (Figure 3.11c), respectively, despite the decrease in particle size dispersity,  $\sigma^*$  (Table 3.3). This is thought to be because the supramolecular structures are located at the interfaces between particles.

### 3.3.5 Particle Size Control

The uniformity of the particle sizes improves with increasing soft segment molecular weight, as indicated by the decrease in  $\sigma^*$  (Table 3.4). For each soft segment Mn, particle radius decreases with increasing hard block content, which contains the acidic stabilising groups. According to the PSC model, proposed by Neal et al.<sup>12</sup> the concentration of hydrophile at the particle/water interface is key in the control of particle size. The acid content in the particle, however, is no longer equal to that originally used in the formulation. The new acid content can be calculated from subtraction of the acid that is found in the second population [assuming molecules of 2:1 HMDI:DMPA, as they are the most abundant species in the GPC trace (Figure 3.6)], and consideration of the remaining mass fraction of acid with respect to the mass of PU found in the particles (Table 3.5).

Table 3.5: The mass fraction of acid groups found in spherical particles of PU in dispersion, compared to the mass fraction of acid in the total PU formulation including supramolecular structures of acidic fragments.

Sample	Mass fraction of acid groups			
Sample	In total PU formulation	In Spherical particles		
HB50_SS650	0.015	0.013		
HB60_SS650	0.028	0.020		
HB70_SS650	0.041	0.029		
HB50_SS1000	0.024	0.022		
HB60_SS1000	0.036	0.030		
HB70_SS1000	0.047	0.035		
HB50_SS2000	0.033	0.032		
HB60_SS2000	0.042	0.037		
HB70_SS2000	0.052	0.043		

This particle size behaviour, with respect to the acid content, shows similarities with the PSC model<sup>12</sup>, developed for amphiphilic statistical copolymers and applicable to a range of acrylic monomers (Figure 3.13).<sup>13</sup>

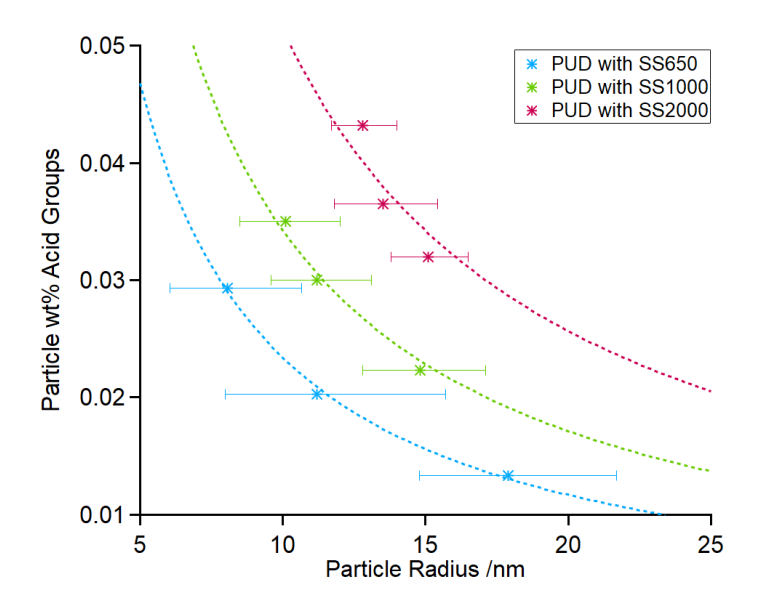


Figure 3.13: Dependence of the geometric mean particle radius on acid content, in PU particles composed of soft segment with Mn = 650 gmol<sup>-1</sup> (blue crosses), Mn = 1000 gmol<sup>-1</sup> (green crosses) and Mn = 2000 gmol<sup>-1</sup> (red crosses). Error bars indicate the multiplicative standard deviation. The dotted curves show fits of the PSC model<sup>13</sup> adapted for wt% acid group content (Equations 3.16-3.20).

According to the PSC model, by calculation of the particle surface area from R, assuming that  $SA_{frac}$  is independent of particle size, the number of hydrophilic B groups per particle ( $N_{B,p}$ ) can be estimated by

$$N_{\rm B,p} = \frac{1}{k} \times \frac{4\pi R^2 \times SA_{\rm frac}}{CS_{\rm R}} \quad [Eq. 3.15]$$

where  $CS_B$  is the cross-sectional area of a single B repeat unit and k is the fraction of B units found at the particle interface. SANS was used to obtain a value of 0.5 for k in the case of acrylic monomers, indicating that half of the hydrophiles are found at the surface of the particle, and the other half are trapped in the interior.<sup>13</sup>

It follows that the number of hydrophobic A units  $(N_{A,p})$  can be estimated from:

$$N_{A,p} = \frac{\frac{4}{3}\pi R^3 - (N_{B,p} \times V_B)}{V_A} \quad [Eq. 3.16]$$

where  $V_B$  volume of anionic B repeat units per particle, and  $V_A$  is the volume of one repeat unit of A. Knowing  $N_{B,p}$  and  $N_{A,p}$ , the mole fraction of hydrophilic groups ( $\chi_B$ ) can be calculated

$$\chi_{\rm B} = \frac{N_{\rm B,p}}{N_{\rm B,p} + N_{\rm A,p}} \quad [Eq. 3.17]$$

 $SA_{\rm frac}$  is dependent on the composition and is obtained from fitting of experimental data. Moreover,  $SA_{\rm frac}$  has been shown to be linearly related to the monomer hydrophobicity, measured by partition coefficient.<sup>13</sup>

As there is a statistical element to the formation of PUs (the distribution of diol and diamine between diisocyanates), and the acid group of DMPA acts as a hydrophile in an otherwise hydrophobic chain, it was thought that the PSC model could be adapted for PUDs. The acidic moieties fulfil the role of the anionic *B* groups, however the

hydrophobic A groups, in the case of PUDs, is made up of PTMO, HMDI and ethylene diamine. This is complicated by the fact that the ratio of these hydrophobes changes depending on the formulation. Subsequently, there is no appropriate  $V_A$  value that is independent of composition. Moreover, due to the complexity of PU formulations, it was deemed that expressing the PSC model as an expression for calculating mass fraction of acid groups would be more appropriate than mole fraction. This can be done by converting  $N_{B,p}$  to the mass of B per particle ( $M_{B,p}$ ) using:

$$M_{\rm B,p} = \frac{N_{\rm B,p} \times M_{\rm w,B}}{N_{\rm A}}$$
 [Eq. 3.18]

where  $M_{w,B}$  is the molecular weight of B and  $N_A$  is Avogadro's number. The mass of the entire particle  $(M_p)$  can be found from:

$$M_p = \frac{4}{3}\pi R^3 \times \rho_{m,part}$$
 [Eq. 3.19]

where  $\rho_{m,sp}$  is the mass density of the whole particle. Due to the minimal deviations in  $\rho_{m,sp}$  across the range of samples (Table 8.2, Appendix), an average value of 1.10 gcm<sup>-3</sup> was used. The mass fraction of B per particle ( $M_{frac,B}$ ) is then given by:

$$M_{\text{frac,B}} = \frac{M_{\text{B,p}}}{M_{\text{p}}} \quad [Eq. 3.20]$$

It is most likely that, in the case of PUDs, k = 1, as any acid groups trapped in the interior of the particle would cause an influx of water, which in turn would influence  $\xi_{\text{part}}$ . This is not seen in the values obtained by SAXS fitting; therefore, it is reasonable to estimate that all acid groups are found at the interface. The PSC model, adapted for wt% acid content in the PU particles, fits the experimental data well, as shown by the dotted lines in Figure 3.13.

Moreover, the greater acid content required for particles of a given size, for longer soft segment lengths, is in good agreement with the findings of Neal et al.<sup>13</sup> It is logical that higher molecular weight soft segment is more hydrophobic, therefore the required  $SA_{frac}$  for stable particles is greater. The values for  $SA_{frac}$ , obtained from fitting of the adapted PSC model (Equations 3.16-3.20) to the experimental values are given in Table 3.6 and plotted in Figure 3.14.

Table 3.6: Fractional surface area coverage of hydrophiles (SA<sub>frac</sub>) required for stable spherical PU particles in aqueous dispersion for each polyether Mn according to fitting of the PSC model<sup>13</sup> to experimental data (Figure 3.12).

Soft segment Mn /gmol <sup>-1</sup>	SA <sub>frac</sub>
650	0.127
1000	0.186
2000	0.279

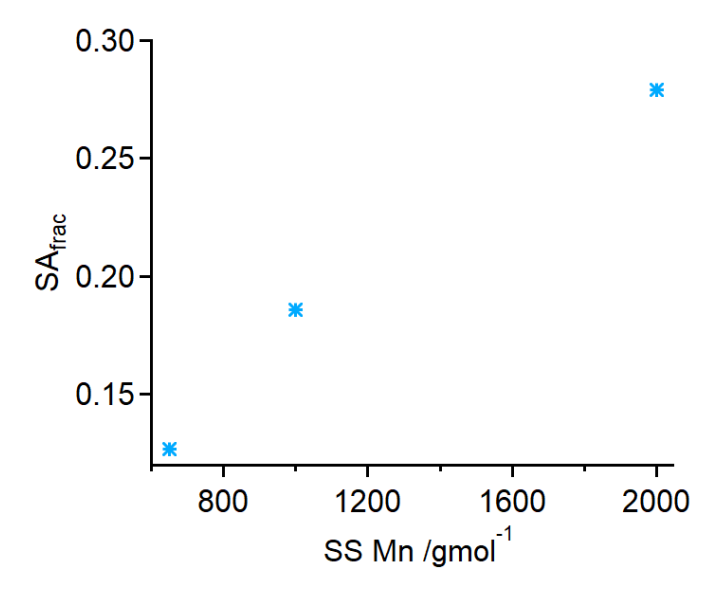


Figure 3.14: Surface area fractional coverage of hydrophiles ( $SA_{frac}$ ) required for stable spherical particles of PU in dispersion, with respect to soft segment Mn.

# 3.4 Conclusions

A set of PU dispersions has been synthesised with variable hard block/soft segment ratio, soft segment length and acid content. It is found that their synthesis produces

by-products, namely acidic fragments of *n* HMDI and *n-1* DMPA. These form during the PU prepolymer synthesis, with the trimer HMDI-DMPA-HMDI as the dominant species. Upon emulsification, the isocyanate end-caps react to give amine groups, and the molecules strongly hydrogen bond forming supramolecular structures.

A SAXS analytical model has been developed to measure the distribution of PU between charge-stabilised spherical particles and supramolecular structures comprising acidic fragments. The model counts the total PU formulation, composition of the acidic fragments, changes of mass density, and the scattering length density of the PU populations. Applying this analysis to the PUDs has shown that the proportion of acid-rich supramolecular structures increases with DMPA content. Fitting of analytical models to the experimental SAXS profiles has demonstrated that the intensity of scattering originating from the supramolecular structures could be described by a general model for polymers in solution.

It is shown that a particle surface charge (PSC) model, originally developed for characterisation of self-assembled amphiphilic statistical copolymers, can be adopted for characterisation of particle size. It was found that the PU particle radius is controlled by acid content in the PU molecules, where an increase in PU acidity resulted in a decrease in particle size. The particle surface area fractional coverage of acid required for stable spheres increases with soft segment Mn, from 0.127 with Mn = 650 gmol<sup>-1</sup>, to 0.279 with Mn = 2000 gmol<sup>-1</sup>. This follows the findings of the PSC model, that a more hydrophobic comonomer requires a greater surface area coverage of acid groups for stable spherical particles.

### 3.5 References

- 1 R. Satguru, J. McMahon, J. C. Padget and R. G. Coogan, *J. Coatings Technol.*, 1994, **66**, 47–55.
- 2 A. K. Nanda and D. A. Wicks, *Polymer (Guildf).*, 2006, **47**, 1805–1811.
- 3 A. K. Nanda, D. A. Wicks, S. A. Madbouly and J. U. Otaigbe, *J. Appl. Polym. Sci.*, 2005, **98**, 2514–2520.
- 4 B. K. Kim, Colloid Polym. Sci., 1996, **611**, 599–611.
- J. Bolze, M. Ballauff, T. Rische, D. Rudhardt and J. Meixner, *Macromol. Chem. Phys.*, 2004, **205**, 165–172.
- O. Jaudouin, J. J. Robin, J. M. Lopez-Cuesta, D. Perrin and C. Imbert, *Polym. Int.*, 2012, **61**, 495–510.
- 7 L. H. Bao, Y. J. Lan and S. F. Zhang, *J. Polym. Res.*, 2006, **13**, 507–514.
- 8 M. A. Pérez-Limiñana, F. Arán-Aís, A. M. Torró-Palau, A. C. Orgilés-Barceló and J. M. Martín-Martínez, *Int. J. Adhes. Adhes.*, 2005, **25**, 507–517.
- 9 X. Zhu, X. Jiang, Z. Zhang and X. Z. Kong, *Prog. Org. Coatings*, 2008, **62**, 251–257.
- 10 M. Li, E. S. Daniels, V. Dimonie, E. D. Sudol and M. S. El-Aasser, *Macromolecules*, 2005, **38**, 4183–4192.
- 11 X. Wang, G. Ma and M. Zheng, *J. Coatings Technol. Res.*, 2018, **15**, 1217–1227.
- T. J. Neal, D. L. Beattie, S. J. Byard, G. N. Smith, M. W. Murray, N. S. J. Williams, S. N. Emmett, S. P. Armes, S. G. Spain and O. O. Mykhaylyk, *Macromolecules*, 2018, **51**, 1474–1487.
- T. J. Neal, A. J. Parnell, S. M. King, D. L. Beattie, M. W. Murray, N. S. J. Williams, S. N. Emmett, S. P. Armes, S. G. Spain and O. O. Mykhaylyk, *Macromolecules*, 2021, **54**, 1425–1440.
- 14 S. Zhang, H. Lv, H. Zhang, B. Wang and Y. Xu, *J. Appl. Polym. Sci.*, 2006, **101**, 597–602.
- 15 B. K. Kim and J. C. Lee, *J. Polym. Sci. Part A Polym. Chem.*, 1996, **34**, 1095–1104.
- 16 J. Yang, Z. Wang, Z. Zeng and Y. Chen, *J. Appl. Polym. Sci.*, 2002, **84**, 1818–1831.
- 17 M. L. Hsaing, C. H. Chang, M. H. Chan and D. Y. Chao, *J. Appl. Polym. Sci.*, 2005, **96**, 103–112.
- 18 F. Boué, J. Combet, B. Demé, M. Heinrich, J. G. Zilliox and M. Rawiso, *Polym.* 2016, Vol. 8, Page 228, 2016, **8**, 228.
- 19 P. Salgi and R. Rajagopalan, Adv. Colloid Interface Sci., 1993, 43, 169–288.
- 20 A. A. Cockram, T. J. Neal, M. J. Derry, O. O. Mykhaylyk, N. S. J. Williams, M.

- W. Murray, S. N. Emmett and S. P. Armes, *Macromolecules*, 2017, **50**, 796–802.
- 21 M. Semsarilar, V. Ladmiral, A. Blanazs and S. P. Armes, *Langmuir*, 2012, **28**, 914–922.
- 22 J. B. Hayter and J. Penfold, *Mol. Phys.*, 2006, **42**, 109–118.
- J. S. Pedersen and M. C. Gerstenberg, *Macromolecules*, 1996, **29**, 1363–1365.
- 24 J. K. Percus and G. J. Yevick, *Phys. Rev.*, 1958, **110**, 1–13.
- F. Li, R. Tuinier, I. Van Casteren, R. Tennebroek, A. Overbeek and F. A. M. Leermakers, *Macromol. Theory Simulations*, 2016, **25**, 16–27.
- 26 J. S. Pedersen, I. W. Hamley, C. Y. Ryu and T. P. Lodge, *Macromolecules*, 2000, **33**, 542–550.
- 27 M. J. Elwell, A. J. Ryan, H. J. M. Grünbauer and H. C. Van Lieshout, *Polymer (Guildf).*, 1996, **37**, 1353–1361.
- 28 E. Yılgör, İ. Yılgör and E. Yurtsever, *Polymer (Guildf).*, 2002, **43**, 6551–6559.
- 29 A. W. Bosman, R. P. Sijbesma and E. W. Meijer, *Mater. Today*, 2004, **7**, 34–39.
- 30 S. Chen and W. H. Binder, Acc. Chem. Res., 2016, 49, 1409–1420.
- J. Courtois, I. Baroudi, N. Nouvel, E. Degrandi, S. Pensec, G. Ducouret, C. Chanéac, L. Bouteiller and C. Creton, *Adv. Funct. Mater.*, 2010, **20**, 1803–1811.
- 32 M. M. Coleman and P. C. Painter, *Prog. Polym. Sci.*
- P. Schurtenberger, Neutrons, X-rays and Light: Scattering Methods Applied to Soft Condensed Matter, Elsevier Science, Amsterdam, 1st edn., 2002.
- 34 R. A. Register, G. Pruckmayr and S. L. Cooper, *Macromolecules*, 1990, **23**, 3023–3026.
- R. Aguiar, O. E. Petel and R. E. Miller, *Compos. Part C Open Access*, 2022, **7**, 100231.
- V. Kašpárková, L. Šimek and M. Bohdanecký, *Macromol. Chem. Phys.*, 1996, **197**, 3757–3772.
- 37 S. Yılgo, E. Yurtsever and B. Erman, *Macromolecules*, 2002, **35**, 9825–9831.
- 38 D. S. Thompson, *J. Phys. Chem.*, 1971, **75**, 789–791.
- 39 G. Herdan, Small Particle Statistics, Butterworths, London, 2nd rev ed., 1960.
- 40 National Institute of Standards and Technology (U.S. Department of Commerce), Lognormal Distribution, https://www.itl.nist.gov/div898/handbook/eda/section3 /eda3669.htm, (accessed 5 January 2023).

# Chapter 4 - Morphology Evolution During Drying

# of Polyurethane Dispersions

## 4.1 Introduction

The properties of coatings are highly influenced by any microstructures in the film morphology that arise during drying or curing. Understanding how these microstructures form, from the morphology in the wet state, is key, therefore, to controlling properties. *In situ* small angle X-ray scattering (SAXS) experiments during drying of various colloidal systems show a loss of long-range order with solvent evaporation.<sup>1–3</sup> Crowley et al. used small angle neutron scattering (SANS) to characterise the intermediate stages during drying of aqueous latexes.<sup>4</sup> Their model highlighted significant early deformation for "soft" particles, whereas "hard" latexes retained their shape until the final stages of drying where the particles are in very close proximity.

Polyurethane (PU) coatings are known for their desirable ability to form films that are abrasion resistant, tough and flexible.<sup>5–8</sup> Due to the wide range of available monomers and polyols for PU design, a broad spectrum of properties can be targeted.<sup>5–10</sup> During drying of aqueous dispersions, the particles are deposited on a surface forming a continuous film. It is well established that the desirable properties of PU materials come from the phase separation between rigid, polar hard blocks and flexible, soft segments formed by polyols.<sup>11–15</sup> As such, understanding how structures evolve during drying is of utmost importance for targeting high performance products.

Despite the importance for rational design, morphology evolution during the drying of PUDs to make coatings, and how the polymer composition effects this process, is not well understood. In this chapter, *in situ* SAXS during the drying of a PUD is employed to characterise morphology evolution. Additionally, the effect of acid content, hard block content and soft segment molecular weight on the morphology of PU films is probed using SAXS and atomic force microscopy (AFM). The film structures are compared to the dispersion morphologies discussed in Chapter 3, to better understand how they arise during the drying process.

## 4.2 Samples and Data Collection

The samples studied in this Chapter are summarised in Table 4.1

Table 4.1: Summary of key compositional details for PUDs studied in this chapter.

Sample	Polymer Hard Block Content (wt%)	Soft Segment M <sub>n</sub> (gmol <sup>-1</sup> )	Polymer COOH Content /wt%
HB50_SS650	50	650	1.52
HB60_SS650	60	650	2.83
HB70_SS650	70	650	4.15
HB50_SS1000a*	50	1000	2.40
HB50_SS1000b	50	1000	2.40
HB60_SS1000	60	1000	3.57
HB70_SS1000	70	1000	4.72
HB50_SS2000	50	2000	3.29
HB60_SS2000	60	2000	4.23
HB70_SS2000	70	2000	5.22

<sup>\*</sup>This sample was made by AkzoNobel Slough, whereas all others, including HB50 SS1000b, were made by AkzoNobel Sassenheim

HB50\_SS1000a was used to study the film formation process by time-resolved grazing incidence SAXS (GISAXS) data collection (described in Section 2.2.5.1). This method was verified by comparison of the dispersion (start of the drying period) and film (end of the drying period) SAXS profiles with the equivalent data collected in transmission

mode (Figure 4.1). The positions of the main features observed in the SAXS patterns are very similar, with the exception of a peak in the GISAXS dispersion data at  $q \approx 0.022 \text{ Å}^{-1}$  that arises due to structuring of the sample through particle interactions at high concentration. This confirms that collection of SAXS data in grazing incidence geometry is a reliable method for observing the evolution of morphology during drying, probing bulk morphology rather than surface effects and replicating data collection in transmission geometry.

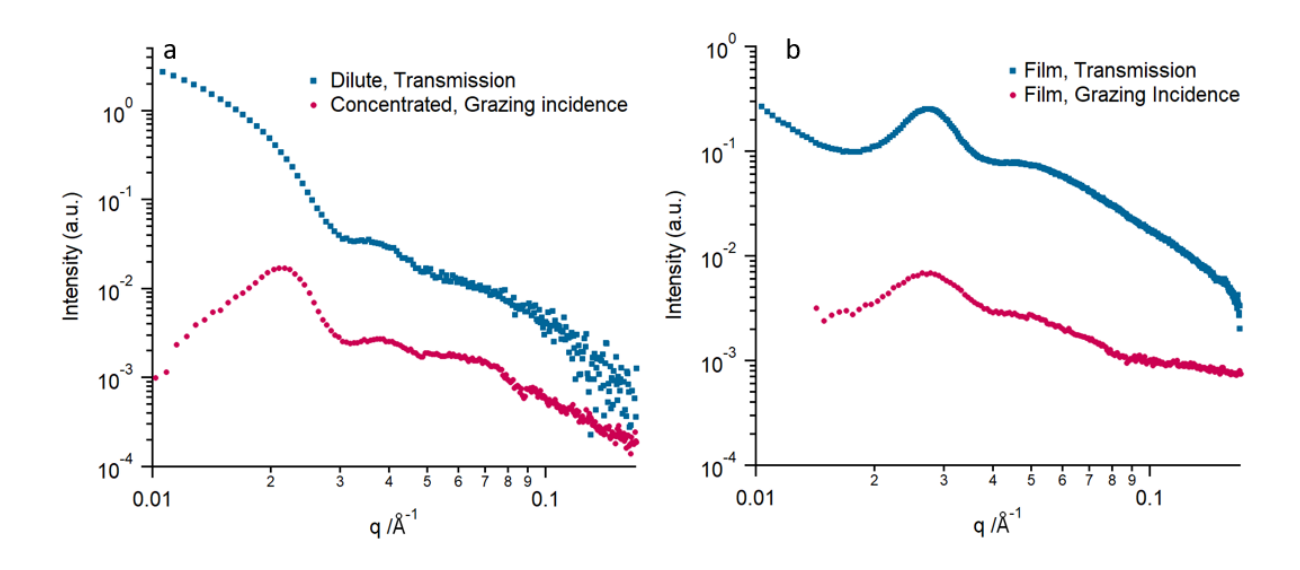


Figure 4.1: Comparison of SAXS patterns collected in transmission (blue symbols) and grazing incidence (red symbols) geometries for samples of a PU comprising 50% hard block and polyether of Mn 1000 gmol<sup>-1</sup> (HB50\_SS1000a) as a) a PU particle dispersion at 1wt % PU (diluted) in transmission and 33 wt% PU (concentrated) in grazing incidence, and b) dried films.

The remaining nine samples (Table 4.1), which are analysed as dispersions in Chapter 3, are studied as dried films using transmission SAXS (described in Section 2.2.5.1).

# 4.3 Results and Discussion

## 4.3.1 Morphology Evolution *in situ* During the Drying of a PU Dispersion

GISAXS data collected *in situ* during the drying of sample *HB50\_SS1000a*, from concentrated PU dispersion, shows the evolution of morphology from dispersion to film (Figures 4.2a and 4.2b).

The analysis in Chapter 3 revealed that, for PUDs at 1 wt%, the polymer is distributed between two populations: PU spherical particles and highly acidic fragments of n HMDI and n-1 DMPA, hydrogen bonded to form a supramolecular polymer-like structure. In the case of  $HB50\_SS1000a$ , spherical particles with a diameter of 30.4 nm, stabilised by acid groups located at the particle surface, are in the majority. The PUD scattering pattern shows a characteristic feature corresponding to the first minimum of a spherical form factor at  $q \approx 0.031$  Å-1 (Figure 4.1a).

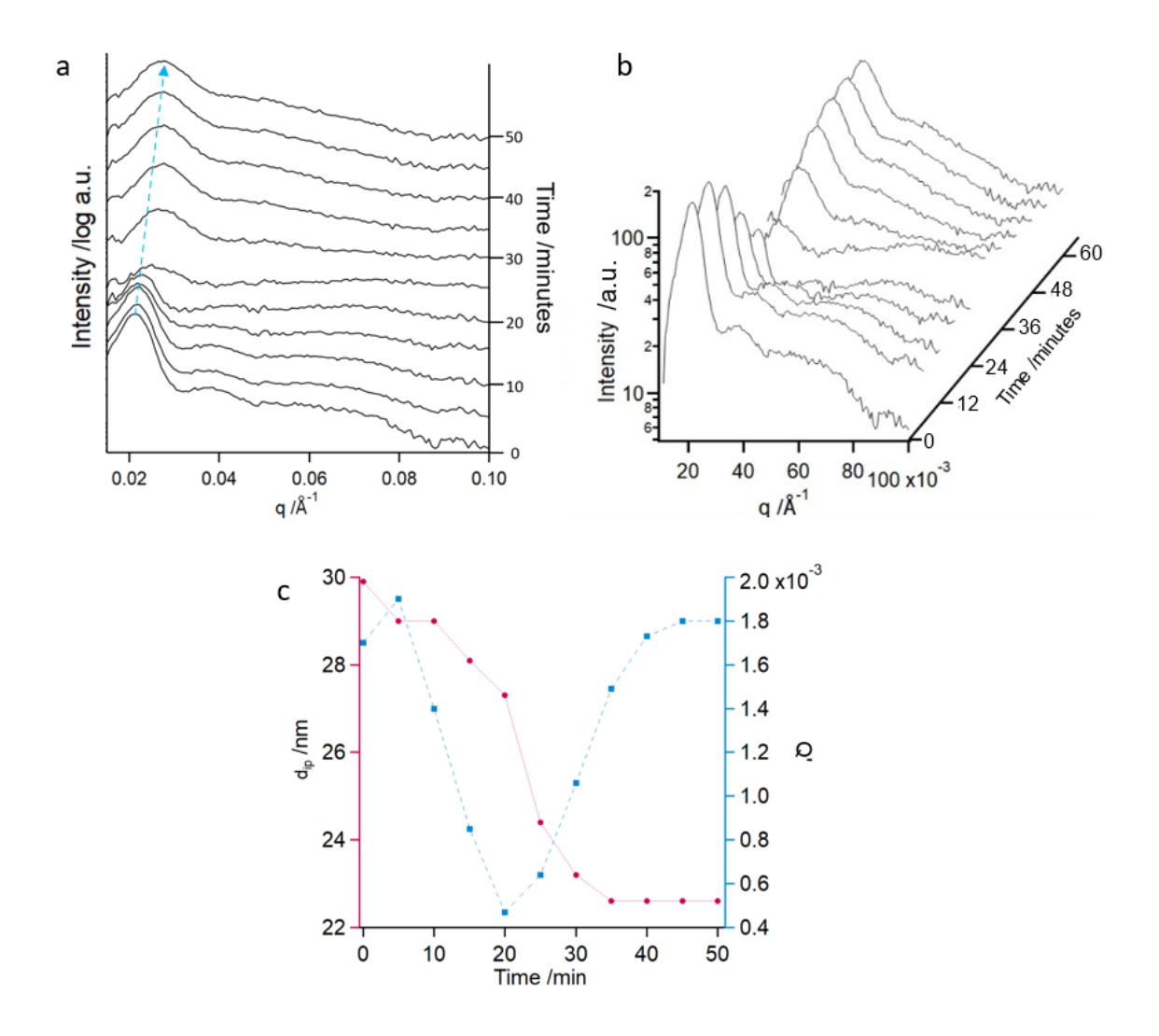


Figure 4.2: GISAXS data collected in situ during the drying of a 33 wt% aqueous dispersion of PU comprising 50% hard block and soft segment of Mn = 1000 gmol<sup>-1</sup> (HB50\_SS1000a). Each profile was collected for 5 minutes. The data are stacked (a) to show the movement of the primary peak to higher q indicated by the blue arrow, and (b) plotted as waterfall to show the change in intensity with time. c) Change in the average correlation distance between centres of adjacent particles (red symbols) and relative scattering invariant (blue symbols) with respect to time during the film formation.

The minority phase of acidic fragments present in  $HB50\_SS1000a$  can be modelled as collapsed polymer chains, with an average radius of gyration of ~ 2.8 nm. This phase is seen in the scattering profile as a pronounced shoulder at  $q > 0.06 \, \text{Å}^{-1}$  (Figure 4.1a). Using the model developed for PUDs (discussed in Section 3.3.4, full model shown in Appendix 8.10), the polymer distribution was found to be 95% PU in particles, and 5% in acidic fragments hydrogen bonded into supramolecular structures.

Due to the high concentration of the PUD used for *in situ* drying measurements, the initial data show an intense peak at  $q_{\text{max}} = 0.022 \,\text{Å}^{-1}$  that is not observed in the SAXS pattern collected for the dilute dispersion (Figure 4.1a). This peak is caused by repulsion of charge-stabilising acid groups at the surface of PU particles that results in a short-range periodic structure, formed by the packed particles across the concentrated sample. The average correlation distance between centres of adjacent particles ( $d_{ip}$ ) can be obtained from the position of the maximum ( $q_{max}$ ) according to Braggs law:

$$d_{\rm ip} = \frac{2\pi}{q_{\rm max}} \quad [Eq. 4.1]$$

The  $d_{\rm ip}$  of 29.9 nm at the beginning of the reaction is less than the 30.4 nm particle diameter in dilute dispersion, indicating that the particles at high concentrations are slightly distorted from a spherical shape. This distortion could be caused by a combination of particle packing and charge repulsion of the acid groups present at the particle surface.  $q_{\rm max}$  increases upon water evaporation, indicating a decrease in  $d_{\rm ip}$  from 29.9 nm in the wet state to 22.6 nm when dry (Figure 4.2c).

The changes in the peak intensity throughout the film formation (Figure 4.2b) can be evaluated by calculation of the SAXS invariant with respect to time (Figure 4.2c). This

is a measure of the scattering power of a sample, found by integrating the area under the  $Iq^2$  vs q curve. Here, the relative invariant (Q') is calculated by integrating in the region of 0.014 Å-1  $\leq q \leq$  0.04 Å-1 to count only the area under the structure peak associated with the interparticle spacing. This region also includes scattering intensity contributions from other structural morphologies present in the sample. However, these contributions are negligible in comparison with the intensity of the peak corresponding to  $d_{\rm ip}$ .

Initially, Q' decreases with time, reaching a minimum after 20 minutes of drying, before increasing again (Figure 4.2b). The invariant can increase (decrease) with a greater (smaller) difference in scattering length density contrast,  $\Delta \xi$ , between phases and/or between particles and their solvent, and is proportional to the square of  $\Delta \xi$ . At high PU concentrations, such as that used for this film formation analysis, the system can be simplified to a two-phase system of PU particles, and a matrix of solvent solution comprising water and acidic fragments. The scattering length density of the acidic fragments ( $\xi_{AF}$ ) and water ( $\xi_{W}$ ) are calculated as 10.91 × 10<sup>10</sup> cm<sup>-2</sup> and 9.42 × 10<sup>10</sup> cm<sup>-2</sup>, respectively (Equation 2.3).

When the matrix is considered as a mixture of acidic fragments and water, the average scattering length density of the matrix ( $\xi_{mat}$ ) is given by:

$$\xi_{\text{mat}} = \phi_{\text{w}} \cdot \xi_{\text{w}} + (1 - \phi_{\text{w}}) \cdot \xi_{\text{AF}} \quad [Eq. 4.2]$$

where  $\phi_w$  is the volume fraction of water in the matrix. The calculated scattering length density for the initial PU particles ( $\xi_{part}$ ), considering the change in composition due to loss of acidic fragments and the formation of the minor phase, is  $10.07 \times 10^{10} \, \text{cm}^{-2}$  (Equation 3.14). Therefore,  $\xi_w < \xi_{part} < \xi_{AF}$ . At the beginning of the drying process, the matrix is predominantly water, giving  $\xi_{part} > \xi_{mat}$  (Figure 4.3a).

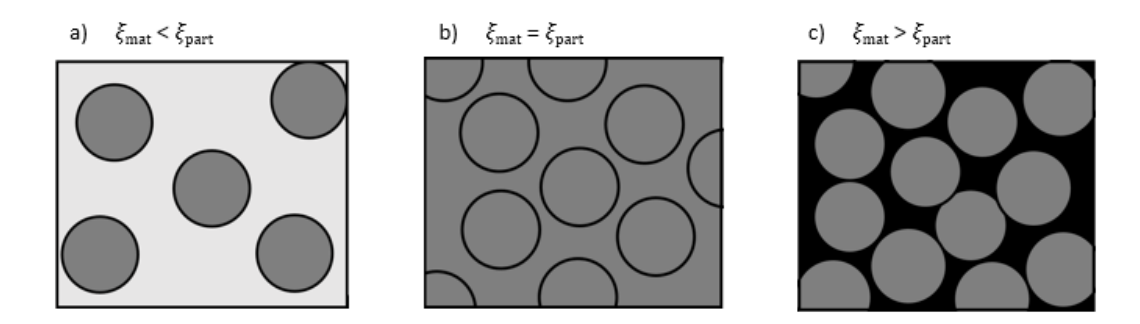


Figure 4.3: Schematic of the drying process of a PU dispersion simplified to a two-phase system of particles in a matrix, showing the change in relationship between the scattering length density of the particles ( $\xi_{part}$ ) and the matrix ( $\xi_{mat}$ ) in three scenarios: a) the beginning of the drying, b) the match point, and c) the dry film.

In the dry state, all water is lost, such that the matrix contains only the supramolecular structures of acidic fragments, packed between the particles (Figure 4.4). At this point  $\xi_{\text{part}} < \xi_{\text{mat}} = \xi_{\text{AF}}$  (Figure 4.3c). The minimum in Q' at 20 mins (Figure 4.2c) shows that a match point is reached, where  $\xi_{\text{part}} = \xi_{\text{mat}}$  (Figure 4.3b). This is achieved when  $\phi_{\text{w}} = 0.56$ . The maxima in Q' (Figure 4.2c) are at the beginning and end of the film formation process, where there is the greatest difference between  $\xi_{\text{part}}$  and  $\xi_{\text{mat}}$ .

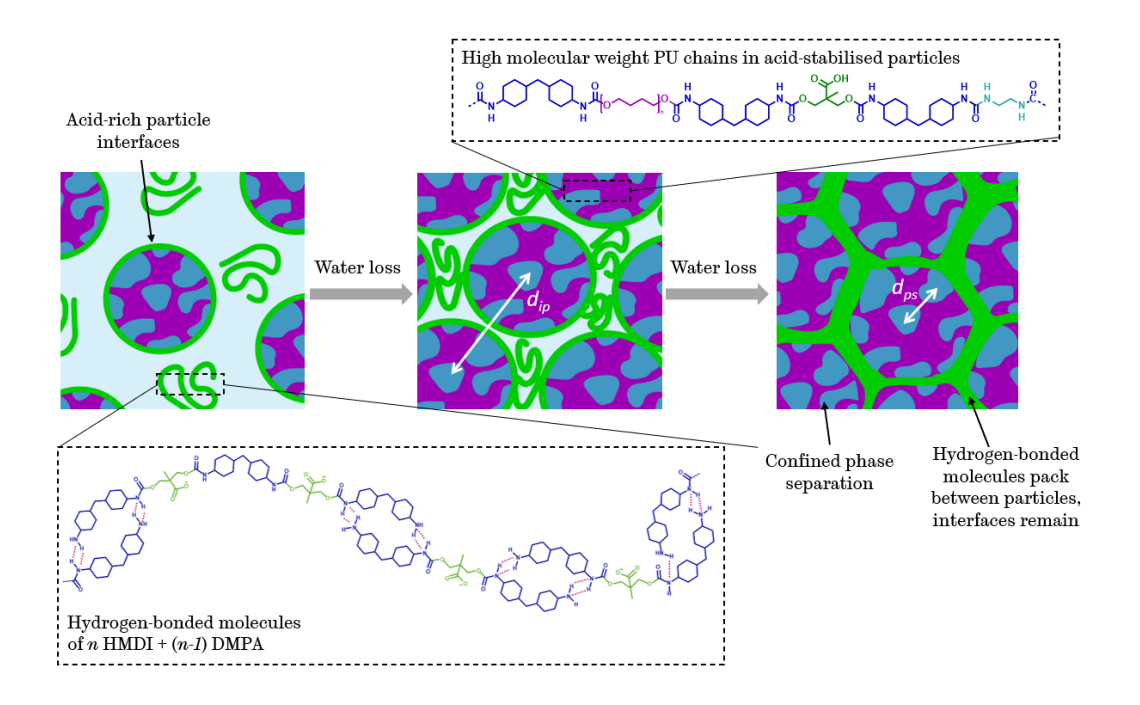


Figure 4.4: Structural morphology evolution during the drying of an aqueous PU dispersion, showing particles of high molecular weight PU with acid rich interfaces, and a second population of hydrogen bonded molecules of n HMDI and n-1 DMPA forming supramolecular structure of acidic fragments. The location of acidic groups is highlighted by green colour.

Time-resolved SAXS patterns of drying  $HB50\_SS1000a$  dispersion show that the scattering intensity shoulder at q > 0.06 Å<sup>-1</sup>, associated with the minor population, disappears (Figures 4.2a and 4.2b). This result indicates that, upon the dispersion drying, the acidic fragments aggregate between the particle interfaces and are no longer discrete (Figure 4.4). Simultaneously, a new shoulder grows at  $q \approx 0.042$  Å<sup>-1</sup> after 30 minutes, suggesting a structure with a correlation length of  $\sim 10.2$  nm (Figures 4.2a and 4.2b). This length scale is comparable with reported results on the periodicity of micro-phase separation in PU containing soft block of a similar molecular weight, <sup>17–19</sup> suggesting microphase separation of the hard blocks and soft segments within the confinement imposed by particle interfaces (Figure 4.4). It is likely that this phase separation also occurs in the dispersed particles, however it cannot be clearly resolved in the PUD scattering profiles because of the other components contributing to the scattering patterns (Figure 3.1d). In particular, the scattering from the PU particles and acidic fragments dominates the q region in which the intensity peak associated with the PU phase separation appears.

#### 4.3.2 Reversibility of Film Formation

Due to the highly acidic nature of the interfaces between particles, the dry film has hydrophilic character. Transmission SAXS profiles of PU comprising 50% hard block and soft segment of  $Mn = 1000 \text{ gmol}^{-1}$  ( $HB50\_SS1000b$ ), show that a fully dried film soaked in water for 10 minutes, and the wet dispersion at 1 wt% PU, produce the same scattering intensity features associated with PU particles (Figure 4.5).

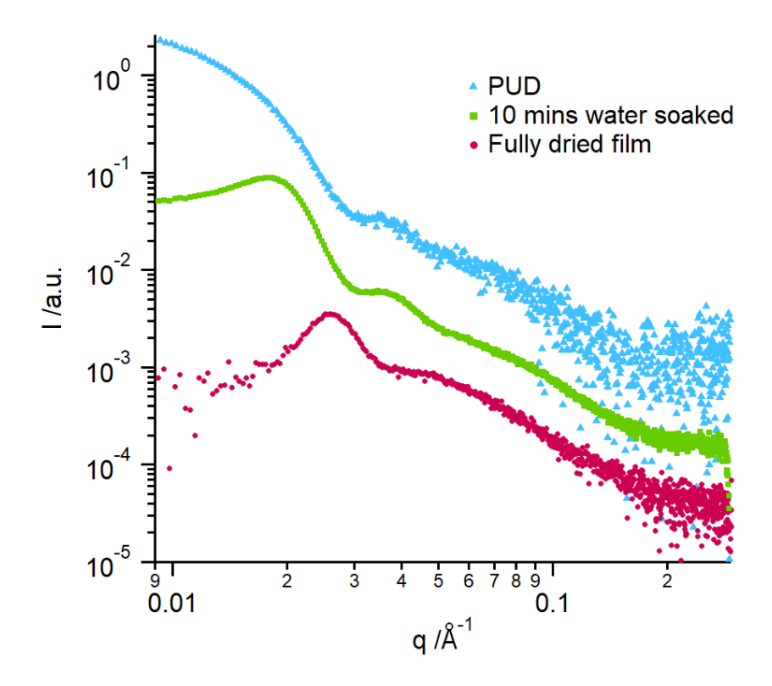


Figure 4.5: SAXS profiles of a PU comprising 50% hard block and soft segment of Mn = 1000 gmol<sup>-1</sup> (HB50\_SS1000b) collected as a dispersion at 1 wt% PU (blue triangles), a fully dried film (red circles) and after soaking the dry film in water for 10 minutes (green squares). Profiles are offset by an arbitrary factor to avoid overlap.

This observation indicates that the morphology evolution during film formation is reversible. The peak arising from  $d_{ip}$  in the film data ( $q_{max} \approx 0.025 \text{ Å}^{-1}$ ) moves to  $q_{max} \approx 0.019 \text{ Å}^{-1}$  after 10 minutes soaking in water (Figure 4.5). This shift to lower q indicates an increase in  $d_{ip}$ , from 25.1 nm to 33.1 nm. Water penetrates the acid-rich matrix first, causing swelling and thus separation of the particles. The scattering arising from acidic fragments, hydrogen-bonded into supramolecular structures, in the PUD ( $q > 0.06 \text{ Å}^{-1}$ ) is also present in the soaked film. The two populations of PU found in dispersion have reformed, showing that the structural organisation of the film is such that the drying is reversible when the film is exposed back to water.

# 4.3.3 <u>Investigation into the Effect of PU Composition on the Film Morphology</u>

The established structural evolution during *HB50\_SS1000a* film formation was applied to study the effect of PU composition on film morphology. Transmission SAXS analysis was carried out on nine compositions of fully dried PU films (Figure 4.6). The diffuse

scattering at high q from thermal background ( $I_b$ ) was removed from all the SAXS profiles (Appendix 8.5).<sup>19</sup> Lorenz-correction was applied to the background-subtracted data by plotting (I(q)- $I_b$ )· $q^2$  vs q.

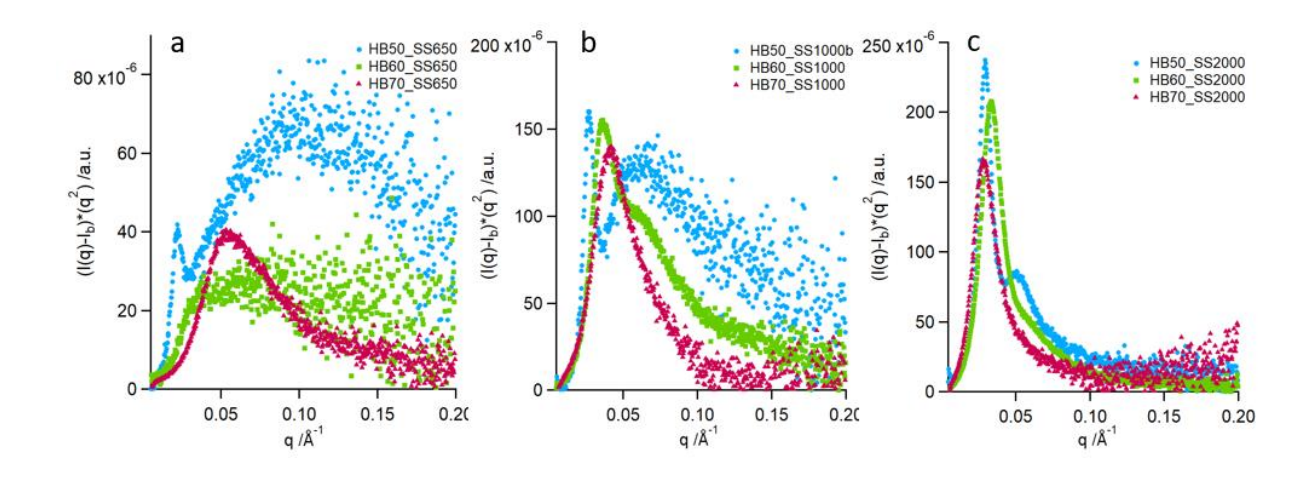


Figure 4.6: Background-subtracted and Lorenz-corrected SAXS profiles of polyurethane films dried from aqueous dispersions, made with soft segment of Mn = a) 650 gmol<sup>-1</sup>, b) 1000 gmol<sup>-1</sup>, and c) 2000 gmol<sup>-1</sup>, with 50% hard block content (blue circles), 60% hard block content (green circles), and 70% hard block content (red circles).

Most of the samples show a pronounced intensity peak at low q associated with particle packing in the dried films. The Lorenz-corrected SAXS data of  $HB60\_SS650$  film show an extremely broad shoulder (Figure 4.6a, green circles). SAXS analysis of the PUD corresponding to this composition indicated a broad log normal distribution of particle sizes (Table 3.2). Thus, it is expected that the particles are not well ordered in this system upon drying, therefore there is a high polydispersity of  $d_{ip}$  in the film.

The correlation distance between particle centres is always less than the mean dispersion particle size (Table 4.2 and Figure 4.7) in analogy with *HB50\_SS1000a* (Figure 4.2c).

Table 4.2: Interparticle correlation distance in films  $(d_{ip})$  cast from PU dispersion, compared to the mean diameter of PU particles in the wet state, measured by SAXS.

Sample	<i>d<sub>ip</sub></i> /nm	Mean dispersion particle diameter /nm
HB50_SS650	28.4	37.8
HB60_SS650	-	22.4*
HB70_SS650	12.3	16.6
HB50_SS1000a	30.4	29.9
HB50_SS1000b	23.3	29.6
HB60_SS1000	17.5	22.4
HB70_SS1000	15.7	20.2
HB50_SS2000	21.1	30.2
HB60_SS2000	18.8	27.0
HB70_SS2000	21.8	25.6

<sup>\*</sup>Broad range of particle sizes. This leads to disordered interfaces in the film.

However, there is good correlation between the particle size and  $d_{ip}$  (Figure 4.7). Sample  $HB70\_SS2000$  shows the least distortion according to this comparison. This arises due to the high volume of the individual hard segments in the polymer chains, and the high proportion of acidic fragments, imparting rigidity and preventing so much distortion.

Without prior knowledge of the dispersion morphologies and evolution during drying, it would be logical to assume that the primary peak shown in the SAXS data arises from micro-phase separation, characteristic of polyurethanes, <sup>19</sup> occurring when particles completely coalesce to make a continuous film. However, as *in situ* drying data reveals (Figure 4.2), this peak must be interpreted as the distance between centres of uncoalesced particles in the film. This is further affirmed by the robust relationship between particle size in dispersion, and  $d_{ip}$  in the film (Table 4.2 and Figure 4.7).

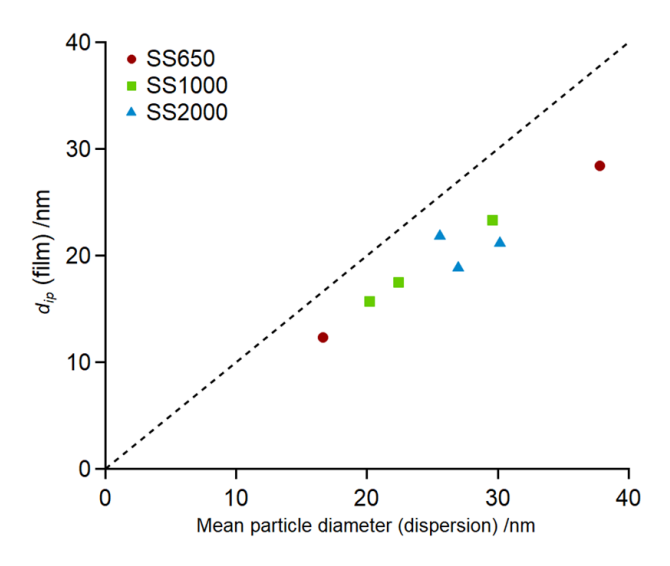


Figure 4.7: Relationship between the mean particle diameter in the dispersion and the mean correlation distance between neighbouring particle centres  $(d_{ip})$ . The data points are grouped by soft segment molecular weight with either Mn of 650 gmol<sup>-1</sup> (red circles), 1000 gmol<sup>-1</sup> (green squares), or 2000 gmol<sup>-1</sup> (blue triangles). The case of no particle deformation (i.e. particle diameter in the wet state  $= d_{ip}$ ) is shown by the dashed black line.

In addition to the primary peak, there is a secondary scattering feature in the SAXS profiles at higher q. Although present in all samples, this peak is well-resolved only in the samples containing 50% hard block, (Figure 4.6, blue circles). It is visible as a shoulder in  $HB60\_SS1000$  and  $HB60\_SS2000$ , and unresolved in the remaining samples. The peak positions are comparable with results published in literature on micro-phase separation of PU containing soft block of a similar molecular weight,  $^{17-19}$  suggesting the peak arises from the correlation distance of phase separation ( $d_{ps}$ ). The scattering invariant of a two-phase system is proportional to volume concentration of the phases according to:

$$Q' \approx \phi \cdot (1 - \phi)$$
 [Eq. 5]

where  $\phi$  is the proportion of one of the phases.<sup>20</sup> Consequently, it reaches a maximum at  $\phi = 0.5$ . Thus, the equal ratio of hard block and SS phases gives the greatest scattered intensity corresponding to  $d_{ps}$ , and a shift towards domination of one of the phases produces a gradual reduction of the peak intensity. This exact behaviour of the peak intensity is observed in the scattering patterns of the dried films (Figure 4.6). It

can be clearly observed that the position of the peak in the samples containing 50% hard block migrates to lower q with increasing soft segment molecular weight (Figures 4.6 and 4.8), which is consistent with an increase in  $d_{ps}$  in the case of longer SS chains, controlling the correlation length of PU micro-phase separation.

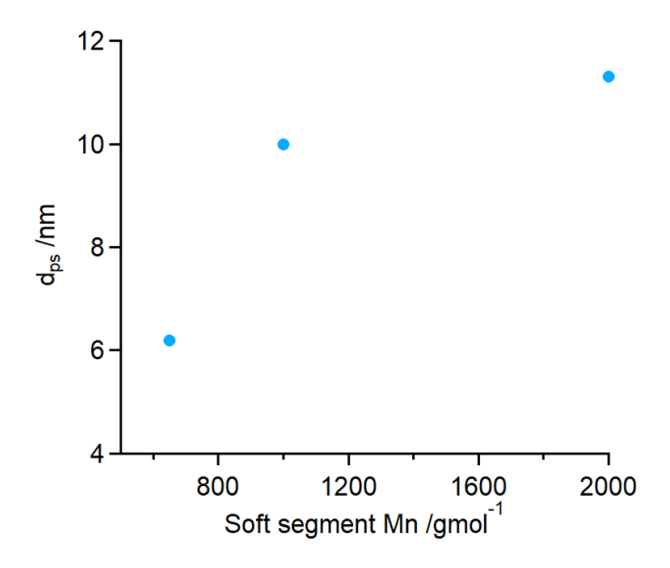


Figure 4.8: Correlation distance of PU phase separation (dps) indicated by the secondary peak or shoulder at high q in SAXS profiles in relation to the molecular weight of polyether soft segment for polyurethane films containing 50% hard block (blue circles), 60% hard block (green squares) or 70% hard block (red triangles).

Additionally, the narrowest phase separation peak is seen in the sample containing SS of  $Mn = 2000 \text{ gmol}^{-1}$  (Figure 4.6c). For a given hard block content at a fixed NCO/OH molar ratio, increasing the length of the soft segments also increases the length of the hard segments, thus the phases achieve better, more uniform separation, with greater  $d_{\rm ps}$ .

Considering all of this analysis gives an expected structure of phase separated particles, set in a matrix of hard, acidic fragments (Figure 4.4). This honeycomb-like structure is confirmed by a representative AFM image of the film of *HB60\_SS1000* (Figure 4.9). By collecting the data in phase mode, the softer, polyether-containing, uncoalesced particles are visible, within a hard-segment-rich matrix formed of the

supramolecular hydrogen bonded structure between particles, combined with the acidrich particle shells.

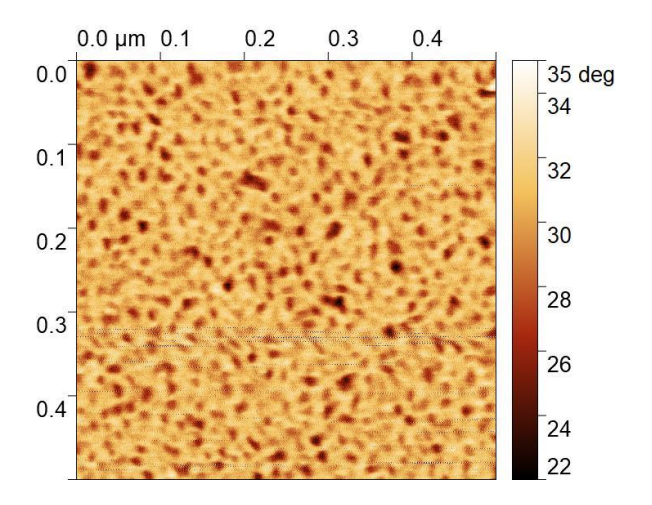


Figure 4.9: AFM image of a PU film comprising 60% hard block and soft segment of Mn = 1000 gmol<sup>-1</sup> (HB60\_SS1000) collected in phase mode. The image shows the soft, polyether containing particles (dark colours), in a continuous matrix of hard segment arising from the acidic particle interfaces and the supramolecular, hydrogen-bonded molecules.

## 4.4 Conclusions

In this chapter, morphology evolution during the drying of a PUD has been studied, along with the effect of soft segment Mn, hard block content, and acid content on the structure of final films. It has been demonstrated that time-resolved GISAXS can be used as an effective tool for structural characterisation of PUD film formation. Moreover, transmission SAXS revealed the effect of composition on the film structures, and the reversibility of the drying

It is shown that the corelation distance between neighbouring particles decreases throughout film formation. In the dry film, they are not fully coalesced, remaining as discrete objects that distort as they pack. The second minor population of acid-rich supramolecular PU structures aggregates between the particle interfaces, giving an overall honeycomb-like structure to the films. Furthermore, when a fully dried sample is exposed to water for 10 minutes, the hydrophilic acid-rich matrix swells, increasing

interparticle distance. Moreover, the reappearance of spherical particle form factor scattering features indicates that particles have returned to their dispersion morphologies, and film formation is essentially reversible.

Varying the PU soft segment *Mn*, hard block content, and acid content shows a direct relationship between the mean particle size in dispersion and the short-range order periodic structure formed by the interfaces of particles in films. In addition, characteristic PU micro-phase separation between the hard blocks and soft segments within particles is most pronounced for films formed from PUDs with soft segment/hard block mass ratios of 50/50. The correlation distance of the phase separation is shown to increase with the soft segment *Mn*.

## 4.5 References

- 1 C. E. Ashley, D. R. Dunphy, Z. Jiang, E. C. Carnes, Z. Yuan, D. N. Petsev, P. B. Atanassov, O. D. Velev, M. Sprung, J. Wang, D. S. Peabody and C. J. Brinker, *Small*, 2011, **7**, 1043–1050.
- S. M. Rupich, E. V. Shevchenko, M. I. Bodnarchuk, B. Lee and D. V. Talapin, J. Am. Chem. Soc., 2010, 132, 289–296.
- Z. Jiang, X.-M. Lin, M. Sprung, S. Narayanan and J. Wang, *Nano Lett.*, 2010,
   10, 799–803.
- T. L. Crowley, A. R. Sanderson, J. D. Morrison, M. D. Barry, A. J. Morton-Jones and A. R. Rennie, *Langmuir*, 1992, **8**, 2110–2123.
- 5 H. Honarkar, *J. Dispers. Sci. Technol.*, 2018, **39**, 507–516.
- 6 A. K. Nanda and D. A. Wicks, *Polymer (Guildf).*, 2006, **47**, 1805–1811.
- 7 M. A. Pérez-Limiñana, F. Arán-Aís, A. M. Torró-Palau, A. C. Orgilés-Barceló and J. M. Martín-Martínez, *Int. J. Adhes. Adhes.*, 2005, **25**, 507–517.
- 8 B. Jiang, J. G. Tsavalas and D. C. Sundberg, *Polymer (Guildf).*, 2018, **139**, 107–122.
- 9 A. K. Nanda, D. A. Wicks, S. A. Madbouly and J. U. Otaigbe, *J. Appl. Polym. Sci.*, 2005, **98**, 2514–2520.
- H. T. Lee, S. Y. Wu and R. J. Jeng, Colloids Surfaces A Physicochem. Eng. Asp., 2006, 276, 176–185.
- 11 L.-H. Bao, Y.-J. Lan and S.-F. Zhang, *J. Polym. Res. 2006 136*, 2006, **13**, 507–514.
- 12 N. S. Schneider, C. S. P. Sung, R. W. Matton and J. L. Illinger, *Macromolecules*, 1975, **8**, 62–67.
- 13 I. Yilgör, E. Yilgör and G. L. Wilkes, *Polymer (Guildf).*, 2015, **58**, A1–A36.
- S. M. Vaidya, S. M. Jadhav, M. J. Patil, S. U. Mestry, U. R. Mahajan and S. T. Mhaske, *Polym. Bull.* 2021, 2021, 1–37.

- 15 I. W. Hamley, J. L. Stanford, A. N. Wilkinson, M. J. Elwell and A. J. Ryan, *Polymer (Guildf).*, 2000, **41**, 2569–2576.
- 16 G. Porod, Kolloid-Zeitschrift, 1951, **124**, 83–114.
- 17 L. M. Leung and J. T. Koberstein, *J. Polym. Sci. Part A-2, Polym. Phys.*, 1985,23, 1883–1913.
- J. T. Koberstein and R. S. Stein, *J. Polym. Sci. Part A-2, Polym. Phys.*, 1983,21, 1439–1472.
- A. J. Ryan, W. R. Willkomm, T. B. Bergstrom, C. W. Macosko, J. T. Koberstein,C. C. Yu and T. P. Russell, *Macromolecules*, 1991, 24, 2883–2889.
- 20 R. J. Roe, *Methods of X-ray and neutron scattering in polymer science*, Oxford University Press, New York, 2000.

# Chapter 5 - Investigations Into PUMA Synthesis

# Methods

# 5.1 Introduction

It is thought that the structure and morphology of polyurethane modified acrylic (PUMA) particles found in commercial paint formulations could be not only a function of their composition, but also their formulation pathway. This is because they are likely to be kinetically trapped, and not equilibrium structures. Particles with the same polyurethane (PU) and/or polyacrylate (PA) composition can have very different size and size distributions, as well as qualitative differences in their internal morphology.<sup>1–3</sup>

In order to undertake a consistent and informative study of the effect of composition on PUMA morphology, it was first necessary to investigate the effect of the production processes, in particular the sequence of polymerisation steps (PU prepolymer formation and chain extension, as well as the acrylic polymerisation), the PU and acrylic monomer mixing, and the method of dispersion in water.

This chapter illustrates the steps taken to develop an appropriate laboratory method that could be used for subsequent time resolved studies of morphology development during acrylic polymerisation.

#### 5.1.1 The PU Seed Particle Method

In some instances, PUMA is made by the swelling of PU seed particles by addition of acrylic monomers, and their subsequent polymerisation (Figure 5.1).<sup>4–8</sup>

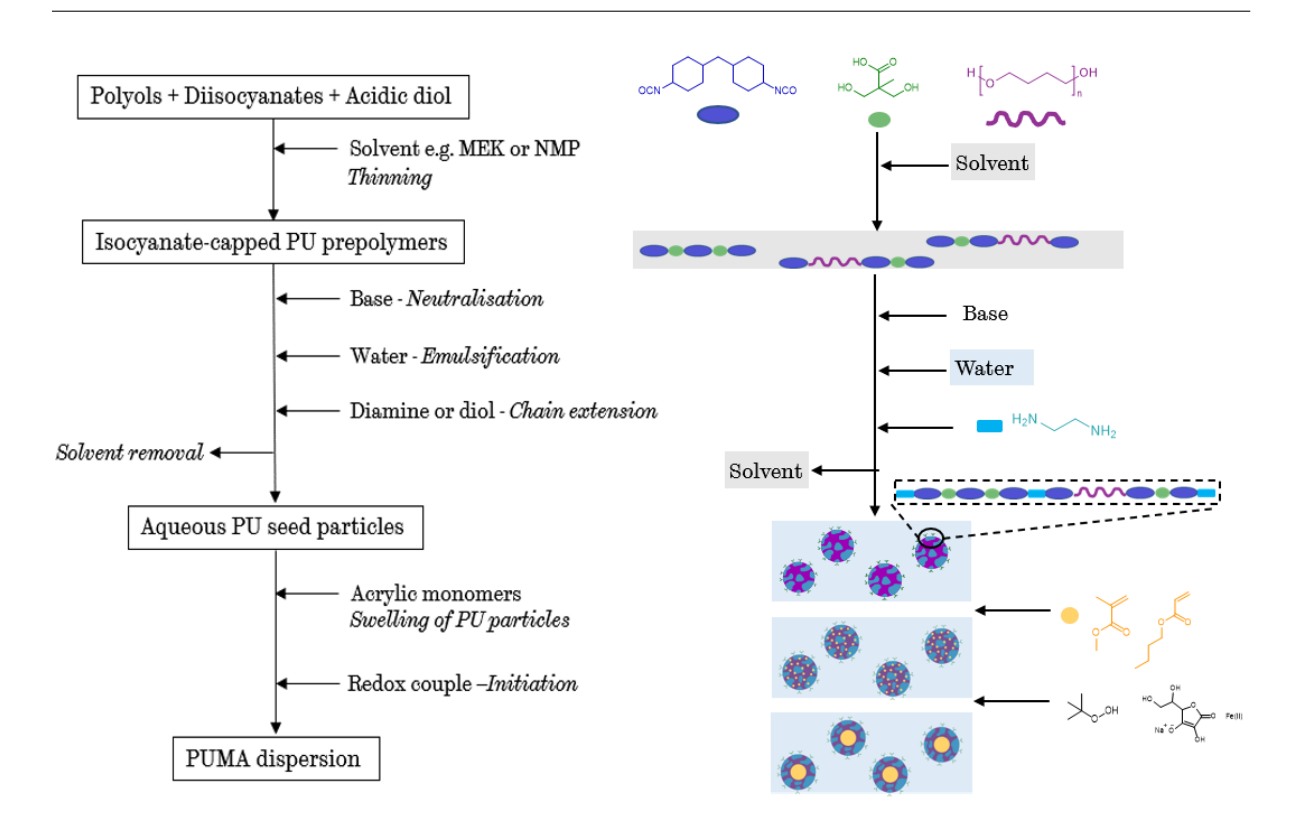


Figure 5.1: Summary of the production of PUMA from PUD seed particles

A PU dispersion (PUD) is first synthesised by the prepolymer method (Figures 5.1) with some thinning solvent such as methyl ethylketone (MEK) or N-methyl pyrrolidone (NMP). After the thinning solvent has been removed, acrylic monomers are added to the dispersion and polymerised by addition of a redox couple to give the final product.

Jiang et al. found that phase separated morphologies were not achieved during acrylic polymerisation using the PU seed particle method.<sup>20</sup> A significant increase in phase separation in the dry films, seen in differential scanning calorimetry data, indicated that thermodynamic equilibrium was only reached after annealing at temperatures ≥130 °C.

#### 5.1.2 The Monomer Solvent Method

An alternative method can be found in the literature,<sup>9,10</sup> where the need for organic solvent during the PUD production is eliminated by use of the acrylic monomers as a thinning solvent for the PU prepolymer reaction. It is assumed that, when particles form during the emulsification step, the acrylic monomer is found inside the PU

particles. The synthesis then proceeds in the same way with polymerisation of the acrylic monomers (Figure 5.2).

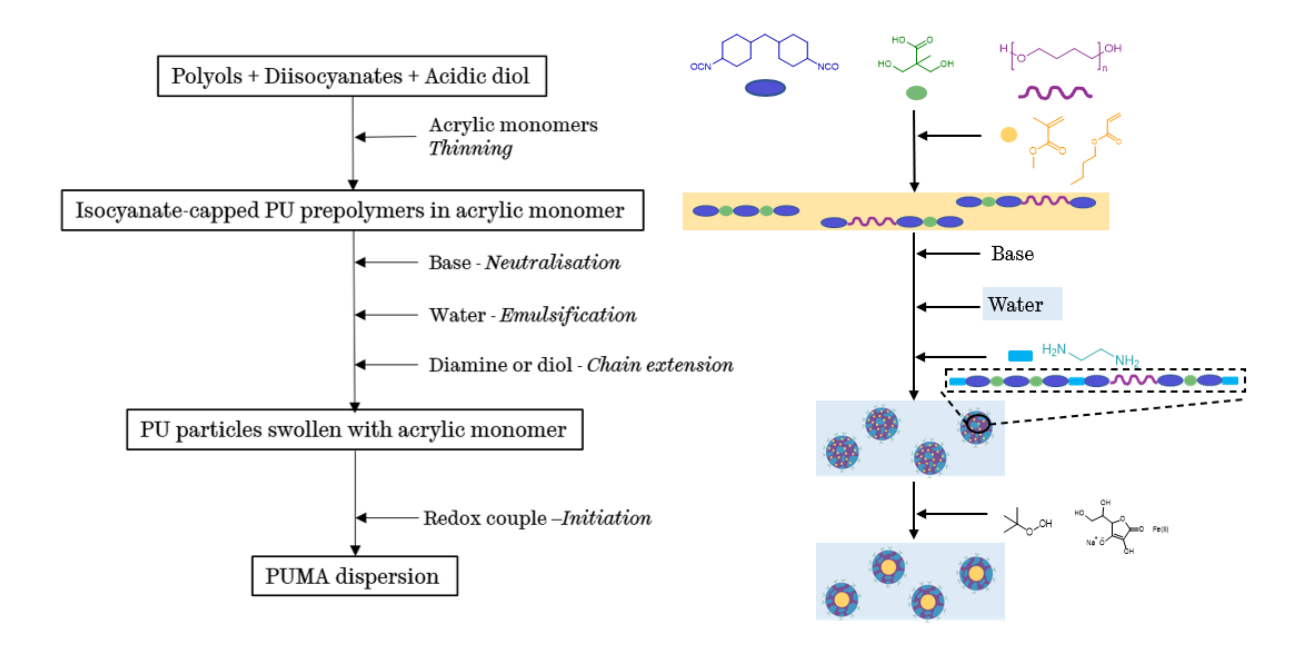


Figure 5.2: Summary of the production of PUMA by the monomer solvent method.

A similar method was used by Alvarez et al. in their comparative study of grafted and non-grafted PUMAs.<sup>11</sup> They synthesised PU prepolymers in NMP and then reacted these with grafting monomer bisphenol-A-glycidyl dimethacrylate (bis-GMA) or hydroxy ethyl methacrylate (HEMA), thinned in 25% of the acrylic monomer. Bis-GMA provided partial chain extension as well as an acrylic grafting point, whereas HEMA end-capped the PU prepolymers with an acrylic grafting point. The remaining 75% of the acrylic monomer was used to thin this mixture after neutralisation of the PU acid groups and before emulsification. Similarly, Zhu et al. used dimethylformamide to solubilise dimethylolpropionic acid (DMPA) in the production of their PU prepolymers, which were end-capped with hydroxyethyl acrylate instead of chain-extended.<sup>12</sup> However, the acrylic monomers were added to the system before dispersing.

#### 5.1.3 Other variations of PUMA particle synthesis

Some PUMA synthesis methods use a combination of the PU seed particle and monomer solvent methods to achieve target PUMA compositions. <sup>13,14</sup> For example, Wang et al. used methyl methacrylate (MMA) and butyl acrylate (BA) to adjust their PU prepolymer viscosity, which was then chain-extended before dispersing in water. <sup>14</sup> Further portions of MMA and BA were added into the aqueous dispersion to reach the target composition for their acrylic polymerisation.

Hirose et al. used organic solvent to carry out acrylic polymerisation before dispersing in water for the synthesis of their grafted PU/PA particles. NMP and ethyl acetate were used as solvents for the production of a PU prepolymer, end-capped with HEMA to give grafting points for the acrylic polymerisation. Further solvents - ethanol and isopropanol - were added to the reaction mixture during the addition and initiation of acrylic monomers. Only the ethyl acetate was removed from the final product under reduced pressure, leaving the other organic solvents in the final product.

## 5.1.4 The Emulsification Step

There are two ways to carry out the emulsification step in the production of a dispersion. For "direct emulsification", the organic phase - usually containing PU prepolymer and acrylic monomers or alternative thinning solvent - is poured into the water phase. For "indirect emulsification", the opposite process is utilised, with water poured into the organic polymer phase. This is sometimes called the phase inversion method<sup>16</sup> due to the necessary transition from a water-in-oil (w/o) to an oil-in-water (o/w) emulsion that takes place during the addition of water. Saw et al. studied the phase inversion point for a range of PUs with varying acid contents using conductivity and torque measurements.<sup>17</sup> PUs fell within three distinct regions – named *RIX*, *RIIX* and *RIIIX* in

Figure 5.3, where X is P (continuous polymer phase) or W (continuous water phase)—dependent on ionic group content. Trends between phase inversion point and ionic content can be drawn within each of these regions, with distinct differences between the regions. However, the phase inversion points (in the regions labelled CRI, CRII and CRIII) lie between approximately 25 wt% water and 38 wt% water in all cases. For the high acid-content samples, a mis-match between the phase inversion points identified by conductivity and by torque is attributed to the high degree of waterswelling of the organic phase before the phase transition.

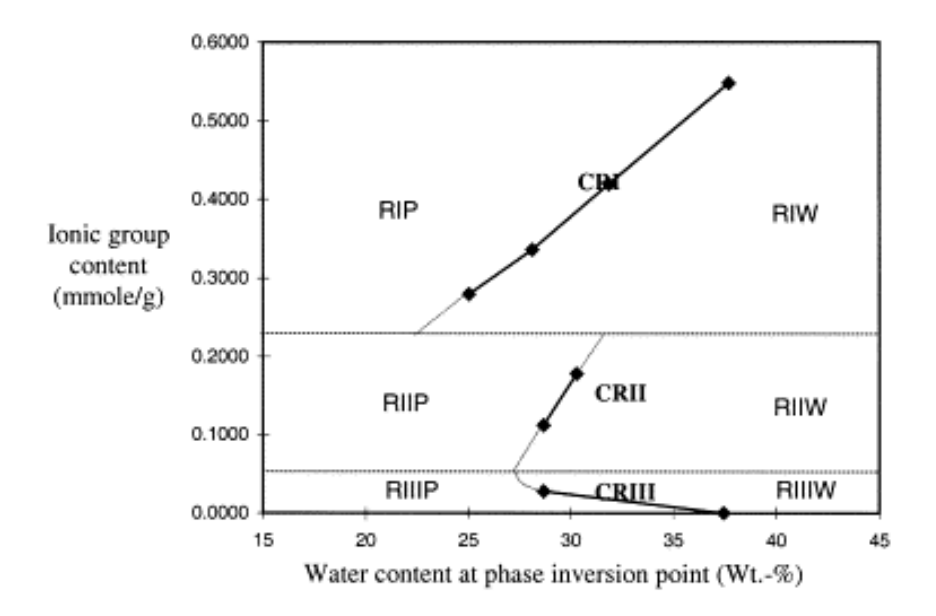


Figure 5.3: Phase inversion map for water-borne PUDs during indirect emulsification from Saw et. al.<sup>17</sup> The data falls into three regions (RI, RII and RIII) dependent on acid content, with continuous polymer phase at lower water contents (suffix P), continuous water phase at higher water contents (suffix W). All phase inversion points fall in a similar central region (CRI CRII and CRIII)

For ease of distinction in this thesis, direct and indirect emulsification are referred to as polymer-into-water (PIW) and water-into-polymer (WIP), respectively. Both PIW<sup>12,13,18</sup> and WIP<sup>11,14–17,19</sup> are employed in literature, although no comparative study of these methods can be found.

## 5.2 Samples

All the investigations in this chapter were carried out on a PUMA made with iso-butyl methacrylate (iBMA) monomer, and PU with 60 wt% hard block, and soft segment of  $Mn = 1000 \text{ gmol}^{-1}$ , at a PU/PA ratio of 50/50 (called iBMA50). Unless specified, profiles were collected at 1 wt% concentration of the final product. Where the data has been collected on precursor samples taken before acrylic polymerisation, they are labelled with the suffix: \_pre, and fully synthesised PUMAs with the suffix: \_post.

# 5.3 Results and Discussion

## 5.3.1 PU seed particle vs Monomer Solvent Methods

Products of the PU seed particle method and monomer solvent method were characterised by small angle X-ray scattering (SAXS), both as PUMAs and precursors (Figure 5.4).

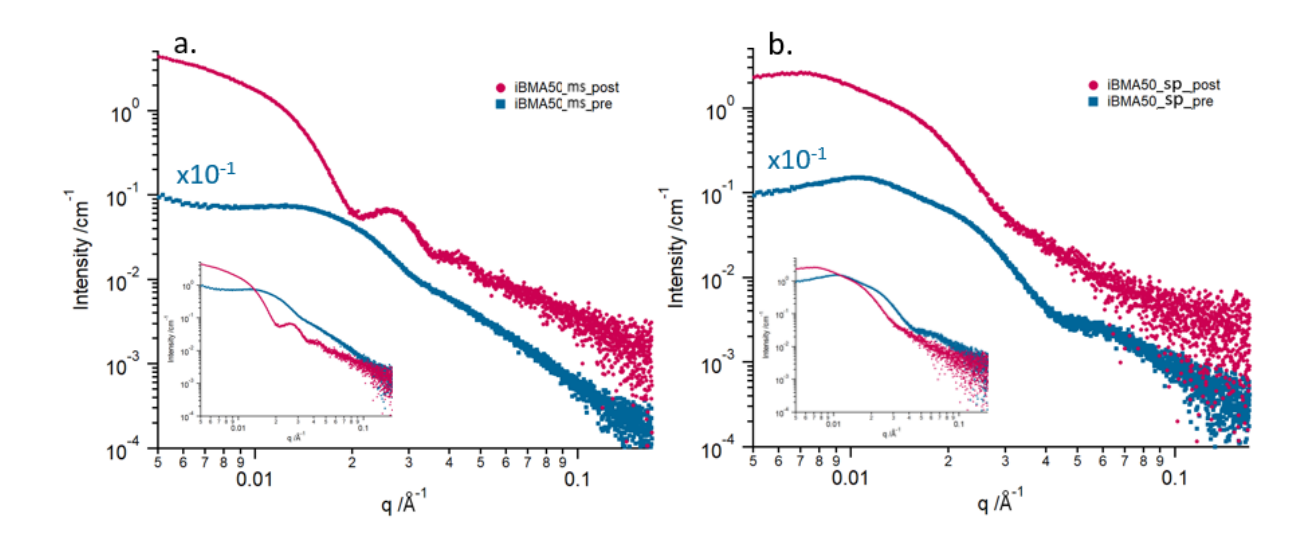


Figure 5.4:Comparison of the \_pre(blue squares) and \_post (red circles) acrylic polymerisation scattering from samples with identical composition (PU comprising 60% hard block, and Mn = 1000 gmol<sup>-1</sup> soft segment, 50:50 with iBMA), collected at 1 total wt% (PU+iBMA) in water, made by a) the monomer solvent method (ms) and b) the PU seed particle method (sp). The offset patterns - by the indicated factor - are dominant to illustrate the q-scale similarity with the absolute intensity inserts given to illustrate differences. Inserts show SAXS data plotted with no offsets for direct comparison.

The SAXS profile of the PUMA particles obtained by the monomer solvent method ( $iBMA50\_ms\_post$ ) exhibits the characteristic minima corresponding to a particle form factor (Figure 5.4a). The presence of 2 minima indicates a relatively narrow particle size distribution. It is expected that PUMA particles will be spherical, with a core-shell morphology. The position of the first minimum gives an estimate of mean particle radius of ~15.7 nm. It has to be noted that scattering intensity gradient at low q for spherical particles should be close to zero. However, the SAXS pattern shows an upturn in intensity which may indicate particle elongation and/or particle aggregation.

The SAXS profile of  $iBMA\_ms\_pre$  (Figure 5.4a) exhibits a plateau at 0.007- 0.013 Å-1, and a diffuse peak with a maximum intensity at  $q \sim 0.15$  Å-1 which could be assigned to the correlation distance between the particles. This structural order at low particle concentration is likely to arise from the interactions of charged particles, due to the acid in the PU found at the particle/water interface. Moreover, according to Porod's law, 24 the scattered intensity of a dispersion of particles with sharp interfaces should follow a gradient of -4 at high q values on a log/log scale. In this respect, the scattering intensity gradient of -2.8 at q > 0.03 Å-1 may indicate additional morphological features associated with particle internal structures, and/or the presence of a second scattering population of smaller objects, that dominates the scattering in this region. These could be features such as inhomogeneities in particles, pockets of solvent, or the supramolecular structures of PU acidic fragments discussed in Chapter 3. The significant upturn at q < 0.007 Å-1 is characteristic of a feature at much larger length scales, such as aggregates.

In contrast, the samples prepared by the PU seed particle method (*iBMA\_sp*) show different structures (Figure 5.4b). The morphology of the product (*iBMA\_sp\_post*) does not show the distinct characteristic minima of a particle form factor. It is likely that a

phase-mixed structure or the presence of nano-domains of iBMA within the PU prevents the formation of core-shell, or homogenous spherical structures. Jiang et al. attribute PU/PA phase mixing to restricted polymer diffusion that is dependent on three factors: the glass transition temperature (T<sub>g</sub>) of the acrylic, the compatibility of the acrylic with the PU, and the hard block proportion of the PU.<sup>20</sup> Since our PUs have a much greater hard block content than theirs, it is probable that the dominant factor causing phase mixing in our case is the high proportion of rigid hydrogen-bonding pseudo-cross links in the PU. These prevent penetration of the iBMA into the particles. Moreover, the lack of features in the SAXS pattern of *iBMA\_sp\_post* (Figure 5.4b) indicate a highly disperse system.

The scattering profile from *iBMA50\_sp\_pre* exhibits some similarities with *HB60\_SS1000* (Figure 5.5) - the equivalent PUD of the same polymer composition without the addition of acrylic monomer.

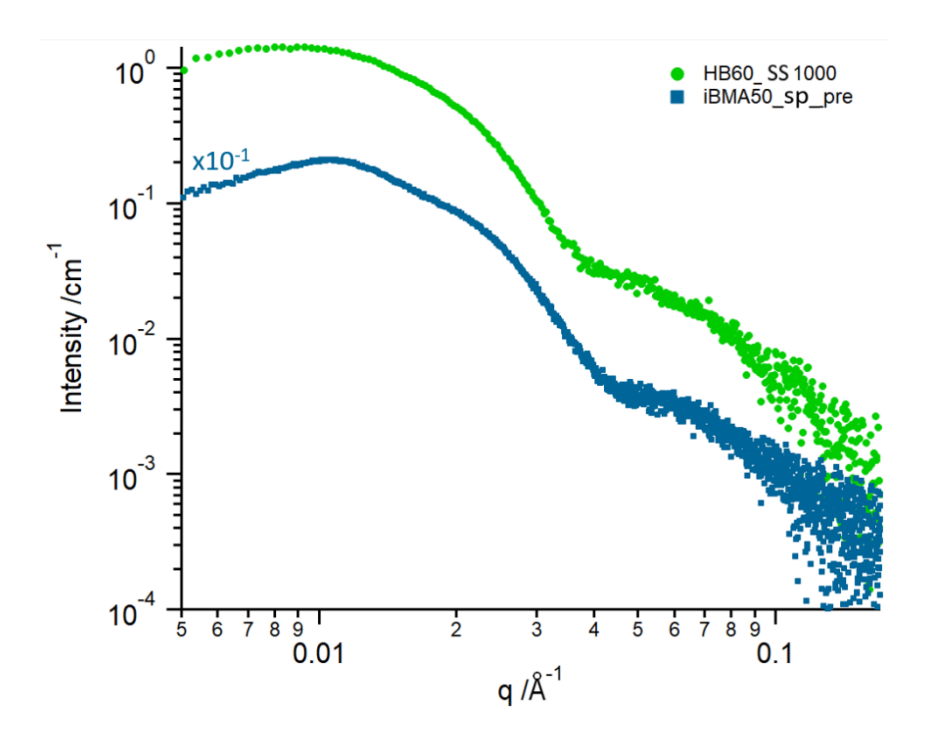


Figure 5.5: Scattering profiles collected at 1 wt% in water for the polyurethane dispersion made at 60% hard block content with Mn = 1000 gmol<sup>-1</sup> soft segment (green circles) and the same composition of PU mixed with iBMA (50:50 mass ratio) using the PU seed particle method (blue squares), offset by the indicated factor.

It is possible, therefore, that the scattering profile of *iBMA50\_sp\_pre* arises from a similar combination of two scattering populations of PU in dispersion, as was described in Chapter 3. The second population – comprising alternating diisocyanate and DMPA units – is very likely to also be present in PUMA made by the monomer solvent method as this process begins with the production of the same PUD. However, due to the increased overall hydrophobicity caused by the iBMA already present prior to emulsification, these oligomers are more likely to be found at the surface of the particles, contributing to the required charge stabilisation. With the PU seed particle method, these molecules will be present as a second population in the PUD before addition of acrylic monomers. Due to the difference in pathway, it may not be as favourable for the molecules to migrate to the spherical particles on addition of iBMA, instead remaining as hydrogen-bonded supramolecular structures. It is reasonable, therefore, to conclude that the similarities with the PUD scattering indicate the same two populations of PU particles are found in *iBMA50 sp pre*.

There is a pronounced peak at low q present in the SAXS data of  $iBMA50\_sp\_pre$  (Figure 5.5) showing that particles are ordered in solution. The position of this peak indicates a spacing of ~54 nm between two particle centres. This peak is significantly broader, and at a lower q, in the data for  $HB60\_SS1000$  (Figure 5.5), suggesting that the presences of iBMA in the solution causes greater inter-particle interaction in PUMA precursor particles. It should be expected that, due to its hydrophobicity, iBMA monomer outside of the particles forms droplets, or is phase-separated from water. The interfaces could be stabilised by the PU particles in the water phase, and as such there is a structure factor associated with the packing of PU particles on the iBMA surface. Such PU particle Pickering emulsion stabilisers have been synthesised in the literature.  $^{25,26}$ 

A comparison of estimated particle size, from the fitting of a spherical particle model (Equation 3.3 - 3.3) to the scattering data at low q, is given in Table 5.1. The standard deviation ( $\sigma$ ) is obtained by applying a Gaussian distribution to describe the range of particle radii (Equation 8.3, Appendix).

Table 5.1: Mean particle radius and standard deviation for samples made with PU with 60 wt% hard block content and soft segment of Mn = 1000 (HB60\_SS1000), and the same PU with iBMA monomer (50:50 ratio), made by the PU seed particle method pre (iBMA50\_sp\_pre) and post (iBMA50\_sp\_post) acrylic polymerisation.

Sample	Particle Radius /nm	σ +/- /nm
HB60_SS1000	11.4	1.8
iBMA50_sp_pre	10.3	1.7
iBMA50_sp_post	14.1	2.8

There is an increase in size during the polymerisation of *iBMA50\_sp\_pre*. This could be a result of successful migration of the acrylic into the PU due to the hydrophobicity increase as the acrylic chain length grows. The particle volume increases by a factor of 2.5 suggesting that some particles may have combined. Additionally, the intensity of the scattering at high *q*, most probably arising from the previously discussed second population of PU molecules, decreases in the fully reacted sample. This suggests that these highly acidic molecules, that form the second PU population, may migrate to the PU/PA particles to provide additional charge stability to counteract the increase in hydrophobicity arising from the polymerisation of iBMA.

As the final particles produced by the PU seed particle method display more complex morphologies than the monomer solvent method, all further samples were made with the monomer solvent method for the sake of consistency.

#### 5.3.2 Chain Extension Post Acrylic Polymerisation

A modified version of the monomer solvent method was utilised to investigate the effect of the sequence of chain extension and acrylic polymerisation on the final morphology. In this case, polymerisation of the acrylic monomers was carried out before chain extension of the PU prepolymers (*iBMA50\_AP-CE*). Figure 5.6 shows the SAXS profile for this sample, compared to that made by the conventional monomer solvent method with chain extension before the acrylic polymerisation (*iBMA50\_CE-AP*).

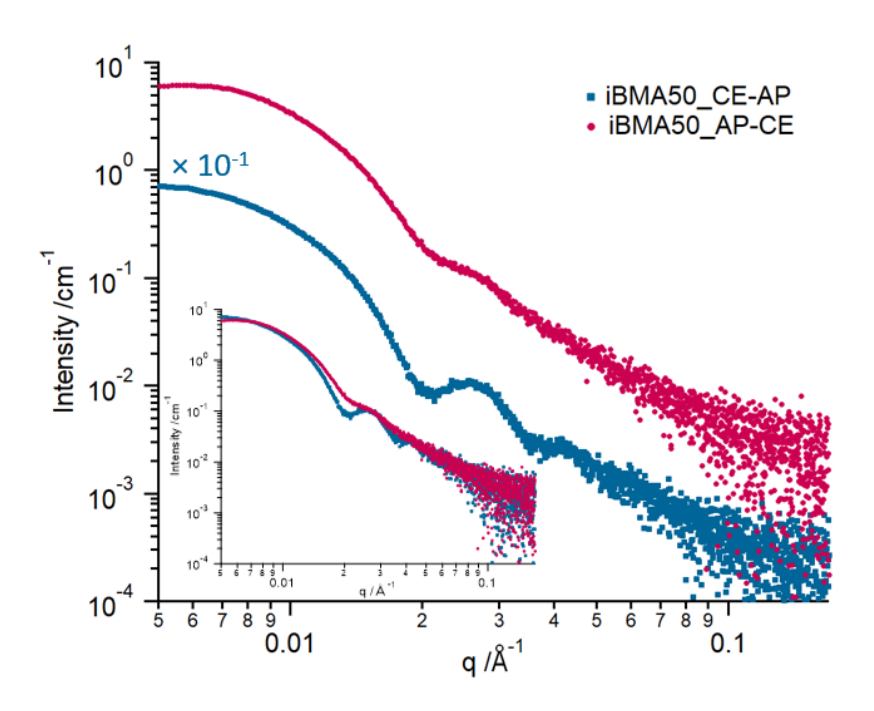


Figure 5.6: Scattering profiles collected at 1 wt% PUMA in water for a PU made at 60% hard block content with Mn = 1000 gmol<sup>-1</sup> soft segment, 50:50 by weight with PiBMA, produced by the conventional monomer solvent method (PU chain extension followed by acrylic polymerisation) (blue circles), and with the order of acrylic polymerisation and PU chain extension reversed (red squares), offset by the indicated factor. The insert compares the data on an absolute scale.

With the data displaced so all features are visible, it is clear that the scattering patterns are similar, however the minima are far less defined for *iBMA50\_AP-CE*. This suggests that carrying out acrylic polymerisation before chain extension produces particles that are less uniform in size, and possibly also in morphology. With the data on the absolute scale (Figure 5.6, inset) it is clear that, despite the differences in

particle size range, the first minimum is seen at approximately the same q, with similar  $l(q \rightarrow 0)$ , suggesting the mean size is very similar for both methods.

Due to the particle uniformity of *iBMA50\_CE-AP*, the conventional monomer solvent method with chain extension of PU before acrylic polymerisation was used for the production of further samples, in particular the time-resolved experiments.

### 5.3.3 Emulsification

When producing PUMA precursor samples in the lab, it is easier from a practical perspective to use WIP for the emulsification step. This eliminates the need to handle the viscous PU prepolymer/acrylic monomer mixture and avoids any loss from PU sticking to the sides of the container. Instead, the water can be added directly into the vessel used for the prepolymer reaction. However, when making commercial PUMAs on an industrial scale, PIW is favoured as it is the more economical option as emulsification happens in a second larger "thinning tank" containing water. If WIP were used industrially, a lot of the specialist prepolymer reaction vessel volume would be wasted, kept free for the addition of water. With PIW, the entire reaction vessel can be used to produce the prepolymer, and the mixture simply poured into a much larger, none-specialist container of water. This option is therefore far more economical on industrial scales in terms of time, reactor utilisation, and energy consumption.

# 5.3.3.1 PUMA precursor particles made from PIW and WIP

Comparative SAXS profiles of samples of PU containing acrylic monomer -  $iBMA\_ms\_pre$  - made by WIP and PIW under four different conditions (Figure 5.7) show that they are most similar at the lowest concentration of 1 wt% at room temperature (RT) (Figure 5.7a). Here, there are only slight differences in the intensity at q < 0.008 Å<sup>-1</sup> that could easily have arisen from minor discrepancies in the

preparation of samples for SAXS analysis. An upturn at  $q < 0.007 \text{ Å}^{-1}$ , appears for the samples produced using WIP, suggesting that larger structures, likely to be particle aggregates, are present in this sample.

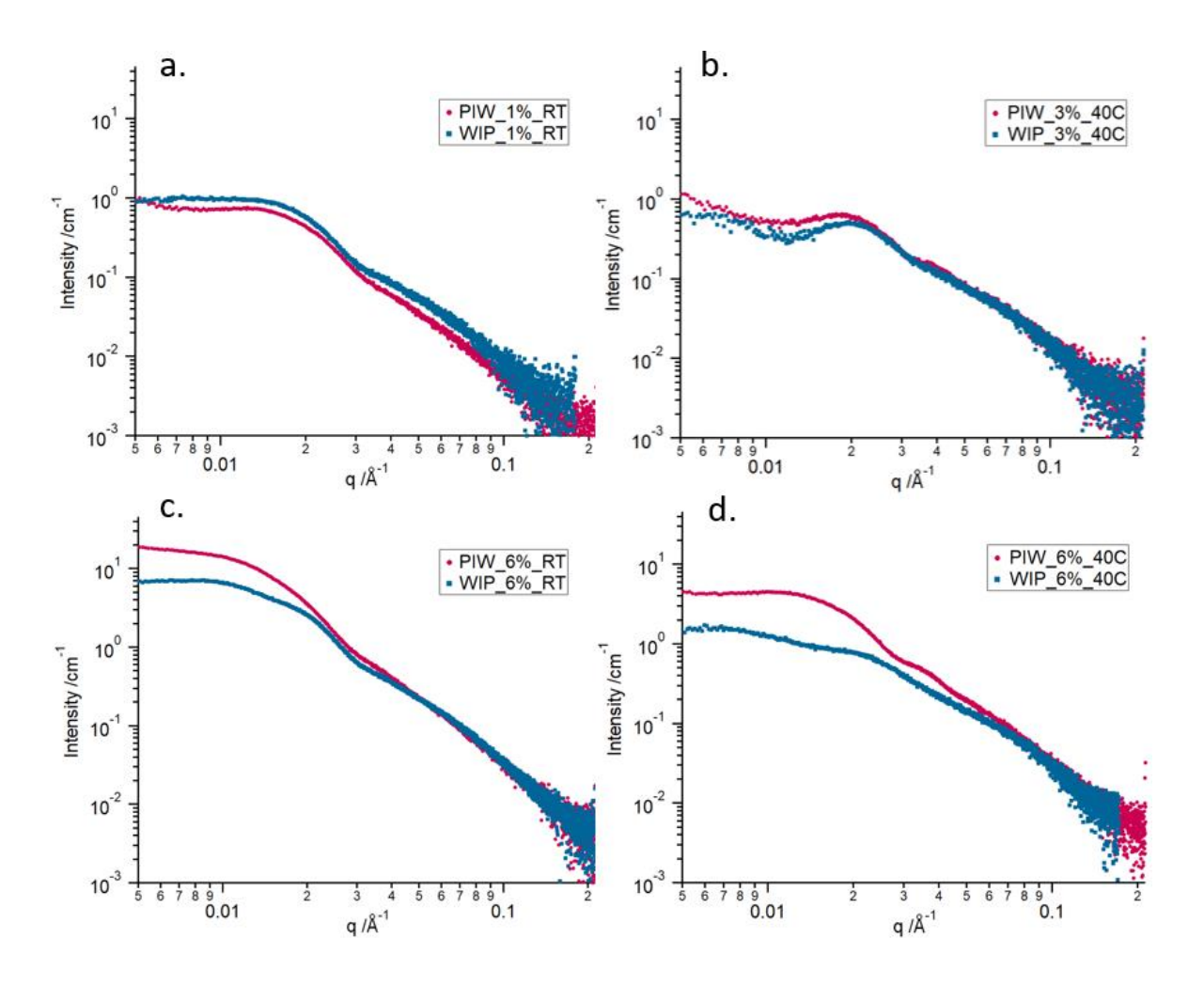


Figure 5.7: SAXS patterns comparing the products of direct emulsification (PIW) (red circles), and indirect emulsification (WIP) for samples of an aqueous dispersion of PU made at 60% hard block content with Mn = 1000 gmol<sup>-1</sup> polyether with iBMA (50:50 mass ratio) made by the monomer solvent method. The data were collected at a) 1 vol % at room temperature, b) 3 vol% at 40 °C, c) 6 vol% at room temperature, and d) 6 vol% at 40 °C, to illustrate the temperature and concentration dependence of the sample morphologies.

Increasing the temperature to 40 °C, and the sample concentrations to 3 wt% (Figure 5.7b), there is a marked change in the scattering profile for both samples compared to 1 wt% at RT (Figure 5.7a). This is true for both PIW and WIP however, such that the curves remain very similar for the two emulsification methods.

At the increased concentration of 6 wt%, comparative curves are collected at RT (Figure 5.7c) and 40 °C (Figure 5.7d). At both temperatures, there are significant differences in morphology indicated by the scattering profiles. For the data collected at room temperature, for q > 0.02 Å<sup>-1</sup> there is overlap of the intensity profiles, suggesting that similar structures in this size range (< 15 nm) possibly present in both samples. At 40 °C there are significant differences in the scattered intensity across the whole q range.

Due to the high acid contents of the PU in these samples, it is highly likely that emulsification by WIP follows the phase inversion mechanism discussed by Saw et al. for highly ionic PUs.<sup>17</sup> In their proposal, there is a large volume of water-swelling of the continuous organic phase before the phase inversion point to a continuous aqueous phase. It is likely that the phase inversion process causes occlusion of water in larger PU agglomerates, resulting in some complex structures with regions of hydrophobic iBMA, water swollen PU or semi-dissolved PU at the interfaces. The stability of these is disrupted by temperature, or the addition of water, to drive the system to complete phase inversion, and particle formation, similar to samples made by PIW.

#### 5.3.3.2 PUMA made from WIP and PIW

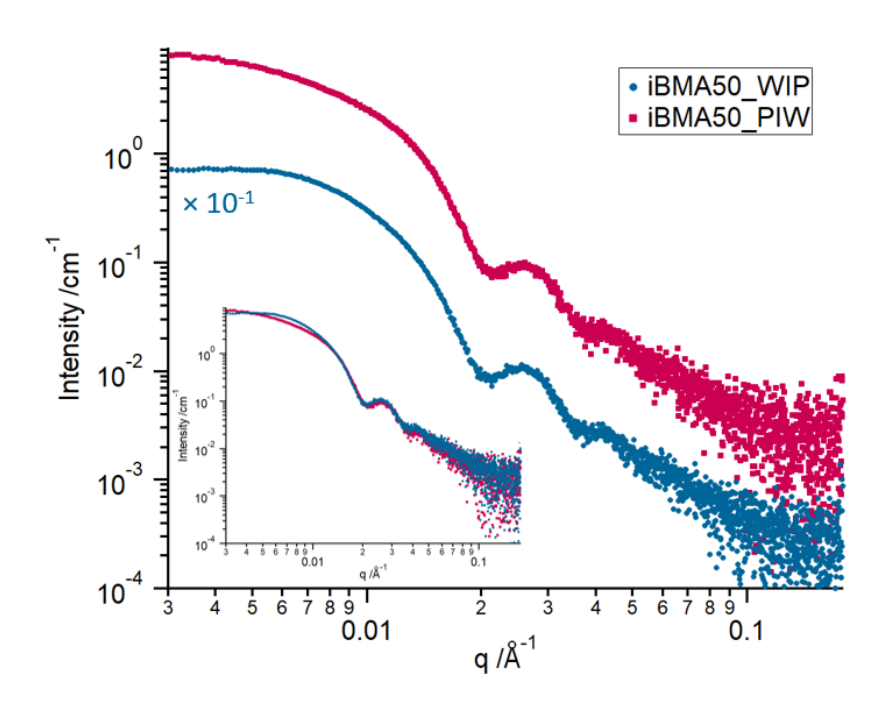


Figure 5.8: Scattering profiles collected at 1 wt% PUMA in water for a dispersion of PU made at 60% hard block content with Mn = 1000 gmol<sup>-1</sup> polyether, 50:50 with PiBMA, using the monomer solvent method. Samples are produced by indirect emulsification (WIP) (red circles) and direct emulsification (WIP) (blue circles), offset by the indicated factor. The insert compares the data on an absolute scale.

Scattering patterns of *iBMA50* samples produced by using PIW (*iBMA50\_PIW*) and WIP (*iBMA50\_WIP*) emulsification methods (Figure 5.8) show that their particle internal morphology and size are similar. There is good overlap of the patterns, including form factor minima and maxima appearing at the same *q* positions (Figure 5.8 insert). The patterns deviate at low *q*, with *iBMA50\_WIP* showing a more prominent structure peak than *iBMA50\_PIW*, indicating some particle interaction causing structural organisation of the particles in the sample.

# 5.4 Conclusions

From these investigations, it is clear that the production process is crucial in controlling the morphology of the products. It was decided that the monomer solvent method, described in Section 5.1.2, would be used in the production of samples for further studies on the effect of composition and the collection of time-resolved data. The

scattering profile collected from the sample made by this method shows the formation of well-defined particles with the least particle interactions and the lowest size polydispersity, which could facilitate SAXS analysis at the following stages of the PUMA particle synthesis.

The addition of acrylic to a PUD in the PU seed particle method resulted in complex morphologies following acrylic polymerisation. Reversal of the steps in the monomer solvent method, such that the acrylic monomers were polymerised before PU chain extension, had an adverse effect on polydispersity. For this reason, these two methods were rejected in favour of the conventional monomer solvent method.

Although the emulsification method appeared to have negligible effect on the final product, PIW emulsification was selected to produce samples for further studies. The scattering profiles of PUMA particle precursors emulsified by WIP suggested that incomplete phase inversion morphologies were kinetically trapped prior to acrylic polymerisation, with dependency on concentration and temperature. To ensure the consistency of time-resolved data during the acrylic polymerisation in future studies, PIW was deemed the favourable pathway.

### 5.5 References

- 1 H. Sardon, L. Irusta, M. J. Fernández-Berridi, J. Luna, M. Lansalot and E. Bourgeat-Lami, *J. Appl. Polym. Sci.*, 2011, **120**, 2054–2062.
- 2 A. K. Nanda and D. A. Wicks, *Polymer (Guildf).*, 2006, **47**, 1805–1811.
- 3 A. K. Nanda, D. A. Wicks, S. A. Madbouly and J. U. Otaigbe, *J. Appl. Polym. Sci.*, 2005, **98**, 2514–2520.
- 4 R. A. Brown, R. G. Coogan, D. G. Fortier, M. S. Reeve and J. D. Rega, *Prog. Org. Coatings*, 2005, **52**, 73–84.
- 5 M. Hirose, F. Kadowaki and J. Zhou, *Prog. Org. Coatings*, 1997, **31**, 157–169.
- I. Drake, G. Cardoen, A. Hughes, A. I. Nakatani, B. Landes, J. Reffner and R. Even, *Polymer (Guildf).*, 2019, **181**, Online.
- 7 V. D. Athawale and M. A. Kulkarni, *Prog. Org. Coatings*, 2009, **65**, 392–400.
- 8 S. L. Chai, M. M. Jin and H. M. Tan, *Eur. Polym. J.*, 2008, **44**, 3306–3313.
- 9 G. Martínez-Rugerio, Á. Alegría, A. Arbe, V. Daniloska and J. Colmenero, *Mater. Today Commun.*, 2016, **8**, 100–107.
- 10 E. Degrandi-Contraires, R. Udagama, E. Bourgeat-Lami, T. Mckenna, K. Ouzineb and C. Creton, *Macromolecules*, 2011, **44**, 2643–2652.
- 11 G. A. Alvarez, M. Fuensanta, V. H. Orozco, L. F. Giraldo and J. M. Martín-Martínez, *Prog. Org. Coatings*, 2018, **118**, 30–39.
- 12 X. Zhu, X. Jiang, Z. Zhang and X. Z. Kong, *Prog. Org. Coatings*, 2008, **62**, 251–257.
- 13 S. Mehravar, N. Ballard, A. Agirre, R. Tomovska and J. M. Asua, *Macromol. Mater. Eng.*, 2019, **304**, 1800532.
- Q. Wang, X. Xin, H. Liu, B. Xu, B. Li and N. Song, *Polym. Adv. Technol.*, 2022,
   33, 524–533.
- 15 M. Hirose, J. Zhou and K. Nagai, *Prog. Org. Coatings*, 2000, **38**, 27–34.
- 16 H. Tanaka, Y. Suzuki and F. Yoshino, Colloids Surfaces A Physiochemical Eng.

- Asp., 1999, **153**, 597–601.
- 17 L. K. Saw, B. W. Brooks, K. J. Carpenter and D. V. Keight, *J. Colloid Interface Sci.*, 2003, **257**, 163–172.
- 18 L. Sheng, X. Zhang, Z. Ge, Z. Liang, X. Liu, C. Chai and Y. Luo, *J. Coatings Technol. Res.*, 2018, **15**, 1283–1292.
- 19 Y. Wei, Y. Luo, B. Li and B. Li, *Colloid Polym Sci*, 2006, **284**, 1171–1178.
- 20 B. Jiang, J. G. Tsavalas and D. C. Sundberg, *Polymer (Guildf).*, 2018, **139**, 107–122.
- 21 O. O. Mykhaylyk, A. J. Ryan, N. Tzokova and N. Williams, *J. Appl. Crystallogr.*, 2007, **40**, 506–511.
- 22 C. Li, W. Chiu and T. Don, *J. Polym. Sci. Part A Polym. Chem.*, 2007, **45**, 3359–3369.
- 23 S. L. Chai and H. M. Tan, *J. Appl. Polym. Sci.*, 2008, **107**, 3499–3504.
- 24 G. Porod, Kolloid-Zeitschrift, 1951, **124**, 83–114.
- 25 C. Ma, X. Bi, T. Ngai and G. Zhang, *J. Mater. Chem. A*, 2013, **1**, 5353–5360.
- J. Wu, X. Guan, C. Wang, T. Ngai and W. Lin, *J. Colloid Interface Sci.*, 2022,610, 994–1004.

# Chapter 6 – Effect of PUMA Composition on

# **Structures in Dispersion**

### 6.1 Introduction

In general, the literature on aqueous dispersions of polyurethane modified acrylics (PUMAs) is in agreement that particles comprise a hydrophobic polyacrylic (PA) core, and a charge-stabilised polyurethane (PU) shell. 1-14 However, there is much discussion over the mixing of acrylic and PU, where pure core-shell morphologies are not achieved. Li et al used computational methods to calculate the extent of phase mixing,8 concluding that a region of mixed PU/PA at the core-shell interface was the most stable morphology with the lowest Gibbs free energy. However, in most studies, differential scanning calorimetry (DSC) is employed to quantify the degree of phase mixing. 1,10,12,14-18 According to the work of Kukanja et al., a single, broad glass transition (T<sub>a</sub>) peak was observed for their PUMA, comprising methyl methacrylate (MMA), butyl acrylate, and acrylic acid PA with a commercial polyester-based PU.15 This is indicative of thorough phase mixing due to entangled PU and PA chains. Jiang et al varied a range of factors, studying their contribution to phase mixing by quantification using DSC. They concluded that high levels of urea linkages are the predominant cause of phase mixing through strong hydrogen bonds with the acrylic carbonyl groups. When the acrylic monomer was replaced by styrene, eliminating carbonyl groups, only 28% of the total polymer mass was found in the interphase region. This is much reduced from the 62% observed for the same system using poly(methyl methacrylate) (PMMA).

However, DSC and other characterisation techniques, such as imaging methods, are limited by the need for sample to be a dry film or powder. Dry state morphologies are strongly dependent on how the polymers structure in the wet state, so information about the dispersion morphologies can be inferred. However, far more reliable information would be obtained by studying the particles in dispersion directly.

In this chapter, the effect of composition on the polymer structuring in the wet state is explored using small angle X-ray scattering (SAXS) for PUMAs and precursors prior to acrylic polymerisation. Butyl methacrylate (BMA), iso-butyl methacrylate (iBMA), MMA, and styrene are used as the PA or polystyrene (PS) phase, at four PU/PA ratios. Additionally, SAXS data collection *in situ* during the polymerisation of the acrylic or styrene monomer reveals how the morphology develops during this final synthesis step.

## 6.2 PUMA Samples

In most commercial PUMA systems, the acrylic phase is a copolymer. For this study, homopolymers were used (Table 6.1) to avoid compositional drift during synthesis, and to isolate which compositional changes were causing which effects. For simplicity, PU/PS samples are also grouped under the term "PUMA".

During the synthesis of the PUMA samples listed in Table 6.1, it was found by AkzoNobel that a higher acid content (and therefore hard block content) in the PU was required for successful emulsification of the PU prepolymer and acrylic/styrene monomer mixture, at greater monomer contents. This is due to the hydrophobicity of the monomer requiring counteraction from the charge-stabilising acid in the PU. However, high hard block content increases the viscosity of the PU prepolymer, therefore samples with low acrylic/styrene content are difficult to handle prior to

emulsification at high hard block contents. Hence, the composition of the PU changes alongside acrylic content, with hard block content increasing with acrylic/styrene proportion. The hard block refers to the portion of the PU comprising hydrogenated methylene diisocyanate, dimethylolpropionic acid, and ethylene diamine. The soft segment of the PU is poly(tetramethylene oxide) of  $Mn = 1000 \text{ gmol}^{-1}$ .

Table 6.1: Polyurethane modified acrylic/styrene samples used for the study of composition on the morphology. As the polyurethane (PU) /polyacrylic (PA) or polystyrene (PS) ratio varies, so does the polyurethane hard block (HB) content. Total concentration refers to the sum of the PU and PA or PS mass fractions for the samples as synthesised by AkzoNobel. C<sub>tot</sub> refers to the sum of the PU and PA or PS mass fractions in a sample.

Name	Monomer	PU/PA or PS	PU HB content /wt%	C <sub>tot</sub> /wt%
MMA20_HB45		80/20	45	29
ММА30_НВ50	MMA	70/30	50	30
MMA40_HB55	IVIIVIA	60/40	55	31
ММА50_НВ60		50/50	60	33
BMA20_HB45		80/20	45	25
BMA30_HB50	DNAA	70/30		30
BMA40_HB55	BMA	60/40	55	30
BMA50_HB60		50/50	60	27
iBMA20_HB45		80/20	45	25
iBMA30_HB50	iBMA	70/30	50	29
iBMA40_HB55	IDIVIA	60/40	55	29
iBMA50_HB60		50/50	60	31
STY20_HB45		80/20	45	30
STY30_HB50	Churana	70/30	50	31
STY40_HB55	Styrene	60/40	55	31
STY50_HB60		50/50	60	31

Throughout this chapter, total concentration (Ctot) refers to the sum of the PU and PA or PS mass fractions in a sample. Precursor samples were also taken prior to

acrylic/styrene polymerisation. These are indicated by the suffix \_pre. For these, C<sub>tot</sub> applies to the sum of the monomer and PU mass fractions.

### 6.3 SAXS Models

The SAXS profiles of the samples discussed in this chapter have been fitted using Model A, or Model B, described below. Both apply General Equation 3.1 for multiple scattering populations, where the number of i populations, m, is 2 and i = 1 corresponds to scattering from a major population of particles, and i = 2 corresponding to scattering from acidic PU fragments forming supramolecular structures. Due to the inherent dependency of the scattering from the particles on the PU fraction forming supramolecular structures, both models require Equations 3.4-3.12 to describe the scattering for i = 2.

#### 6.3.1 Model A – Mixed Phase Spherical Particles and Supramolecular Structures

This model was used specifically for precursor samples, which comprise a dispersion of PU, and acrylic or styrene monomer. The particles (population i = 1) in this model are considered as homogeneous spheres of mixed PU and monomer (Figure 6.1).

For a single population of spherical particles, Equation 3.1 can be rewritten as

$$I_{\text{tot}}(q) = I_1(q) = N_1 S_1(q) \int_0^\infty P_1(q, r) \Psi_1(r) dr$$
 [Eq. 6.1]

In addition, dispersity of only a single parameter such as particles radius (r) is considered.

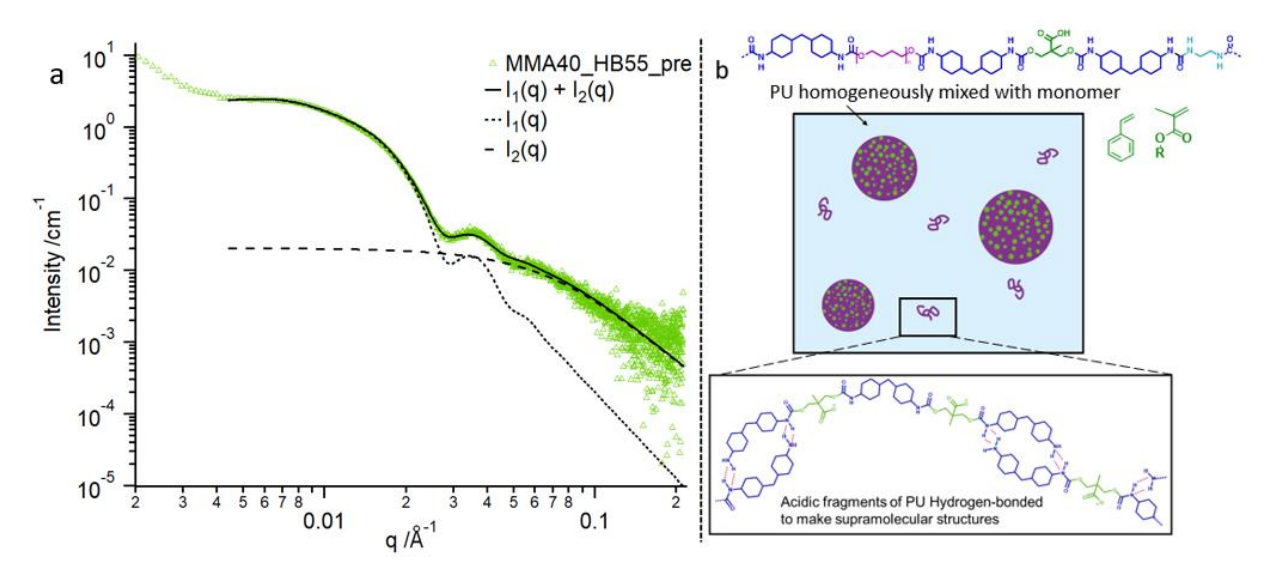


Figure 6.1: Scattering from an aqueous polyurethane dispersion containing 55% hard block, made in MMA monomer solution at a PU/MMA ratio of 60/40 (green triangles). Structural Model A is fit to the data (solid line) by summing the contributions from spherical particles ( $l_1(q)$ , dotted line) and acidic fragments ( $l_2(q)$ , dashed line). b) Schematic cartoon of the two populations.

The form factor of a spherical particle is

$$P_1(q,r) = (\Delta \xi_{\text{part}})^2 \cdot V_{\text{part}}(r)^2 \cdot \frac{9(\sin(qr) - qr\cos(qr))^2}{(qr)^6} \qquad [Eq. 6.2]$$

where  $\Delta \xi_{part}$  is the scattering length density contrast between the particles and the solvent, and  $V(r)_{part}$  is the particle volume:

$$V(r)_{\text{part}} = \frac{4}{3}\pi r^3$$
 [Eq. 6.3]

The volume fraction of PU in particles ( $\phi_{PU,part}$ ), is calculated from the total volume fraction of PU present in the sample ( $\phi_{PU,tot}$ ). This is known from the sample preparation, and the volume fraction of PU as acidic fragments ( $\phi_{PU,AF}$ ), found from fitting of the second population (i = 2) (Equations 3.4-3.12):

$$\phi_{\text{PU,part}} = \phi_{\text{PU,tot}} - \phi_{\text{PU,AF}}$$
 [Eq. 6.4]

The volume fraction of monomer inside particles ( $\phi_{\text{mon.part}}$ ) is expressed by:

$$\phi_{\text{mon,part}} = x \cdot \phi_{\text{mon,tot}}$$
 [Eq. 6.5]

where  $\phi_{\mathrm{mon,tot}}$  is the total volume fraction of acrylic or styrene in the sample, known from sample preparation, and x is the volume fraction of monomer found in the particles. This gives the total volume fraction of particles in the sample ( $\phi_{\mathrm{part}}$ ) as,

$$\phi_{\text{part}} = \phi_{\text{mon,part}} + \phi_{\text{PU,part}}$$
 [Eq. 6.6]

The scattering length density of the PU component of the particles ( $\xi_{PU,part}$ ) is calculated by considering the total scattering length density of the PU ( $\xi_{PU,tot}$ ), and the PU acidic fragments ( $\xi_{PU,AF}$ ) (Equation 6.7), both of which are calculated from Equation 2.3.

$$\xi_{\text{PU,part}} = \frac{\xi_{\text{PU,tot}} - \frac{\phi_{\text{PU,AF}}}{\phi_{\text{PU,tot}}} \cdot \xi_{\text{PU,AF}}}{1 - \frac{\phi_{\text{PU,AF}}}{\phi_{\text{PU,tot}}}} \quad [Eq. 6.7]$$

The scattering length density of the monomer ( $\xi_{mon}$ ) is also calculated from Equation 2.3. By weighted sum of  $\xi_{PU,part}$  and  $\xi_{mon}$ , the total scattering length density of the particles ( $\xi_{part}$ ) is:

$$\xi_{\text{part}} = \frac{\phi_{\text{PU,part}}}{\phi_{\text{part}}} \cdot \xi_{\text{PU,part}} + \frac{\phi_{\text{mon,part}}}{\phi_{\text{part}}} \cdot \xi_{\text{mon}} \quad [Eq. 6.8]$$

Subsequently, the square of the scattering length density contrast between the particles and water ( $\Delta \xi_{part^2}$ ) is given by:

$$\Delta \xi_{\text{part}}^2 = (\xi_{\text{part}} - \xi_{\text{water}})^2 \quad [Eq. 6.9]$$

Any structure peak, arising from inter-particle interactions (repulsion), was minimised by diluting dispersions to a low concentration ( $C_{tot} = 1 \text{ wt}\%$ ). Despite this, the influence of a structure peak is present in some profiles and was fit by a hard-sphere structure factor, S(q).<sup>19–21</sup> This choice of S(q) is discussed in Section 3.3.

Due to the reliance of both populations on the distribution of PU, it is necessary to consider the contribution of the two populations to the scattered intensities simultaneously, by fitting Equation 3.1 (Figure 6.1). The polydispersity of particle radius of the first population,  $\Psi(r)$ , is accounted for by a Gaussian Distributions (Equation 8.3, Appendix 8.6) to give mean values (R) with relative standard deviations (R). For the second population, the polydispersity of the radius of gyration (R) of the supramolecular structures,  $\Psi(R_g)$ , is assumed to be 1.

The fitting was performed by fixing the known parameters [ $\phi_{PU,tot}$ ,  $\xi_{PU,tot}$ ,  $\xi_{PU,AF}$ ,  $\xi_{mon}$ ,  $\phi_{mon,tot}$ ] whilst letting the parameters of interest float [R,  $\sigma$ , x,  $\phi_{PU,part}$ ,  $R_g$ ,  $\nu$ ]. The remaining parameters, including  $\phi_{PU,AF}$  and volume terms, are inherently calculated in the model, described in Appendix 8.10.

#### 6.3.2 Model B – Core-shell Particles and Supramolecular Structures

This model was used for both precursor and final PUMA samples. The particles (population i = 1) in this model are considered as core-shells with PA, PS or monomer in the core, and PU in the shell (Figure 6.2).

The form factor of the scattered intensity from core-shell particles  $(P_{cs}(q,r))$  is given by the equation:

$$P_{cs}(q,r) = A_{cs}^{2}(q,r)$$
 [Eq. 6.10]

where  $A_{cs}$  is the form factor amplitude. In this case,  $A_{cs}$  contains information about the scattering length density contrasts of the acrylic or styrene core ( $\xi_{co}$ ), the PU shell ( $\xi_{sh}$ ) and solvent ( $\xi_{sol}$ ).

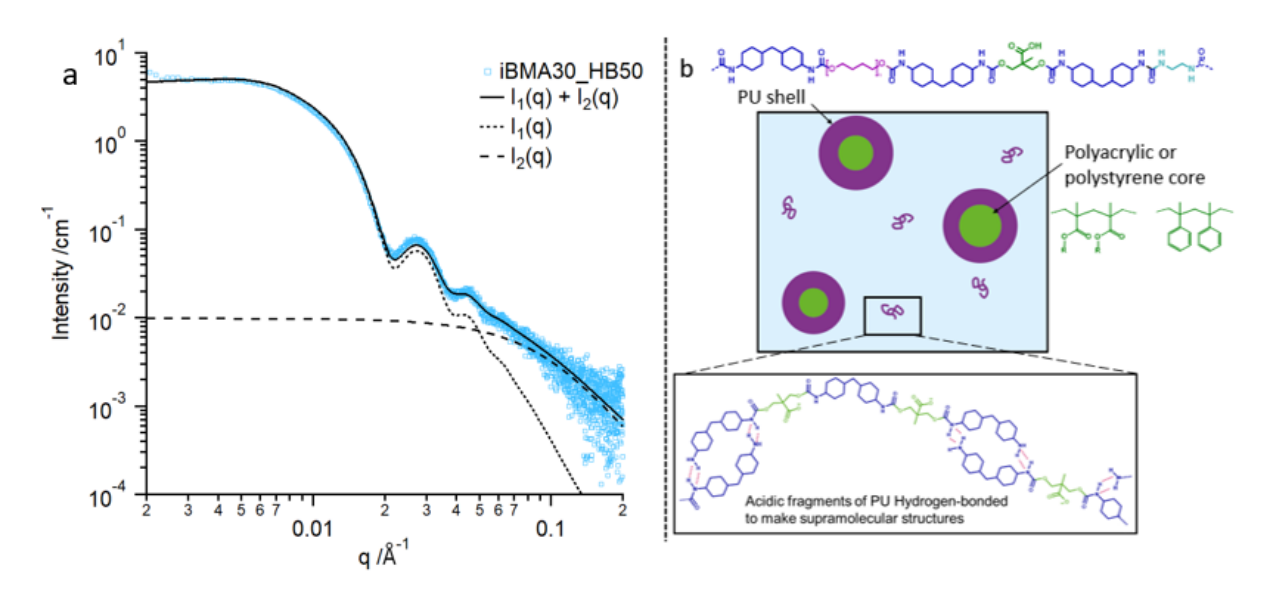


Figure 6.2: a) Scattering profile for an aqueous polyurethane modified iBMA dispersion containing 55% hard block, and a PU/iBMA ratio of 60/40 (blue squares). A structural model is fit to the data (black line) by summing the contributions from spherical particles.

This is defined as:

$$A_{cs}(q,r) = (\xi_{co} - \xi_{sol})V_{co}A_{sph}(q,r_{co}) + (\xi_{co} - \xi_{sh})V_{total}A_{sph}(q,r_{sh}) \quad [Eq. 6.11]$$

where the scattering amplitude of a spherical particle ( $A_{sph}$ ) is:

$$A_{\rm sph}(q,r) = \frac{3[\sin(qr) - qr\cos(qr)]}{(qr)^3} \quad [Eq. 6.12]$$

and the volume ( $V_{\rm sh}$ ) and thickness ( $t_{\rm sh}$ ) of the shell are:

$$V_{\rm sh} = V_{\rm total} - V_{\rm co} \quad [Eq. 6.13]$$

$$t_{\rm sh} = r_{\rm total} - r_{\rm co}$$
 [Eq. 6.14]

 $r_{co}$  and  $V_{co}$  are the radius and volume of the core, and  $r_{total}$  and  $V_{total}$  are the radius and volume of the entire core-shell particle, respectively, with

$$V_{\rm co} = \frac{4}{3}\pi r_{\rm co}^3 \quad [Eq. 6.15]$$

$$V_{\text{total}} = \frac{4}{3}\pi r_{\text{total}}^3 \quad [Eq. 6.16]$$

The volume fraction of the sample comprising PU in the shell of particles ( $\phi_{\rm sh}$ ), is calculated from  $\phi_{\rm PU,tot}$ , known from the sample preparation, and  $\phi_{\rm PU,AF}$ , found from fitting the population with i=2 (Equations 3.4-3.12).

$$\phi_{\rm sh} = \phi_{\rm PU.tot} - \phi_{\rm PU.AF}$$
 [Eq. 6.17]

The volume fraction of the sample comprising particle cores  $(\phi_{co})$  is calculated from:

$$\phi_{co} = x \cdot \phi_{AC,tot}$$
 [Eq. 6.18]

$$\phi_{AC,tot} = \phi_{mon,tot} + \phi_{PA,tot}$$
 [Eq. 6.19]

The total volume fraction of acrylic or styrene  $\phi_{AC,tot}$  is known from the sample composition. For static PUMA samples, this is equal to the total volume fraction of PA or PS( $\phi_{PA,tot}$ ), and for the initial precursor particles,  $\phi_{AC,tot} = \phi_{mon,tot}$ . This gives the total volume fraction of core-shell particles in the sample ( $\phi_{cs}$ ) as,

$$\phi_{\rm cs} = \phi_{\rm co} + \phi_{\rm sh} \quad [Eq. 6.20]$$

The scattering length density of the PU shell ( $\xi_{sh}$ ) is calculated in analogy to Equation 6.7, by substituting  $\xi_{PU,part}$  for  $\xi_{sh}$ . The scattering length densities of the acrylic or styrene core ( $\xi_{co}$ ) and the water ( $\xi_{sol}$ ) are given by Equation 2.3.

To give physically viable solutions, the fitting is constrained by the known ratio  $\frac{\phi_{\rm AC,tot}}{\phi_{\rm PU,tot}}$ , and the distribution of PU between the two scattering populations calculated from volume fraction of the second population of the acidic PU. Additionally,  $\frac{V_{\rm co}}{V_{\rm sh}} = \frac{\phi_{\rm co}}{\phi_{\rm sh}}$ . Consequently, Equation 6.16 can be combined with Equation 6.17:

$$V_{\text{total}} = V_{\text{co}} \cdot \left(1 - \frac{\phi_{\text{PU,tot}} - \phi_{\text{PU,AF}}}{\phi_{\text{co}}}\right) \quad [Eq. 6.21]$$

and

$$r_{\text{total}} = \sqrt[3]{\frac{3V_{\text{total}}}{4\pi}} \quad [Eq. 6.22]$$

This way,  $t_{\rm sh}$  is calculated from Equation 6.14 in the model, considering its inherent relationship to  $r_{\rm co}$ , according to the formulation.

Any structure peak, arising from inter-particle repulsion, was minimised by diluting dispersions to a low concentration ( $C_{tot} = 1 \text{ wt\%}$ ). Despite this, a structure factor peak present in some patterns was counted in the model fitting by a hard-sphere interaction structure factor, S(q).<sup>19–21</sup>

Due to the reliance of  $\xi_{\rm sh}$  on  $\phi_{\rm PU,AF}$ , it is necessary to consider the scattering intensity from both populations simultaneously, by fitting Equation 3.1. (Figure 6.2). The polydispersity of  $r_{\rm co}$ ,  $\Psi(r_{\rm co})$ , is accounted for by a Gaussian Distribution (Equation 8.3, Appendix 8.6) to give mean radius of the particle cores ( $R_{\rm co}$ ) with relative standard deviations  $\sigma_{\rm co}$ , and mean shell thicknesses ( $T_{\rm sh}$ ). No polydisperse parameters was considered for the second population of supramolecular structures.

The fitting was performed by fixing the known parameters [ $\phi_{PU,tot}$ ,  $\xi_{PU,tot}$ ,  $\xi_{PU,AF}$ ,  $\xi_{mon}$ ,  $\phi_{mon,tot}$ ] whilst letting the parameters of interest float [ $R_{co}$ ,  $\sigma_{co}$ , x,  $\phi_{PU,part}$ ,  $R_g$ ,  $\nu$ ]. The remaining parameters, including  $T_{sh}$ ,  $\phi_{PU,AF}$  and volume terms, are inherently calculated in the model, described in Appendix 8.10.

## 6.4 Static SAXS analysis

#### 6.4.1 Precursor Dispersions

The final step in the synthesis of the PUMA is polymerisation of the acrylic or styrene monomer. This is a rapid free-radical reaction; therefore, it was suspected that there is not much time for restructuring, and products could be kinetically trapped. As such,

the PUMA morphology would be greatly dependent on the morphology of the precursor.

SAXS profiles were collected on precursors diluted to  $C_{tot} = 1$  wt% (Figure 6.3). This concentration was chosen to minimise the interactions between neighbouring particles, which result in a strong contribution from S(q) to the scattered intensity, and therefore affect the interpretation of P(q,r), which contains the desired morphological information.

Most samples show scattering features characteristic of particles, with a population of supramolecular structures dominating the scattering at q > 0.4 Å<sup>-1</sup>. Initially, it was assumed that the particles would comprise a monomer core and a PU shell. An upturn at low q suggests bigger objects are present in all the precursors (Figure 6.3). Moreover, the dispersions appear white (Figure 6.4). This is indicative of objects commensurate with the wavelength of light, such as monomer droplets. It is possible that these are stabilised by the PU particles, or supramolecular structures, acting as Pickering emulsion stabilisers.<sup>22,23</sup>

Initially, Model B was used to fit the SAXS profiles of the precursor dispersions (Figure 6.3), allowing  $0 \le x \le 1$  to allow for the monomer distributing between particle cores, and large droplet reservoirs outside of the particles. This accounts for the presence of an upturn in the scattering profiles, and hazy solutions. It was found that this gave SAXS satisfactory fitting curves the profiles for STY30 HB50 pre, to STY40 HB55 pre. STY50 HB60 pre, BMA30 HB50 pre, BMA40 HB55 pre. BMA50\_HB60\_pre, iBMA30\_HB50\_pre, iBMA40\_HB55\_pre and iBMA50\_HB60\_pre. The parameters obtained from fitting for the samples containing core-shell particles are given in Table 6.2.

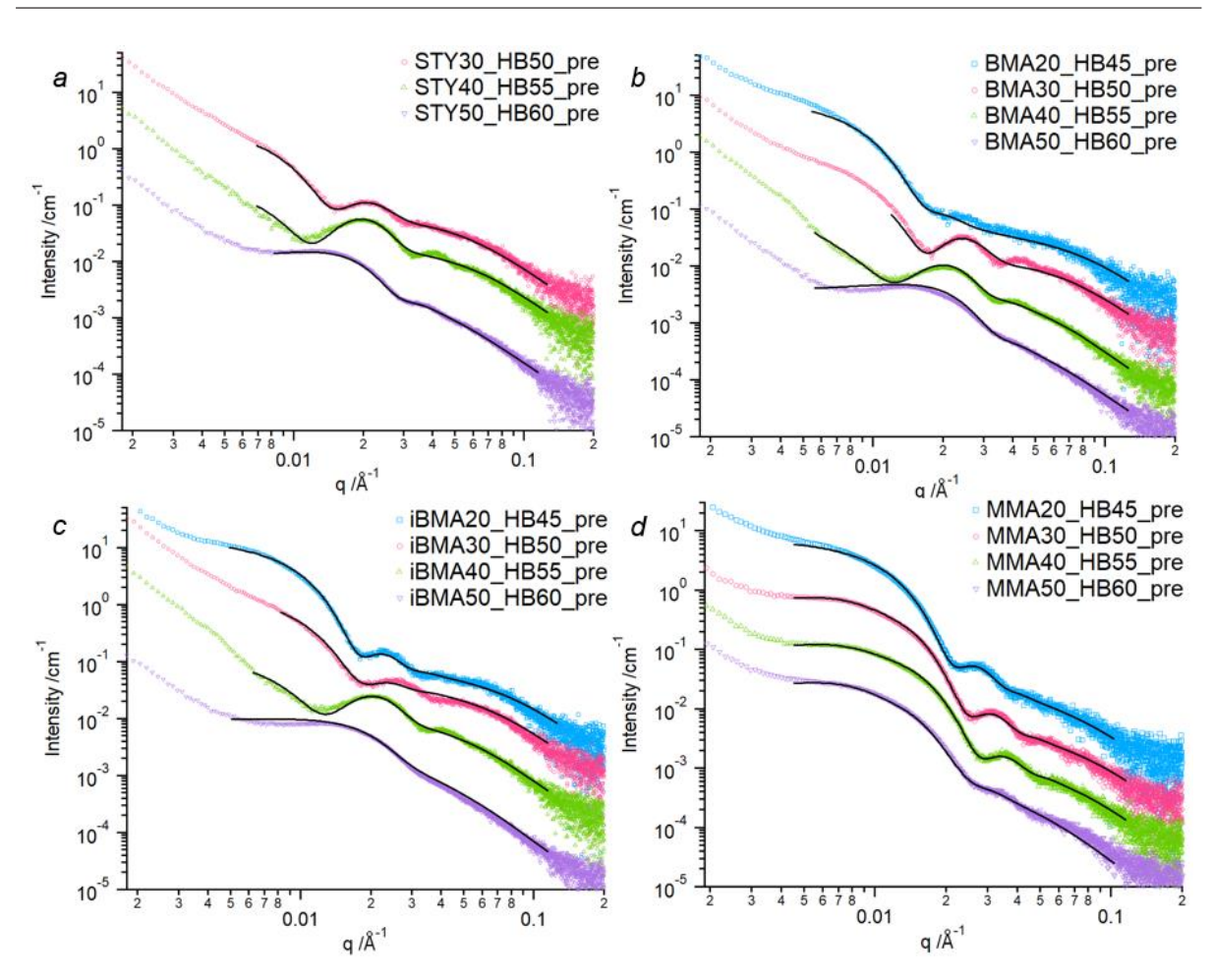


Figure 6.3: SAXS profiles for aqueous PUDs, made in acrylic or styrene monomer, collected at  $C_{tot} = 1$  wt% at PU/monomer ratios of 80/20 (blue squares), 70/30 (red circles), 60/40 (green triangles) and 50/50 (purple triangles). The monomer is a) styrene, b) butyl methacrylate, c) iso-butyl methacrylate, and d) methyl methacrylate. Fitting curves produced by structural models are shown by black lines.

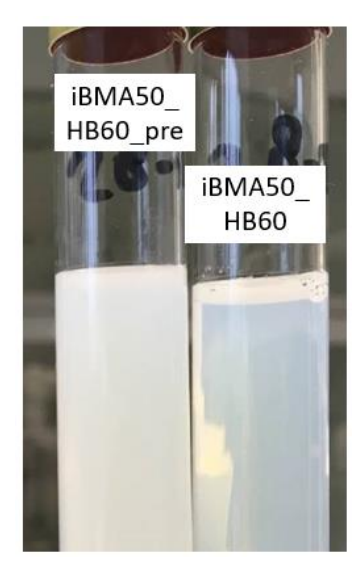


Figure 6.4: Photos of a sample comprising PU of 60% hard block as a precursor with iBMA (left) and a final PUMA with PiBMA (right) at a PU/Acrylic ratio of 50/50 by mass, at the industrial concentration  $C_{tot} = 31$  wt%.

Table 6.2: Structural parameters obtained from fitting of core-shell particles, and supramolecular structures of acidic PU fragments, to SAXS profiles of PUDs made in methacrylic or styrene monomer at  $C_{tot} = 1$  wt%. HB refers to the hard block in the PU.  $R_{co}$  is the mean radius of the monomer core with a relative standard deviation of  $\sigma_{co}$ , and x is the proportion of monomer in the sample that is found in the particles.  $T_{sh}$  is the mean PU shell thickness. The proportion of the PU in supramolecular structures is quantified by  $\phi_{PU,AF}/\phi_{PU,tot}$ .  $R_g$  gives the radius of gyration of these structures, and v is a structural parameter that indicates solubilisation of these polymer-like structures.

Sample	PU HB content	content wt% in Parameters parameter				fragment			
	/wt% PU	$R_{\rm co}$ /nm	$\sigma_{ m co}$	$T_{ m sh}$ /nm	x	$\phi_{ ext{PU,AF}}/\phi_{ ext{PU,tot}}$	$R_g$ /nm	ν	
STY30_HB50_pre	50	2.39	8.7	0.12	18.7	0.05	0.22	3.3	0.34
STY40_HB55_pre	55	2.97	12.2	0.10	13.6	0.10	0.32	3.1	0.34
STY50_HB60_pre	60	3.56	15.6	0.16	7.2	0.20	0.39	3.7	0.34
BMA30_HB50_pre	50	2.39	7.8	0.09	15.4	0.06	0.25	2.7	0.34
BMA40_HB55_pre	55	2.97	12.3	0.10	13.0	0.11	0.30	2.7	0.34
BMA50_HB60_pre	60	3.56	13.9	0.20	6.3	0.25	0.36	2.9	0.34
iBMA40_HB55_pre	55	2.97	11.8	0.10	13.5	0.10	0.28	3.9	0.34
iBMA50_HB60_pre	60	3.56	13.9	0.24	5.5	0.33	0.29	3.2	0.34

For each data set,  $R_{co}$  increases with the monomer content (Figure 6.5a), and  $T_{sh}$  decreases (Figure 6.5b), as expected considering the change in PU/monomer ratio. There is also a clear correlation between the monomer content and the volume fraction of monomer inside the particle, x (Figure 6.5c). At higher monomer contents, a larger proportion is found inside the core of particles. However, in all cases, at least two thirds of the monomer is distributed in droplets outside of the particles, with  $x \le 0.33$ .

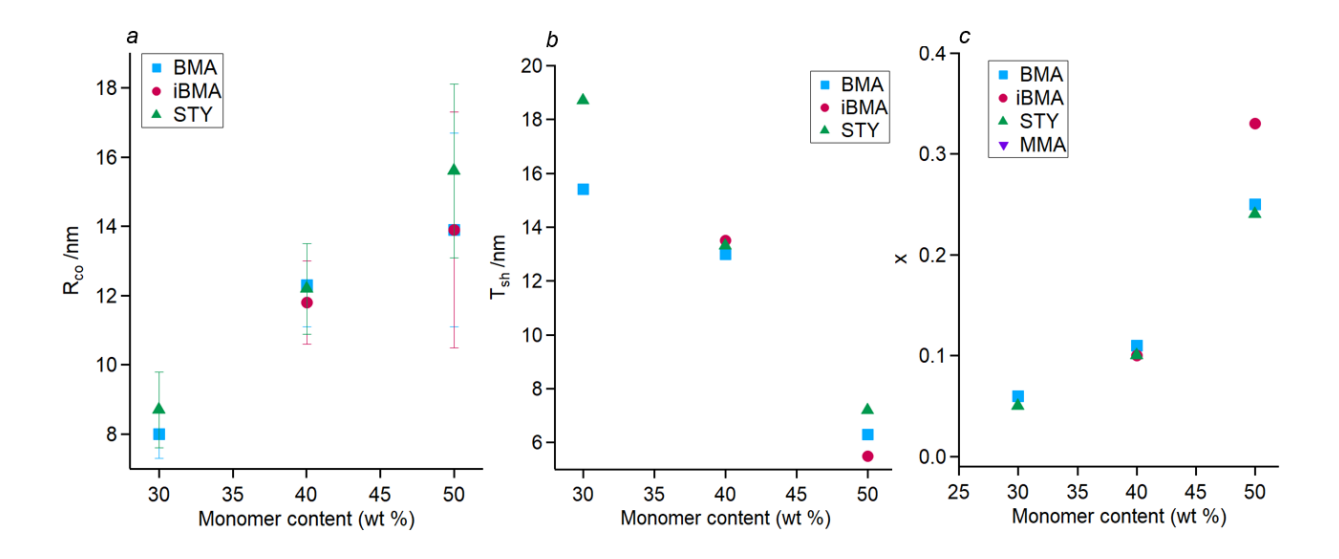


Figure 6.5: Dependency of: a) R<sub>co</sub>, its standard deviation is shown by error bars; b) T<sub>sh</sub>; and c) the volume fraction of monomer inside the particles (x), on monomer content in the PU/monomer mixture for precursor samples that contain particles with core-shell morphology. The monomer is BMA (blue squares), iBMA (red circles), or styrene (green triangles).

For the remaining precursor particles, Model B produced unsatisfactory results, where the analytical expression could not give a profile that adequately reproduced the experimental data. Thus, Model A, assuming mixing of the PU and monomer in the particles, was applied. Again, distribution of monomer between droplets and particles is accounted for by letting  $0 \le x \le 1$ . This model was found to be appropriate for all the remaining samples, suggesting that they did not have core-shell morphology. The parameters obtained from the fittings are given in Table 6.3.

The trends in total particle radius (R, or  $R_{co} + T_{sh}$ ), for both core-shell and mixed phase particles, are shown in Figure 6.6a.

Table 6.3: Structural parameters obtained from fitting of SAXS profiles for samples of PU precursor dispersions, made in methacrylic or styrene monomer, in aqueous dispersion at  $C_{tot} = 1$  wt%. HB refers to the hard block in the PU. For the spherical particles, R is the mean radius with a relative standard deviation of  $\sigma$ , and x is the proportion of the monomer in the sample that is found in the particles. The proportion of the PU that is distributed as acidic fragments in supramolecular structures is quantified by  $\phi_{PU,AF}/\phi_{PU,tot}$ .  $R_g$  gives the radius of gyration of these structures, and v is a structural parameter that indicates solubilisation of these polymer-like structures.

Sample	PU HB content	COOH wt% in		ical Par rameter		Supramolecular structures of acid fragments parameters			
	/wt%	PU	R /nm	<b>ο</b> χ		$\phi_{ ext{PU,AF}}/\phi_{ ext{PU,tot}}$	$R_g$ /nm	ν	
MMA20_HB45_pre	45	1.82	20.9	0.13	0.54	0.11	2.6	0.33	
MMA30_HB50_pre	50	2.39	18.0	0.12	0.11	0.19	2.4	0.33	
MMA40_HB55_pre	55	2.97	16.0	0.12	0	0.18	2.6	0.33	
MMA50_HB60_pre	60	3.56	17.1	0.18	0	0.11	3.7	0.32	
BMA20_HB45_pre	45	1.82	25.1	0.17	0.40	0.26	2.5	0.34	
iBMA20_HB45_pre	45	2.39	24.8	0.12	0.43	0.22	2.6	0.34	
iBMA30_HB50_pre	50	1.82	23.6	0.10	0.35	0.25	3.0	0.34	

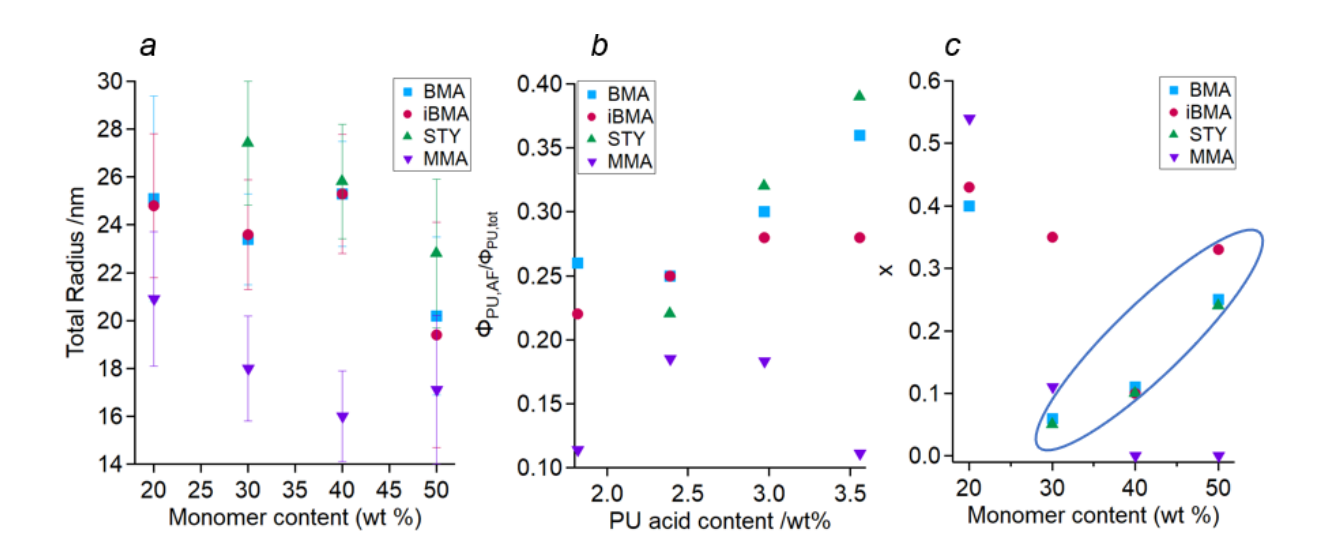


Figure 6.6: a) Total particle radius versus monomer content in the PU/monomer blend, error bars indicate its standard deviation; b) volume fraction of the total PU content distributed in the samples as acidic fragments hydrogen-bonded into supramolecular structures,  $\phi_{PU,AF}/\phi_{PU,tot}$ , versus the acid content of the PU. c) volume fraction of the monomer inside the PU particles vs monomer content in the PU/monomer blend, the blue circle encapsulates samples containing core-shell particles. Samples were made with BMA (blue squares), iBMA (red circles), styrene (green triangles), or MMA (purple triangles).

The general trend is for particle size decreasing with increasing monomer content and PU acidity, although there are exceptions with  $BMA40\_HB55\_pre$ ,  $iBMA40\_HB55\_pre$  and  $MMA50\_HB60\_pre$  (Figure 6.6a and Table 6.4). Similarly, the general trend in  $\phi_{PU,AF}/\phi_{PU,tot}$  is increasing with PU acid content (Figure 6.6b), with the exception of

*MMA50\_HB60\_pre*. Overall, this is in agreement with the findings of Chapter 3 where, for PUDs, both of these parameters are controlled by the PU acid content, which is also increasing with monomer content (Table 6.1). As it would be expected,<sup>24</sup> the overall smallest particles are obtained with the most hydrophilic monomer, MMA, and the largest with the most hydrophobic monomer, styrene (Figure 6.6a and Table 6.4).

Table 6.4: Summary of particle morphology in precursors, made with the specified monomer at the given PU/monomer mass ratio and PU hard block content. Particles comprise either phase separated PU (green) and monomer (red) in core-shell particles, phase mixed PU and monomer (striped green and red), or pure PU (green). The sizes are relative to the indicated scale bar.

PU:monomer [PU hard block content]	Styrene	ВМА	іВМА	ММА
80:20 [45%]	-		25 nm	
70:30 [50%]	•	•		
60:40 [55%]				
50:50 [60%]				

The trends in the volume fraction of monomer found inside the particles, x (Figure 6.6c) appears to be dependent on the structure of the particles. The samples that contain core-shell particles show a consistent trend, with increasing monomer content in the PU/monomer mix causing an increase in x (Figure 6.6c, blue circle, and Figure 6.5c). The samples that contain phase mixed particles show the opposite behaviour, with x decreasing with increasing monomer content in the PU/monomer mix (Figure 6.6c). In

addition, for samples  $MMA40\_HB55\_pre$  and  $MMA50\_HB60\_pre$ , x = 0. This indicates that all of the solvent is outside of the particles, in droplets or dissolved in the water phase, <sup>25</sup> and the primary population is therefore pure PU particles.

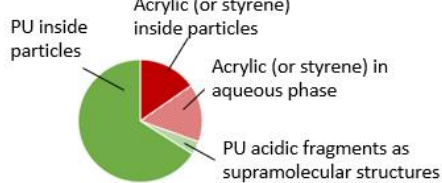
As the precursors are effectively PUDs containing the thinning solvent, they can be compared to their equivalent PUD samples discussed in Chapter 3 in order to demonstrate effect of the solvent. For example, for MMA30 HB50 pre, the equivalent PUD (with the same polymer composition but no MMA, see Table 3.1, sample HB50 SS1000) has R of 14.8 nm, compared to 18.0 nm for MMA30 HB50 pre. Moreover, a greater volume fraction of the PU component is found as supramolecular structures for MMA30\_HB50\_pre (0.185 compared to 0.114), so the precursor particles are slightly less acidic than the PUD analogue. It might be expected that, since the MMA50 HB60 pre precursor particles do not contain monomer, particles would have a similar radius to the equivalent PUD with the same composition (see Table 3.1, sample *HB60 SS1000*). However, the precursor particles have a greater *R* (17.1 nm compared to 11.2 nm) but the same volume fraction of PU as acidic fragments (0.11). Both the chemistry and amount of the solvent are known to have a significant effect on the particle size for PUDs. 18,19 MMA fulfils the role of solvent in the prepolymer reaction and during the emulsification process for these samples, hence the differences compared to the PUDs made in MEK.

The volume distribution of PU and monomer, between particles, droplets, and supramolecular structures, is summarised in Table 6.5. The monomers are ordered from most hydrophobic on the left to least hydrophobic on the right.<sup>24</sup> There is a tendency for particles to form core-shell structures with more hydrophobic monomers, and higher hard block content in the PU, with a greater proportion of monomer in the PU/monomer blend (Table 6.4). Furthermore, for the BMA and iBMA sets, there is a

significantly smaller fraction of monomer in the particles for the samples that are coreshell, compared to the samples that are phase-mixed spheres (Table 6.5).

Table 6.5: Pie charts showing the distribution by volume of PU (green) and monomer (red) between particles (bold colours), acidic fragments of PU hydrogen-bonded to supramolecular structures (pale green) and monomer outside of particle (pale red). The particle composition was measured using SAXS analysis. The SAXS data were fit by either a) homogenous spheres of mixed PU and monomer (Model A), or b) monomer cores surrounded by a PU shell (Model B).

PU:Acrylic (or styrene) by mass, [PU Hard block content]	Styrene	вма	івма	ММА
80:20 [45%]	-	а	а	а
70:30 [50%]	b	b	а	a
60:40 [55%]	b	b	b	a
50:50 [60%]	b	b	b	a



It was suspected that the PU/monomer compatibility was controlling the morphology of the particles. One way to consider compatibilities is by solubility parameters. Based on the principle of like dissolves like, a semi-empirical approach to calculating the solubility parameter of a small molecule component,  $\delta$ , is given by

$$\delta = \left(\frac{E}{V}\right)^{\frac{1}{2}} \quad [Eq. 6.23]$$

where E is the molar energy of vaporisation and V is the molar volume of the component. It follows that two components with similar solubility parameters have a low enthalpy of mixing. Since it is not possible to measure E experimentally for polymers, the solubility parameter must be estimated by summing the contributions from the various molar attraction constants, F, that are present in the repeat unit:

$$\delta = \frac{(\Sigma F)\rho}{M} \quad [Eq. 6.24]$$

where  $\rho$  is the mass density of the polymer and M is the molar mass of the repeat unit. Estimates from the literature of the solubility parameter for HMDI ( $\delta_{HB}$ ) (prevalent in PU hard block),<sup>28</sup> PTMO ( $\delta_{SS}$ ) (making up the PU soft segment),<sup>28</sup> and monomers<sup>29,30</sup> are given in Table 6.6. It is assumed that the solubility parameter of iBMA is very similar to that of BMA, due to the similarity in structure.

Table 6.6: Literature solubility parameters for PU constituents (HMDI and PTMO) compared to the monomers used in precursors.

Material	Solubility parameter δ / (calcm <sup>-3</sup> ) <sup>1/2</sup>
HMDI	11.57 <sup>28</sup>
PTMO	9.06 <sup>28</sup>
MMA	8.9 <sup>29</sup>
BMA*	8.4 <sup>29</sup>
Styrene	8.7 <sup>30</sup>

<sup>\*</sup>It is estimated that the solubility parameter of iBMA will be very similar to that of BMA

In all cases, the monomer solubility parameter is less than the PU components. Moreover,  $\delta_{SS} < \delta_{HB}$ , so as the hard block content increases, the overall solubility parameter of the PU increases, deviating further from the monomer values. This

explains the observed behaviour for precursors containing iBMA, BMA, and MMA. At low PU hard block (high soft segment) content, homogeneous spherical particles form with the monomer acting as a solvent for the PU inside the particles. As hard block content increases, the monomer becomes a less appropriate solvent for the PU, and thus separation of the two phases occurs to make core-shell particles. This happens at PU hard block contents of 55 wt% for iBMA, and 50 wt% for BMA. For the more hydrophilic MMA, all the monomer is found outside the particle at PU hard block contents of 55 wt% and 60 wt%. Due to the 1.5 wt% solubility of MMA in water, 25 some of the monomer will be dissolved in the water, however the upturn in the SAXS profile suggests there are also MMA droplets in dispersion.

This interpretation of compatibility, however, cannot be used to explain the behaviour of precursors containing styrene, where core-shell particles form at all compositions. Equations 6.23 and 6.24 are designed for non-polar components therefore fall short when polar interactions are involved. Hydrogen-bonding, as is present in PUs, is often the main source of these secondary polar interactions. As such, a better understanding of the differences in the behaviour of the monomers as PU solvents is given by their Hansen Solubility Parameters (HSPs) (Table 6.7).<sup>31–33</sup>

Table 6.7: Dispersion ( $\delta D$ ), polarity ( $\delta P$ ), and hydrogen-bonding ( $\delta H$ ) Hansen Solubility Parameters of monomers, and some PUs, found in the literature.<sup>31–33</sup> The PU compositions are not the same as those studied in this chapter, however the values provide a reasonable estimate.

	Paran	neter /M	Pa <sup>1/2</sup>
	δD	δР	δН
MMA	15.8	6.5	5.4
BMA	15.4	5.9	5.2
iBMA	15.3	5.9	5.3
Styrene	18.6	1.0	4.1
PU	16.5-19.5	3.5-5	6.5-9.5

HSPs separate the solubility parameter into the individual contributions from van der Waals dispersion forces,  $\delta D$ , dipole-dipole interactions,  $\delta P$ , and hydrogen bonding,  $\delta H$ . Although the HSP ranges for PU given in table 6.7 are not for the exact compositions used in this chapter, they do provide a reasonable estimate. MMA, BMA and iBMA HSPs are very similar to those of PU, whereas  $\delta P$  and  $\delta H$  HSPs of styrene differ greatly. This demonstrates why styrene is not a good solvent for the PU and, as a result, the water insoluble styrene inside the particles is found in the core for all samples, phase-separated from the PU shell.

SAXS profiles for precursors were collected at  $C_{tot} = 1$  wt% and  $C_{tot} = 6$  wt% to investigate the effect of concentration (Figure 6.7). This shows a concentration dependence of the particle morphologies, and distributions of monomer and PU. The iBMA data set is fit as a representative example of the differences (Figure 6.7c), and the parameters compared in Table 6.8.

Table 6.8: Parameters obtained from fitting of core-shell or homogenous spherical particles, and supramolecular structures of acidic PU fragments, to SAXS profiles for PUDs made in iBMA monomer at  $C_{tot} = 1$  wt% or  $C_{tot} = 6$  wt%. HB refers to the hard block in the PU.  $R_{co}$  is the mean radius of the monomer core with its relative standard deviation of  $\sigma_{co}$ ,  $T_{sh}$  is the mean PU shell thickness.  $R_{co}$  is the mean radius for a spherical particle with its relative standard deviation  $\sigma_{co}$ , and  $r_{co}$  is the proportion of iBMA in the sample that is found in the particles. The proportion of the PU in supramolecular structures is quantified by  $\phi_{PU,AF}/\phi_{PU,tot}$ .  $R_{g}$  gives the radius of gyration of these structures, and  $r_{co}$  is a structural parameter that indicates their solubility.

Sample	*** /0	C <sub>tot</sub>	Core-shell Particle Parameters			Spherical Particle Parameters			Supramolecular structures of acid fragments parameters				
	in PU		$R_{\rm co}/{\rm nm}$	$\sigma_{ m co}$	$T_{\rm sh}$ /nm	R /nm	$\sigma$	x	$\phi_{ ext{PU,AF}}/\phi_{ ext{PU,tot}}$	$R_g$ /nm	ν		
:DA4400 11D45 4.0	1 00	1	-	-	-	24.8	0.12	0.43	0.11	2.6	0.33		
iBMA20_HB45_pre	1.82	6	-	-	-	26.3	0.13	0.71	0.19	3.0	0.34		
:DMAAQQ LIDEQ mag	2.39	1	-	-	-	23.6	0.10	0.35	0.25	3.0	0.34		
iBMA30_HB50_pre		6	9.7	0.15	14.6	-	-	0.09	0.33	3.0	0.34		
DAAAAA LIDEE maa	2.07	1	11.8	0.10	13.5	-	-	0.10	0.28	3.9	0.34		
iBMA40_HB55_pre	2.97	2.97	2.97	6	14.0	0.15	8.7	-	-	0.26	0.32	3.4	0.34
iBMA50_HB60_pre	3.56	1	13.9	0.24	5.5	-	-	0.33	0.29	3.2	0.34		
		6	12.9	0.36	3.4	-	-	0.44	0.45	4.6	0.34		

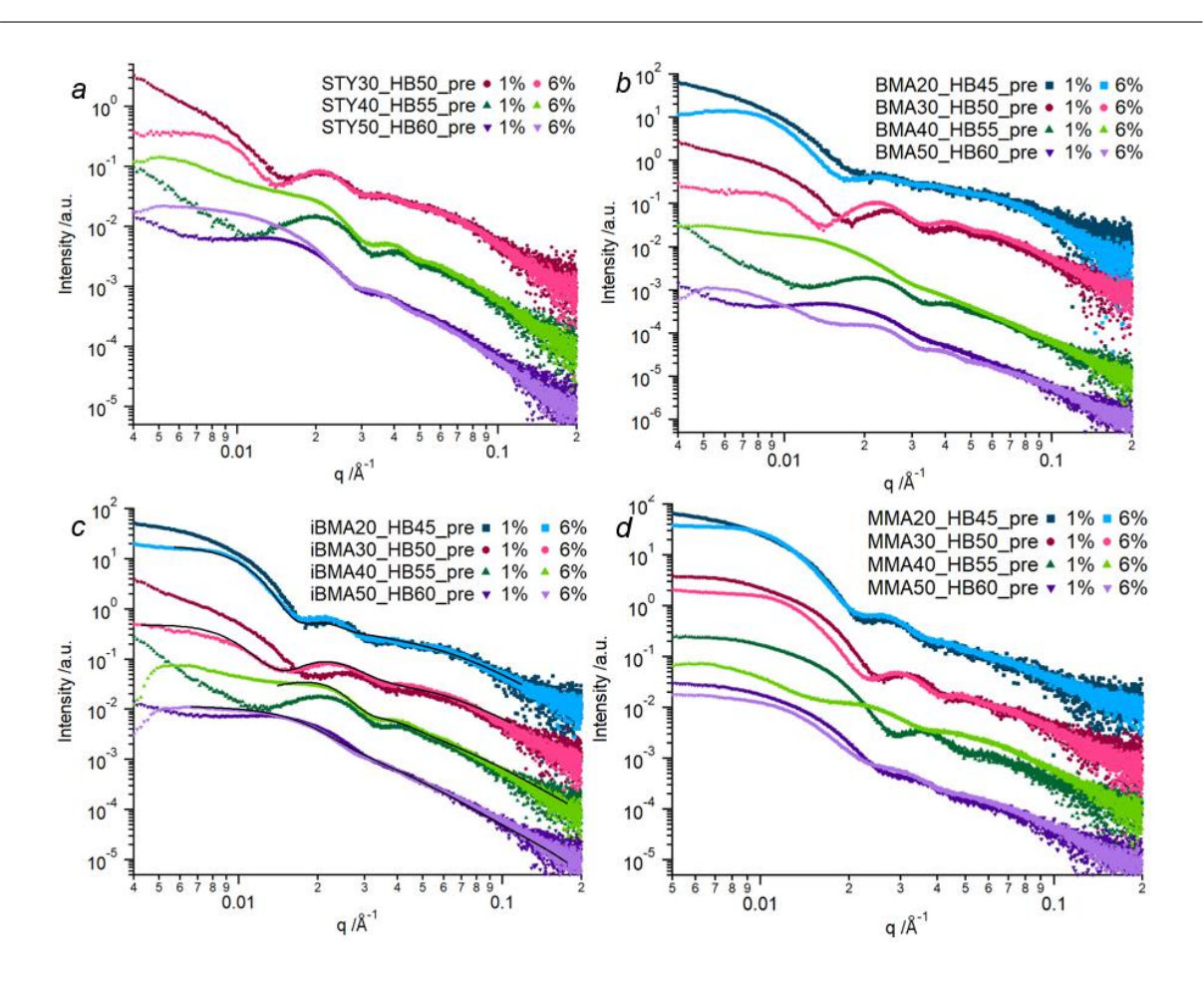


Figure 6.7: SAXS profiles for aqueous PUDs, made in acrylic or styrene monomer, collected at  $C_{tot}$  = 1 wt% (dark colours) and  $C_{tot}$  = 6 wt% (pale colours), at PU/monomer ratios of 80/20 (blue squares), 70/30 (red circles), 60/40 (green triangles) and 50/50 (purple triangles). The monomer is a) styrene, b) BMA, c) iBMA, and d) MMA. Representative structural models fitted to the iBMA set of 6 wt% are shown by black lines. Patterns are scaled by dispersion concentration and offset by an arbitrary factor to avoid overlap.

The most notable difference is for sample  $iBMA30\_HB50\_pre$ , which forms homogenous spherical particles at  $C_{tot} = 1$  wt%, and core-shell particles at  $C_{tot} = 6$  wt%. For  $iBMA20\_HB45\_pre$  and  $iBMA40\_HB55\_pre$ , the increase in R and  $R_{co}$  respectively agrees with the increase in x at higher concentrations. The opposite is true for  $iBMA30\_HB50\_pre$ , with smaller particles and lesser x at  $C_{tot} = 6$  wt %. The situation is more complex for  $iBMA50\_HB60\_pre$ , which has smaller particle cores despite the increase in x at  $C_{tot} = 6$  wt %. However, the PU shell is also thinner, so the proportion of the particle made up of acrylic has increased. In all cases, the volume fraction of PU found in supramolecular structures is greater at  $C_{tot} = 6$  wt%, suggesting that the particles at higher concentrations require less acidic units for stabilisation.

#### 6.4.2 PUMA Dispersions

The scattering profiles for the final PUMAs, listed in Table 6.1, are shown in Figure 6.8. Like the precursors, the scattering intensity appears to comprise contributions from a major population of particles, and a second minor population of supramolecular structures of acidic PU fragments. Literature predicts that the major population will comprise particles with a PA or PS core, and PU shell. 1–14 Therefore, Model B was used to fit to the SAXS profiles. This was found to be applicable to all samples containing PS, poly(isobutyl methacrylate) (PiBMA) or poly(butyl methacrylate) (PBMA), except for *STY20\_HB45*. Neither Model B for core-shell particles, nor Model A for phase mixed homogeneous spheres could be fit to the profiles of samples containing PMMA.

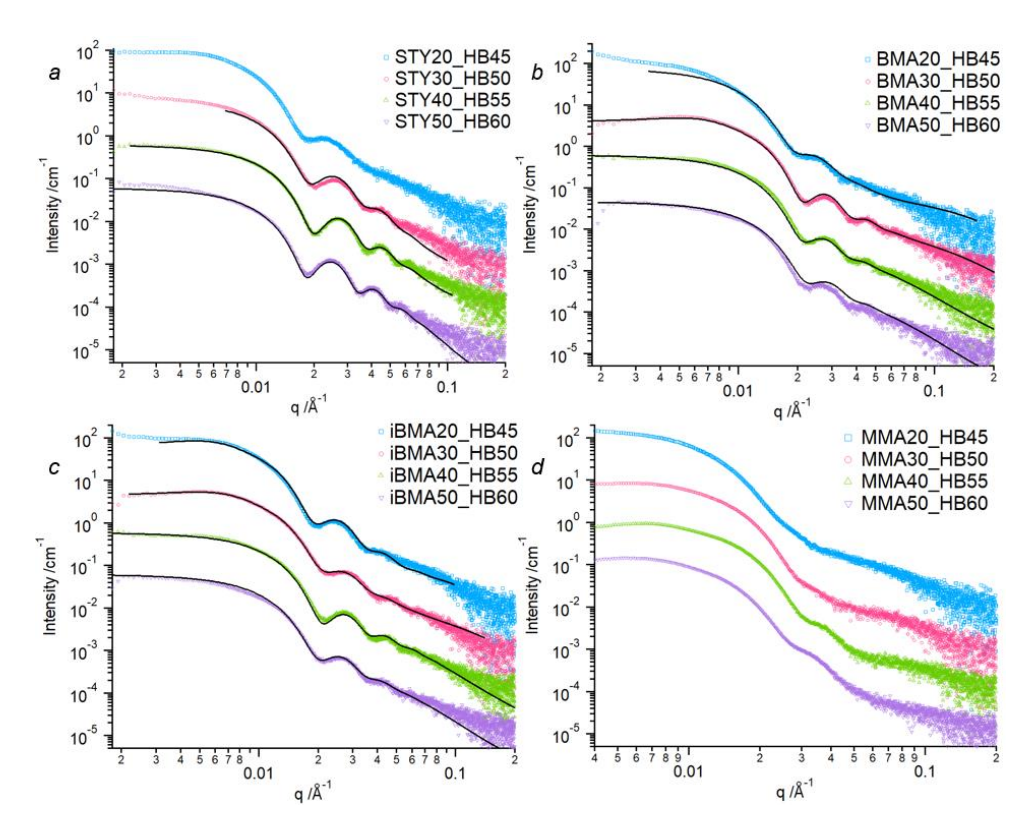


Figure 6.8: SAXS profiles for PUMAs, collected at 1 wt% in aqueous dispersions for PU/PA (or PU/PS) ratios of 80/20 (blue squares), 70/30 (red circles), 60/40 (green triangles) and 50/50 (purple triangles). The PA (or PS) portion is a) Polystyrene, b) Poly(butyl methacrylate), c) Poly(isobutyl methacrylate), and d) Poly(methyl methacrylate). Fitting curves of the structural models are shown by black lines. Patterns are offset by an arbitrary factor to avoid overlap.

The parameters obtained from the successful fittings are given in Table 6.8. For most samples, x = 1, therefore all the acrylic or styrene is inside the particles, not as droplets, suggesting that the monomer present in the sample at the beginning of the reaction was fully consumed during methacrylate (or styrene) polymerisation. This can be seen by the clarity of the solutions compared to the precursors (Figure 6.4). There are two exceptions:  $BMA20\_HB45$ , and  $STY30\_HB50$ , for which x < 1 indicating acrylic or styrene monomer is still present outside of the particles. Furthermore, given that  $STY20\_HB45$  can't be fit by either of the SAXS models, this suggests that the combination of hydrophobicity and low monomer content is causing deviations from the expected morphology of core-shell particles containing all of the acrylic phase.

Table 6.9: Structural parameters obtained from fitting of a two-population model of core-shell particles, and supramolecular structures of acidic PU fragments, to SAXS profiles for samples of PUMA in aqueous dispersion ( $C_{tot} = 1 \text{ wt}\%$ ). HB refers to the hard block in the PU.  $R_{co}$  is the mean radius of the polyacrylic (or polystyrene) core with its relative standard deviation of  $\sigma_{co}$ ,  $T_{sh}$  is the mean PU shell thickness and x is the proportion of PA (or PS) in the sample that is found in the particles. The proportion of the PU that is distributed as acidic fragments in supramolecular structures is quantified by  $\Phi_{PU,AF}/\Phi_{PU,tot}$ .  $R_g$  gives the radius of gyration of these structures, and v is a structural parameter that indicates solubilisation of these polymer-like structures.

Sample	PU HB content	COOH wt% in	Co		ell Partic meters	le	Supramolecular structures of acid fragments parameters				
•	/wt%	PU	$R_{\rm co}$ /nm	$\sigma_{co}$	$T_{sh}$ /nm	X	$\phi_{ ext{PU,AF}}/\phi_{ ext{PU,tot}}$	$R_g$ /nm	ν		
STY30_HB50	50	2.39	12.3	0.10	9.5	0.50	0.05	2.5	0.33		
STY40_HB55	55	2.97	14.2	0.10	5.9	1	0.06	2.0	0.33		
STY50_HB60	60	3.56	16.4	0.11	5.1	1	0.02	2.1	0.33		
BMA20_HB45	45	1.82	11.0	0.10	11.8	0.40	0.06	2.6	0.33		
BMA30_HB50	50	2.39	14.1	0.10	6.9	1	0.25	1.6	0.33		
BMA40_HB55	55	2.97	14.4	0.12	5.7	1	0.14	1.8	0.33		
BMA50_HB60	60	3.56	17.9	0.11	4.2	1	0.29	1.7	0.33		
iBMA20_HB45	45	1.82	13.6	0.10	11.2	1	0.08	3.0	0.33		
iBMA30_HB50	50	2.39	14.2	0.12	7.4	1	0.23	1.6	0.33		
iBMA40_HB55	55	2.97	15.2	0.10	5.5	1	0.20	2.0	0.33		
iBMA50_HB60	60	3.56	16.6	0.12	4.5	1	0.18	2.4	0.33		

For each data set,  $R_{co}$  increases with increasing PA or PS content (Figure 6.9a), and  $T_{sh}$  decreases (Figure 6.9b), as expected. There is consistency in the trends of total

particle size (Figure 6.9c) for each data set, showing reduction from 80/20 to 60/40 PU/PA or PU/PS. This is in keeping with the findings of Chapter 3, and literature, 19,27,34–40 on the effect of acid content on the size of amphiphilic particles. When the PA or PS content increases again to 50/50 PU/PA or PS, the total particle sizes increase. Chapter 3, and the PSC model, 19,34 demonstrate that a hydrophobicity increase results in bigger particles, with a greater required surface area coverage of acid groups for stable spheres. xx

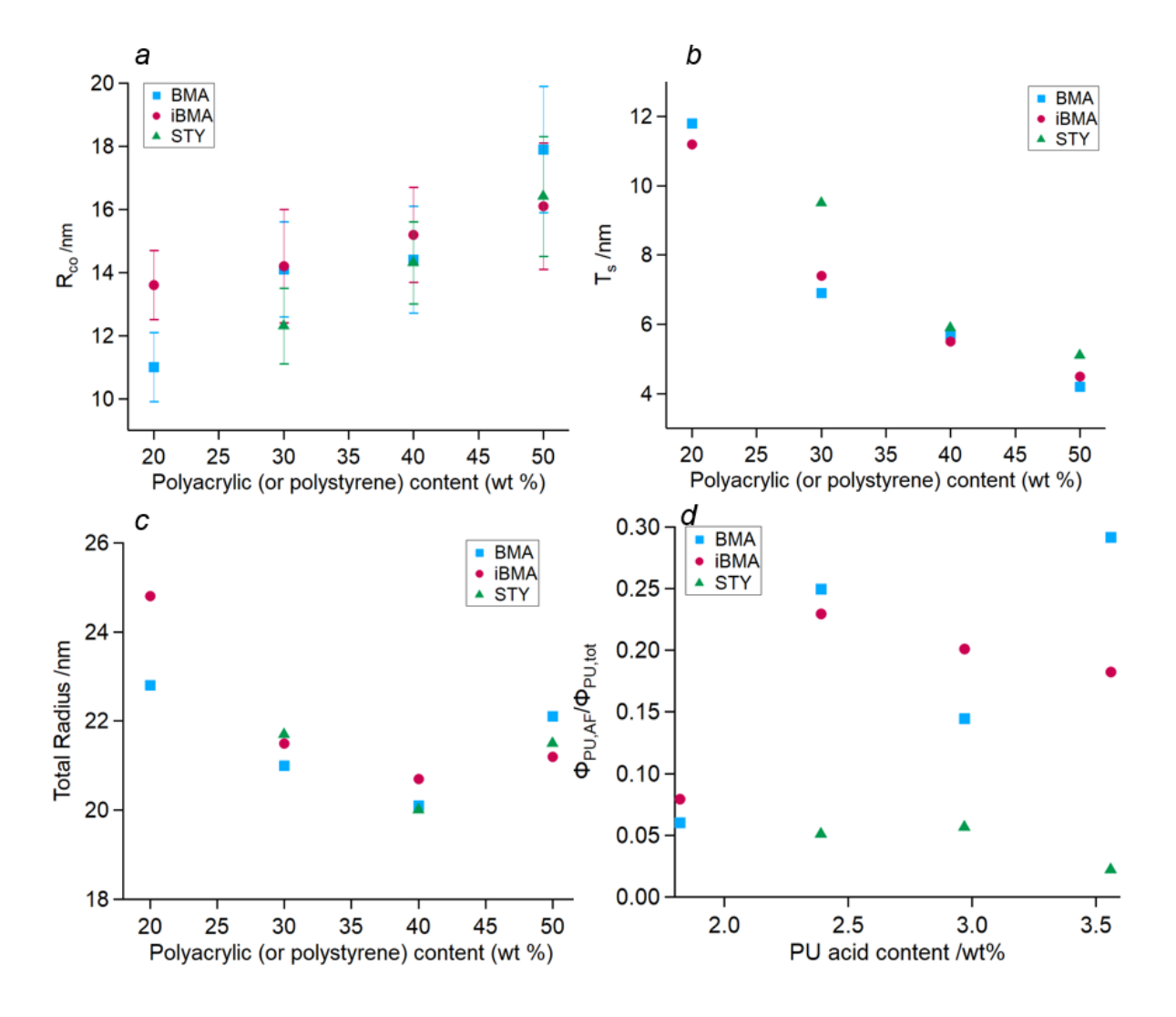
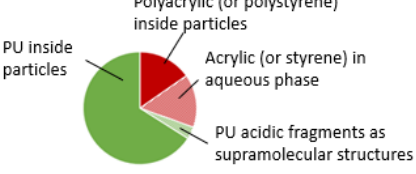


Figure 6.9: a)  $R_{co}$  and its standard deviation shown by error bars, b)  $T_{sh}$ , and c) total particle size, versus PA or PS content in the PU/PA (or PU/PS) blend, and d) volume fraction of the total PU content distributed as acidic fragments hydrogen-bonded to supramolecular structures,  $\Phi_{PU,AF}/\Phi_{PU,tot}$ , vs the acid content of the PU. Samples were made with BMA (blue squares), iBMA (red circles), or styrene (green triangles).

It is due to these counteracting effects on particle size that it is difficult to extract meaningful trends from the relationship between PU acid content and the volume fraction of PU distributed as supramolecular structures of acidic fragments ( $\phi_{\text{PU,AF}}/\phi_{\text{PU,tot}}$ ) (Figure 6.9d and Table 6.10). As total particle hydrophobicity increases, acidic PU fragments are more likely to be found at the surface of particles, contributing to charge stabilisation. However, simultaneously, the acid content of the PU is increasing. In Chapter 3, it was shown that increasing PU acid content increases the volume fraction of these supramolecular structures (Figure 3.10).

Table 6.10: Pie charts showing the volume distribution of PU (green) and PA or PS (red) between core-shell particles (bold colours), acidic fragments of PU hydrogen-bonded to supramolecular structures (pale green) and PA or PS outside of particle (pale red).

Polystyrene	P(BMA)	P(iBMA)	P(MMA)
Could not be fit as core-shell with supramolecular structures			
			Could not be fit as core-shell
			with supramolecular structures
	as core-shell with supramolecular	Could not be fit as core-shell with supramolecular structures	Could not be fit as core-shell with supramolecular structures



It can be seen, however, that  $\phi_{PU,AF}/\phi_{PU,tot}$  is lowest for the systems containing PS, which is the most hydrophobic monomer.<sup>24</sup> This suggests that more acidic fragments

are absorbed and contributing to the colloidal stability of the core-shell particles, rather than found as supramolecular structures.

Since they cannot be fit with either SAXS model, PUMAs containing PMMA likely have more complex, or less ordered, morphologies. The scattering from the population of acidic fragments of PU forming supramolecular structures, that dominates at q > 0.04 Å-1 in the other PUMAs, is not as apparent in the profiles of PUMAs containing PMMA (Figure 6.8d). This is especially true of  $MMA40\_HB55$  and  $MMA50\_HB60$ , suggesting that the acidic fragments are in the particles, rather than in supramolecular structures. Additionally, the slight downturn at q < 0.006 Å-1 is evidence of a structural peak. These are more apparent in the samples containing PMMA than in any of the other PUMAs, indicating more significant interactions between neighbouring particles. This could be due to the reduced population of acidic fragments screening their interactions. The precursors of the MMA samples have little or no monomer in the particles (Table 6.3), therefore during polymerisation, there must be penetration of growing polymer chains into the PU particles.

# 6.5 *In situ* Polymerisation of Precursors to PUMAs

#### 6.5.1 Selection of Reaction Conditions

In order to better understand how and why the differences in morphology arise with composition, SAXS profiles were collected *in situ* during the polymerisation of precursors to make PUMAs. This could not be done at the high concentrations used for polymerisation industrially (Table 6.1) due to two factors: the viscosity of the high concentration samples would not be suitable for the experimental set up (described in Section 2.2.5.2); the SAXS profiles would be dominated by S(q) with strong particle interactions at short-range making meaningful analysis of P(q) unreliable. The

concentration used for the analysis of static SAXS profiles,  $C_{tot} = 1$  wt%, would also be inappropriate for *in situ* data collection as dilution to lower concentration reduces particle uniformity, increasing polydispersity (Figure 2.17). It is thought that this is due to the reduction in the reaction exotherm caused by dilution (Table 2.4). The exotherm of polymerisation occurring inside one particle causes a local increase in temperature, initiating neighbouring particles, setting off a rapid chain reaction of polymerisation inside particles (Figure 6.10). At lower concentrations, this is slower as neighbouring particles are more spaced, so any monomer feed process from droplets to particles will be non-uniform. Particles initiated at an early stage will consume any monomer reservoirs, resulting in more PA or PS in the particle than those initiated at a later stage (Figure 6.10).  $C_{tot} = 6$  wt% was chosen for *in situ* SAXS data collection, as the best compromise of these factors.

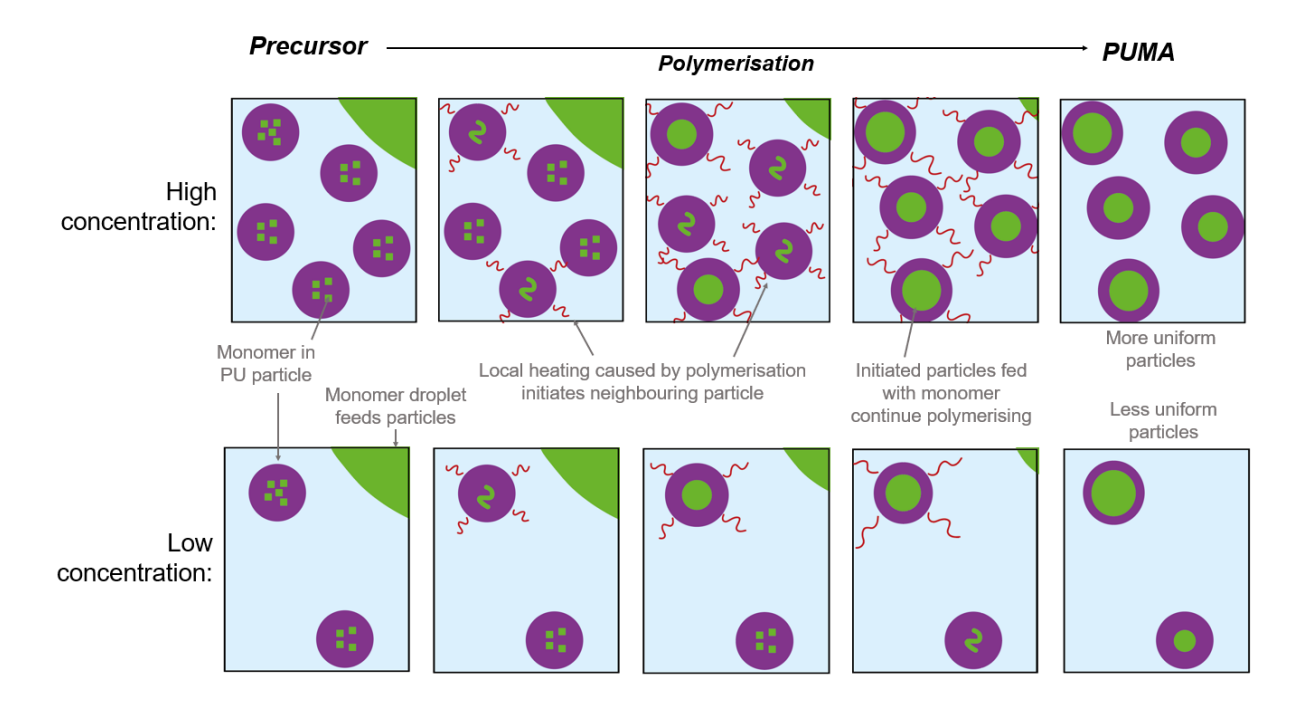


Figure 6.10: Schematic of polymerisation of the acrylic or styrene monomer in PU particles at high and low concentrations, showing the effect on polydispersity of the particle size. The PU is shown in purple, and the acrylic in green, with only a segment of the acrylic droplet shown in the top right-hand corner. The second population of PU is omitted for clarity, and exotherms are represented by red lines.

The final product of each *in situ* polymerisation is shown in Figure 6.11, compared to the equivalent PUMAs polymerised at industrial concentrations and diluted to  $C_{tot} = 1$  wt%. Unlike the precursor samples, the polymerisation of the monomer is expected to "lock in" the particle morphologies formed at the polymerisation concentration. Therefore, the features of P(q) for the samples diluted to  $C_{tot} = 1$  wt% should be unchanged by dilution and it is assumed that any differences in P(q) arise from the polymerisation concentration.

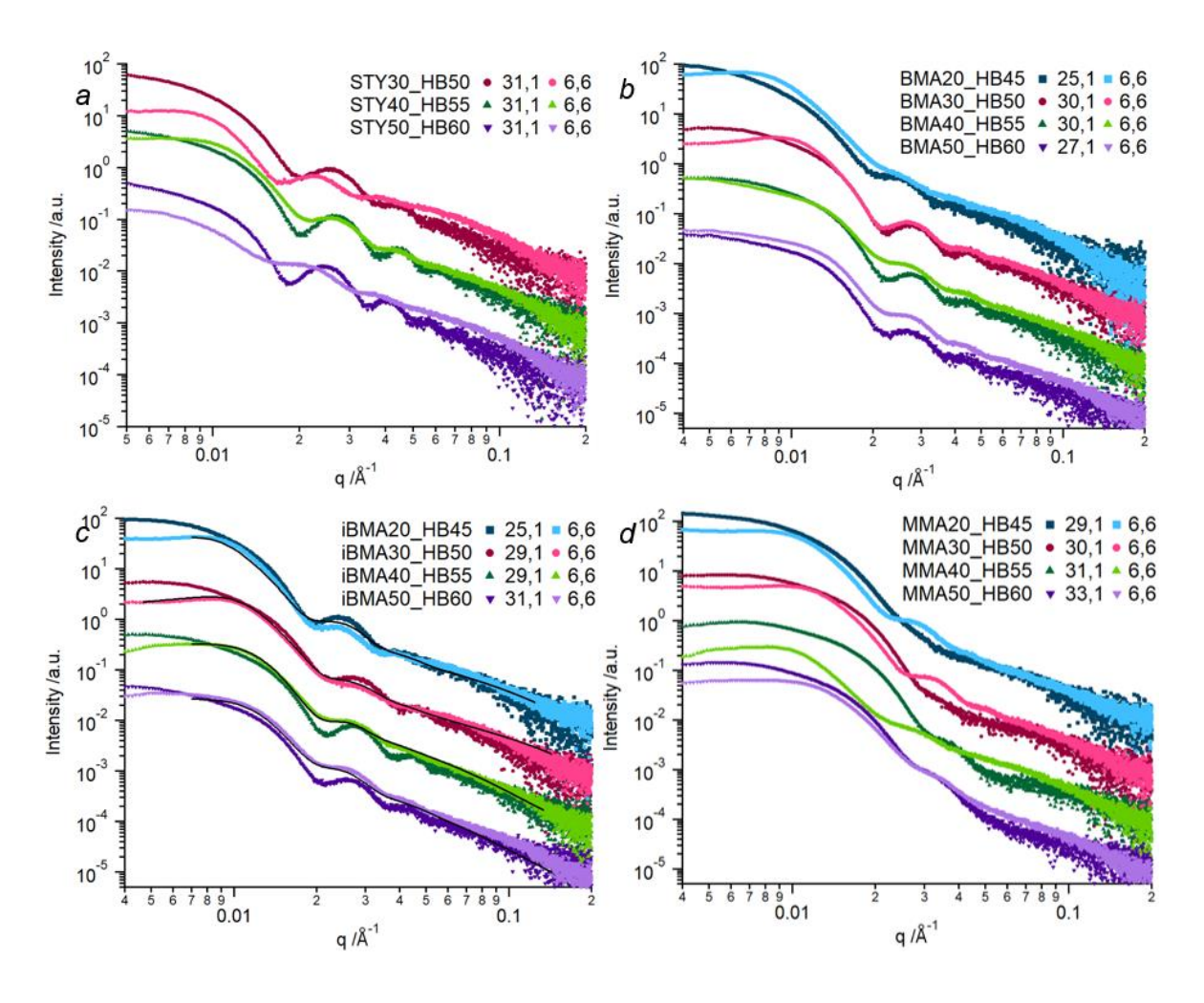


Figure 6.11: SAXS profiles for aqueous PUMAs, polymerised at industrial concentrations and collected at  $C_{tot} = 1$  wt% (dark colours), or polymerised and collected at  $C_{tot} = 6$  wt% (pale colours), at PU/PA or PU/PS ratios of 80/20 (blue squares), 70/30 (red circles), 60/40 (green triangles) and 50/50 (purple triangles). The PA or PS is a) PS, b) PBMA, c) PiBMA, and d) PMMA. Patterns are scaled by concentration and offset by an arbitrary factor to avoid overlap. The numbers in the key refer to "mass % polymerisation concertation", "mass % acquisition concentration".

Samples containing PiBMA and PBMA give scattering profiles with very similar features arising from P(q) at both concentrations. The main differences are due to a

broader polydispersity and a more prominent structure factor from the products of the *in situ* polymerisation. These are a result of the polymerisation at lower concentrations, and data collection at higher concentrations, respectively.

The polymerisation temperature (40 °C) is greater than the  $T_g$  of PBMA (~32 °C).<sup>45</sup> This reduces the barrier to phase separation of the soft PBMA from PU to make coreshell particles. Similarly, the  $T_g$  of PiBMA, at ~64 °C,<sup>45</sup> is close to the polymerisation temperature, so any local heating from the exotherm of polymerisation will raise the temperature sufficiently to soften the polymer and allow phase separation. As such, although the morphology of the precursors differs with concentration, this is not so influential on the final PUMA particle morphology.

For PUMAs containing PMMA or PS, a greater reaction concentration dependence of the final PUMA particle morphologies is observed (Figure 6.11, a and d). In addition to the prominent structural peaks, the P(q) features, relating to particle sizes and morphologies, are markedly different in the SAXS profiles when PUMAs are made at  $C_{tot} = 6$  wt%, compared to those made industrially. PMMA and PS have  $T_g$ s of 105 °C and 107 °C,<sup>45</sup> respectively, so their polymers would be in the glassy state at the polymerisation temperature, even if the plasticised mixture of monomer, PA or PS, and PU was not. The rate of polymerisation must, therefore, be faster than the rate of phase separation. The polymer chain has already grown sufficiently long to be entangled with the PU before phase separation can occur, which is then hindered by chain rigidity. As a consequence, the morphology of the precursor is more influential on the PUMA. The more monomer outside the particle at the beginning of the reaction, the more must penetrate during the reaction, and the more phase-mixed the product will be.

Representative fittings of Model B, illustrating the differences in morphology of the final PUMA product when iBMA samples are polymerised under *in situ* conditions, are shown in Figure 6.11c. The structural model parameters obtained from these fittings are given in Table 6.11. The best fit to  $iBMA20\_HB45$ , polymerised at  $C_{tot} = 6$  wt%, does not model the data particularly well in the region 0.016 Å<sup>-1</sup> < q < 0.04 Å<sup>-1</sup>. Model A does not provide a good fit at all, therefore it was deemed that the morphology is close to core-shell.

Table 6.11: Structural parameters obtained from fitting of core-shell particles and supramolecular structures of acidic PU fragments to SAXS profiles for PUMAs containing PiBMA, polymerised at industrial concentrations, or at  $C_{tot} = 6$  wt%. HB refers to the hard block in the PU.  $R_{co}$  is the mean radius of the monomer core with its relative standard deviation of  $\sigma_{co}$ ,  $T_{sh}$  is the mean PU shell thickness, and x is the proportion of PiBMA in the sample that is found in the particles. The proportion of the PU in supramolecular structures is quantified by  $\phi_{PU,AF}/\phi_{PU,tot}$ .  $R_g$  gives the radius of gyration of these structures, and v is a structural parameter that indicates solubilisation of these polymer-like structures.

Sample	COOH wt%	Polymerisation C <sub>tot</sub> /wt%	Core-shell Particle Parameters				Supramo structure fragments p	s of acid	d
	in PU	in PU		$\sigma_{ m co}$	$T_{ m sh}$ /nm	x	$\phi_{ ext{PU,AF}}/\phi_{ ext{PU,tot}}$	$R_g$ /nm	ν
iDMA20 UD45	1.82	25	13.6	0.10	11.2	1	0.06	3.0	0.33
iBMA20_HB45	1.02	6	14.2	0.11	11.2	1	0.14	2.2	0.33
iDMA20 UD50	2.39	29	14.2	0.12	7.4	1	0.59	1.6	0.33
iBMA30_HB50	2.39	6	15.3	0.15	7.7	1	0.25	1.8	0.33
iDMA 40 LIDEE	2.07	28	15.2	0.10	5.5	1	0.12	2.0	0.33
<i>iBMA40_HB55</i>   2.97	2.97	6	15.3	0.16	6.5	1	0.15	2.9	0.33
iBMA50_HB60 3.56	2.56	31	16.1	0.12	4.4	1	0.09	2.8	0.33
	3.36	6	15.2	0.10	4.4	1	0.08	3.5	0.33

Across the samples,  $R_{co}$  and  $T_{sh}$  are very similar to those obtained by polymerisation at industrial conditions, however for all but *iBMA50\_HB60*, the  $\sigma_{co}$  are greater.

### 6.5.2 Polymerisations of iBMA PUMAs

There is influx of iBMA into the particle from monomer droplets during polymerisation, as x < 1 in the precursors, yet x = 1 in the final products. The constant increase in  $I(q \rightarrow 0)$  throughout the reactions for  $iBMA20\_HB45$  (Figure 6.12a) and  $iBMA30\_HB50$ 

(Figure 6.12b) can be attributed to the increase in mass density. iBMA has a mass density of 0.88 gcm<sup>-3</sup>,<sup>41</sup> whereas for PiBMA this is 1.05 gcm<sup>-3</sup>.<sup>42</sup> This directly effects the scattering length density of the acrylic component, with  $\xi_{\rm iBMA} < \xi_{\rm PiBMA}$ , therefore  $\xi_{\rm part}$  is greater in the product than in the precursor. Subsequently, the contrast between the particles and water increases. In contrast, for  $iBMA40\_HB55$  (Figure 6.12c) and  $iBMA50\_HB60$  (Figure 6.12d),  $I(q\rightarrow0)$  passes through a minimum during the reaction. There must be an influx of monomer to the particles that initially decreases  $\xi_{\rm part}$ . It increases again as polymerisation of iBMA inside the particles proceeds.

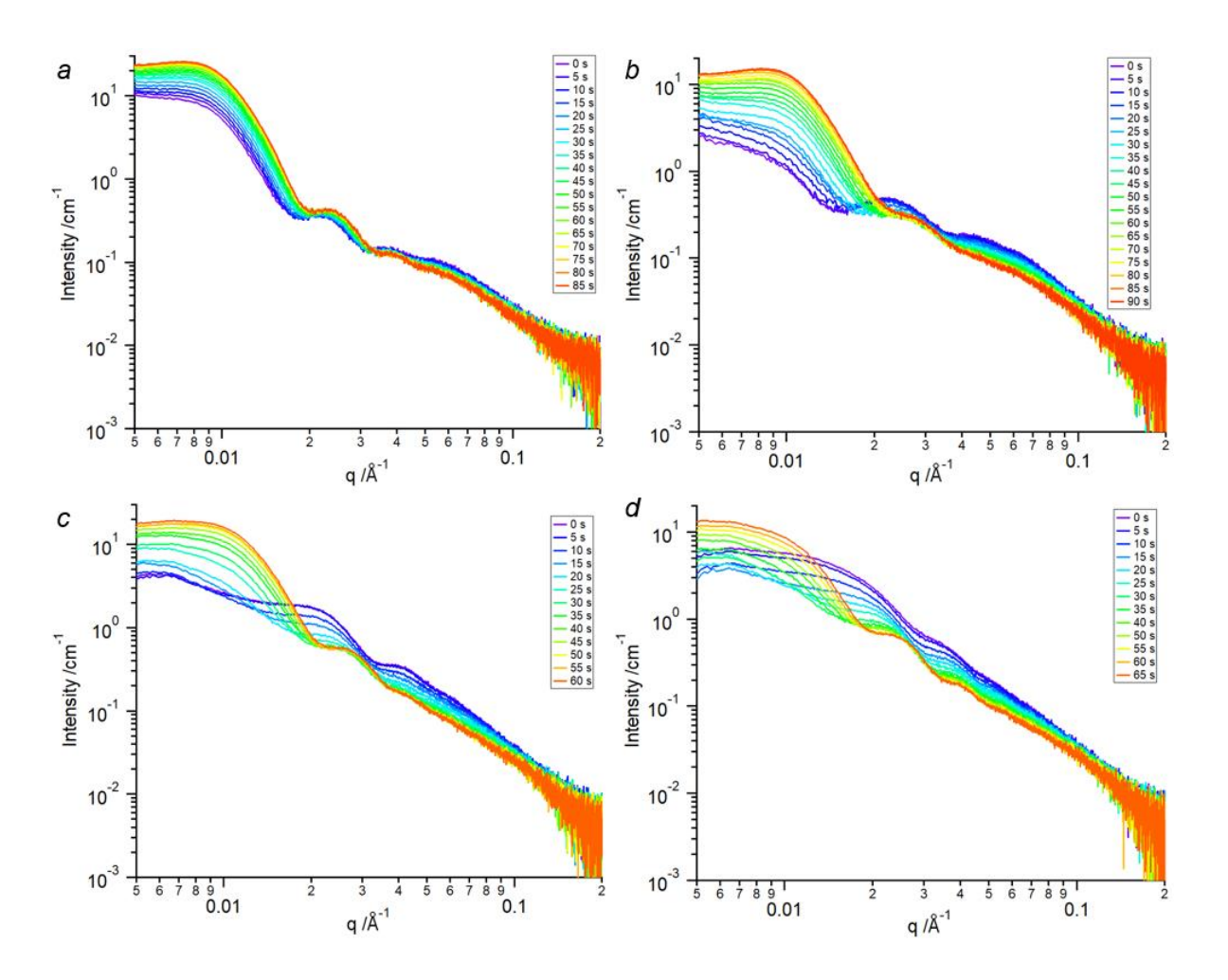


Figure 6.12: SAXS profiles collected in situ during the polymerisation of iBMA in an aqueous dispersion at PU/iBMA mass ratios of a) 80/20 (iBMA20\_HB45), b) 70/30 (iBMA30\_HB50), c) 60/40 (iBMA40\_HB55), and d) 50/50 (iBMA50\_HB60). The scattering at t=0 is shown in purple, and the final product in red, with the intermediates between.

For the *iBMA20\_HB45* polymerisation (Figure 6.12a), fitting of the precursor gives a primary population of spherical particles of homogenously phase-mixed iBMA and PU, however the primary population of the final polymerised product has a morphology close to core-shell. This shows that the internal phase separation is driven by polymerisation.<sup>43</sup> For the other iBMA polymerisations, both the precursor and the product have core-shell particles, indicating that any influx of monomer is added to the core. It is known that, in conventional emulsion polymerisation, initiation is most likely to occur inside the particles because of the greater surface area/volume ratio compared to large droplets.<sup>44</sup> The monomer in large droplets then feeds the particles, adding to the growing PiBMA chains in the cores. Hence a core-shell precursor results in a core-shell PUMA.

The scattering contribution from the supramolecular structures (seen at  $q > 0.04 \text{ Å}^{-1}$ ), reduces in intensity throughout the reaction for all of the polymerisations in Figure 6.12. This suggests that the volume fraction of this population is decreasing throughout the reaction, with migration of the acidic fragments to the particles to provide charge stability to compensate for the increasing hydrophobicity caused by the influx of iBMA and its polymerisation.

In order to follow the extent of acrylic polymerisation during time-resolved SAXS measurements, Model B was adjusted to allow a proportion of the acrylic in the particle cores to be polymerised, by letting  $\xi_{co}$  be the weighted sum of the polymerised ( $\xi_{PA}$ ) and unpolymerised ( $\xi_{mon}$ ) scattering length densities:

$$\xi_{\rm co} = \frac{\phi_{\rm PA}}{\phi_{\rm co}} * \xi_{\rm PA} + \frac{\phi_{\rm co} - \phi_{\rm PA}}{\phi_{\rm co}} * \xi_{\rm mon} \quad [Eq. 6.25]$$

Additionally, the PU/methacrylic volume ratio changes with polymerisation. The mass ratio is constant, however the volume of the methacrylic fraction decreases with the

increasing density during polymerisation. Therefore, the volume ratio, which provides a physical parameter by which to confine the fitting, is dependent on the acrylic mass density ( $\rho_{m,AC}$ ):

$$\rho_{\text{m.AC}} = \frac{\phi_{\text{PA}}}{\phi_{\text{AC,tot}}} * \rho_{\text{m.PA}} + \frac{\phi_{\text{mon}}}{\phi_{\text{AC,tot}}} * \rho_{\text{m,mon}} \quad [Eq. 6.26]$$

where  $\rho_{\rm m.PA}$  and  $\rho_{\rm m,mon}$  are the mass densities of the PiBMA and iBMA, respectively.

This modified Model B was fit to patterns collected every 10 s for *iBMA30\_HB50* (Figure 6.13a), as a representative example for reactions where precursors and final PUMAs are both core-shell. This sample was chosen as it displays behaviour consistent with the expectations of core-shell particle evolution. This model assumes that the polymerisation of each polymer core is gradual. The fitting was performed using the same fixed and floating parameters as model B, with the addition of the extent of polymerisation as a fitting parameter. The code for this population is give in Appendix 8.10.6. Using this assumption provides reasonable fittings of the average morphologies, however it does not give perfect fits, as it does not account for the fact that reaction will always contain a mixture of particle morphologies during polymerisation.

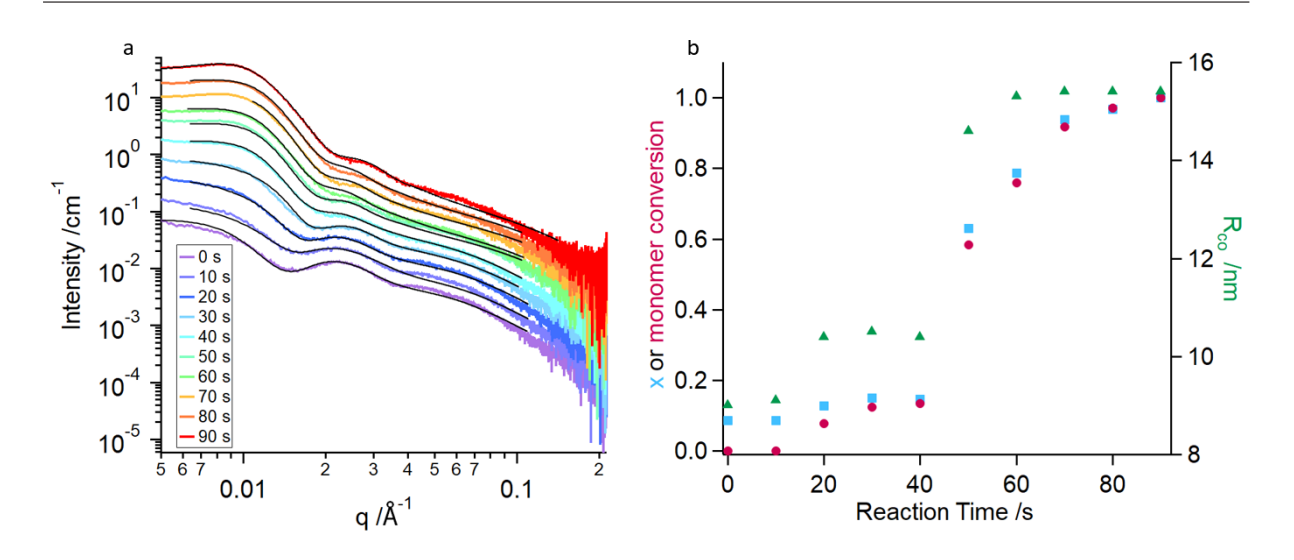


Figure 6.13: a) SAXS profiles collected in situ during the polymerisation of sample iBMA30\_HB50, offset to avoid overlap. Black lines show best fit models describing core-shell particles with a proportion of iBMA polymerised, and supramolecular structures of acidic fragments of PU. b) Volume fraction of acrylic found inside the particles 'x' (blue squares, left axis) monomer conversion (red circles, left axis) and  $R_{co}$  (green triangles, right axis) with time, obtained from SAXS fitting.

The volume proportion of acrylic inside the particles, x, the extent of monomer conversion, and the mean radius of the particle cores,  $R_{co}$ , are obtained from the SAXS fittings (Figure 6.13b). At first, the extent of polymerisation increases faster than the influx of monomer, as the monomer already present in the precursors polymerises. At 40 s, the amount of acrylic that has polymerised is only marginally smaller than the amount inside the particles, therefore the monomer feed from the droplets to the particles accelerates. Simultaneously, the extent of reaction accelerates, such that the core of the particles is always almost all polymerised. This shows that the diffusion of monomer from droplets to particles controls the rate of the polymerisation. The monomer feed and polymerisation rate both slow significantly after 70 s, and the reaction is complete at 90 s. The same behaviour is observed in the size of particle cores throughout the reaction, as monomer feeds the polymerising iBMA in the core causing an increase in radius (Figure 6.13b).

Applying this model to the other *in situ* reactions, where core-shell precursors form core-shell PUMAs, was unsuccessful, giving solutions that did not fit the whole *q* range

of each profile well. This shows that there are limitations to this model, and it requires further development to be suitable for fitting *in situ* data for the other reactions.

#### 6.5.3 Polymerisations of BMA and Styrene PUMAs

The results of *in situ* SAXS data collection for polymerisations of BMA (Figure 6.14) and styrene (Figure 6.15) follow the same trends as those discussed for iBMA polymerisations (Figure 6.12).

There is either an increase in  $I(q\rightarrow 0)$ , or it passes through a minimum, during the reaction. The intensity of the scattering from the second population of supramolecular structures (seen at q > 0.04 Å<sup>-1</sup>) follows the same behaviour as the iBMA polymerisations, decreasing during the reaction, suggesting migration of the acidic fragments to the PUMA particles.

It is noteworthy that the styrene polymerisations have a much longer reaction times than the methacrylic polymerisations (Table 6.12). As the fitting of time resolved profiles for sample *iBMA30\_HB50* revealed that the rate of polymerisation is controlled by the monomer diffusion (Figure 6.13), this could be due to the hydrophobicity of styrene<sup>24</sup> slowing diffusion through the water from the droplets to the polymerising particles. Additionally, the styrene radical is more stable than the methacrylic radicals, due to the delocalisation arising from the aromatic ring. This is known to slow the rate of free-radical polymerisation.

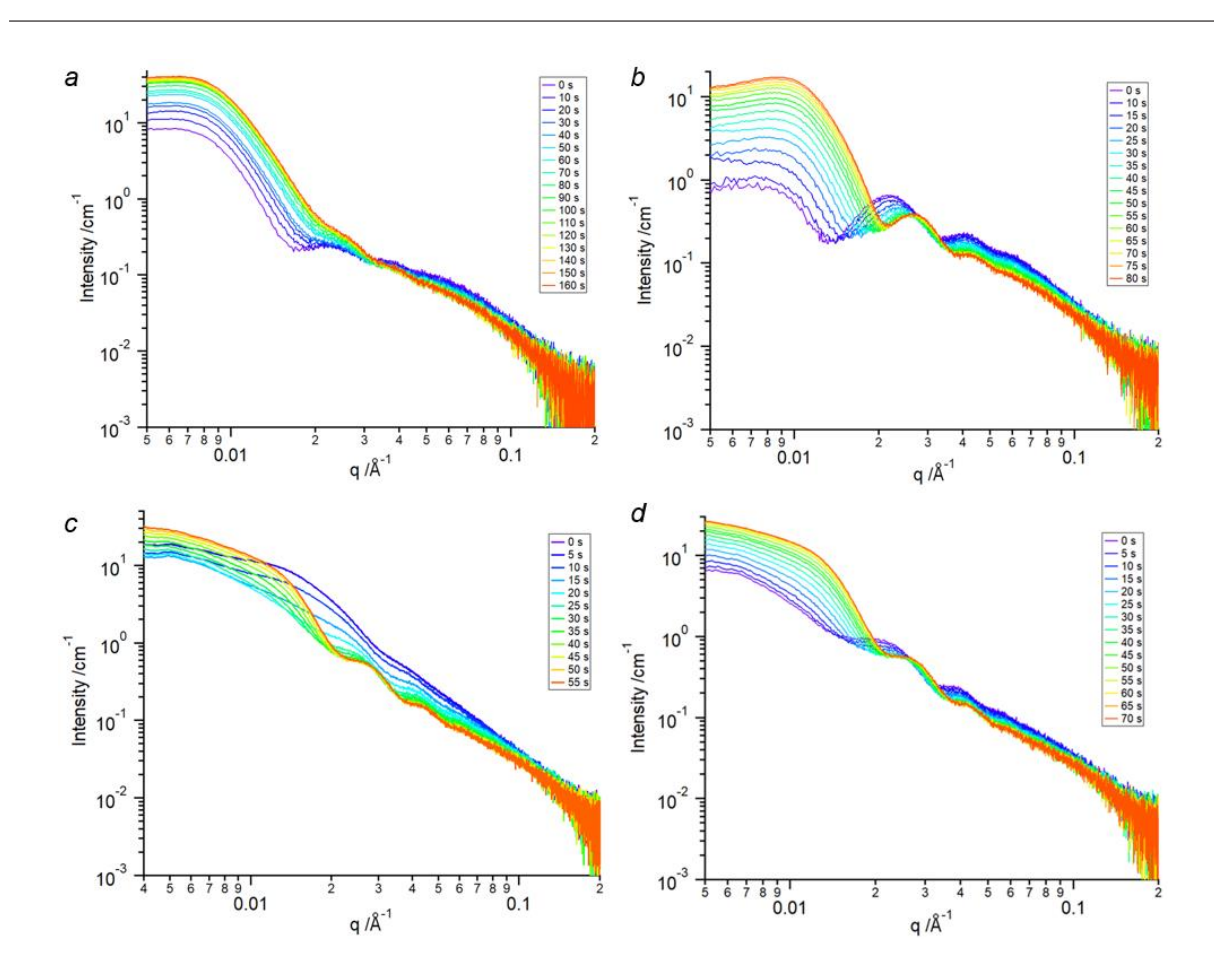


Figure 6.14: Time-resolved SAXS profiles collected in situ during the polymerisation of BMA in an aqueous dispersion at PU/BMA mass ratios of a) 80/20 (BMA20\_HB45), b) 70/30 (BMA30\_HB50), c) 60/40 (BMA40\_HB55), and d) 50/50 (BMA50\_HB60). The scattering at t=0 is shown in purple, and the final product in red, with the intermediates between.

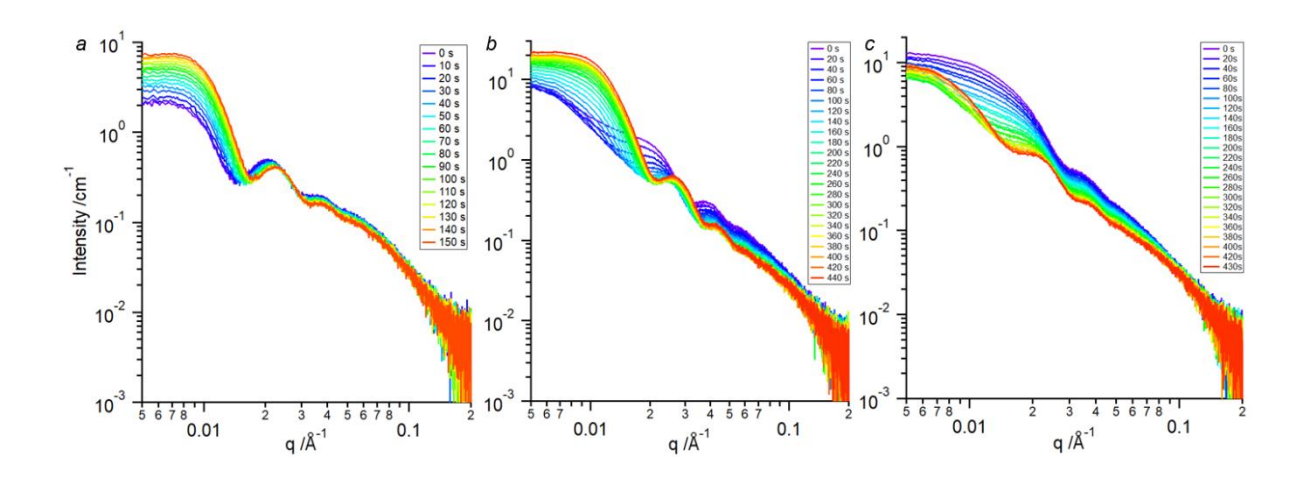


Figure 6.15: Time-resolved SAXS profiles collected in situ during the polymerisation of styrene in an aqueous dispersion at PU/styrene mass ratios of a) 70/30 (STY30\_HB50), b) 60/40 (STY40\_HB55), and c) 50/50 (STY50\_HB60). The scattering at t=0 is shown in purple, and the final product in red, with the intermediates between.

Table 6.12: Reaction times for polymerisations of precursors to make PUMA under the conditions used for in situ SAXS data collection, judged by the time from starting the reaction (t=0) to the point when the particle morphology does not change according to time-resolved SAXS patterns.

Sample	Time to reach final morphology /s
MMA20_HB45	90
ММА30_НВ50	120
MMA40_HB55	95
ММА50_НВ60	130
BMA20_HB45	160
ВМА30_НВ50	80
BMA40_HB55	55
ВМА50_НВ60	70
iBMA20_HB45	85
іВМАЗО_НВ50	90
iBMA40_HB55	60
iBMA50_HB60	65
STY20_HB45	*
STY30_HB50	150
STY40_HB55	440
STY50_HB60	430

<sup>\*</sup> Sample STY20\_HB45 made a thick sticky substance on the surface during polymerisation, blocking the tubes

#### 6.5.4 Polymerisation of MMA PUMAs

SAXS profiles collected *in situ* during the polymerisation of MMA to make PUMA particles are shown in Figure 6.16. Although the major differences in PUMA scattering profiles indicate different morphologies comparing polymerisation at  $C_{tot} = 1$  wt% and 6 wt% (Figure 6.11d), the dilute polymerisation conditions also produce particles that cannot be fit by Model A, as phased mixed spheres, or Model B, as core-shells. For all PU/MMA ratios, time resolved data show similar trends, with increasing  $I(q \rightarrow 0)$  throughout the reaction (Figure 6.16). As such, a representative set of time resolved SAXS data, for *MMA30 HB50* (Figure 6.16b), is discussed.

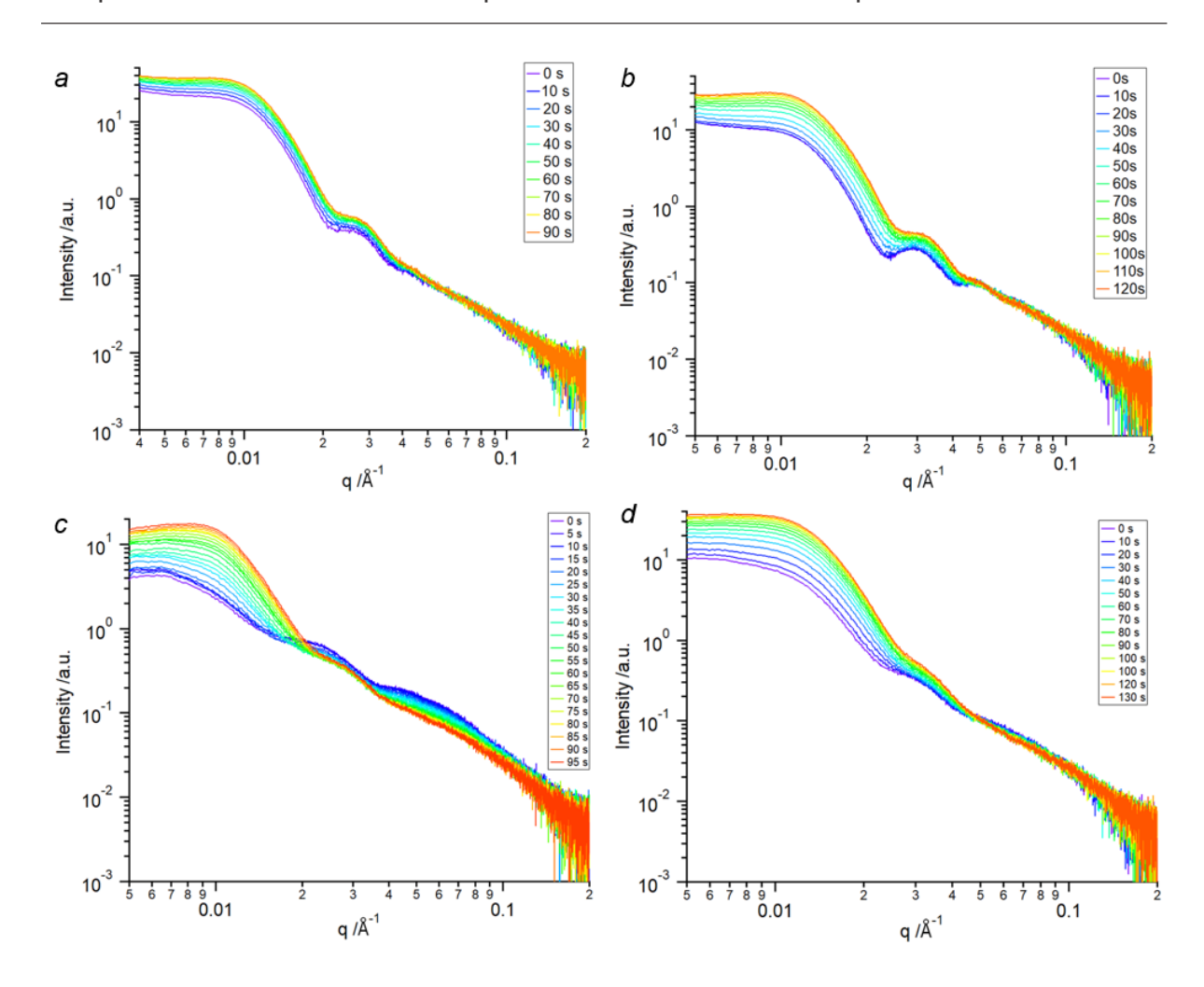


Figure 6.16: Time-resolved SAXS profiles collected in situ during the polymerisation of MMA in an aqueous dispersion at PU/MMA mass ratios of a) 80/20 (MMA20\_HB45), b) 70/30 (MMA30\_HB50), c) 60/40 (MMA50\_HB55), and d) 50/50 (MMA50\_HB60). The scattering at t=0 is shown in purple, and the final product in red, with the intermediates between.

Table 6.13: Structural parameters obtained from the model fitting of the SAXS profile for a PU containing 50% hard block, made in MMA, with an PU/MMA ratio of 70/30, collected at the start point of MMA polymerisation. R is the mean radius with its relative standard deviation of  $\sigma$ , and x is the proportion of the MMA in the sample that is found in the particles. The proportion of the PU that is distributed as acidic fragments in supramolecular structures is quantified by  $\phi_{PU,AF}/\phi_{PU,tot}$ .  $R_g$  gives the radius of gyration of these structures, and v is a structural parameter that indicates solubilisation of these polymer-like structures.

Sample	C <sub>tot</sub> /mass%	Spherical Particle Parameters			Supramolecular structures of acid fragments parameters		
		R/nm	σ	х	Φ <sub>PU,AF</sub> /Φ <sub>PU,tot</sub>	Rg /nm	v
MMA20 UDEO pro	1	19.6	0.10	0.36	0.11	2.7	0.33
MMA30_HB50_pre	6	18.0	0.12	0.11	0.19	2.4	0.33

The first pattern, at t = 0, was fit with Model A. This gives the parameters in Table 6.13.

Comparing these fitting results with the static sample of  $MMA30\_HB50\_pre$ , collected at  $C_{tot} = 1$  wt% (Table 6.13), shows some key differences. R is 1.6 nm larger, with a greater volume fraction of MMA in the particles (x = 0.36 compared to x = 0.11), and a lesser volume fraction of the PU as acidic fragments ( $\phi_{PU,AF}/\phi_{PU,tot} = 0.10$  compared to 0.19). More charge stabilisation is required for the particles containing more MMA monomer, possibly resulting in more of the acidic fragments migrating to the particles, and less as a minor population of supramolecular structures.

The time-resolved data (Figure 6.16b) show significant changes in P(q) as the polymerisation proceeds. In this region, the intensity profile is dominated by the scattering from particles. At q > 0.05 Å<sup>-1</sup>, where the scattering from supramolecular structures can be seen, the scattered intensity is relatively unchanged, suggesting that these structures are not involved in the morphological evolution during polymerisation.

There is a significant increase in  $I(q\rightarrow 0)$  during polymerisation. Again, this can be interpreted by considering the mass density increase from 0.95 g cm<sup>-3</sup> for MMA,<sup>25</sup> to 1.18 g cm<sup>-3</sup> for PMMA.<sup>46</sup> Moreover, this will cause an increase in the scattering length density arising from the MMA portion from  $\xi_{\text{mon}} = 8.60 \times 10^{10} \text{ cm}^{-2}$  to  $\xi_{\text{PA}} = 10.80 \times 10^{10} \text{ cm}^{-2}$ . Using the parameters in Table 6.13,  $\xi_{\text{PU,part}}$  can be calculated at the beginning of the polymerisation as  $10.10 \times 10^{10} \text{ cm}^{-2}$  (Equation 6.7) and, therefore,  $\xi_{\text{part}} = 9.84 \times 10^{10} \text{ cm}^{-2}$  (Equation 6.8). As  $\xi_{\text{part}} > \xi_{\text{water}}$ , and this difference increases with polymerisation of MMA, the corresponding increase in  $I(q\rightarrow 0)$  is observed.

Fittings of Model A to the profiles for  $MMA40\_HB55\_pre$  and  $MMA50\_HB60\_pre$  shows that, at  $C_{tot} = 1$  wt%, none of the monomer is inside the particles. It is likely, therefore, that initiation must occur in the water phase. As MMA monomers polymerise, their hydrophobicity increases with chain length, and the growing hydrophobic chains

will preferentially penetrate the hydrophobic interior of PU particles. This mirrors the swelling method, discussed in Section 5.2.1. As the precursors contain no monomer core, the final PUMA is unlikely to have a well-defined core-shell morphology either.

During emulsification and polymerisation at AkzoNobel's concentrated industrial conditions, for *MMA40\_HB55* and *MMA50\_HB60*, the proportion of MMA in the sample is well above the solubility threshold of MMA in water.<sup>25</sup> Consequently, it is likely that some of the MMA is found inside the PU particles and there is less need for penetration of active PMMA chains into the PU (Figure 6.17), causing the dependence of the final PUMA morphology on C<sub>tot</sub> of the reaction (Figure 6.11d).

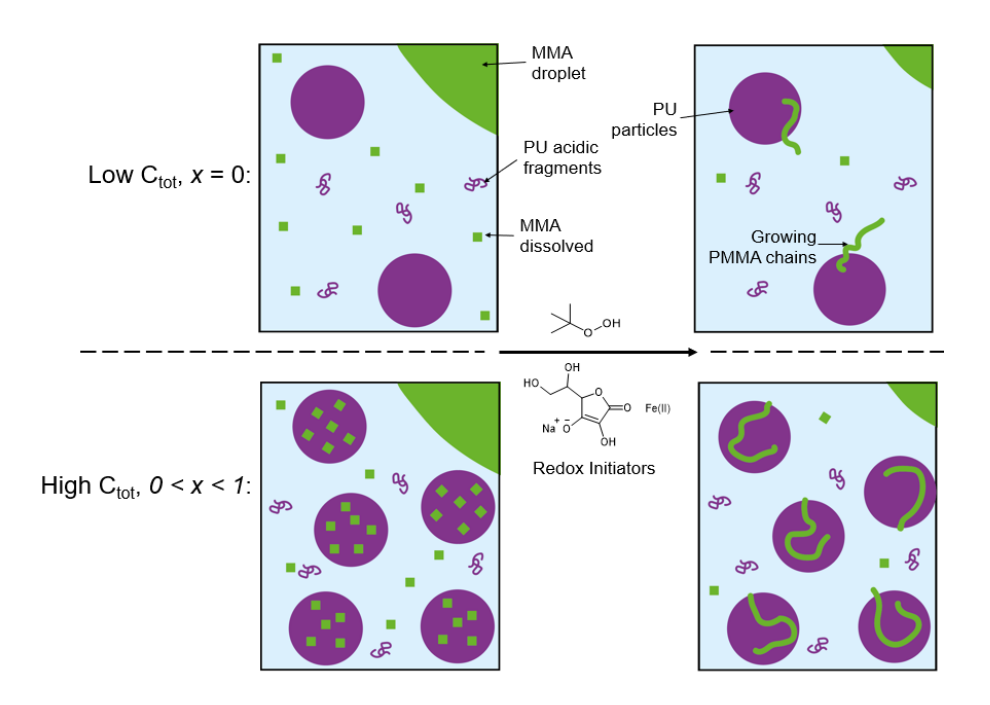


Figure 6.17: Schematic of the early stages of PMMA polymerisation when a 50/50 solution of PU/MMA is initiated at different concentrations. C<sub>tot</sub> refers to the sum of the mass fractions of PU, MMA and PMMA, and x refers to the proportion of the MMA found inside the particles. The solubility of MMA in water, and hydrophilic initiator lead to differences in the particle morphology.

It is also possible that initiation of MMA in the water phase induces the formation of a new, separate population of particles. PU acidic fragments from the supramolecular structures could migrate to the growing PMMA chains in the water phase, providing stabilisation, and forming new core-shell particles. This would justify the low

contribution to the scattered intensity from the minor population of PU supramolecular structures for PUMAs containing PMMA, as these would be consumed in the formation of this new population. Additionally, the time resolved data for  $MMA40\_HB50$  and  $MMA50\_HB60$  (the former in particular) show a decrease in the scattering intensity from supramolecular structures of PU acidic fragments as polymerisation proceeds. The presence of two particle populations in the scattering pattern would significantly complicate the analysis of P(q).

# 6.6 Conclusions

Analytical equations for SAXS profiles produced by precursor PU-monomer particle dispersions and synthesised PUMA particles are derived. It was assumed for the structural SAXS models that the particles are of spherical shape composed of either randomly mixed acrylic (or styrene) and PU components, or separated acrylic (or styrene) core and PU shell. More importantly, the models count conservation of mass of PU components and PU/acrylic or PU/styrene ratio in the sample compositions.

Analysis of SAXS profiles of PUMAs and their precursors, using the structural models and analytical equations derived in this work, shows that each dispersion is composed of a major population of PU/PA, PU/PS or PU/monomer particles, and a minor population of supramolecular structures formed by the hydrogen bonding of acidic fragments of PU. Moreover, not all of the acrylic is found inside the particles. Upturns at low q in the SAXS profiles, and the cloudiness of solutions, suggests that some monomer locates outside of the particles in droplets.

SAXS analysis of the precursors indicates that the primary population of scatterers in the samples is either particles with a monomer core and PU shell, or particles of phasemixed PU and monomer. This depends on the compatibility of the monomer and the PU. When they are compatible, the monomer can act as a solvent for the PU forming phase-mixed particles. Solubility parameters demonstrate that, as the hard block content of the PU increases, the monomer and the PU become less compatible, and core-shell particles form. For precursors containing MMA, at high hard block contents, none of the monomer is found inside the particles. The HSPs of styrene, particularly  $\delta H$  and  $\delta P$ , are far from the values found for PUs in the literature, therefore they are incompatible and core-shell particles form at all PU/styrene ratios.

For all the PUMA samples containing PS, PBMA or PiBMA, except for *STY20\_HB45*, the major population comprises core-shell particles. Samples containing PMMA cannot be fit using the scattering equations developed for a primary population of coreshell particles or phase-mixed spheres. Samples containing PMMA and PS show the greatest morphology dependence on polymerisation concentration. This is thought to be due to the high T<sub>9</sub>s, restricting phase separation, whereas for samples containing PiBMA and PBMA, the low T<sub>9</sub>s mean the polyacrylic is mobile and can more easily phase separate from the PU at the reaction temperature. Additionally, the polymerisation is much slower for PUMAs containing styrene.

Time-resolved SAXS profiles, collected *in situ* during the polymerisation reactions to make PUMA. show that  $I(q\rightarrow 0)$  increases, or passes through a minimum, during the reaction. This is attributed to the greater mass density of PA or PS compared to their monomers, increasing the scattering length density of the particles. A structural model counting conservation of mass of acrylic components in the sample, and letting the core of the particles be composed of both acrylic monomer and polyacrylic, has been developed to analyse time-resolved SAXS patterns recorded during the polymerisation reaction. It was assumed that the particles have core-shell morphology, and the core composition gradually changes from monomer to polymer during the

course of polymerisation. This way, the volume fraction of acrylic inside the particles and the extent of acrylic polymerisation with time can be extracted. However, the model has not produced satisfactory fits for most of the studied compositions. This suggests that the model needs further development to account for a mixture of particles morphologies in the samples, as initiation of particles is unlikely to be synchronous. Nevertheless, the developed model produced satisfactory fits to the set of time-resolved data collected *in situ* for polymerisation of *iBMA30\_HB50*. The result showed that the iBMA monomer inside the particles polymerises first, following which there is an acceleration in polymerisation rate and the monomer feed from droplets to particles, such that the particle core contains PiBMA with only a minimal amount of iBMA monomer, until the reaction is complete.

### 6.7 References

- 1 B. Jiang, J. G. Tsavalas and D. C. Sundberg, *Polymer (Guildf).*, 2018, **139**, 107–122.
- 2 M. Hirose, F. Kadowaki and J. Zhou, *Prog. Org. Coatings*, 1997, **31**, 157–169.
- 3 S. Mehravar, N. Ballard, A. Agirre, R. Tomovska and J. M. Asua, *Macromol. Mater. Eng.*, 2019, **304**, 1800532.
- 4 Y. H. Guo, S. C. Li, G. S. Wang, W. Ma and Z. Huang, *Prog. Org. Coatings*, 2012, **74**, 248–256.
- 5 I. Drake, G. Cardoen, A. Hughes, A. I. Nakatani, B. Landes, J. Reffner and R. Even, *Polymer (Guildf).*, 2019, **181**, Online.
- 6 H.-J. Adler, K. Jahny and B. Vogt-Birnbrich, *Prog. Org. Coatings*, 2001, **43**, 251–257.
- O. O. Mykhaylyk, A. J. Ryan, N. Tzokova and N. Williams, *J. Appl. Crystallogr.*, 2007, **40**, 506–511.
- 8 C. Li, W. Chiu and T. Don, *J. Polym. Sci. Part A Polym. Chem.*, 2007, **45**, 3359–3369.
- 9 M. Hirose, J. Zhou and K. Nagai, *Prog. Org. Coatings*, 2000, **38**, 27–34.
- 10 S. L. Chai and H. M. Tan, *J. Appl. Polym. Sci.*, 2008, **107**, 3499–3504.
- 11 E. Degrandi-Contraires, R. Udagama, T. McKenna, E. Bourgeat-Lami, C. J. G. Plummer and C. Creton, *Int. J. Adhes. Adhes.*, 2014, **50**, 176–182.
- 12 S. L. Chai, M. M. Jin and H. M. Tan, *Eur. Polym. J.*, 2008, **44**, 3306–3313.
- P. J. Peruzzo, P. S. Anbinder, O. R. Pardini, J. Vega, C. A. Costa, F. Galembeck and J. I. Amalvy, *Prog. Org. Coatings*, 2011, **72**, 429–437.
- 14 Y. Lu, Y. Xia and R. C. Larock, *Prog. Org. Coatings*, 2011, **71**, 336–342.
- D. Kukanja, J. Golob, A. Zupancic-Valant and M. Krajnc, *J. Appl. Polym. Sci.*, 2000, **78**, 67–80.
- 16 H. T. Lee and C. C. Wang, *J. Polym. Res.*, 2005, **12**, 271–277.
- 17 O. R. Pardini and J. I. Amalvy, *J. Appl. Polym. Sci.*, 2008, **107**, 1207–1214.
- 18 L. Chen and S. Chen, *Prog. Org. Coatings*, 2004, **49**, 252–258.
- T. J. Neal, A. J. Parnell, S. M. King, D. L. Beattie, M. W. Murray, N. S. J. Williams, S. N. Emmett, S. P. Armes, S. G. Spain and O. O. Mykhaylyk, *Macromolecules*, 2021, **54**, 1425–1440.
- J. S. Pedersen and M. C. Gerstenberg, *Macromolecules*, 1996, **29**, 1363–1365.
- 21 J. K. Percus and G. J. Yevick, *Phys. Rev.*, 1958, **110**, 1–13.
- 22 C. Ma, X. Bi, T. Ngai and G. Zhang, *J. Mater. Chem. A*, 2013, **1**, 5353–5360.

- 23 J. Wu, X. Guan, C. Wang, T. Ngai and W. Lin, *J. Colloakzoid Interface Sci.*, 2022, **610**, 994–1004.
- 24 C. Hansch, A. Leo and D. Hoekman, *Exploring QSAR Hydrophobic, Electronic and Steric Constants*, American Chemical Socety, Washington DC, 1995.
- N. L. of Medicine, Hazardous Substances Data Bank Methyl Methacrylate, https://pubchem.ncbi.nlm.nih.gov/source/hsdb/195, (accessed 7 August 2023).
- 26 H. Sardon, L. Irusta, M. J. Fernández-Berridi, J. Luna, M. Lansalot and E. Bourgeat-Lami, *J. Appl. Polym. Sci.*, 2011, **120**, 2054–2062.
- 27 A. K. Nanda, D. A. Wicks, S. A. Madbouly and J. U. Otaigbe, *J. Appl. Polym. Sci.*, 2005, **98**, 2514–2520.
- 28 J.-H. Chen and E. Ruckenstein, .
- 29 J. L. Lewin, K. A. Maerzke, N. E. Schultz, R. B. Ross and J. I. Siepmann, *J. Appl. Polym. Sci.*, 2010, **116**, 1–9.
- 30 Y. Cai, W. Yan, X. Peng, M. Liang, L. Yu and H. Zou, *J. Appl. Polym. Sci.*, 2019, **136**, 46979.
- 31 S. Abbott, Hansen Solubility Parameters, https://www.hansen-solubility.com, (accessed 23 August 2023).
- 32 R. Mieczkowski, Eur. Polym. J., 1992, 28, 53–55.
- 33 R. Gallu, F. Méchin, J.-F. Gérard and F. Dalmas, *Constr. Build. Mater.*, 2022, **328**, 127061.
- T. J. Neal, D. L. Beattie, S. J. Byard, G. N. Smith, M. W. Murray, N. S. J. Williams, S. N. Emmett, S. P. Armes, S. G. Spain and O. O. Mykhaylyk, *Macromolecules*, 2018, **51**, 1474–1487.
- R. Satguru, J. McMahon, J. C. Padget and R. G. Coogan, *J. Coatings Technol.*, 1994, **66**, 47–55.
- 36 M. A. Pérez-Limiñana, F. Arán-Aís, A. M. Torró-Palau, A. C. Orgilés-Barceló and J. M. Martín-Martínez, *Int. J. Adhes. Adhes.*, 2005, **25**, 507–517.
- 37 X. Zhu, X. Jiang, Z. Zhang and X. Z. Kong, *Prog. Org. Coatings*, 2008, **62**, 251–257.
- 38 S. Zhang, H. Lv, H. Zhang, B. Wang and Y. Xu, *J. Appl. Polym. Sci.*, 2006, **101**, 597–602.
- 39 M. Li, E. S. Daniels, V. Dimonie, E. D. Sudol and M. S. El-Aasser, *Macromolecules*, 2005, **38**, 4183–4192.
- 40 X. Wang, G. Ma and M. Zheng, *J. Coatings Technol. Res.*, 2018, **15**, 1217–1227.
- 41 R. J. S. Lewis, *Hawley's Condensed Chemical Dictionary*, John Wiley & Sons, Incorporated, New York, NY, 15th Editi., 2007.
- 42 G. Z. Li, H. Cho, L. Wang, H. Toghiani and C. U. Pittman, *J. Polym. Sci. Part A Polym. Chem.*, 2005, **43**, 355–372.

- 43 P. J. Flory, *Principles of Polymer Chemistry*, Cornell University Press, New York, 1953.
- 44 P. A. Lovell and F. J. Schork, *Biomacromolecules*, 2020, **21**, 4396–4441.
- 45 E. Penzel, J. Rieger and H. A. Schneider, *Polymer (Guildf).*, 1997, **38**, 325–337.
- 46 R. Goseki and T. Ishizone, *Encyclopedia of Polymeric Nanomaterials*, Springer Berlin Heidelberg, Berlin, Heidelberg, 2015.

# Chapter 7 - Conclusions and Future Work

# 7.1 Conclusions

This study investigates the morphology of aqueous polyurethane dispersions (PUDs), and their structural evolution during drying to form films, using static and time-resolved small angle X-ray scattering (SAXS) measurements as well as grazing incidence SAXS (GISAXS). Additionally, synthetic routes to polyurethane modified acrylics (PUMAs) are studied, and the best choice for SAXS form factor (P(q)) analysis taken forward to probe the effect of composition on PUMA morphology. Other analytical techniques such as GPC, MALDI, FTIR and AFM are also used in the study to corroborate the SAXS analysis results.

Both PUDs and PUMAs are available commercially, hence there is ample literature on these materials. However, analysis is usually carried out post-mortem on the dry product to infer information on the particle in dispersion, using methods such as microscopy or differential scanning calorimetry. Chapters 3 – 6 show that SAXS is a far more effective tool for probing morphologies in dispersion, and collecting time resolved data *in-vivo* during key processes such as drying and particle formation.

The effect of acid content, hard block/soft segment ratio, and soft segment molecular weight have been investigated in PUDs by development of a SAXS structural model based on conservation of mass that counts the total polyurethane (PU) formulation, composition of the acidic fragments, changes of mass density, and the scattering length density of the PU populations. It was found that commonly used PU formulations (based on hydrogenated methylene diphenyl diisocyanate (HMDI), dimethylolpropionic acid (DMPA) and poly(tetramethylene oxide) (PTMO) components)

produce two PU molecular populations: a major population of segmented (hard block and soft segment) PU forming spherical particles, and a minor population of hard segment molecules comprising n HMDI and n-1 DMPA. The latter population of molecules strongly hydrogen bonds, forming supramolecular structures in dispersion, producing scattering that can be modelled as a collapsed polymer chain. There is a strong correlation between the fraction of PU forming these supramolecular structures and the total acid content in the formulation, showing that a greater proportion of PU is found as acid-rich supramolecular structures when the formulation comprises more DMPA. The major population of high molecular weight PU polymers forms spherical particles. It was found that the particle size is related to the particle acid content: the higher the acid content, the smaller the particles. This relationship can be analytically described using a particle surface charge model, developed for amphiphilic statistical acrylic copolymers, 1 supporting universality of the model which could be used as a predictive tool for the statistical copolymer self-assembly. In addition, the molecular weight of the PTMO soft segment in the PU polymers is also shown to effect the particle size. In this case, the hydrophobicity increase caused by the greater PTMO molecular weight results in a greater surface area coverage of acid groups required for the formation of stable spherical particles.

It has been demonstrated that time-resolved grazing incidence SAXS (GISAXS) can be used as an effective tool for structural characterisation of aqueous PU dispersions upon PU film formation by drying. These results, in combination with AFM, have revealed that the particles present in PUDs do not fully coalesce, remaining as discrete objects that distort as they pack. There is a direct relationship between the mean particle size in PUDs and the short-range order periodic structure formed by the interfaces of coalesced particles. The minor population of acid-rich supramolecular

structures aggregates between the PU particle interfaces forming a matrix between the particles, resulting in a honeycomb-like structure. SAXS analysis on a fully dried film that is subsequently soaked in water demonstrated that the PU film formation is essentially reversible. The scattering profile showed that the acid-rich matrix swells first, increasing interparticle distance. In addition to the structural morphology formed by the particle interfaces in the dried films, PU hard blocks and soft segments microphase separate into another short-range periodic structure. The correlation length of the microphase separation, which is smaller than the PU dispersion particle diameter, suggests that the hard block and soft segment phase-separation is confined by the PU particle interfaces. As expected, the phase separation was the most pronounced for films formed from PUDs with soft segment/hard block mass ratios of 50/50. It has also been found that the polymer composition in the PUDs has a strong effect on the microphase separation in the dried films. The correlation distance of the phase separation increases with the soft segment length.

A few PUMA synthesis methods are explored in this study. Firstly, two common methods are compared: one in which the acrylic monomer is used as a solvent for the PU prepolymer reaction; the other using addition of acrylic monomer to a PUD. The former, referred to as the monomer solvent method, gave a well-defined particle system with the least contribution to scattered intensity from particle interactions, and the lowest size polydispersity. The latter is termed the PU seed particle method and resulted in particles with SAXS profiles indicating more complex morphologies. Reversal of the steps in the monomer solvent method, such that the acrylic monomers were polymerised before PU chain extension, increased the particle size polydispersity. For this reason, these two synthetic methods were rejected in favour the conventional monomer solvent method.

It transpires that different emulsification methods result in kinetic traps for unreacted particles containing methacrylic monomers. Subsequent polymerisation overcomes these traps and the final PUMA particles have essentially the same morphology. Although this demonstrates that the emulsification method has negligible effect on the final PUMA product for the studied formulation, polymer-into-water (PIW) emulsification was selected to produce samples for further studies. Incomplete phase inversion morphologies were kinetically trapped prior to acrylic polymerisation with water-into-polymer (WIP) emulsification. To ensure the consistency of time-resolved data during the acrylic polymerisation, PIW was deemed the favourable pathway and used for the further study on the effect on composition on PUMA morphology.

PUMA and PU/polystyrene (PS) samples were synthesised with methyl methacrylate (MMA), butyl methacrylate (BMA), iBMA and styrene at four PU/monomer ratios. The PU acid and hard block contents increase with acrylic content, due to the complexity of balancing viscosity and particle stability in the formulations. The minor population of supramolecular structures, observed in the PUDs, was also shown to be present in the PUMA and PU/PS samples, and their precursors. For precursors, the primary population is either particles with a monomer core and PU shell, or particles of phase-mixed PU and monomer. This was shown to be dependent on the compatibility of the monomer and the PU, according to their solubility parameters. BMA, MMA and iBMA, are compatible with the PU soft segment. Consequently, phase-mixed particles form with PUs comprising a high soft segment content. With low soft segment content PUs, or with styrene in all cases, phase separated particles, with a monomer core and PU shell, form. The exception is precursors containing MMA at low PU soft segment contents, where none of the monomer is found inside the particles, existing as large monomer droplets.

The final PUMAs containing PS with a PU/PS ratio of 80/20, or those containing poly(MMA) (PMMA), comprise a primary population of particles that are neither fully phase-separated core-shells, or fully phase-mixed homogenous spheres. The remaining PUMAs, however, comprise a primary population of core-shell particles. Samples containing PMMA and PS show the greatest morphology dependence on polymerisation concentration, due to the high glass transition temperatures ( $T_9$ s) restricting phase separation.

Time-resolved data, collected *in situ* during the polymerisation of acrylic from precursors to PUMAs, have SAXS patterns where scattering intensity at very small *q* increases throughout the reaction, or passes through a minimum. This is a product of the greater mass density of the acrylic/styrene polymers compared to the monomers, which in turn increases scattering length density. The minimum could be caused by an influx of monomer to the particles, causing an initial decrease in particle scattering length density.

A structural model, describing gradual polymerisation of particle cores, has been developed to perform analysis of time-resolved SAXS patterns collected during acrylic polymerisation. Although this model has limitations, due to the assumption of gradual polymerisation in particle cores, it produced satisfactory fitting curves to the profiles collected *in situ* during the polymerisation from precursor to final PUMA for a sample with a PU/iBMA ratio of 70/30. The obtained results showed that the monomer is mainly present in the sample as large droplets and feed of the monomer from droplets to PUMA particles takes place during the polymerisation. The rate of iBMA polymerisation is such that most of the core was always polymerised, with only a very small fraction of monomer, and the rate of polymerisation was controlled by the rate of monomer diffusion from the droplets to the particles.

# 7.2 Future Work

There are many directions in which the study of PUDs could be expanded. Through systematic variation in the acid content, the boundaries in which the structural model developed for PUDs is applicable could be explored. There is likely a lower acid content boundary, at which the minor population of supramolecular structures does not form. Additionally, there may be an upper boundary where high acidity in the formulation causes the formation of structural morphologies in PU dispersions different from spherical particles. It is important to understand the formation and nature of these supramolecular structures because they cause water susceptibility of the resulting films. This could be overcome with chemical cross-linking of the particles to prevent re-dispersion, or attempts to eliminate the supramolecular structures completely through composition or synthesis pathway.

The PU hard block and acid contents are intrinsically linked by the fixed NCO/OH ratio constraint applied to formulations in this thesis. Using a non-acidic chain extender, such as butanediol, in conjunction with DMPA, would facilitate isolation of the hard block content from the acid content. This way, their individual influences on molecule self-assembly and particle formation could be observed. There are many other ways to explore compositional space in PUDs. For example, in this work they are made with polyether soft block, however polyesters<sup>2–4</sup> and polycarbonates<sup>5,6</sup> are also commonly used in PU chemistry. Similarly, the HMDI used in this work could be substituted by an asymmetric alternative such as isophorone diisocyanate<sup>6</sup> or toluene diisocyanate.<sup>7</sup>

There is more work to be done in understanding the processes occurring during the monomer polymerisation from precursors to PUMAs. The development of SAXS structural models that better describe the morphologies occurring during the

polymerisation would offer further insight into the reaction processes. It would be of particular interest to understand how precursors comprising phase-mixed particles form PUMAs comprising core-shell particles. Additionally, a second method, such as Raman spectroscopy, could be used to track monomer conversion in conjunction with SAXS.<sup>8</sup> The more complex morphologies of PUMAs containing PMMA and low PS content could be revealed using contrast variation scattering techniques.<sup>9</sup> By altering the scattering length density of the solvent, the scattering length density of one of the phases could be matched, isolating the contribution to scattered intensity from the other.

The findings on PUMAs with homopolymers of acrylic should be expanded to investigate the copolymers that are used in commercial formulations. This would be especially interesting for polymer systems with various T<sub>g</sub>s, considering the fact that the final PUMA morphology is directed by the precursor morphology, particularly for polyacrylics with T<sub>g</sub> greater than the reaction temperature. In addition, the precursor morphology is dependent on the emulsification process, therefore this is an important step in controlling morphology. As such, emulsification will be the primary subject of interest in a follow-on PhD funded by AkzoNobel. If a method can be developed for collection of SAXS data *in situ* during emulsification, then better understanding of the processes occurring in WIP and PIW can be developed. By combining this with a time-resolved imaging method, such as optical microscopy, <sup>10</sup> processes occurring on both a macro and micro scale can be investigated. Moreover, whether these processes are primarily diffusion controlled, or influenced by mechanical stirring, can be studied across formulation space.

Ultimately, the work carried out for this thesis is intended to deepen the understanding of morphology control in PUDs and PUMAs to guide product development for

AkzoNobel. Logically, follow-on work should investigate the relationship between these morphologies, and the properties of the final product with respect to consumer interests.

# 7.3 References

- T. J. Neal, D. L. Beattie, S. J. Byard, G. N. Smith, M. W. Murray, N. S. J. Williams,
   S. N. Emmett, S. P. Armes, S. G. Spain and O. O. Mykhaylyk, *Macromolecules*,
   2018, 51, 1474–1487.
- 2 A. K. Nanda and D. A. Wicks, *Polymer (Guildf).*, 2006, **47**, 1805–1811.
- 3 A. Barni and M. Levi, *J. Appl. Polym. Sci.*, 2003, **88**, 716–723.
- 4 M. L. Hsaing, C. H. Chang, M. H. Chan and D. Y. Chao, *J. Appl. Polym. Sci.*, 2005, **96**, 103–112.
- 5 R. Hernandez, J. Weksler, A. Padsalgikar, C. Taeyi, E. Angelo, J. S. Lin, L. C. Xu, C. A. Siedlecki and J. Runt, *Macromolecules*, 2008, **41**, 9767–9776.
- 6 B. K. Kim, T. K. Kim and H. M. Jeong, *J. Appl. Polym. Sci.*, 1994, **53**, 371–378.
- S. M. Negim, S. Bahruddin, R. Mahyuddin and M. S. Idiris, *J. Appl. Polym. Sci.*,
   2011, 121, 8–13.
- 8 G. K. Bryant, H. F. Gleeson, A. J. Ryan, J. P. A. Fairclough, D. Bogg, J. G. P. Goossens and W. Bras, *Rev. Sci. Instrum.*, 1998, **69**, 2114.
- 9 O. O. Mykhaylyk, A. J. Ryan, N. Tzokova and N. Williams, *J. Appl. Crystallogr.*, 2007, **40**, 506–511.
- 10 R. M. Fernandez, K. A. Riske, L. Q. Amaral, R. Itri and M. T. Lamy, *Biochim. Biophys. Acta Biomembr.*, 2008, **1778**, 907–916.

# **Chapter 8 - Appendices**

# 8.1 Time Resolved GPC for PU Prepolymer

To check the polyurethane (PU)-prepolymer molecular weight distribution as a function of reaction time, the prepolymer synthesis of HB60\_SS1000 was followed by gel permeation chromatography (GPC). A 1L 4-necked flask (under N<sub>2</sub> atmosphere), equipped with a mechanical stirrer, a reflux condenser, and a thermocouple was charged with poly(tetramethylene oxide) PTMO (Mn =1000  $gmol^{-1}),$ dimethylolpropionic acid (DMPA) and methyl ethyl ketone (MEK). The mixture was heated to 70 °C using an oil bath while applying mild agitation. Next, hydrogenated methylene diphenyl diisocyanate (HMDI) was added as fast as possible, making sure the temperature of the solution did not exceed 92 °C (~15 min addition time). The batch temperature was maintained at 92 °C and samples (~2 g) taken after 1, 2, and 3 hours from the moment of complete HMDI addition. The free isocyanate in the samples was quenched by diluting in dry ethanol (100 wt%), and one drop of dibutyl tin dilaurate (DBTDL) added to catalyse the OH-NCO reaction at room temperature. The molecular weight distributions of the guenched samples were analysed by GPC, using an APC low 200 125 45 column and tetrahydrofuran/acetic acid as eluent, at 1 mlmin<sup>-1</sup> (10 µl injection volume). Refractive index was used as the detection method. The distribution plots are depicted in Figure 8.1.

Naturally, Figure 8.1 demonstrates that the PU molecular weight distribution is changing over time. The following observations can be made:

 The GPC data demonstrate that the reaction product consists of two molecular weight (MW) fractions:

- a. A high MW fraction which increases in intensity (larger area) and increases in MW (shifts to shorter retention times) throughout the reaction. This originates from the PTMO-rich PU pre-polymer chains which increase in MW while the conversion progresses.
- b. An oligomeric fraction producing GPC peaks which are reducing in intensity, therefore concentration, throughout time: this mostly originates from HMDI and DMPA. As the conversion progresses, some of these oligomers react to form higher MW chains, and as such are incorporated in the higher MW fraction.

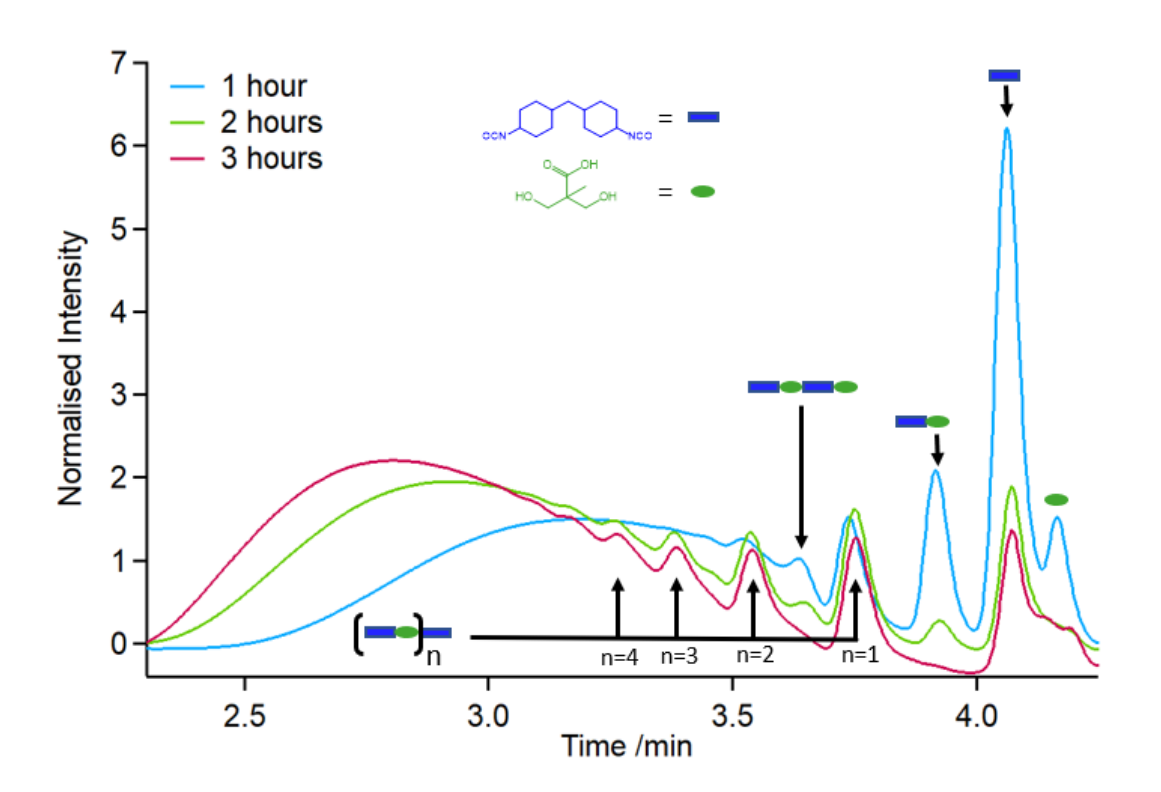


Figure 8.1: GPC retention time curves of sample taken at 1 hour (blue curve), 2 hours (green curve) and 3 hours (red curve) into the prepolymer reaction for HB60\_SS1000. Intensity is normalised by total area under the curve. The composition of prominent peaks comprising HMDI (blue rectangles) and DMPA (green circles) are labelled.

2. After 1 hour reaction time, the oligomeric fraction dominates the GPC spectrum in a comparison patter with the GPC results collected for the sample after 3 hours. Some signals (e.g., peaks at ~3.6 min and 3.9 min) reduce in intensity

to the baseline upon complete conversion. It is most likely that these signals originate from molecules with an equal number of HMDI and DMPA. Based on the observation that 3 hours at 92°C in the absence of catalyst is sufficient to reduce the intensity of these signals to the baseline, it is assumed that full conversion (no hydroxyl end groups due to the 1.5/1 NCO/OH ratio) is reached for all PU designs in 4 hours reaction time with catalyst. The peaks that remain in the low MW region (e.g., 3.40 minutes, 3.55 minutes and 3.75 minutes) most likely originate from isocyanate-capped molecules of *n* HMDI and *n-1* DMPA.

# 8.2 PUD SAXS Data Plotted on Absolute Scale of Intensity

SAXS profiles of polyurethane dispersions (PUDs) containing PTMO of Mn = 650 gmol<sup>-1</sup> and Mn = 2000 gmol<sup>-1</sup> presented in Figures 3.1a and 3.1c, respectively, are replotted on absolute scale of intensity (Figures 8.2a and 8.2b, respectively). These plots are provided for a comparison with the SAXS observations described for PUD made with PTMO of Mn = 1000 gmol<sup>-1</sup> (Figure 3.1b).

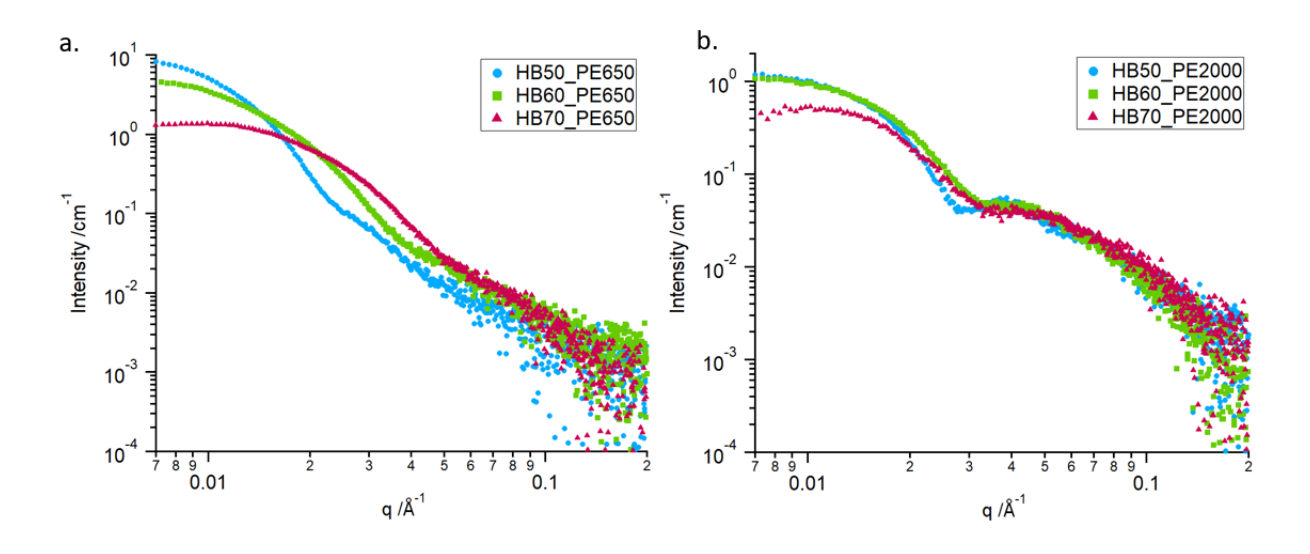


Figure 8.2: SAXS profiles for PUDs (1 wt% PU in water) containing SS of Mn a)650 gmol-1 and b) 2000 gmol-1, with 50% hard block (blue circles), 60% hard block (green squares) and 70% hard block (red triangles).

# **8.3** MALDI Sample Preparation and Data Collection

For all matrix-assisted laser desorption ionisation (MALDI) spectra, the raw files were processed in R Studio and the following data formatting methods (Table 8.1) were applied. In all run samples, the ion peak of interest [M-] was detected at 604 m/z, along with its isotope peaks.

Table 8.1: Formatting	a Methods applied to	o the processing	g of MALDI data	a collected on PUDs.

Data formatting step	Method
Transform Intensity	Square Root
Smooth Data	Savitzky
Baseline Correction	SNIP, iteration = 250
Normalise	Total Ion Count
Peak Alignment	halfWindowSize = 5, Signal-to-noise = 4, tolerance = 100e-6

# 8.4 PUD Solution Density Measurements

In order to measure PU density in the aqueous particle dispersions, solution density measurements were carried out at four PU concentrations, and for pure water. A linear equation was found for each data set (Figure 8.3). An extrapolation of the obtained linear equations to 100% PU gave polymer densities (Table 8.2).

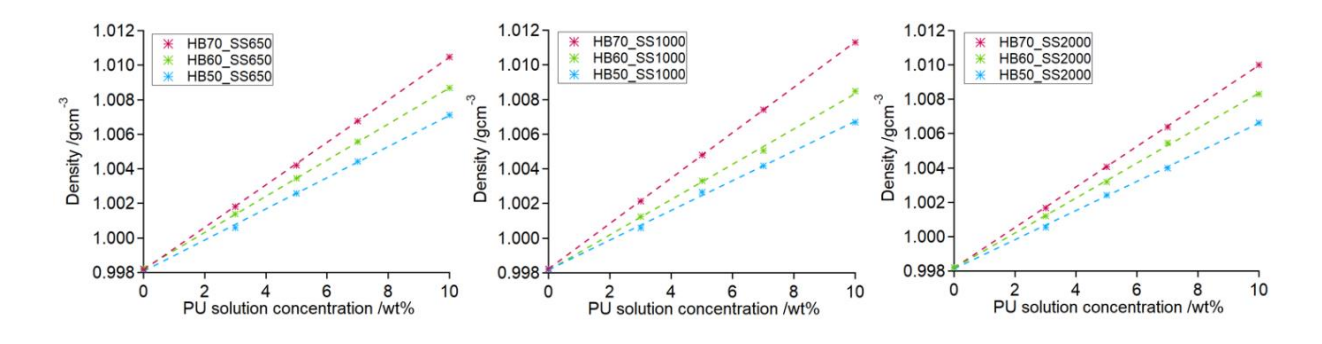


Figure 8.3: Solution density measurements for sample containing PTMO of Mn = a) 650 gmol<sup>-1</sup>, b) 1000 gmol<sup>-1</sup>, and c) 2000 gmol<sup>-1</sup> with 50% hard block (blue crosses), 60% hard block (green crosses) and 70% hard block (red crosses).

Table 8.2: Density of PU extrapolated from solution densities measured for PUD samples.

Sample	Density /gcm <sup>-3</sup>
HB50_SS650	1.1009
HB60_SS650	1.1033
HB70_SS650	1.1211
HB50_SS1000	1.0839
HB60_SS1000	1.1001
HB70_SS1000	1.1090
HB50_SS2000	1.0828
HB60_SS2000	1.1001
HB70_SS2000	1.1162

The PUD series with PTMO of  $Mn = 2000 \text{ gmol}^{-1}$  (Figure 8.4) was used to extrapolate the density of hard block and soft segment, which were found to be 1.1695 gcm<sup>-3</sup> and 0.9995 gcm<sup>-3</sup>, respectively.

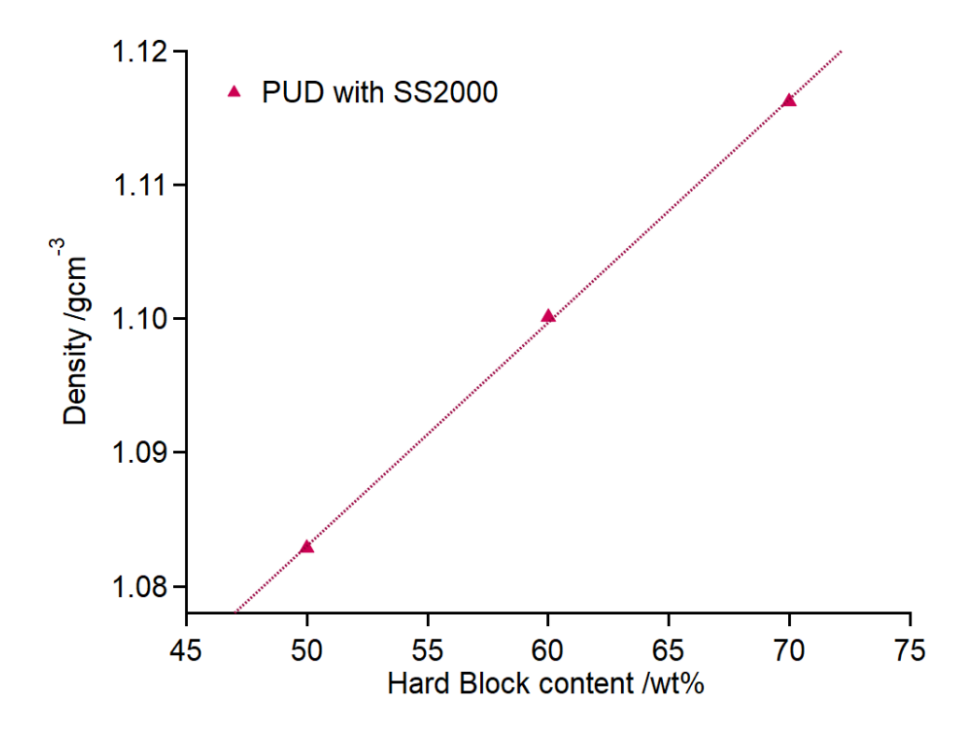


Figure 8.4: Density of PUDs containing PTMO of  $Mn = 2000 gmol^{-1}$ , fit with a linear equation, to obtain density values for hard block and soft segment

# 8.5 Subtraction of thermal background from film scattering

The diffuse scattering at high q from thermal background ( $I_b$ ) was removed from all the PU film data (Figure 4.6) by quantifying the positive deviation from Porod's Law:<sup>1,2</sup>

$$\lim_{q \to \infty} I(q) = \frac{K_{\rm p}}{q^4} + I_{\rm b} \ [Eq. 8.1]$$

where  $K_p$  is the Porod constant. For sharp interfaces, a straight line fit to a plot of  $I(q)^*q^4$  versus  $q^4$ , at high q, gives:

$$Iq^4 = K_p + I_b \cdot q^4 \quad [Eq. 8.2]$$

Thus,  $I_b$  is extracted from the gradient (Figure 8.5) and subtracted from I(q).

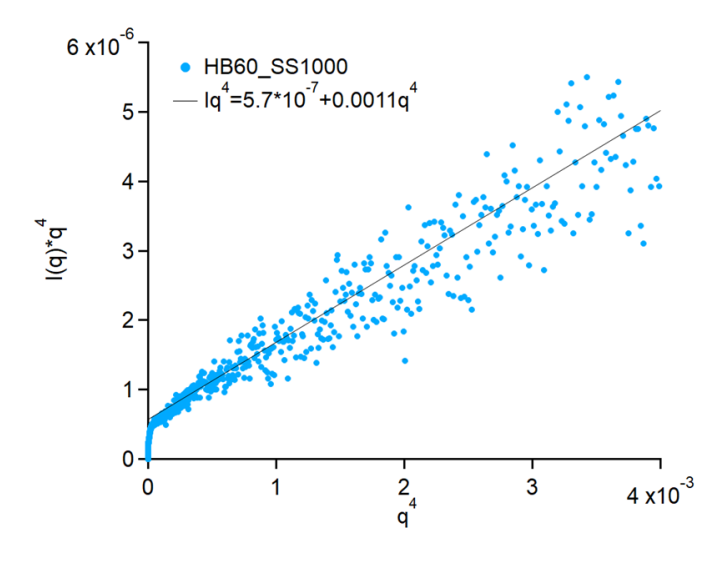


Figure 8.5: Porod plot for a film of a PUD made with 60% hard block content and PTMO of Mn = 1000 gmol<sup>-1</sup>, used to calculate the thermal background from the slope of a straight line fit to the linear region at high q.

# 8.6 The Gaussian Distribution

The polydispersity of a parameter, p, expressed as a Gaussian distribution, is defined as:

$$\Psi(p) = \frac{1}{\sqrt{2\pi\sigma_p^2}} e^{-\frac{(p-P)^2}{2\sigma_p^2}} \quad [Eq. 8.3]$$

where *P* is the mean of *p*, and  $\sigma_P$  is its standard deviation.

# 8.7 Lognormal Distribution of Particle Sizes

The standard deviation in the PUD particle radii,  $\Psi(r)$ , according to the lognormal size distribution is:

$$\Psi(r) = \frac{e^{-((\ln((r-\theta)/m))^2/(2\sigma^2))}}{(r-\theta)\sigma\sqrt{2\pi}} \quad [Eq. 8.4]$$

where  $\sigma$  is the shape parameter –the standard deviation of  $ln[r] - \theta$  is the location parameter (translation on the r axis) and m is the scale parameter.<sup>3</sup>

The geometric mean radius (R), according to the lognormal distribution, is related to the mean of ln[r]  $(\bar{R})$  as:

$$R = e^{\bar{R}} \quad [Eq. 8.5]$$

By definition of a lognormal distribution, ln[r] has a normal distribution, therefore values of  $\overline{R}$  were found by the fitting of a gaussian curve to ln(r) and used in Equation 8.5 for calculation of R.

Similarly, the multiplicative standard deviation<sup>4</sup> of R ( $\sigma$ \*) is related to  $\sigma$  by

$$\sigma^* = e^{\sigma} \quad [Eq. 8.6]$$

# 8.8 The "blob" model

Pedersen et al. proposed a "blob" model to describe the concentration fluctuation in micelles resulting from solvent swelling<sup>5</sup>. This has been adapted to describe PU particles in dispersion with internal water molecules where it was assumed that the water molecules are associated with the acidic units of the PU molecules and follow the polymer movement in the sample. Hence, the polymer molecule form factor could

be applied for describing water "blobs". Scattering from such particles, as a one population system, can be expressed by Equation 3.2 with the form factor defined as:

$$P_{1}(q,r) = (\Delta \xi)^{2} \left( V_{1}^{2}(r) A_{s}^{2}(q,r) - 2n_{bl} V_{bl} A_{bl}(q, R_{g,bl}) A_{s}^{2}(q,r) + n_{bl} (n_{bl} - 1) V_{bl}^{2} A_{bl}^{2}(q, R_{g,bl}) + n_{bl} V_{bl}^{2} D_{bl}(q, R_{g,bl}) \right) [Eq. 8.7]$$

 $A_{\rm s}$  and  $A_{\rm bl}$  are the scattering amplitudes of a sphere, and a Gaussian coil representing the "blob" (water pocket), respectively:

$$A_{\rm s}(q,r) = \frac{3[\sin(qr) - qr\cos(qr)]}{(qr)^3}$$
 [Eq. 8.8]

$$A_{\rm bl}(q, Rg_{\rm bl}) = \frac{1 - e^{-qRg_{\rm bl}}}{qR_{\rm g,bl}}$$
 [Eq. 8.9]

The form factor of a Gaussian polymer coil is given by the Debye function:

$$D_{\rm bl}(q, R_{\rm g,bl}) = \frac{2(e^{-qR_{\rm g,bl}} + qR_{\rm g,bl} - 1)}{(qR_{\rm g,bl})^2} \quad [Eq. 8.10]$$

 $Rg_{\rm bl}$ ,  $n_{\rm bl}$ , and  $V_{\rm bl}=\frac{4}{3}\pi R_{\rm g,bl}^{\ 3}$  are the radius of gyration, the relative number, and the volume occupied by a blob, respectively. r and  $V_1=\frac{4}{3}\pi r^3$  are the radius and volume of each spherical particle, respectively.  $\Delta\xi$  is the scattering length density difference between the PU and the water.

## 8.9 Densities of Polymethacrylics, Polystyrene, and Monomers

Table 8.3: Literature densities of acrylic & styrene monomers and polymers, used in precursors and final PUMAs

Material	Density /gcm <sup>-3</sup>
Styrene	0.91 <sup>6</sup>
BMA	0.89 <sup>7</sup>
iBMA	0.89 <sup>8</sup>
MMA	0.94 <sup>9</sup>
PS	1.05 <sup>6</sup>
PBMA	1.05 <sup>10</sup>
PiBMA	1.05 <sup>11</sup>
PMMA	1.18 <sup>12</sup>

# 8.10 Code for two-population fitting of PUD and PUMA samples.

The code used for fitting of the PUD and PUMA samples using Irena macro for Igor pro<sup>13</sup> is given in this section. The particles are assigned to populations 1 (*pop1*), the supramolecular structures to population 2 (*pop2*) and a dummy population to population 3 (*pop3*). The volume fraction term in the dummy population is assigned as the known concentration of polymer(s) in the sample.

The functions for the dummy populations and the supramolecular structures remain the same for all fittings. The code for the primary particle population is dependent on the nature, i.e. spherical PU particles, homogeneously phase-mixed PU/monomer particles, core-shell PUMA or PU/monomer particles, or partially reacted core-shell particles.

#### 8.10.1Code used for fitting of supramolecular structures (pop2)

```
//supramolecular structure calculations
Function IR1T GenGauss (Q, radius, par1, par2, par3, par4, par5) //returns the
generalized Gaussian coil
        variable Q, radius, par1, par2, par3, par4, par5
        variable Rg=radius
       variable nu=par3
       variable U=(2*nu+1)*(2*nu+2)*(Q*Rg)^2/6
        variable In=(U^{(1/2/nu)*gamma}(1/2/nu)-gamma(1/nu)-gamma(1/nu)
U^(1/2/nu) *gammaInc(1/2/nu,U) +gammaInc(1/nu,U)) /nu/U^(1/nu)
       variable SLDpol = par1 // scattering length density of the polymer
       variable SLDw = par2 // scattering length density of water
       variable contrast = (SLDpol-SLDw) //calculate polymer contrast with
water
       variable I PC=In*contrast^2 //contribution to scattering from
polymer coils
       return sqrt(I PC)
end
Function IR1T GenGaussV(radius, par1,par2,par3,par4,par5) //returns volume
of a polymer coil
        variable radius,par1,par2,par3,par4,par5
       variable Rg=radius
       variable nu=par3
       variable b = 10
        // PU Kuhn length
       variable Density = par4 // PU density
        variable LperM = par5 //define conversion from length to mass
        variable L = ((Rg*sqrt(6))/b^(1-nu))^(1/nu) //calculate polymer
length
       variable Mw = L/LperM //calculate molecular weight
       variable vol PC=(Mw/(Density*6.02*10^23))*10^24 // calculate volume
of polymer coil in Angstroms^3
       return vol PC
end
```

#### 8.10.2 Code for fitting of dummy population (pop3)

```
return 1
```

#### 8.10.3 Code for fitting of Spherical PU particles (pop1)

```
//particle calculations
Function IR1T Sphere (Q, radius, par1, par2, par3, par4, par5) //Sphere Form
factor
       variable Q, radius, par1,par2,par3,par4,par5
       variable QR=Q*radius
       NVAR fc1=root:Packages:IR2L NLSQF:Volume pop1
       NVAR fc2=root:Packages:IR2L NLSQF:Volume pop2
       NVAR fc3=root:Packages:IR2L NLSQF:Volume pop3
       fc2=fc3-fc1
       variable PqSP = (3/(QR*QR*QR))*(sin(QR)-(QR*cos(QR))) //form factor
of spherical particles
       variable vol SP = 4/3*pi*radius*radius*radius //calculate volume of
one particle
       variable SLDpol = parl // scattering length density of the polymer
       variable SLDw = par2 // scattering length density of water
       variable contrast = (SLDpol-SLDw) //calculate polymer particle
contrast with water in the particles
       variable I SP = PqSP^2*contrast^2 //calculate intensity from
spherical particles
       return sqrt(I SP)
end
Function IR1T SphereV(radius, par1,par2,par3,par4,par5)
       //returns the sphere volume
       variable radius, par1,par2,par3,par4,par5
       return 4/3*pi*radius*radius*radius
end
```

#### 8.10.4 Code for fitting of homogeneously phase-mixed PU/acrylic particles

```
// spherical particles of PU & acrylic calculations
Function mixedsphere(Q, radius, par1, par2, par3, par4, par5)
       variable Q, radius, par1,par2,par3,par4,par5
       //parl is volume fraction of total formulation that is PU (eq. 7030
would be 0.7)
       //par2 is PU SLD
       //par3 is Acrylic SLD
       //par4 is proportion of the total acrylic found in particles
       //par5 is not used
       //calculate volume fraction of the core-shell particles
       NVAR fc1=root:Packages:IR2L NLSQF:Volume pop1 //fc1 is vol fraction
of supramolecular structure
       NVAR fc2=root:Packages:IR2L NLSQF:Volume pop2 //fc2 is vol fraction
of coreshell particles
       NVAR fc3=root:Packages:IR2L NLSQF:Volume pop3 //fc3 is total vol
fraction of PUMA
```

```
variable ratioPU=par1 // par 1 is assigned to vol fraction of PU in
the PU/Ac blend
       variable formulated ratioAC=1-ratioPU //vol fraction of Ac in the
PU/AC blend is calculated
       variable ratioAC=par4*formulated ratioAC //accounting for some
acrylic not in the particles
       variable VfPU=fc3*ratioPU //volume fraction of PU in sample
       variable VfPU sph=VfPU-fc1 // volume fraction of PU in core-shell
       variable VfAc=fc3*ratioAc //volume fraction of acrylic in core-
shell particles
       fc2=VfAc+VfPU sph //volume concentration of mixed particles
       //calculate contrasts
       variable dist PC=fc1/VfPU
       variable sld PU=(par2-dist PC*10.91)/(1-dist PC) //calculate SLD of
the PU in the shell considering amount as H-bonded chains
       variable
sld sphere=sld PU*(VfPU sph/(VfPU sph+VfAc))+par3*(VfAC/(VfAc+VfPU sph))
       variable contrast = sld sphere-9.42
       //form factor calculations
       variable QR=Q*radius
       variable PqSP = (3/(QR*QR*QR))*(sin(QR)-(QR*cos(QR))) //spherical
form factor of core
       variable I SP=PqSP*PqSP*contrast*contrast
       return sqrt(I SP)
end
function mixedsphereV(radius,par1,par2,par3,par4,par5)
       variable radius, par1,par2,par3,par4,par5
       return 4/3*pi*radius*radius*radius
end
```

#### 8.10.5 Code for fitting of core-shell PUMA or PU/monomer particles

```
//coreshell particle calculations
Function CoSh FFPoints13(Q, radius, par1, par2, par3, par4, par5) //Core Shell
Sphere Form factor
       radius
       //parl is volume fraction of total formulation that is PU (eq. 7030
would be 0.7)
       //par2 is PU SLD
       //par3 is Acrylic SLD
       //par4 is variable
       //par5 is %stdev shell
       //it is assumed that shell thickness has gaussian distribution and
area under curve is 1, the programmed function represent 0.97 of the area,
the gaussian was split into 13 bands
       //calculate volume fraction of the core-shell particles
      NVAR fc1=root:Packages:IR2L NLSQF:Volume pop1 //fc1 is vol fraction
of supramolecular structure
       NVAR fc2=root:Packages:IR2L NLSQF:Volume pop2 //fc2 is vol fraction
of coreshell particles
```

```
NVAR fc3=root:Packages:IR2L NLSQF:Volume pop3 //fc3 is total vol
fraction of PUMA
       variable ratioPU=par1 // par 1 is assigned to vol fraction of PU in
the PU/Ac blend
       variable formulated ratioAC=1-ratioPU //vol fraction of Ac in the
PU/AC blend is calculated
       variable ratioAC=par4*formulated ratioAC //accounting for some
acrylic not in the particles
       variable VfPU=fc3*ratioPU //volume fraction of PU in sample
       variable VfPU CS=VfPU-fc1 // volume fraction of PU in core-shell
       variable VfAc=fc3*ratioAc //volume fraction of acrylic in core-
shell particles
       fc2=VfAc+VfPU CS //volume concentration of core-shell particles
       //calculate contrasts
       variable dist PC=fc1/VfPU
       variable sld sh=(par2-dist PC*10.91)/(1-dist PC) //calculate SLD of
the PU in the shell considering amount as H-bonded chains
       variable Contrast1 = (par3-sld sh) //*10^-10 core/shell contrast
       variable Contrast2 = (sld sh-9.42) //*10^-10 shell/water contrast
       //form factor calculations
       variable QR1=Q*radius
       variable Re1=3/(QR1*QR1*QR1)*(sin(QR1)-
QR1*cos(QR1))*Contrast1*(4/3*pi*radius^3) //spherical form factor of core
       //calculate shell thickness
       variable Vco=(4/3)*pi*radius*radius*radius //volume of core
       variable Pco=VfAC/fc2 //proportion of core-shell particle that is
       variable Psh=1-Pco //proportion of core shell particle that is PU
shell
       variable Vsh=Vco*(Psh/Pco) //volume of PU shell
       variable Vtot=Vco+Vsh //total volume
       variable Rtot=((3/4)*(Vtot/pi))^(1/3) //total radius
       variable t=Rtot-radius //shell thickness
       variable t dev=t*par5 //calculate stdev of shell
       //Now the shell, shell thickness is calculated t
       variable R2 = radius+t
       variable QR2=Q*R2
       variable Re2 = 3/(QR2*QR2*QR2)*(sin(QR2)-
QR2*cos(QR2))*Contrast2*(4/3*pi*R2^3)
       variable R3 = radius+t-12*t dev/6
       variable QR3=Q*R3
       variable Re3 = 3/(QR3*QR3*QR3)*(sin(QR3) -
QR3*cos(QR3))*Contrast2*(4/3*pi*R3^3)
       variable R4 = radius+t-10*t dev/6
       variable QR4=Q*R4
       variable Re4 = 3/(QR4*QR4*QR4)*(sin(QR4)-
QR4*cos(QR4))*Contrast2*(4/3*pi*R4^3)
       variable R5 = radius+t-8*t dev/6
       variable QR5=Q*R5
       variable Re5 = 3/(QR5*QR5*QR5)*(sin(QR5)-
QR5*cos(QR5))*Contrast2*(4/3*pi*R5^3)
       variable R6 = radius+t-6*t dev/6
       variable QR6=Q*R6
       variable Re6 = 3/(QR6*QR6*QR6)*(sin(QR6)-
QR6*cos(QR6))*Contrast2*(4/3*pi*R6^3)
       variable R7 = radius+t-4*t dev/6
```

```
variable QR7=Q*R7
                variable Re7 = 3/(QR7*QR7*QR7)*(sin(QR7)-
QR7*cos(QR7))*Contrast2*(4/3*pi*R7^3)
                variable R8 = radius+t-2*t dev/6
                variable QR8=Q*R8
                variable Re8 = 3/(QR8*QR8*QR8)*(sin(QR8)-
QR8*\cos(QR8)) *Contrast2* (4/3*pi*R8^3)
                variable R9 = radius+t+2*t dev/6
                variable QR9=Q*R9
                variable Re9 = 3/(QR9*QR9*QR9)*(sin(QR9)-
QR9*cos(QR9))*Contrast2*(4/3*pi*R9^3)
                variable R10 = radius+t+4*t dev/6
                variable QR10=Q*R10
                variable Re10 = 3/(QR10*QR10*QR10)*(sin(QR10) -
QR10*cos(QR10))*Contrast2*(4/3*pi*R10^3)
                variable R11 = radius+t+6*t dev/6
                variable QR11=Q*R11
                variable Re11 = 3/(QR11*QR11*QR11)*(sin(QR11) -
QR11*cos(QR11))*Contrast2*(4/3*pi*R11^3)
                variable R12 = radius+t+8*t dev/6
                variable QR12=Q*R12
                variable Re12 = 3/(QR12*QR12*QR12)*(sin(QR12)-
QR12*cos(QR12))*Contrast2*(4/3*pi*R12^3)
                variable R13 = radius+t+10*t dev/6
                variable QR13=Q*R13
                variable Re13 = 3/(QR13*QR13*QR13)*(sin(QR13) -
QR13*cos(QR13))*Contrast2*(4/3*pi*R13^3)
                variable R14 = radius+t+12*t dev/6
                variable QR14=Q*R14
                variable Re14 = 3/(QR14*QR14*QR14)*(sin(QR14) -
QR14*cos(QR14))*Contrast2*(4/3*pi*R14^3)
                //summ Result1 and Result2 together
                return
3/4/pi*sqrt(0.1324*((Re1+Re2)/R2^3)^2+0.0182*((Re1+Re3)/R3^3)^2+0.0334*((Re1+Re3)/R3^3)^2+0.0334*((Re1+Re3)/R3^3)^2+0.0334*((Re1+Re3)/R3^3)^2+0.0334*((Re1+Re3)/R3^3)^2+0.0334*((Re1+Re3)/R3^3)^2+0.0334*((Re1+Re3)/R3^3)^2+0.0334*((Re1+Re3)/R3^3)^2+0.0334*((Re1+Re3)/R3^3)^2+0.0334*((Re1+Re3)/R3^3)^2+0.0334*((Re1+Re3)/R3^3)^2+0.0334*((Re1+Re3)/R3^3)^2+0.0334*((Re1+Re3)/R3^3)^2+0.0334*((Re1+Re3)/R3^3)^2+0.0334*((Re1+Re3)/R3^3)^2+0.0334*((Re1+Re3)/R3^3)^2+0.0334*((Re1+Re3)/R3^3)^2+0.0334*((Re1+Re3)/R3^3)^2+0.0334*((Re1+Re3)/R3^3)^2+0.0334*((Re1+Re3)/R3^3)^2+0.0334*((Re1+Re3)/R3^3)^2+0.0334*((Re1+Re3)/R3^3)^2+0.0334*((Re1+Re3)/R3^3)^2+0.0334*((Re1+Re3)/R3^3)^2+0.0334*((Re1+Re3)/R3^3)^2+0.0334*((Re1+Re3)/R3^3)^2+0.0334*((Re1+Re3)/R3^2)^2+0.0334*((Re1+Re3)/R3^2)^2+0.0334*((Re1+Re3)/R3^2)^2+0.0334*((Re1+Re3)/R3^2)^2+0.0334*((Re1+Re3)/R3^2)^2+0.0334*((Re1+Re3)/R3^2)^2+0.0334*((Re1+Re3)/R3^2)^2+0.0334*((Re1+Re3)/R3^2)^2+0.0334*((Re1+Re3)/R3^2)^2+0.0334*((Re1+Re3)/R3^2)^2+0.0334*((Re1+Re3)/R3^2)^2+0.0334*((Re1+Re3)/R3^2)^2+0.0334*((Re1+Re3)/R3^2)^2+0.0334*((Re1+Re3)/R3^2)^2+0.0334*((Re1+Re3)/R3^2)^2+0.0334*((Re1+Re3)/R3^2)^2+0.0334*((Re1+Re3)/R3^2)^2+0.0334*((Re1+Re3)/R3^2)^2+0.034*((Re1+Re3)/R3^2)^2+0.034*((Re1+Re3)/R3^2)^2+0.034*((Re1+Re3)/R3^2)^2+0.034*((Re1+Re3)/R3^2)^2+0.034*((Re1+Re3)/R3^2)^2+0.034*((Re1+Re3)/R3^2)^2+0.034*((Re1+Re3)/R3^2)^2+0.034*((Re1+Re3)/R3^2)^2+0.034*((Re1+Re3)/R3^2)^2+0.034*((Re1+Re3)/R3^2)^2+0.034*((Re1+Re3)/R3^2)^2+0.034*((Re1+Re3)/R3^2)^2+0.034*((Re1+Re3)/R3^2)^2+0.034*((Re1+Re3)/R3^2)^2+0.034*((Re1+Re3)/R3^2)^2+0.034*((Re1+Re3)/R3^2)^2+0.034*((Re1+Re3)/R3^2)^2+0.034*((Re1+Re3)/R3^2)^2+0.034*((Re1+Re3)/R3^2)^2+0.034*((Re1+Re3)/R3^2)^2+0.034*((Re1+Re3)/R3^2)^2+0.034*((Re1+Re3)/R3^2)^2+0.03*((Re1+Re3)/R3^2)^2+0.03*((Re1+Re3)/R3^2)^2+0.03*((Re1+Re3)/R3^2)^2+0.03*((Re1+Re3)/R3^2)^2+0.03*((Re1+Re3)/R3^2)^2+0.03*((Re1+Re3)/R3^2)^2+0.03*((Re1+Re3)/R3^2)^2+0.03*((Re1+Re3)/R3^2)^2+0.03*((Re1+Re3)/R3^2)^2+0.03*((Re1+Re3)/R3^2)^2+0.03*((Re1+Re3)/R3^2)^2+0.03*((Re1+Re3)/R3^2)^2+0.03*((Re1+Re3)/R3^2)^2+
1+Re4)/R4^3)^2+0.0549*((Re1+Re5)/R5^3)^2+0.0807*((Re1+Re6)/R6^3)^2+0.1062*(
(Re1+Re7)/R7^3)^2+0.1253*((Re1+Re8)/R8^3)^2+0.1253*((Re1+Re9)/R9^3)^2+0.106
2*((Re1+Re10)/R10^3)^2+0.0807*((Re1+Re11)/R11^3)^2+0.0549*((Re1+Re12)/R12^3
)^2+0.0334*((Re1+Re13)/R13^3)^2+0.0182*((Re1+Re14)/R14^3)^2) //coreshell
form factor F
end
Function IR1T CoSh Volume13 (radius, par1,par2,par3,par4,par5)
                //returns the coreshell sphere volume
                variable radius, par1,par2,par3,par4,par5
                NVAR t=t
                return 4/3*pi*(radius+t)^3
end
8.10.6 Code for partially reacted core-shell particles
```

```
//partially reacted coreshell particle calculations
Function CoSh FFPoints13(Q, radius, par1, par2, par3, par4, par5) //Core Shell
Sphere Form factor
       variable Q, radius, par1,par2,par3,par4,par5 // q in A-1, core
radius
       //parl is proportion of iBMA polymerised
       //par2 is PU SLD
       //par3 is not used
       //par4 is the proportion of iBMA in the particles (x in chapter)
```

```
//par5 is %stdev shell
       //it is assumed that shell thickness has gaussian distribution and
area under curve is 1, the programmed function represent 0.97 of the area,
the gaussian was split into 13 bands
       //calculate volume fraction of the core-shell particles
       NVAR fc1=root:Packages:IR2L NLSQF:Volume pop1 //fc1 is vol fraction
of supramolecular structure
       NVAR fc2=root:Packages:IR2L NLSQF:Volume pop2 //fc2 is vol fraction
of coreshell particles
       NVAR fc3=root:Packages:IR2L NLSQF:Volume pop3 //fc3 is total vol
fraction of PUMA
       variable polyfrac=par1
       variable Acdensity = polyfrac*1.05+(1-polyfrac)*0.886 //caluclate
density of the acrylic phase
       variable TotV=70/1.08+30/Acdensity //renormlising PU/AC ratio by
volume
       variable ratioPU=(70/1.08)/TotV // caalculate the volfrac of the
PU/iBMA mix that is PU
       variable formulated ratioAC=1-ratioPU //vol fraction of Ac in the
PU/AC blend is calculated
       variable ratioAC=par4*formulated ratioAC //accounting for some
acrylic not in the particles
       variable VfPU=fc3*ratioPU //volume fraction of PU in sample
       variable VfPU CS=VfPU-fc1 // volume fraction of PU in core-shell
       variable VfAc=fc3*ratioAc //volume fraction of acrylic in core-
shell particles
       fc2=VfAc+VfPU CS //volume concentration of core-shell particles
       //calculate contrasts
       variable dist PC=fc1/VfPU
       variable sld sh=(10.24-dist PC*10.91)/(1-dist PC) //calculate SLD
of the PU in the shell considering amount as H-bonded chains
       variable sld co=(polyfrac/par4)*9.77+((par4-polyfrac)/par4)*8.24
//calculate SLD of core based on extent polymerised and x
       variable Contrast1 = (sld co-sld sh) //*10^-10 core/shell contrast
       variable Contrast2 = (sld sh-9.42) //*10^-10 shell/water contrast
       //form factor calculations
       variable QR1=Q*radius
       variable Re1=3/(QR1*QR1*QR1)*(sin(QR1)-
QR1*cos(QR1))*Contrast1*(4/3*pi*radius^3) //spherical form factor of core
       //calculate shell thickness
       NVAR t=root:Packages:IR2L NLSQF:FormFactor Param2 pop2
       variable Vco=(4/3)*pi*radius*radius*radius //volume of core
       variable Pco=VfAC/fc2 //proportion of core-shell particle that is
acrylic core
       variable Psh=1-Pco //proportion of core shell particle that is PU
shell
       variable Vsh=Vco*(Psh/Pco) //volume of PU shell
       variable Vtot=Vco+Vsh //total volume
       variable Rtot=((3/4)*(Vtot/pi))^(1/3) //total radius
       t=Rtot-radius //shell thickness
       variable t dev=t*par5 //calculate stdev of shell
       //Now the shell, shell thickness is calculated t
       variable R2 = radius+t
       variable QR2=Q*R2
```

```
variable Re2 = 3/(QR2*QR2*QR2)*(sin(QR2)-
QR2*cos(QR2))*Contrast2*(4/3*pi*R2^3)
                     variable R3 = radius+t-12*t dev/6
                     variable QR3=Q*R3
                     variable Re3 = 3/(QR3*QR3*QR3)*(sin(QR3)-
QR3*cos(QR3))*Contrast2*(4/3*pi*R3^3)
                     variable R4 = radius+t-10*t dev/6
                     variable QR4=Q*R4
                     variable Re4 = 3/(QR4*QR4*QR4)*(sin(QR4)-
QR4*cos(QR4))*Contrast2*(4/3*pi*R4^3)
                     variable R5 = radius+t-8*t dev/6
                     variable QR5=Q*R5
                     variable Re5 = 3/(QR5*QR5*QR5)*(sin(QR5)-
QR5*cos(QR5))*Contrast2*(4/3*pi*R5^3)
                     variable R6 = radius+t-6*t dev/6
                     variable QR6=Q*R6
                     variable Re6 = 3/(QR6*QR6*QR6)*(sin(OR6)-
QR6*cos(QR6))*Contrast2*(4/3*pi*R6^3)
                     variable R7 = radius+t-4*t dev/6
                     variable QR7=Q*R7
                     variable Re7 = 3/(QR7*QR7*QR7)*(sin(QR7)-
QR7*cos(QR7))*Contrast2*(4/3*pi*R7^3)
                     variable R8 = radius+t-2*t dev/6
                     variable QR8=Q*R8
                     variable Re8 = 3/(QR8*QR8*QR8)*(sin(QR8)-
QR8*cos(QR8))*Contrast2*(4/3*pi*R8^3)
                     variable R9 = radius+t+2*t dev/6
                     variable QR9=Q*R9
                     variable Re9 = 3/(QR9*QR9*QR9)*(sin(QR9) -
QR9*cos(QR9))*Contrast2*(4/3*pi*R9^3)
                     variable R10 = radius+t+4*t dev/6
                     variable QR10=Q*R10
                     variable Re10 = 3/(QR10*QR10*QR10)*(sin(QR10) -
QR10*\cos(QR10))*Contrast2*(4/3*pi*R10^3)
                     variable R11 = radius+t+6*t dev/6
                     variable QR11=Q*R11
                     variable Re11 = 3/(QR11*QR11*QR11)*(sin(QR11) -
QR11*cos(QR11))*Contrast2*(4/3*pi*R11^3)
                     variable R12 = radius+t+8*t dev/6
                     variable QR12=Q*R12
                     variable Re12 = 3/(QR12*QR12*QR12)*(sin(QR12)-
QR12*cos(QR12))*Contrast2*(4/3*pi*R12^3)
                     variable R13 = radius+t+10*t dev/6
                     variable QR13=Q*R13
                     variable Re13 = 3/(QR13*QR13*QR13)*(sin(QR13) -
QR13*cos(QR13))*Contrast2*(4/3*pi*R13^3)
                     variable R14 = radius+t+12*t dev/6
                     variable OR14=0*R14
                     variable Re14 = 3/(QR14*QR14*QR14)*(sin(QR14) -
QR14*cos(QR14))*Contrast2*(4/3*pi*R14^3)
                      //summ Result1 and Result2 together
                     return
3/4/pi*sqrt(0.1324*((Re1+Re2)/R2^3)^2+0.0182*((Re1+Re3)/R3^3)^2+0.0334*((Re1+Re3)/R3^3)^2+0.0334*((Re1+Re3)/R3^3)^2+0.0334*((Re1+Re3)/R3^3)^2+0.0334*((Re1+Re3)/R3^3)^2+0.0334*((Re1+Re3)/R3^3)^2+0.0334*((Re1+Re3)/R3^3)^2+0.0334*((Re1+Re3)/R3^3)^2+0.0334*((Re1+Re3)/R3^3)^2+0.0334*((Re1+Re3)/R3^3)^2+0.0334*((Re1+Re3)/R3^3)^2+0.0334*((Re1+Re3)/R3^3)^2+0.0334*((Re1+Re3)/R3^3)^2+0.0334*((Re1+Re3)/R3^3)^2+0.0334*((Re1+Re3)/R3^3)^2+0.0334*((Re1+Re3)/R3^3)^2+0.0334*((Re1+Re3)/R3^3)^2+0.0334*((Re1+Re3)/R3^3)^2+0.0334*((Re1+Re3)/R3^3)^2+0.0334*((Re1+Re3)/R3^3)^2+0.0334*((Re1+Re3)/R3^3)^2+0.0334*((Re1+Re3)/R3^3)^2+0.0334*((Re1+Re3)/R3^3)^2+0.0334*((Re1+Re3)/R3^3)^2+0.0334*((Re1+Re3)/R3^3)^2+0.0334*((Re1+Re3)/R3^3)^2+0.0334*((Re1+Re3)/R3^3)^2+0.0334*((Re1+Re3)/R3^2)^2+0.0334*((Re1+Re3)/R3^2)^2+0.0334*((Re1+Re3)/R3^2)^2+0.0334*((Re1+Re3)/R3^2)^2+0.0334*((Re1+Re3)/R3^2)^2+0.0334*((Re1+Re3)/R3^2)^2+0.0334*((Re1+Re3)/R3^2)^2+0.0334*((Re1+Re3)/R3^2)^2+0.0334*((Re1+Re3)/R3^2)^2+0.0334*((Re1+Re3)/R3^2)^2+0.0334*((Re1+Re3)/R3^2)^2+0.0334*((Re1+Re3)/R3^2)^2+0.0334*((Re1+Re3)/R3^2)^2+0.0334*((Re1+Re3)/R3^2)^2+0.0334*((Re1+Re3)/R3^2)^2+0.0334*((Re1+Re3)/R3^2)^2+0.0334*((Re1+Re3)/R3^2)^2+0.034*((Re1+Re3)/R3^2)^2+0.034*((Re1+Re3)/R3^2)^2+0.034*((Re1+Re3)/R3^2)^2+0.034*((Re1+Re3)/R3^2)^2+0.034*((Re1+Re3)/R3^2)^2+0.034*((Re1+Re3)/R3^2)^2+0.034*((Re1+Re3)/R3^2)^2+0.034*((Re1+Re3)/R3^2)^2+0.034*((Re1+Re3)/R3^2)^2+0.034*((Re1+Re3)/R3^2)^2+0.034*((Re1+Re3)/R3^2)^2+0.034*((Re1+Re3)/R3^2)^2+0.034*((Re1+Re3)/R3^2)^2+0.034*((Re1+Re3)/R3^2)^2+0.034*((Re1+Re3)/R3^2)^2+0.034*((Re1+Re3)/R3^2)^2+0.034*((Re1+Re3)/R3^2)^2+0.034*((Re1+Re3)/R3^2)^2+0.034*((Re1+Re3)/R3^2)^2+0.034*((Re1+Re3)/R3^2)^2+0.034*((Re1+Re3)/R3^2)^2+0.034*((Re1+Re3)/R3^2)^2+0.03*((Re1+Re3)/R3^2)^2+0.03*((Re1+Re3)/R3^2)^2+0.03*((Re1+Re3)/R3^2)^2+0.03*((Re1+Re3)/R3^2)^2+0.03*((Re1+Re3)/R3^2)^2+0.03*((Re1+Re3)/R3^2)^2+0.03*((Re1+Re3)/R3^2)^2+0.03*((Re1+Re3)/R3^2)^2+0.03*((Re1+Re3)/R3^2)^2+0.03*((Re1+Re3)/R3^2)^2+0.03*((Re1+Re3)/R3^2)^2+0.03*((Re1+Re3)/R3^2)^2+0.03*((Re1+Re3)/R3^2)^2+
1+Re4)/R4^3)^2+0.0549*((Re1+Re5)/R5^3)^2+0.0807*((Re1+Re6)/R6^3)^2+0.1062*(Re1+Re4)/R4^3)^2+0.0807*((Re1+Re4)/R4^3)^2+0.0807*((Re1+Re4)/R4^3)^2+0.0807*((Re1+Re4)/R4^3)^2+0.0807*((Re1+Re4)/R4^3)^2+0.0807*((Re1+Re4)/R4^3)^2+0.0807*((Re1+Re4)/R4^3)^2+0.0807*((Re1+Re4)/R4^3)^2+0.0807*((Re1+Re4)/R4^3)^2+0.0807*((Re1+Re4)/R4^3)^2+0.0807*((Re1+Re4)/R4^3)^2+0.0807*((Re1+Re4)/R4^3)^2+0.0807*((Re1+Re4)/R4^3)^2+0.0807*((Re1+Re4)/R4^3)^2+0.0807*((Re1+Re4)/R4^3)^2+0.0807*((Re1+Re4)/R4^3)^2+0.0807*((Re1+Re4)/R4^3)^2+0.0807*((Re1+Re4)/R4^3)^2+0.0807*((Re1+Re4)/R4^3)^2+0.0807*((Re1+Re4)/R4^3)^2+0.0807*((Re1+Re4)/R4^3)^2+0.0807*((Re1+Re4)/R4^3)^2+0.0807*((Re1+Re4)/R4^3)^2+0.0807*((Re1+Re4)/R4^3)^2+0.0807*((Re1+Re4)/R4^3)^2+0.0807*((Re1+Re4)/R4^3)^2+0.0807*((Re1+Re4)/R4^3)^2+0.0807*((Re1+Re4)/R4^3)^2+0.0807*((Re1+Re4)/R4^3)^2+0.0807*((Re1+Re4)/R4^3)^2+0.0807*((Re1+Re4)/R4^3)^2+0.0807*((Re1+Re4)/R4^3)^2+0.0807*((Re1+Re4)/R4^3)^2+0.0807*((Re1+Re4)/R4^3)^2+0.0807*((Re1+Re4)/R4^3)^2+0.0807*((Re1+Re4)/R4^3)^2+0.0807*((Re1+Re4)/R4^3)^2+0.0807*((Re1+Re4)/R4^3)^2+0.0807*((Re1+Re4)/R4^3)^2+0.0807*((Re1+Re4)/R4^3)^2+0.0807*((Re1+Re4)/R4^3)^2+0.0807*((Re1+Re4)/R4^3)^2+0.0807*((Re1+Re4)/R4^3)^2+0.0807*((Re1+Re4)/R4^3)^2+0.0807*((Re1+Re4)/R4^3)^2+0.0807*((Re1+Re4)/R4^3)^2+0.0807*((Re1+Re4)/R4^3)^2+0.0807*((Re1+Re4)/R4^3)^2+0.0807*((Re1+Re4)/R4^3)^2+0.0807*((Re1+Re4)/R4^3)^2+0.0807*((Re1+Re4)/R4^2)^2+0.0807*((Re1+Re4)/R4^2)^2+0.0807*((Re1+Re4)/R4^2)^2+0.0807*((Re1+Re4)/R4^2)^2+0.0807*((Re1+Re4)/R4^2)^2+0.0807*((Re1+Re4)/R4^2)^2+0.0807*((Re1+Re4)/R4^2)^2+0.0807*((Re1+Re4)/R4^2)^2+0.0807*((Re1+Re4)/R4^2)^2+0.0807*((Re1+Re4)/R4^2)^2+0.0807*((Re1+Re4)/R4^2)^2+0.0807*((Re1+Re4)/R4^2)^2+0.0807*((Re1+Re4)/R4^2)^2+0.0807*((Re1+Re4)/R4^2)^2+0.0807*((Re1+Re4)/R4^2)^2+0.0807*((Re1+Re4)/R4^2)^2+0.0807*((Re1+Re4)/R4^2)^2+0.0807*((Re1+Re4)/R4^2)^2+0.0807*((Re1+Re4)/R4^2)^2+0.0807*((Re1+Re4)/R4^2)^2+0.0807*((Re1+Re4)/R4^2)^2+0.0807*((Re1+Re4)/R4^2)^2+0.0807*((Re1+Re4)/R4^2)^2+0.0807*((Re1+Re4)/R4^2)^2+0.0807*((Re1+Re4)/R4^2)^2+0.0807*((Re1+Re4)/R4^2)^2+0.
(Re1+Re7)/R7^3)^2+0.1253*((Re1+Re8)/R8^3)^2+0.1253*((Re1+Re9)/R9^3)^2+0.106
2*((Re1+Re10)/R10^3)^2+0.0807*((Re1+Re11)/R11^3)^2+0.0549*((Re1+Re12)/R12^3
)^2+0.0334*((Re1+Re13)/R13^3)^2+0.0182*((Re1+Re14)/R14^3)^2) //coreshell
form factor F
end
```

```
Function IR1T_Cosh_Volume13(radius, par1,par2,par3,par4,par5)
    //returns the coreshell sphere volume
    variable radius, par1,par2,par3,par4,par5
    NVAR t=t
    return 4/3*pi*(radius+t)^3
end
```

### 8.11 References

- 1 G. Porod, Kolloid-Zeitschrift, 1951, **124**, 83–114.
- A. J. Ryan, W. Bras, G. R. Mant and G. E. Derbyshire, *Polymer (Guildf).*, 1994,
   35, 4537–4544.
- National Institute of Standards and Technology (U.S. Department of Commerce),
  Lognormal Distribution,
  https://www.itl.nist.gov/div898/handbook/eda/section3/eda3669.htm, (accessed
  5 January 2023).
- 4 G. Herdan, Small Particle Statistics, Butterworths, London, 2nd rev ed., 1960.
- J. S. Pedersen, I. W. Hamley, C. Y. Ryu and T. P. Lodge, *Macromolecules*, 2000, **33**, 542–550.
- 6 W. Patnode and W. J. Scheiber, *J. Am. Chem. Soc.*, 1939, **61**, 3449–3451.
- J. Wisniak, G. Cortez, R. D. Peralta, R. Infante, L. E. Elizalde, T. A. Amaro, O. García and H. Soto, *J. Chem. Thermodyn.*, 2008, **40**, 1671–1683.
- 8 R. J. S. Lewis, *Hawley's Condensed Chemical Dictionary*, John Wiley & Sons, Incorporated, New York, NY, 15th Editi., 2007.
- 9 N. L. of Medicine, Hazardous Substances Data Bank Methyl Methacrylate, https://pubchem.ncbi.nlm.nih.gov/source/hsdb/195, (accessed 7 August 2023).
- 10 W. C. Child and J. D. Ferry, *J. Colloid Sci.*, 1957, **12**, 327–341.
- 11 G. Z. Li, H. Cho, L. Wang, H. Toghiani and C. U. Pittman, *J. Polym. Sci. Part A Polym. Chem.*, 2005, **43**, 355–372.
- 12 R. Goseki and T. Ishizone, *Encyclopedia of Polymeric Nanomaterials*, Springer Berlin Heidelberg, Berlin, Heidelberg, 2015.
- 13 J. Ilavsky and P. R. Jemian, *J. Appl. Crystallogr.*, 2009, **42**, 347–353.